



Title	High-Pressure Synthesis, Crystal Structures and Physical Properties of Perovskite-Related Mercury and Osmium Oxides
Author(s)	陳, 潔
Citation	北海道大学. 博士(理学) 甲第13807号
Issue Date	2019-09-25
DOI	10.14943/doctoral.k13807
Doc URL	<a href="http://hdl.handle.net/2115/79299">http://hdl.handle.net/2115/79299</a>
Type	theses (doctoral)
File Information	Jie_Chen.pdf



[Instructions for use](#)

# **High-Pressure Synthesis, Crystal Structures and Physical Properties of Perovskite- Related Mercury and Osmium Oxides**

A Thesis

Submitted by

Jie Chen

In fulfillment for the award of the degree of

**Doctor of Science**

**Graduate School of Chemical Sciences and Engineering**

**Hokkaido University**

**2019**



## Abstract

Transition metal oxides with partially filled  $3d$  and  $4d$  shells have dominated materials research in past decades, while  $5d$  oxides are being of great current interest as  $5d$  oxides exhibit spectacular phenomena. The unique properties of  $5d$  oxides stem from the nature of  $5d$  electrons themselves. On one hand, upon descending the periodic table from the  $3d$  to  $5d$  series, the  $d$  orbitals become spatially extended, resulting in smaller on-site Coulomb repulsion for  $5d$  electrons. On the other hand, the spin-orbit coupling increases considerably in  $5d$  orbital, leading to enhanced splitting degenerate orbitals and bands. The interplay between spin-orbit coupling, Coulomb repulsion and crystal-electric field can lead to novel phases of matter. In this thesis, eight  $5d$  oxides were synthesized under high-pressure and high-temperature conditions to elucidate the novel physical properties involving  $5d$  oxides.

Chapter 1 is the introduction of background behind this thesis. Chapter 2 provides information about the experimental methods and technologies used in this thesis.

In Chapter 3,  $\text{HgPbO}_3$  is introduced, which was synthesized at 6 GPa and its crystal structure was studied by single-crystal X-ray diffraction and powder synchrotron X-ray diffraction measurements.  $\text{HgPbO}_3$  crystallizes into a hexagonal structure ( $R\bar{3}m$ ) with  $a = 5.74413(6)$  Å and  $c = 7.25464(8)$  Å. The metallic behavior was observed from temperature dependence of resistivity measurement for  $\text{HgPbO}_3$ , but its weak temperature dependence of the electrical resistivity, significant diamagnetism, and remarkably small Sommerfeld coefficient imply that  $\text{HgPbO}_3$  is a semimetal. The discovery of semimetal in oxide compounds is quite rare, which could be useful for the advanced material research and the development of multifunctional devices.

Chapter 4 summarizes two new osmium triple perovskite oxides synthesized at 6 GPa and 1100 °C; a polymorph of the triple perovskite  $\text{Ba}_3\text{CuOs}_2\text{O}_9$ , which exists in the orthorhombic phase ( $Cmcm$ ), is reported. The crystal structure of  $\text{Ba}_3\text{CuOs}_2\text{O}_9$  transfers to a

hexagonal structure ( $P6_3/mmc$ ) under a high-pressure and high-temperature condition. Although  $\text{Ba}_3\text{CuOs}_2\text{O}_9$  maintains the 6H perovskite-type lattice basis, the distribution of Cu and Os atoms are dramatically altered over the lattice. The new distribution brings about distinct magnetic properties; for example, the hexagonal  $\text{Ba}_3\text{CuOs}_2\text{O}_9$  exhibits a ferrimagnetic transition at 290 K in stark contrast to the antiferromagnetic transition at 47 K exhibited by the orthorhombic  $\text{Ba}_3\text{CuOs}_2\text{O}_9$ . Furthermore, it was achieved by replacement of Cu by Ni that the  $T_c$  was successfully increased to 370 K for  $\text{Ba}_3\text{NiOs}_2\text{O}_9$ . In this chapter, a new class of  $3d$ - $5d$  hybrid ferrimagnetic materials with high- $T_c$  emerged from the application of high-pressure technique.  $\text{Ba}_3\text{CuOs}_2\text{O}_9$  as well as  $\text{Ba}_3\text{NiOs}_2\text{O}_9$  could serve as a worthwhile platform for developing high- $T_c$  ferrimagnetic material.

In Chapter 5, the study of substitutional series double perovskite oxides  $\text{Sr}_2\text{Cr}_{1-x}\text{Ni}_x\text{OsO}_6$  ( $x = 0, 0.25, 0.5, 0.75$  and  $1$ ) prepared at 6 GPa is presented.  $\text{Sr}_2\text{Cr}_{1-x}\text{Ni}_x\text{OsO}_6$  ( $x = 0, 0.25, 0.5, 0.75$  and  $1$ ) exhibit structural transition from cubic to tetragonal at  $x = 0.5$ . The former three samples ( $x = 0, 0.25$  and  $0.5$ ) exhibit ferrimagnetic ordering below  $T_c$ , while the other two Ni-rich samples ( $x = 0.75$  and  $1$ ) are antiferromagnetic. Remarkable variation of the magnetic properties among the five samples seems not to be simply explained by the structural transition, but rather by  $5d$  electron nature. The series of Ni-substituted  $\text{Sr}_2\text{CrOsO}_6$  likely gives an insight into the effect of spin-orbital coupling on the novel physical properties.

In Chapter 6, the general conclusion is provided, and prospects for future research of  $5d$  oxide are presented.

**Keywords:**

$5d$  transition metal, High-pressure synthesis, Crystal structure, transport property, magnetic property

## List of Abbreviations

LN	LiNbO <sub>3</sub>
TM	Transition metal
SOC	Spin-orbit coupling
CEF	Crystal-electric field
$T_C$	Curie temperature
VB	Valence band
CB	Conduction band
ARPES	Angle-resolved photoemission spectroscopy
CFS	Crystal field splitting
MIT	Metal-Insulator transition
AF	Antiferromagnetic
$E_F$	Fermi energy
2D	Two-dimensional
3D	Three-dimensional
VRH	Variable-range hopping
DPO	Double perovskite oxide
$T_c$	Critical temperature
XMCD	X-ray magnetic circular dichroism
MPMS	Magnetic property measurement system

PPMS	Physical property measurement system
NIMS	National Institute for Materials Science
XRD	X-ray diffraction
SPring-8	Super Photon ring-8 GeV
SXRD	Synchrotron X-ray diffraction
FC	Field cooling
ZFC	Zero field cooling
FIM	Ferrimagnetic
FM	Ferromagnetic
DOS	Density of states
$t$	Tolerance factor
$\theta$	Weiss temperature
$C$	Curie constant
$\mu_{\text{eff}}$	Effective magnetic moment
$\mu_{\text{s}}$	Spin only magnetic moment
BVS	Bond valance sum
$C_{\text{p}}$	Heat capacity
$T_{\text{N}}$	Neel temperature

# High-Pressure Synthesis, Crystal Structures and Physical Properties of *5d* Transition Metal Oxides

## Contents

Chapter 1 Introduction .....	1
1.1 Crystal structure .....	1
1.1.1 lithium niobite ( $\text{LiNbO}_3$ ) structure.....	1
1.1.2 Perovskite structure.....	2
1.2 <i>5d</i> metal oxides .....	5
1.3 Some novel physical properties of d-block metal compounds .....	7
1.3.1 Ferroelectricity .....	7
1.3.2 Semimetal .....	8
1.3.3 Half metallicity .....	10
1.3.4 Metal-Insulator transition (MIT).....	12
1.3.5 High- $T_c$ ferrimagnetism in double perovskite oxides .....	15
1.4 Objectvie of this thesis.....	17
References in Chapter 1 .....	19
Chapter 2 Experimental methods.....	29
2.1 Sample preparation: high-pressure method .....	29
2.1.1 Belt-type high-pressure apparatus (Kobe Steel, Ltd.).....	29
2.1.2 Multi-anvil-type high-pressure apparatus (CTF-MA1500P, C&T Factory Co., Ltd, Japan).....	30



2.2 X-ray diffraction measurement .....	31
2.2.1 Laboratory powder X-ray diffraction.....	32
2.2.2 Synchrotron powder X-ray diffraction.....	32
2.2.3 Single crystal X-ray diffraction.....	34
2.3 Magnetic properties measurement .....	34
2.4 Electrical properties measurement .....	35
2.5 Thermal properties measurement.....	35
References in chapter 2 .....	36
Chapter 3 High-pressure synthesis, crystal structure, and semi-metallic properties of $\text{HgPbO}_3$ .....	37
3.1 Introduction.....	37
3.2 Experimental details.....	38
3.3 Results and discussion .....	40
3.4 Summary of Chapter 3 .....	58
References in Chapter 3 .....	59
Chapter 4 High-pressure synthesis, crystal structure, and magnetic properties of $\text{Ba}_3\text{CuOs}_2\text{O}_9$ and $\text{Ba}_3\text{NiOs}_2\text{O}_9$ .....	65
4.1 Crystal structure and magnetic properties of hexagonal $\text{Ba}_3\text{CuOs}_2\text{O}_9$ : a ferrimagnetic material with large coercive field .....	67
4.1.1 Experimental Details.....	67
4.1.2 Results and Discussion .....	68
4.2 Crystal structure and magnetic properties of hexagonal $\text{Ba}_3\text{NiOs}_2\text{O}_9$ .....	86

4.2.1 Experiment Details.....	86
4.2.2 Results and Discussion .....	87
4.3 Summary of Chapter 4 .....	99
References in chapter 4 .....	100
Chapter 5 The evolution of structure and magnetic properties from $\text{Sr}_2\text{CrOsO}_6$ to $\text{Sr}_2\text{NiOsO}_6$ by substitution.....	108
5.1 Introduction.....	108
5.2 Experimental Details.....	110
5.3 Results and Discussion .....	111
5.4 Summary of chapter 5 .....	138
References in chapter 5 .....	140
Chapter 6 General Conclusions and Future Prospects .....	146
6.1 General Conclusions .....	146
6.2 Future Prospects.....	148
References in chapter 6 .....	149
List of appended publications .....	151
Acknowledgement .....	153

# Chapter 1 Introduction

## 1.1 Crystal structure

To search for new materials for developing of magnetic, electronic and optical functions is one of the main aims in materials science. A fundamental methodology for materials science stems from the structure–property relations. The wealth of physical properties observed in solid-state chemistry can be contributed from diverse type of structures, compositions, various cation orderings, distortional transitions, and defects or vacancy compensation. [1].  $ABO_3$  -type oxide with plenty of types have been studied extensively in solid-stated chemistry. Most of oxide compounds with lithium niobite ( $LiNbO_3$ ) structure, perovskite structure, ilmenite structure and corundum structure can be denoted as  $ABO_3$  -type oxide. The lithium niobite ( $LiNbO_3$ ) and perovskite structure will be discussed in detail.

### 1.1.1 lithium niobite ( $LiNbO_3$ ) structure

In the LN-type structures, two-thirds of the octahedra sites are occupied by the cations (A or B) and vacancy fill another one third. The cations arrange long the  $c$  axis as A-B-Vacancy-A-B-Vacancy-A-... and A and B cations are located in the plane perpendicular to the  $c$  axis [2]. As shown in Fig 1.1, each layer in the  $LiNbO_3$  contains both  $NbO_6$  and  $LiO_6$  in equal proportions.

$LiNbO_3$  was discovered to be a ferroelectric material [3]. In the paraelectric phase of  $LiNbO_3$  (above Curie temperature), the Li atoms are located either above or below the oxygen layers by  $0.37\text{\AA}$ , which can be regarded as lying in an oxygen layer in average. Nb atoms are centered between these oxygen layers which is  $c/4$  away from Li atoms. The positions of Li and Nb atoms make it non-polar [4]. When the temperatures below its ferroelectric Curie temperature, the Li and Nb atoms are forced to shift into new positions. The separation of

charge stems from the shifts of Li and Nb atoms relative to oxygen octahedra, which leads to displacement ferroelectrics.

Only a limited number of  $\text{LiNbO}_3$ -type oxides have been synthesized at ambient pressure, for example,  $\text{LiReO}_3$  [5],  $(\text{Li}, \text{Cu})\text{TaO}_3$  [6], and  $\text{Li}_{1-x}\text{Cu}_x\text{NbO}_3$  [7] were prepared by high-temperature solid state reaction. High-pressure and high-temperature conditions have been regarded as an efficient technique for stabilizing  $\text{LiNbO}_3$ -type oxides such as  $\text{FeMO}_3$  ( $M = \text{Ti}, \text{Ge}$ ) [8, 9],  $\text{MnMO}_3$  ( $M = \text{Ti}, \text{Sn}$ ) [10, 11],  $\text{ZnGeO}_3$  [12],  $\text{ZnSnO}_3$  [13].

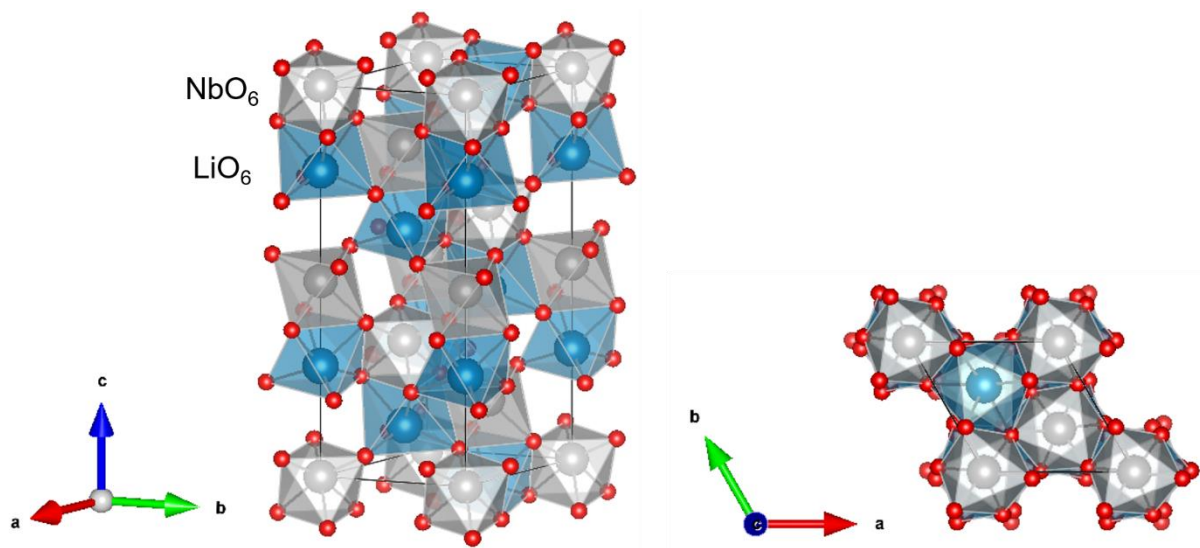


**Fig. 1.1** Crystal structure of  $\text{LiNbO}_3$  at 297 K. Space group:  $R3c$  (hexagonal; no. 161); lattice constants  $a = 5.14829(2) \text{ \AA}$ ,  $c = 13.8631(4) \text{ \AA}$  [4]

### 1.1.2 Perovskite structure

When the A cations in  $\text{ABO}_3$  require a higher coordination number and longer bond length than B cations, the perovskite structure can form. Ideally, perovskite structure is cubic lattice that consists of a framework of regular  $\text{BO}_6$  octahedra linked by their corners (shown in **Fig. 1.2**). A atoms are located at the interstices between arrays of  $\text{BO}_6$  octahedra, which are surrounded by 12 anions.

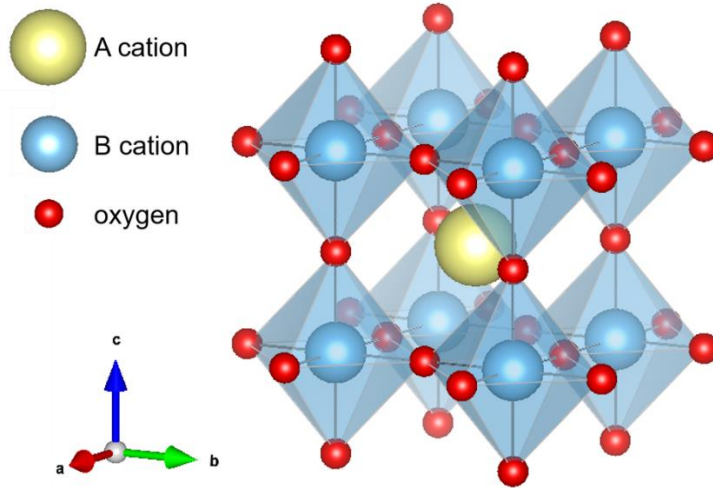


**Fig. 1.2** Crystal structure of ideal cubic perovskite ( $\text{ABO}_3$ )

The interconnected framework of perovskite structure formed can be distorted by tilting or puckering of the octahedra, whereby the bond lengths of A-O change and coordination number decreases from 12 to 10, 8, or even smaller. The distortion from ideal cubic perovskite structure allows a wider range of cations to be accommodated. A tolerance factor,  $t$ , can describe the distortion of perovskite as

$$t = \frac{r_{AO}}{\sqrt{2}r_{BO}}$$

where  $r_{AO}$  and  $r_{BO}$  are bond lengths of A-O and B-O. The ideal cubic perovskite is presented if  $t = 1$ . If  $t$  deviates from 1, a distorted perovskite will form. Resulting from the structural flexibility, perovskites possesses compositional flexibility.

Chemical substitution makes perovskite-structure compounds much more abundant. In particular, substitution of B cations has been studied widely, in order to improve physical properties of materials.  $A_2BB'\text{O}_6$  is a kind of significant B-substituted double perovskite, in which B and B' cations take on an ordered pattern. Generally, a great difference in oxidation states of B and B' leads to an ordered arrangement. The cation ordering in double perovskite was identified as three simple patterns that can be for either the A- or B-site cations. These three

types of B-site ordering in  $A_2BB'O_6$  are shown in **Fig. 1.3** [14].



**Fig. 1.3** B-site ordering schemes in double perovskites  $A_2BB'O_6$  [14]

Generally, plenty of perovskite oxides are formed by a closed-packed arrangement of A-cation layers with B cations occupying octahedral positions. There are three stacking sequences of the A-cation layers, cubic (ABC), hexagonal (ABAB), and a combination of ABC and ABAB. The cubic close packing (ccp) structure leads to a family of perovskite compound where all  $BO_6$  octahedra linked by corners. The hexagonal close packing (hcp) perovskites consists of infinite strings of face-sharing  $BO_6$  octahedra. Combinations of cubic and hexagonal stacking of A-cation layers lead to a wide varieties of perovskite compounds containing corner-sharing and face-sharing octahedra. The number of layers and symmetry can be denoted as  $nL$ ,  $nH$ , and  $nR$ , where L or H is hexagonal and R represents rhombohedral [15]. Derived from double perovskite, 4H (chch), 6H (cchcch) and 8H (chhhchhh) hexagonal-perovskite polytypes can be produced [16-18]. Among these hexagonal-perovskite polytypes, 6H structure is the most common. An example of 6H double perovskite  $Ba_3MRu_2O_9$  ( $M = Y, In, La, Sm, Eu$ , and  $Lu$ ) is shown in **Fig. 1.4**, comprising dimeric units of face-sharing octahedra and octahedra.

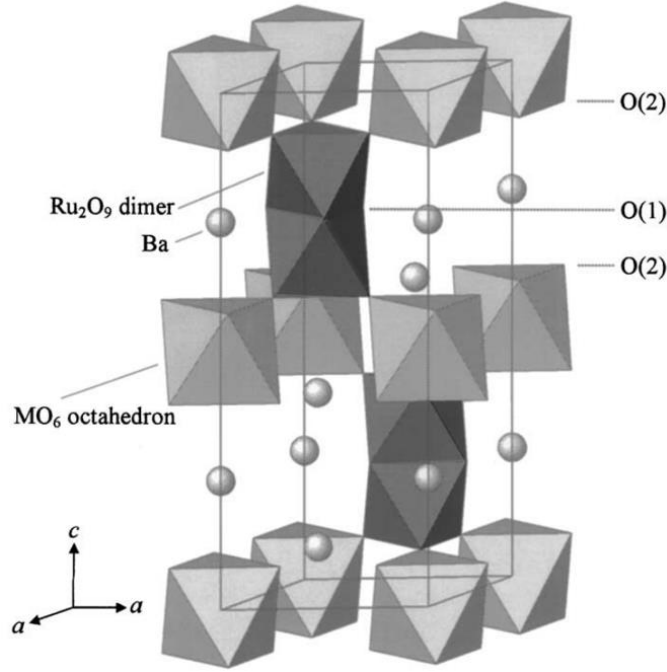


**Fig. 1.4** The crystal structure of  $\text{Ba}_3\text{MRu}_2\text{O}_9$  ( $\text{M} = \text{Y, In, La, Sm, Eu, and Lu}$ ) [19]

## 1.2 *5d* metal oxides

Oxides containing the third-row (*5d*) metals display an impressive variety of physical properties and become the platform to investigate novel materials. Various anomalous electronic or magnetic properties have been observed in the *5d* metal oxides. The *5d* oxides have been attracting much attention as a candidate of Mott insulator in the past few years. Iridate oxide  $\text{Sr}_2\text{IrO}_4$  is the most famous one that was revealed to be the  $J_{\text{eff}} = 1/2$  Mott ground state by both measurements and first-principles electronic structure calculations [20, 21]. Further, the Mott physics of  $\text{Sr}_2\text{IrO}_4$  leads to a series of interesting predictions about  $\text{Sr}_2\text{IrO}_4$ -related *5d* oxides, such as the high  $T_c$  superconductivity [22], topological insulating behavior [23], quantum spin liquid [24], and etc. In addition, topological semimetal was realized in a class of pyrochlore iridates such as  $\text{Y}_2\text{Ir}_2\text{O}_7$  [25]. Some novel phenomena have been also discovered in osmate oxides, such as extremely high-temperature ferrimagnetism [26], metallic ferroelectricity [27], ferromagnetic Dirac-Mott insulating state [28], and Slater insulating

property [29].

The unique properties of  $5d$  oxides stem from the nature of  $5d$  electrons themselves. Upon descending the periodic table from the  $3d$  to  $5d$  series, the  $d$  orbitals become spatially extended, resulting in smaller on-site Coulomb repulsion ( $U$ ) for  $5d$  electrons ( $\sim 1-3$  eV). Simultaneously, the spin-orbit coupling (SOC) increases considerably in  $5d$  orbital ( $\sim 0.1-1$  eV), leading to enhanced splitting degenerate orbitals and bands [30, 31]. On the other hand,  $5d$  ions prefer to be low-spin configurations rather than high-spin configurations, resulting from large crystal-field. The strong SOC competing with  $U$  and crystal-electric field (CEF) enables  $5d$  metal oxides present intriguing magnetic properties. In general, the ground state properties of  $5d$  metal oxides is the balanced result of these interactions. A schematic model for the Mott ground state of  $5d^5$  metal oxides was proposed by B. J. Kim and etc. As shown in **Fig. 1.5** [20], the strong SOC splits the  $t_{2g}$  band into  $J_{\text{eff}} = 1/2$  doublet and  $J_{\text{eff}} = 3/2$  quartet bands. The modified  $t_{2g}$  band is easier to be opened even by a small  $U$ . SOC effect plays a dominant role in  $\text{Ir}^{4+}$  ( $5d^5$ ) oxides, which has been readily evidenced. However, it is less clear that the role of SOC plays in other non- $5d^5$  configurations. For example, the large strength of SOC does not dominate the electronic and magnetic properties of  $\text{Os}^{5+}$  ( $5d^3$ ) oxide compounds, such as  $\text{NaOsO}_3$  [29] and  $\text{Cd}_2\text{Os}_2\text{O}_7$  [32], in contrast to iridates. Even though, SOC is still realized to have impacts on creating the magnetic ground state for  $\text{Cd}_2\text{Os}_2\text{O}_7$ . In summary,  $5d$  metal oxides provide a good platform to study the interplay of SOC, Coulomb interactions and CEF.



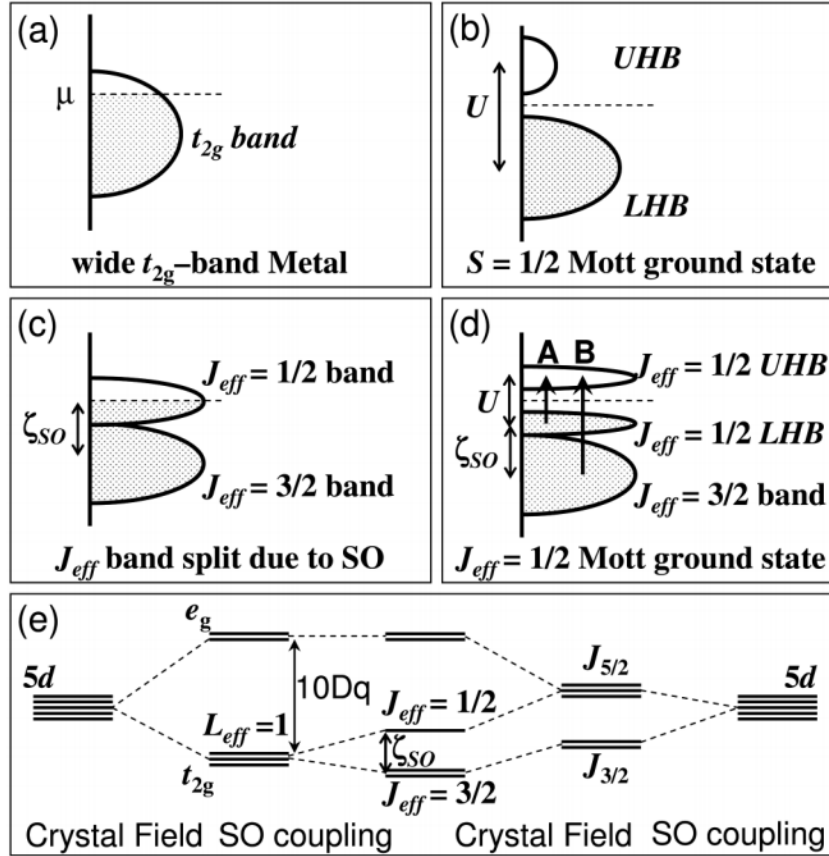


**Fig. 1.5** Schematic energy diagrams for the  $5d^5$  configuration [20]

## 1.3 Some novel physical properties of d-block metal compounds

### 1.3.1 Ferroelectricity

Ferroelectricity stems from the separation of the center of positive and negative electric charge in the crystal, exhibiting spontaneous electric polarization which can be controlled and reversed by external electric fields [33]. Ferroelectric materials have been of special interest since the ferroelectricity of  $\text{BaTiO}_3$  was discovered in 1946 [34]. There are two symmetrically equivalent ground states existing in ferroelectric materials and these two oppositely polarized states are separated by an energy barrier  $U_0$ , as shown in **Fig. 1.6**. If an electric field is applied, each state will be reversible [35]. A typical feature of ferroelectric materials is a phase transition at the Curie temperature ( $T_C$ ), from a non-polarized paraelectric state to a polarized ferroelectric state with the decrease of temperature. Essentially, the

spontaneous polarization is caused by the structural transition at  $T_C$  and accompanied by the loss of a center of symmetry.

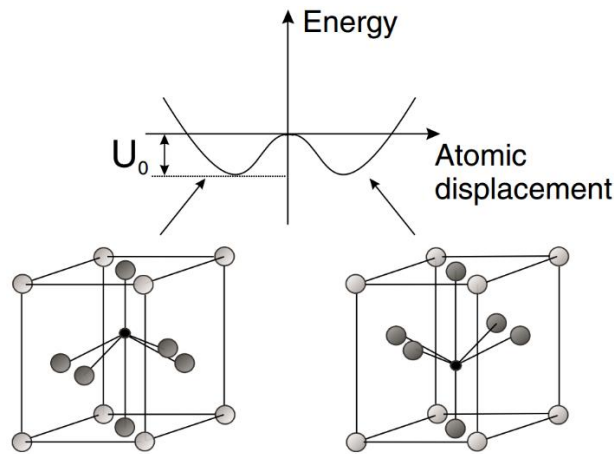


**Fig. 1.6** Schematic of a tetragonal perovskite ferroelectric [35]

Ferroelectricity was long thought to occur only in insulating materials since itinerant electrons in metallic materials screen electric fields and inhibit ferroelectric distortions in general. However, a class of materials called as ferroelectric metals was predicted theoretically by Anderson and Blount [36]. They suggested that metallic transitions accompanied by the appearance of a polar axis and the loss of an inversion center should be ferroelectric, accordingly, this kind of material is the ferroelectric metal. Although the mechanism about ferroelectric metal were proposed in 1965, only a limited number of this class of material has been experimentally evidenced until now.  $\text{Cd}_2\text{Re}_2\text{O}_7$  was shortly regarded as a potential ferroelectric metal, however, it was eventually identified to be piezoelectric but not ferroelectric [37, 38]. The first realization of the ferroelectric transition in a metallic compound is the discovery of the  $\text{LiNbO}_3$ -type oxide  $\text{LiOsO}_3$  reported in 2013 [39]. The origin of ferroelectric-like structural transition in  $\text{LiOsO}_3$  has been discussing [40-42].

### 1.3.2 Semimetal

According to electronic band theory, the electronic properties of solid-state materials

are simply classified as conducting and insulating. If there is a gap between the valence bands (VB) and the conduction bands (CB), the solid is insulator or semiconductor, while metals possess partially filled bands and no band gap exist. Furthermore, another class of materials have realized theoretically and experimentally that is semimetallic. Unlike metal, semimetal has a gap between the VB and the CB, but the gap is either extremely small or vanishing, or a tiny overlap exist in the gap [43]. The schematic of different types of semimetals are shown in **Fig. 1.7** [44]. Resulting from the unique band structure, semimetals show remarkably different electronic properties from metals and insulators. The two-dimensional material graphene is the most famous example of semimetal with a vanishing gap. The CB and VB intersect at Dirac points, so graphene is a Dirac semimetal. In the past few years, another type of semimetal has been proposed for a number of three-dimensional compounds [25, 45, 46]. In Weyl semimetal, discrete band-crossing points near the Fermi level are called as Weyl nodes. The Weyl equation is used to describe the behavior of Weyl semimetal in particle physics.

Experimentally, Weyl semimetal phase have been realized in bulk materials by Angle-resolved photoemission spectroscopy (ARPES) measurements, such as TaAs-class materials and MoTe<sub>2</sub> [47, 48]. For oxides, 5d TM oxides are considered to be ideal systems to look for topological semimetal phase because the strength of SOC and that of interaction are comparable for 5d transition metal [46]. For example, the pyrochlore iridates A<sub>2</sub>Ir<sub>2</sub>O<sub>7</sub> (A = yttrium or a lanthanide element) and perovskite iridates were suggested to be Weyl semimetals [25, 49, 50]. The studies of topological semimetal are still on progress which induces many manifestations in transport properties of materials [51].

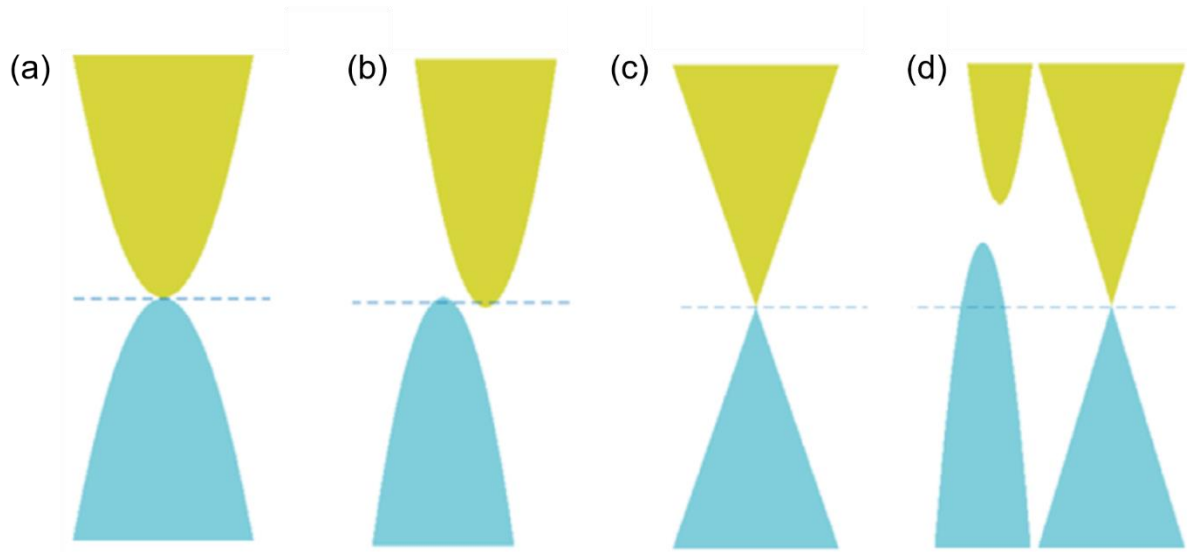


**Fig. 1.7** Schematic illustration of different types of semimetals. (a) Semimetal with VB and CB touching. (b) Semimetal with VB and CB overlapping in different momentum point. (c) Topological semimetal owns linear energy dispersion in the bulk. (d) Topological semimetal has additional hole pockets near the Weyl point [44]

### 1.3.3 Half metallicity

Half metal is defined by a unique electronic structure, showing conduction by charge carriers of one spin direction exclusively. In the half metallic materials, only one of the two spin directions are metallic. In another word, the electrons sharing the same spin are responsible for the metallic behavior and the electrons with opposite spin are insulating [52]. The half metallicity has been proposed since the early 1980s. In the past two decades, the materials with half metallicity has been realized in real compounds. A number of alloys and oxides compounds have been suggested to be half metals with 100% spin polarization, such as semi-Heusler alloy NiMnSb [52],  $\text{Sr}_2\text{FeMoO}_6$  [53],  $\text{La}_{1-x}\text{Sr}_x\text{MnO}_3$  [54],  $\text{CrO}_2$  [55] and etc. From the view of point of band gap, the origin of half metal can be classified as three types, covalent band gap, charge-transfer band gap, and  $d-d$  band gap [56]. NiMnSb is a well-known example for the first category, covalent band gap. Half metals in this category are weak magnets [56]. In contrast, half metals with charge-transfer band gaps were found in strongly magnetic compounds such as  $\text{CrO}_2$  [55, 57] and double perovskite  $\text{Sr}_2\text{FeMoO}_6$  [53]. In this category, the  $d$  bands of

transition metals are empty for the minority spin direction while the itinerant electrons of the transition metal's  $s$  and  $p$  orbitals are localized on the anions [56]. The third category of half metals show narrow bands occurred between crystal field splitting (CFS) bands. Materials in this class are weak magnets such as  $\text{Fe}_3\text{O}_4$  [58], and  $\text{Fe}_x\text{Co}_{1-x}\text{S}_2$  [59].

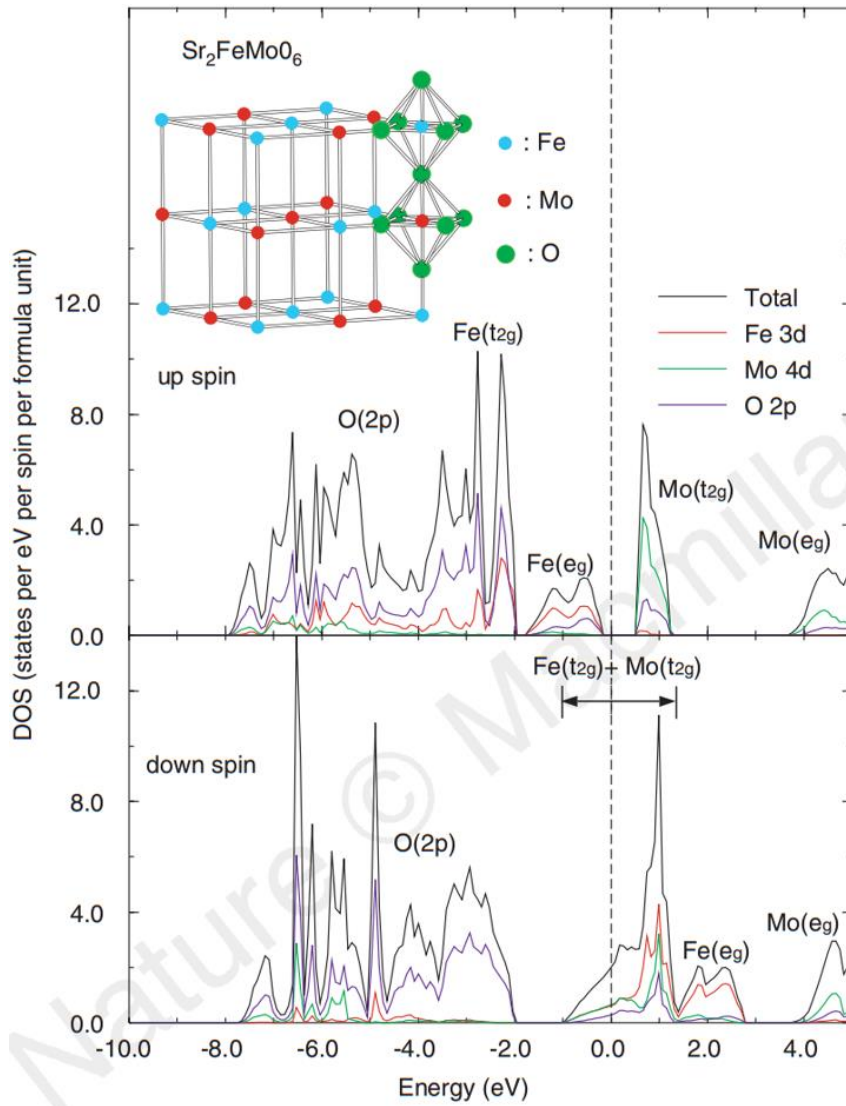


**Fig. 1.8** The density of states of  $\text{Sr}_2\text{FeMoO}_6$  [53]

In the past two decades, the unique class of double perovskite compounds was reported to be half-metallic material accompanied by high Curie temperature ( $T_C$ ) ferrimagnetic property. Apart from  $\text{Sr}_2\text{FeMoO}_6$ , the high- $T_C$  half metals crystallizing into double perovskite structure still include  $\text{Sr}_2\text{CrWO}_6$  [60],  $\text{Sr}_2\text{CrReO}_6$  [61, 62],  $\text{Sr}_2\text{CrMoO}_6$  [63], and  $\text{Sr}_2\text{FeReO}_6$  [64]. The

spins of  $\text{Fe}^{3+}$  ( $S = 5/2$ ) and  $\text{Mo}^{5+}$  ( $S = 1/2$ ) couple antiferromagnetically in a cubic ordered perovskite structure  $\text{Sr}_2\text{FeMoO}_6$ , it has only one electron in the  $5d$   $t_{2g}$  minority-spin orbital which is located at the Fermi level. This delocalized electron shared by Fe and Mo through the oxygen orbitals, behaving like a conduction electron and show spin-polarized. Its density of states is shown in **Fig 1.8**. The ferrimagnetic transition temperature observed for  $\text{Sr}_2\text{FeMoO}_6$  is 420 K, which make it possible to be applied for a practice device at room temperature. Resulting from its half metallic property, the resistivity is as low as  $8 \times 10^{-3} \Omega \text{ cm}$ . The magnetic and transport properties for this family of half metallic materials are listed in the **Table 1.1**.

**Table 1.1** Comparison of and several half-metallic compounds.  $\rho_{298 \text{ K}}$ ,  $T_m$  and  $M_s$  are resistivity at 298 K, magnetic transition temperature and saturation magnetization, respectively.

Compound	$\rho_{298 \text{ K}} (\Omega \text{ cm})$	$T_m (\text{K})$	$M_s (\mu_B/\text{f.u.})$	Reference
$\text{Sr}_2\text{FeMoO}_6$	$8 \times 10^{-3}$	420	3.1	[53]
$\text{Sr}_2\text{FeReO}_6$	$1 \times 10^{-2}$	400	2.6	[64]
$\text{Sr}_2\text{CrMoO}_6$	$8 \times 10^{-2}$	$\sim 300$	0.5	[63]
$\text{Sr}_2\text{CrWO}_6$	$\sim 1.1 \times 10^2$	458	1.1	[60]
$\text{Sr}_2\text{CrReO}_6$	$10^{-3}-10^{-2}$	635	0.86	[64]

### 1.3.4 Metal-Insulator transition (MIT)

Normally, a material is either to be a metal or an insulator, according to the position of the Fermi energy. However, in some certain cases, the electronic states in a metallic material can leave from extended states to localized states, thus a transition takes place. MITs can be divided into two groups, structural phase transition induced MIT and purely electronic transition [65, 66]. There are two types for the insulating phase associated with MITs, either band insulators or Mott insulators [67]. The MIT for band insulator is induced by change in crystal structure which belongs to the structural MIT. If the onsite Coulomb interaction ( $U$ ) is

comparable to the bandwidth ( $W$ ), leading a material to become a Mott insulator. The transition from the Mott insulator to the metal can be induced by the conditions like temperature, magnetic field, pressure, or doping [68]. The physical properties of Mott insulator are quite different from those of band insulator, as measured by transport, magnetic, and optical. Except for Mott transition, Anderson proposed another mechanism that the disorder can drive a MIT in a system of noninteracting electrons which is caused by impurities [69]. In addition, Slater suggested that long-range magnetic order drives another type of MIT in a three dimensional system [70]. The experimental studies of MITs in correlated metals mostly occur in transition metal compounds because of d-electron [68].

#### 1.3.4.1 Mott transition

Mott MIT transitions are driven by electron-electron interactions, which should be purely electronic in origin but not assisted by structural transitions. However, the MITs are usually accompanied by structural transition in bulk materials in practice [67]. In Mott's original formulation, the existence of the insulator does not depend on whether it is magnetic or not. The strong Coulomb interactions ( $U$ ) in Mott systems open a gap at the Fermi energy, forcing the Mott MIT to occur, which is independent of magnetic correlations.  $V_2O_3$  and its derivatives are classical Mott-Hubbard system and  $V_2O_3$  shows a MIT at 160 K [71].

#### 1.3.4.2 Slater transition

Unlike Mott transition, the long-range ordering plays a significant role in Slater transition. The continuous MIT for pyrochlore  $Cd_2Os_2O_7$  was suggested to be driven by antiferromagnetic (AF) order at 226 K although its magnetic frustration complicates the MIT [72, 73]. Perovskite  $NaOsO_3$  was found to show a transition from metallic phase to an AF insulator at 410 K on cooling [74, 75]. The schematic of a Slater MIT is shown in **Fig. 1.9**. The insulating band gap is created with the occurrence of AF order.

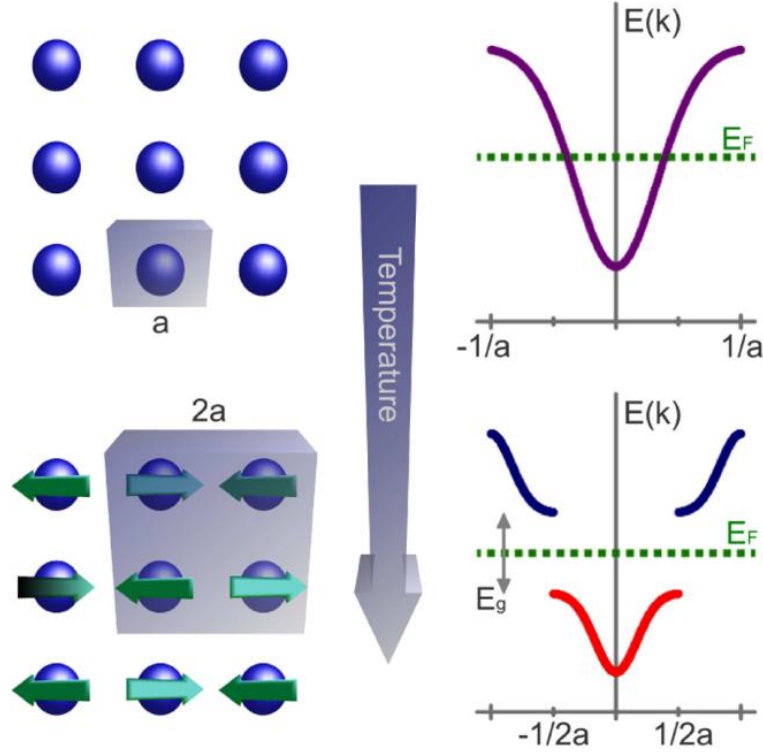


**Fig. 1.9** Schematic of Slater MIT [75]

#### 1.3.4.3 Anderson transition

Anderson localization is another driving force to produce a continuous MIT in solids. Anderson localization was firstly suggested by Anderson in 1958 [69], which describes strong disorder can localized electronic states at the Fermi energy, leading to the transition to an insulator associated with localized states from a metal displaying diffusive transport. The transitions driven by Anderson localization differ from ones by Mott transition, which is quantum interference effects relying on degree of disorder in the system [76]. Anderson localization has been confirmed experimentally in one-dimension (1D) materials [77, 78] and two-dimension (2D) materials [79, 80], but for three-dimension materials, the MITs are not purely caused by Anderson localization generally [81]. Polycrystalline  $\text{GeTe-Sb}_2\text{Te}_3$  system was one of the limited examples reported to occur MIT solely driven by disorder [82, 83]. Recently, MIT in single crystal  $\text{Li}_x\text{Fe}_7\text{Se}_8$  was found to stem from a strong disordered potential associated with Li doping to  $\text{Fe}_7\text{Se}_8$  [84]. **Fig. 1.10** shows the schematic of DOS evolution in



$\text{Li}_x\text{Fe}_7\text{Se}_8$  system. With the doping of Li, the disorder is introduced and MIT occurs when the mobility edge  $E_M$  shifts below Fermi energy  $E_F$ . Further, the higher doping of Li leads variable-range hopping (VRH) to become more prominent in this system.

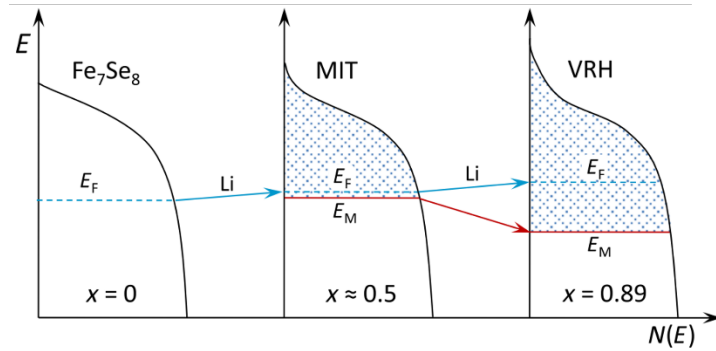


**Fig. 1.10** Schematic of DOS evolution in  $\text{Li}_x\text{Fe}_7\text{Se}_8$  system [84]

### 1.3.5 High- $T_c$ ferrimagnetism in double perovskite oxides

A class of ferrimagnetic double perovskite oxides (DPOs) has been discovered to exhibit considerably high  $T_c$  and novel electronic ground state. The high  $T_c$  ferrimagnetic DPOs range over several orders of resistivity from metallic and insulating materials. At the metallic side, the high- $T_c$  ferrimagnetic DPOs show half metallic properties, such as  $\text{Sr}_2\text{FeMoO}_6$  ( $M = \text{Mo, Re}$ ) [53, 64],  $\text{Sr}_2\text{CrMoO}_6$  ( $M = \text{Mo, W, Re}$ ) [60, 63, 64]. At another side,  $\text{Sr}_2\text{CrCrO}_6$  is unique, exhibiting the highest magnetic transition temperature ( $T_c = 725 \text{ K}$ ) [26] and insulating behavior.

As the most well-known half-metal with high  $T_c$ , the half-metallic nature of  $\text{Sr}_2\text{FeMoO}_6$  was discussed above. Erten et al. proposed a comprehensive theory for understanding the electronic and magnetic properties of  $\text{Sr}_2\text{FeMoO}_6$  through deriving and validating a new effective spin Hamiltonian, which can be amenable to other materials in this class [85]. The itinerant electrons from electron from  $t_{2g}$  orbitals of  $\text{Mo}^{5+}$  ( $4d^1$ ) ions hybridizes with the  $\text{Fe}^{3+}$  ( $3d^5$ )  $t_{2g}$  state via  $\text{O}^{2+}$  ions and double exchange mechanism can describe the

interaction between the local moment and the itinerant electrons (shown in **Fig. 1.11**). It has been suggested the ferrimagnetism in this class of high- $T_c$  ferrimagnetic DPOs is kinetic energy driven. Erten et al. also concluded that the ferrimagnetic  $T_c$  can be enhanced by adding excess Fe with substitution of Sr by La.

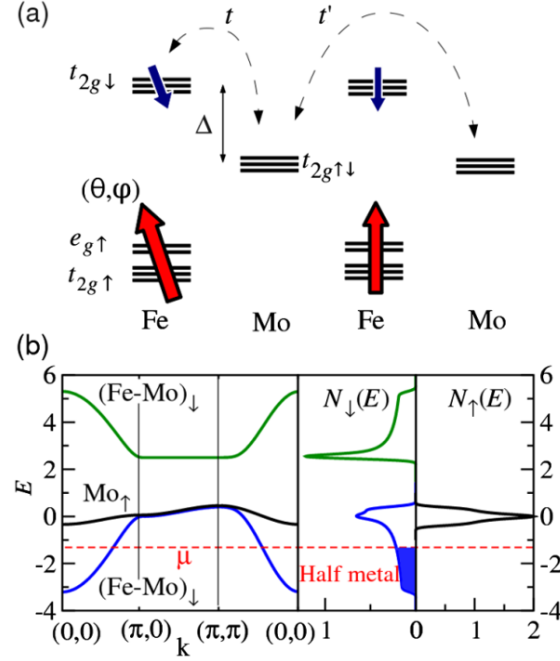


**Fig. 1.11** (a) Schematic of energy levels at Fe<sup>3+</sup> (3d<sup>5</sup>,  $S = 5/2$ ) and Mo<sup>5+</sup> (4d<sup>1</sup>,  $S = 1/2$ ) in two unit cells of Sr<sub>2</sub>FeMoO<sub>6</sub>. The parameters  $t$ ,  $t'$  and  $\Delta$  are Hamiltonian, governing the dynamics of the itinerant electrons in  $t_{2g}$  orbitals. (b) Calculated electronic structure  $E(\mathbf{k})$  and the spin-resolved DOSs. [85]

Unlike the class of half-metallic DPOs with high  $T_c$ , Sr<sub>2</sub>CrOsO<sub>6</sub> has completely filled 5d  $t_{2g}$  minority-spin orbitals and the majority-spin ones are still gapped, which make it become the end point of a fully spin-polarized metal-insulator transition. The spin-polarized 5d band of Sr<sub>2</sub>CrCrO<sub>6</sub> was thought to shift below the Fermi energy, resulting its insulating behavior, shown in **Fig. 1.12** [26]. The magnetic transition temperature is scaled with the bandwidth in the conducting minority-spin channel. Doping La<sup>3+</sup> into alkaline earth sites is thought to be an effective way to change the band filling such as LaSrFeMoO<sub>6</sub> and LaCaCrWO<sub>6</sub> [86, 87]. Alternatively, replacement of W<sup>5+</sup> (5d<sup>1</sup>) or Re<sup>5+</sup> (5d<sup>2</sup>) in Sr<sub>2</sub>CrWO<sub>6</sub> or Sr<sub>2</sub>CrReO<sub>6</sub> by Os<sup>5+</sup> (5d<sup>3</sup>)

raise the  $T_c$  from 458 K for  $\text{Sr}_2\text{CrWO}_6$  [60], 635 K for  $\text{Sr}_2\text{CrReO}_6$  [64] to 725 K for  $\text{Sr}_2\text{CrOsO}_6$  [26].

So far, several density function theory calculations for  $\text{Sr}_2\text{CrCrO}_6$  have been proposed, however, the mechanism for its high  $T_c$  ferrimagnetism is still an open question. K.-W. Lee and W. E. Pickett proposed that  $\text{Sr}_2\text{CrOsO}_6$  is a near-half metallic antiferromagnet and a large spin-orbit coupling reduces Os spin moment [88]. However, the significant SOC of Os is not supported by X-ray magnetic circular dichroism (XMCD) experimental results, a quite small magnetic moment of 0.015  $\mu\text{B}/\text{f.u.}$  was observed on Os orbital [26]. A model for multiorbital material suggested that it is a Mott insulator and the net moment observed in  $\text{Sr}_2\text{CrOsO}_6$  arises from spin canting [89]. But the canted magnetic structure did not confirm with neutron powder diffraction measurement [90]. So far, the physical nature of  $\text{Sr}_2\text{CrOsO}_6$  is ambiguous.

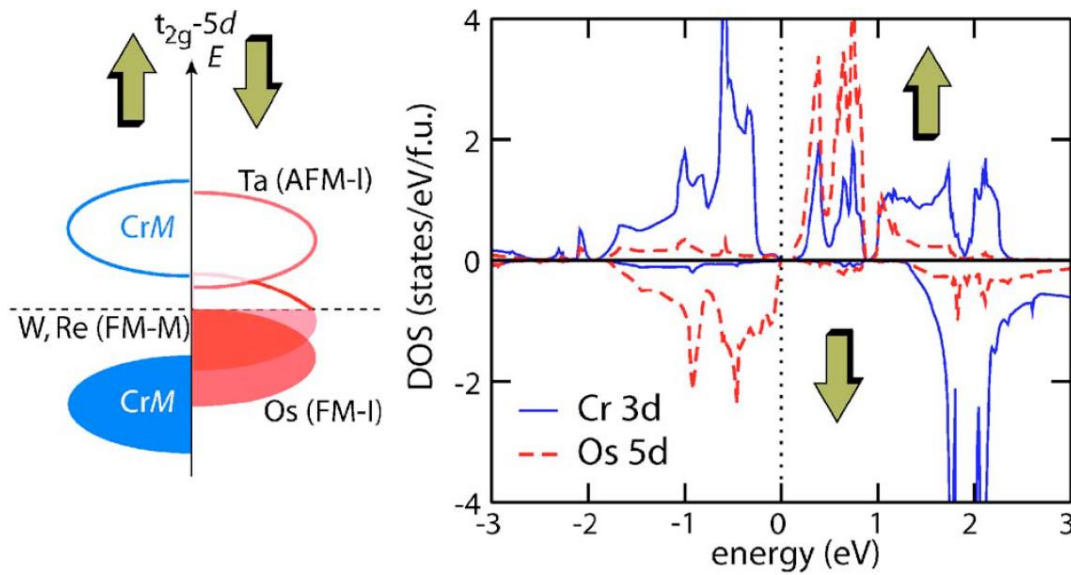


**Fig. 1.12** Left: band-structure sketch for different fillings of the 5d spin-down band ( $\text{Sr}_2\text{CrMO}_6$  with  $M = \text{Ta}, \text{W}, \text{Re}, \text{Os}$ ). Right: band-structure calculation for  $\text{Sr}_2\text{CrOsO}_6$  with GGA+SO [26]

## 1.4 Objectvie of this thesis

The main motivations behind this thesis work are to explore novel properties of 5d metal related oxide compounds, as well as to enhance the electronic or magnetic behavior of

material. In this thesis, several new  $5d$  metal containing oxides were synthesized under high-pressure and high-temperature conditions. Through studying the crystal structures and physical properties of these compounds, there are three main topics discussed in this thesis as below.

**(i) Crystal structure and physical properties of a mercury oxide  $\text{HgPbO}_3$**

$5d$  TM oxides are considered to be ideal systems to look for topological semimetal phase because the strength of SOC and that of interaction are comparable for  $5d$  transition metal [46]. Recently,  $\text{HgPbO}_3$  was suggested to be a candidate of Weyl semimetal according to first-principles calculation [91]. Although  $\text{HgPbO}_3$  was firstly synthesized in 1973 by Sleight and Prewitt, its crystal structure has not been solved well because of oxygen placement issue [92]. The crystal structure of  $\text{HgPbO}_3$  will be characterized by single-crystal X-ray diffraction and powder synchrotron X-ray diffraction and its electronic properties will be discussed in **Chapter 3**.

**(ii) The effect of high-pressure treatment on the crystal structures and magnetic properties of hexagonal-perovskite osmium oxides  $\text{Ba}_3\text{MOs}_2\text{O}_9$  ( $M = \text{Cu, Ni}$ )**

High-pressure synthesis method promotes the discovery of new solid-state materials. In some cases, high pressure can stabilize phases with high density. For example, the hexagonal perovskite can transform gradually under high pressure in the sequence of 9R (chhchhchh)-4H (chch)-6H (cchcch)-3C, such as  $\text{BaRuO}_3$  [93]. A new 6H perovskite oxide  $\text{Ba}_3\text{CuOs}_2\text{O}_9$  was synthesized under ambient pressure and reported recently, which exhibits antiferromagnetically ordered state below 47 K [94]. In **Chapter 4**, the effect of the high-pressure and high-temperature treatment on the structure and magnetic behavior of  $\text{Ba}_3\text{CuOs}_2\text{O}_9$  will be discussed.

**(iii) The effect of substitution of Cr by Ni on the magnetic and electronic properties of  $3d$ - $5d$  hybrid double perovskite  $\text{Sr}_2\text{CrOsO}_6$**

As aforementioned, the physical nature of high  $T_c$  ferrimagnetism for  $\text{Sr}_2\text{CrOsO}_6$  is still an open question. As the end point of a fully spin-polarized metal-insulator transition, the completely filled  $5d\ t_{2g}$  minority-spin and the majority-spin orbitals in  $\text{Sr}_2\text{CrCrO}_6$  play vital roles in its unique properties. The change of the band filling is thought to be an effective way to enhance materials' magnetic behavior [26]. In order to further understand the mechanism behind physical properties of  $\text{Sr}_2\text{CrOsO}_6$ , the replacement of Cr by another  $3d$  transition metal Ni partially will be employed to change the band filling of  $\text{Sr}_2\text{CrOsO}_6$  and the variations of structure, electronic and magnetic properties of these Ni-substituted  $\text{Sr}_2\text{CrOsO}_6$  will be discussed in **Chapter 5**.

## References in Chapter 1

- [1] A. Navrotsky, Energetics and crystal chemical systematics among ilmenite, lithium niobate, and perovskite structures, *Chemistry of Materials* 10(10) (1998) 2787-2793.
- [2] A. Aimi, T. Katsumata, D. Mori, D. Fu, M. Itoh, T. Kyomen, K.-i. Hiraki, T. Takahashi, Y. Inaguma, High-pressure synthesis and correlation between structure, magnetic, and dielectric properties in  $\text{LiNbO}_3$ -type  $\text{MnMO}_3$  ( $M = \text{Ti, Sn}$ ), *Inorganic chemistry* 50(13) (2011) 6392-6398.
- [3] R. Weis, T. Gaylord, Lithium niobate: summary of physical properties and crystal structure, *Applied Physics A* 37(4) (1985) 191-203.
- [4] S. Abrahams, J. Reddy, J. Bernstein, Ferroelectric lithium niobate. 3. Single crystal X-ray diffraction study at 24 C, *Journal of Physics and Chemistry of Solids* 27(6-7) (1966) 997-1012.
- [5] R. Cava, A. Santoro, D. Murphy, S. Zahurak, R. Roth, The structures of lithium-inserted metal oxides:  $\text{LiReO}_3$  and  $\text{Li}_2\text{ReO}_3$ , *Journal of Solid State Chemistry* 42(3) (1982) 251-262.
- [6] N. Kumada, S. Hosoda, F. Muto, N. Kinomura, A new lithium insertion compound (lithium, copper) tantalum oxide,  $(\text{Li, Cu})\text{TaO}_3$ , with the  $\text{LiNbO}_3$ -type structure, *Inorganic chemistry* 28(18) (1989) 3592-3595.
- [7] N. Kumada, N. Kinomura, Topochemical preparation of  $\text{LiNbO}_3$  type  $\text{Li}_{1-x}\text{Cu}_x\text{NbO}_3$  from

CuNb<sub>2</sub>O<sub>6</sub>, Materials research bulletin 25(7) (1990) 881-889.

[8] E. Ito, Y. Matsui, High-pressure transformations in silicates, germanates, and titanates with ABO<sub>3</sub> stoichiometry, Physics and Chemistry of Minerals 4(3) (1979) 265-273.

[9] T. Hattori, T. Matsuda, T. Tsuchiya, T. Nagai, T. Yamanaka, Clinopyroxene-perovskite phase transition of FeGeO<sub>3</sub> under high pressure and room temperature, Physics and Chemistry of Minerals 26(3) (1999) 212-216.

[10] Y. Syono, S.-I. Akimoto, Y. Ishikawa, Y. Endoh, A new high pressure phase of MnTiO<sub>3</sub> and its magnetic property, Journal of Physics and Chemistry of Solids 30(7) (1969) 1665-1672.

[11] Y. Syono, H. Sawamoto, S. Akimoto, Disordered ilmenite MnSnO<sub>3</sub> and its magnetic property, Solid State Communications 7(9) (1969) 713-716.

[12] M. Akaogi, H. Kojitani, H. Yusa, R. Yamamoto, M. Kido, K. Koyama, High-pressure transitions and thermochemistry of MGeO<sub>3</sub> (*M*= Mg, Zn and Sr) and Sr-silicates: systematics in enthalpies of formation of A<sup>2+</sup>B<sup>4+</sup>O<sub>3</sub> perovskites, Physics and Chemistry of Minerals 32(8-9) (2005) 603-613.

[13] Y. Inaguma, M. Yoshida, T. Katsumata, A polar oxide ZnSnO<sub>3</sub> with a LiNbO<sub>3</sub>-type structure, Journal of the American Chemical Society 130(21) (2008) 6704-6705.

[14] G. King, P.M. Woodward, Cation ordering in perovskites, Journal of Materials Chemistry 20(28) (2010) 5785-5796.

[15] G.M. Keith, C.A. Kirk, K. Sarma, N.M. Alford, E.J. Cussen, M.J. Rosseinsky, D.C. Sinclair, Synthesis, crystal structure, and characterization of Ba(Ti<sub>1/2</sub>Mn<sub>1/2</sub>)O<sub>3</sub>: a high permittivity 12R-type hexagonal perovskite, Chemistry of Materials 16(10) (2004) 2007-2015.

[16] P. Köhl, D. Reinen, Strukturelle und spektroskopische Untersuchungen am Ba<sub>2</sub>CuTeO<sub>6</sub>, Zeitschrift für anorganische und allgemeine Chemie 409(3) (1974) 257-272.

[17] Y. Doi, Y. Hinatsu, The structural and magnetic characterization of 6H-perovskite-type oxides Ba<sub>3</sub>LnIr<sub>2</sub>O<sub>9</sub> (Ln= Y, lanthanides), Journal of Physics: Condensed Matter 16(16) (2004)

2849.

- [18] J. Darriet, C. Dussarrat, F. Weill, B. Darriet, R. Bontchev, The system  $\text{BaRuO}_3\text{-BaBiO}_3$ . II. Crystal structure and magnetic properties of  $\text{Ba}_2\text{RuBiO}_6$ , *European Journal of Solid State and Inorganic Chemistry* 30(3) (1993) 287-296.
- [19] Y. Doi, K. Matsuhira, Y. Hinatsu, Crystal structures and magnetic properties of 6H-perovskites  $\text{Ba}_3\text{MRu}_2\text{O}_9$  ( $\text{M} = \text{Y, In, La, Sm, Eu, and Lu}$ ), *Journal of Solid State Chemistry* 165(2) (2002) 317-323.
- [20] B. Kim, H. Jin, S. Moon, J.-Y. Kim, B.-G. Park, C. Leem, J. Yu, T. Noh, C. Kim, S.-J. Oh, Novel  $J_{\text{eff}} = 1/2$  Mott state induced by relativistic spin-orbit coupling in  $\text{Sr}_2\text{IrO}_4$ , *Physical review letters* 101(7) (2008) 076402.
- [21] B. Kim, H. Ohsumi, T. Komesu, S. Sakai, T. Morita, H. Takagi, T.-h. Arima, Phase-sensitive observation of a spin-orbital Mott state in  $\text{Sr}_2\text{IrO}_4$ , *Science* 323(5919) (2009) 1329-1332.
- [22] F. Wang, T. Senthil, Twisted Hubbard model for  $\text{Sr}_2\text{IrO}_4$ : magnetism and possible high temperature superconductivity, *Physical review letters* 106(13) (2011) 136402.
- [23] A. Shitade, H. Katsura, J. Kuneš, X.-L. Qi, S.-C. Zhang, N. Nagaosa, Quantum spin Hall effect in a transition metal oxide  $\text{Na}_2\text{IrO}_3$ , *Physical review letters* 102(25) (2009) 256403.
- [24] J. Chaloupka, G. Jackeli, G. Khaliullin, Kitaev-Heisenberg model on a honeycomb lattice: possible exotic phases in iridium oxides  $A_2\text{IrO}_3$ , *Physical review letters* 105(2) (2010) 027204.
- [25] X. Wan, A.M. Turner, A. Vishwanath, S.Y. Savrasov, Topological semimetal and Fermi-arc surface states in the electronic structure of pyrochlore iridates, *Physical Review B* 83(20) (2011) 205101.
- [26] Y. Krockenberger, K. Mogare, M. Reehuis, M. Tovar, M. Jansen, G. Vaitheeswaran, V. Kanchana, F. Bultmark, A. Delin, F. Wilhelm,  $\text{Sr}_2\text{CrOsO}_6$ : End point of a spin-polarized metal-insulator transition by 5d band filling, *Physical Review B* 75(2) (2007) 020404.

- [27] H.L. Feng, Y. Shi, Y. Guo, J. Li, A. Sato, Y. Sun, X. Wang, S. Yu, C.I. Sathish, K. Yamaura, High-pressure crystal growth and electromagnetic properties of  $5d$  double-perovskite  $\text{Ca}_3\text{OsO}_6$ , *Journal of Solid State Chemistry* 201 (2013) 186-190.
- [28] H.L. Feng, S. Calder, M.P. Ghimire, Y.-H. Yuan, Y. Shirako, Y. Tsujimoto, Y. Matsushita, Z. Hu, C.-Y. Kuo, L.H. Tjeng, T.-W. Pi, Y.-L. Soo, J. He, M. Tanaka, Y. Katsuya, M. Richter, K. Yamaura,  $\text{Ba}_2\text{NiOsO}_6$ : A Dirac-Mott insulator with ferromagnetism near 100 K, *Physical Review B* 94(23) (2016) 235158.
- [29] Y.G. Shi, Y.F. Guo, S. Yu, M. Arai, A.A. Belik, A. Sato, K. Yamaura, E. Takayama-Muromachi, H.F. Tian, H.X. Yang, J.Q. Li, T. Varga, J.F. Mitchell, S. Okamoto, Continuous metal-insulator transition of the antiferromagnetic perovskite  $\text{NaOsO}_3$ , *Physical Review B* 80(16) (2009).
- [30] H. Watanabe, T. Shirakawa, S. Yunoki, Microscopic study of a spin-orbit-induced Mott insulator in Ir oxides, *Physical review letters* 105(21) (2010) 216410.
- [31] W. Witczak-Krempa, G. Chen, Y.B. Kim, L. Balents, Correlated Quantum Phenomena in the Strong Spin-Orbit Regime, in: J.S. Langer (Ed.), *Annual Review of Condensed Matter Physics*, Vol 5, Annual Reviews, Palo Alto, 2014, pp. 57-82.
- [32] S. Calder, J.G. Vale, N. Bogdanov, X. Liu, C. Donnerer, M. Upton, D. Casa, A. Said, M. Lumsden, Z. Zhao, Spin-orbit-driven magnetic structure and excitation in the  $5d$  pyrochlore  $\text{Cd}_2\text{Os}_2\text{O}_7$ , *Nature communications* 7 (2016) 11651.
- [33] M.E. Lines, A.M. Glass, *Principles and applications of ferroelectrics and related materials*, Oxford university press 2001.
- [34] A. Von Hippel, R. Breckenridge, F. Chesley, L. Tisza, High dielectric constant ceramics, *Industrial & Engineering Chemistry* 38(11) (1946) 1097-1109.
- [35] T. Tybell, P. Paruch, T. Giamarchi, J.-M. Triscone, Domain Wall Creep in Epitaxial Ferroelectric  $\text{Pb}(\text{Zr}_{0.2}\text{Ti}_{0.8})\text{O}_3$  Thin Films, *Physical review letters* 89(9) (2002) 097601.



- [36] P.W. Anderson, E.I. Blount, Symmetry Considerations on Martensitic Transformations: "Ferroelectric" Metals?, *Physical Review Letters* 14(7) (1965) 217-219.
- [37] V. Keppens, Structural transitions: 'Ferroelectricity' in a metal, *Nature materials* 12(11) (2013) 952.
- [38] I. Sergienko, V. Keppens, M. McGuire, R. Jin, J. He, S. Curnoe, B.C. Sales, P. Blaha, D.J. Singh, K. Schwarz, Metallic "Ferroelectricity" in the Pyrochlore  $\text{Cd}_2\text{Re}_2\text{O}_7$ , *Physical review letters* 92(6) (2004) 065501.
- [39] Y. Shi, Y. Guo, X. Wang, A.J. Princep, D. Khalyavin, P. Manuel, Y. Michiue, A. Sato, K. Tsuda, S. Yu, A ferroelectric-like structural transition in a metal, *Nature materials* 12(11) (2013) 1024.
- [40] I.L. Vecchio, G. Giovannetti, M. Autore, P. Di Pietro, A. Perucchi, J. He, K. Yamaura, M. Capone, S. Lupi, Electronic correlations in the ferroelectric metallic state of  $\text{LiOsO}_3$ , *Physical Review B* 93(16) (2016) 161113.
- [41] H. Liu, Y. Du, Y. Xie, J.-M. Liu, C.-G. Duan, X. Wan, Metallic ferroelectricity induced by anisotropic unscreened Coulomb interaction in  $\text{LiOsO}_3$ , *Physical Review B* 91(6) (2015) 064104.
- [42] Q. Yao, H. Wu, K. Deng, E. Kan, Ferroelectric-like structural transition in metallic  $\text{LiOsO}_3$ , *RSC Advances* 4(51) (2014) 26843-26846.
- [43] P. Hosur, X. Qi, Recent developments in transport phenomena in Weyl semimetals, *Comptes Rendus Physique* 14(9-10) (2013) 857-870.
- [44] S. Wang, B.-C. Lin, A.-Q. Wang, D.-P. Yu, Z.-M. Liao, Quantum transport in Dirac and Weyl semimetals: a review, *Advances in Physics: X* 2(3) (2017) 518-544.
- [45] A. Burkov, M. Hook, L. Balents, Topological nodal semimetals, *Physical Review B* 84(23) (2011) 235126.
- [46] W. Witczak-Krempa, Y.B. Kim, Topological and magnetic phases of interacting electrons

in the pyrochlore iridates, *Physical Review B* 85(4) (2012) 045124.

[47] B. Lv, H. Weng, B. Fu, X. Wang, H. Miao, J. Ma, P. Richard, X. Huang, L. Zhao, G. Chen, Experimental discovery of Weyl semimetal TaAs, *Physical Review X* 5(3) (2015) 031013.

[48] K. Deng, G. Wan, P. Deng, K. Zhang, S. Ding, E. Wang, M. Yan, H. Huang, H. Zhang, Z. Xu, Experimental observation of topological Fermi arcs in type-II Weyl semimetal MoTe<sub>2</sub>, *Nature Physics* 12(12) (2016) 1105.

[49] M. Kargarian, J. Wen, G.A. Fiete, Competing exotic topological insulator phases in transition-metal oxides on the pyrochlore lattice with distortion, *Physical Review B* 83(16) (2011) 165112.

[50] J.-M. Carter, V.V. Shankar, M.A. Zeb, H.-Y. Kee, Semimetal and topological insulator in perovskite iridates, *Physical Review B* 85(11) (2012) 115105.

[51] J. Ruan, S.-K. Jian, H. Yao, H. Zhang, S.-C. Zhang, D. Xing, Symmetry-protected ideal Weyl semimetal in HgTe-class materials, *Nature communications* 7 (2016) 11136.

[52] R. De Groot, F. Mueller, P. Van Engen, K. Buschow, New class of materials: half-metallic ferromagnets, *Physical review letters* 50(25) (1983) 2024.

[53] K.-I. Kobayashi, T. Kimura, H. Sawada, K. Terakura, Y. Tokura, Room-temperature magnetoresistance in an oxide material with an ordered double-perovskite structure, *Nature* 395(6703) (1998) 677.

[54] W.E. Pickett, D.J. Singh, Electronic structure and half-metallic transport in the La<sub>1-x</sub>Ca<sub>x</sub>MnO<sub>3</sub> system, *Physical Review B* 53(3) (1996) 1146.

[55] K. Schwarz, CrO<sub>2</sub> predicted as a half-metallic ferromagnet, *Journal of Physics F: Metal Physics* 16(9) (1986) L211.

[56] C.M. Fang, G. De Wijs, R. De Groot, Spin-polarization in half-metals, *Journal of Applied Physics* 91(10) (2002) 8340-8344.

[57] I. Solovyev, I. Kashin, V. Mazurenko, Mechanisms and origins of half-metallic

ferromagnetism in  $\text{CrO}_2$ , *Physical Review B* 92(14) (2015) 144407.

[58] A. Yanase, K. Siratori, Band structure in the high temperature phase of  $\text{Fe}_3\text{O}_4$ , *Journal of the Physical Society of Japan* 53(1) (1984) 312-317.

[59] I. Mazin, Robust half metallicity in  $\text{Fe}_x\text{Co}_{1-x}\text{S}_2$ , *Applied Physics Letters* 77(19) (2000) 3000-3002.

[60] J. Philipp, P. Majewski, L. Alff, A. Erb, R. Gross, T. Graf, M. Brandt, J. Simon, T. Walther, W. Mader, Structural and doping effects in the half-metallic double perovskite  $\text{A}_2\text{CrWO}_6$  ( $\text{A} = \text{Sr}, \text{Ba}, \text{and Ca}$ ), *Physical Review B* 68(14) (2003) 144431.

[61] H. Kato, T. Okuda, Y. Okimoto, Y. Tomioka, Y. Takenoya, A. Ohkubo, M. Kawasaki, Y. Tokura, Metallic ordered double-perovskite  $\text{Sr}_2\text{CrReO}_6$  with maximal Curie temperature of 635 K, *Applied physics letters* 81(2) (2002) 328-330.

[62] J. De Teresa, D. Serrate, C. Ritter, J. Blasco, M. Ibarra, L. Morellon, W. Tokarz, Investigation of the high Curie temperature in  $\text{Sr}_2\text{CrReO}_6$ , *Physical Review B* 71(9) (2005) 092408.

[63] Y. Moritomo, S. Xu, A. Machida, T. Akimoto, E. Nishibori, M. Takata, M. Sakata, Electronic structure of double-perovskite transition-metal oxides, *Physical Review B* 61(12) (2000) R7827.

[64] H. Kato, T. Okuda, Y. Okimoto, Y. Tomioka, K. Oikawa, T. Kamiyama, Y. Tokura, Structural and electronic properties of the ordered double perovskites  $\text{A}_2\text{MReO}_6$  ( $\text{A} = \text{Sr}, \text{Ca}$ ;  $\text{M} = \text{Mg}, \text{Sc}, \text{Cr}, \text{Mn}, \text{Fe}, \text{Co}, \text{Ni}, \text{Zn}$ ), *Physical Review B* 69(18) (2004) 184412.

[65] N. Mott, *Metal-insulator transitions*, CRC Press 1990.

[66] G. Stefanovich, A. Pergament, D. Stefanovich, Electrical switching and Mott transition in  $\text{VO}_2$ , *Journal of Physics: Condensed Matter* 12(41) (2000) 8837.

[67] N.F. Mott, The basis of the electron theory of metals, with special reference to the transition metals, *Proceedings of the Physical Society. Section A* 62(7) (1949) 416.

- [68] M. Imada, A. Fujimori, Y. Tokura, Metal-insulator transitions, *Reviews of modern physics* 70(4) (1998) 1039.
- [69] P.W. Anderson, Absence of diffusion in certain random lattices, *Physical review* 109(5) (1958) 1492.
- [70] J. Slater, Magnetic effects and the Hartree-Fock equation, *Physical review* 82(4) (1951) 538.
- [71] D. McWhan, A. Menth, J. Remeika, W. Brinkman, T. Rice, Metal-insulator transitions in pure and doped  $V_2O_3$ , *Physical Review B* 7(5) (1973) 1920.
- [72] D. Mandrus, J. Thompson, R. Gaal, L. Forro, J. Bryan, B. Chakoumakos, L. Woods, B. Sales, R. Fishman, V. Keppens, Continuous metal-insulator transition in the pyrochlore  $Cd_2Os_2O_7$ , *Physical Review B* 63(19) (2001) 195104.
- [73] W. Padilla, D. Mandrus, D. Basov, Searching for the Slater transition in the pyrochlore  $Cd_2Os_2O_7$  with infrared spectroscopy, *Physical Review B* 66(3) (2002) 035120.
- [74] Y. Shi, Y. Guo, S. Yu, M. Arai, A. Belik, A. Sato, K. Yamaura, E. Takayama-Muromachi, H. Tian, H. Yang, Continuous metal-insulator transition of the antiferromagnetic perovskite  $NaOsO_3$ , *Physical Review B* 80(16) (2009) 161104.
- [75] S. Calder, V. Garlea, D. McMorro, M. Lumsden, M.B. Stone, J. Lang, J.-W. Kim, J. Schlueter, Y. Shi, K. Yamaura, Magnetically driven metal-insulator transition in  $NaOsO_3$ , *Physical review letters* 108(25) (2012) 257209.
- [76] J. Chabé, G. Lemarié, B. Grémaud, D. Delande, P. Szriftgiser, J.C. Garreau, Experimental observation of the Anderson metal-insulator transition with atomic matter waves, *Physical review letters* 101(25) (2008) 255702.
- [77] J. Pascual, J. Mendez, J. Gomez-Herrero, A. Baro, N. Garcia, U. Landman, W. Luedtke, E. Bogachek, H.-P. Cheng, Properties of metallic nanowires: from conductance quantization to localization, *Science* 267(5205) (1995) 1793-1795.

- [78] C. Gómez-Navarro, P. De Pablo, J. Gómez-Herrero, B. Biel, F. Garcia-Vidal, A. Rubio, F. Flores, Tuning the conductance of single-walled carbon nanotubes by ion irradiation in the Anderson localization regime, *Nature materials* 4(7) (2005) 534.
- [79] Y. Asada, K. Slevin, T. Ohtsuki, Anderson transition in two-dimensional systems with spin-orbit coupling, *Physical review letters* 89(25) (2002) 256601.
- [80] A. Punnoose, A.M. Finkel'stein, Metal-insulator transition in disordered two-dimensional electron systems, *Science* 310(5746) (2005) 289-291.
- [81] D. Belitz, T. Kirkpatrick, The Anderson-Mott transition, *Reviews of modern physics* 66(2) (1994) 261.
- [82] T. Siegrist, P. Jost, H. Volker, M. Woda, P. Merkelbach, C. Schlockermann, M. Wuttig, Disorder-induced localization in crystalline phase-change materials, *Nature materials* 10(3) (2011) 202.
- [83] W. Zhang, A. Thiess, P. Zalden, R. Zeller, P. Dederichs, J.-Y. Raty, M. Wuttig, S. Blügel, R. Mazzarello, Role of vacancies in metal–insulator transitions of crystalline phase-change materials, *Nature materials* 11(11) (2012) 952.
- [84] T. Ying, Y. Gu, X. Chen, X. Wang, S. Jin, L. Zhao, W. Zhang, X. Chen, Anderson localization of electrons in single crystals:  $\text{Li}_x\text{Fe}_7\text{Se}_8$ , *Science advances* 2(2) (2016) e1501283.
- [85] O. Erten, O.N. Meetei, A. Mukherjee, M. Randeria, N. Trivedi, P. Woodward, Theory of half-metallic ferrimagnetism in double perovskites, *Physical review letters* 107(25) (2011) 257201.
- [86] S. Geprägs, P. Majewski, R. Gross, C. Ritter, L. Alff, Electron doping in the double perovskite  $\text{La}_x\text{A}_{2-x}\text{CrWO}_6$  with  $A = \text{Sr}$  and  $\text{Ca}$ , *Journal of applied physics* 99(8) (2006) 08J102.
- [87] J. Navarro, C. Frontera, L. Balcells, B. Martinez, J. Fontcuberta, Raising the Curie temperature in  $\text{Sr}_2\text{FeMoO}_6$  double perovskites by electron doping, *Physical Review B* 64(9) (2001) 092411.

- [88] K.-W. Lee, W. Pickett, Half semimetallic antiferromagnetism in the  $\text{Sr}_2\text{CrTO}_6$  system ( $T = \text{Os, Ru}$ ), *Physical Review B* 77(11) (2008) 115101.
- [89] O.N. Meetei, O. Erten, M. Randeria, N. Trivedi, P. Woodward, Theory of High  $T_C$  Ferrimagnetism in a Multiorbital Mott Insulator, *Physical review letters* 110(8) (2013) 087203.
- [90] R. Morrow, J.R. Soliz, A.J. Hauser, J.C. Gallagher, M.A. Susner, M.D. Sumption, A.A. Aczel, J. Yan, F. Yang, P.M. Woodward, The effect of chemical pressure on the structure and properties of  $A_2\text{CrOsO}_6$  ( $A = \text{Sr, Ca}$ ) ferrimagnetic double perovskite, *Journal of Solid State Chemistry* 238 (2016) 46-52.
- [91] R. Li, Y. Xu, J. He, S. Ullah, J. Li, J.-M. Liu, D. Li, C. Franchini, H. Weng, X.-Q. Chen, Weyl Ferroelectric Semimetal, eprint arXiv 1610.07142v1 (2016).
- [92] A.W. Sleight, C.T. Prewitt, High-pressure  $\text{HgTiO}_3$  and  $\text{HgPbO}_3$ : Preparation, characterization, and structure, *Journal of Solid State Chemistry* 6(4) (1973) 509-512.
- [93] C.-Q. Jin, J.-S. Zhou, J. Goodenough, Q. Liu, J. Zhao, L. Yang, Y. Yu, R. Yu, T. Katsura, A. Shatskiy, High-pressure synthesis of the cubic perovskite  $\text{BaRuO}_3$  and evolution of ferromagnetism in  $\text{ARuO}_3$  ( $A = \text{Ca, Sr, Ba}$ ) ruthenates, *Proceedings of the National Academy of Sciences* 105(20) (2008) 7115-7119.
- [94] H.L. Feng, M. Jansen,  $\text{Ba}_3\text{CuOs}_2\text{O}_9$  and  $\text{Ba}_3\text{ZnOs}_2\text{O}_9$ , a comparative study, *Journal of Solid State Chemistry* 258 (2018) 776-780.

## Chapter 2 Experimental methods

### 2.1 Sample preparation: high-pressure method

Pressure is an important variable in materials science. In the past few decades, high-pressure synthesis has undergone a renaissance with improvement of designs and techniques. The ‘large-volume’ synthesis presses have developed several different types, including belt, multi-anvil, toroidal and piston-cylinder designs [1]. In this thesis, the high-pressure synthesis methods were employed to all the samples, involving in belt and multi-anvil two types of instrument.

#### 2.1.1 Belt-type high-pressure apparatus (Kobe Steel, Ltd.)

The belt-type high-pressure apparatus can yield static pressures up to 6 GPa. The electrical heating system is installed in the high-pressure apparatus, which can heat the sample to 2000 °C with simultaneous maintaining pressures. **Fig 2.1** shows the image of the belt-type high-pressure apparatus and its control panels of press and heating. The apparatus contains two high-pressure anvils, upper and lower, and a high-pressure cylinder installed between the two anvils. Pyrophyllite cell in addition to gaskets are utilized as pressure transmitting medium, electrical insulation, and thermal insulation. The samples are sealed in the Pt capsules, which are heated by passage of an electric current through a tabular graphite.

The powders of starting materials were thoroughly mixed, followed by sealing in a Pt capsule. The whole procedures were conducted in an Ar-filled glove box. The sealed Pt capsules and pyrophyllite cell assembly was shown in the right of **Fig 2.1**. The assembled samples and gaskets were set in the apparatus and compressed to 6 GPa. The samples were being heated at various temperatures for 1 hour with maintaining the pressure of 6 GPa. Subsequently, the temperature was quenched to room temperature before the gradual release

of pressure.

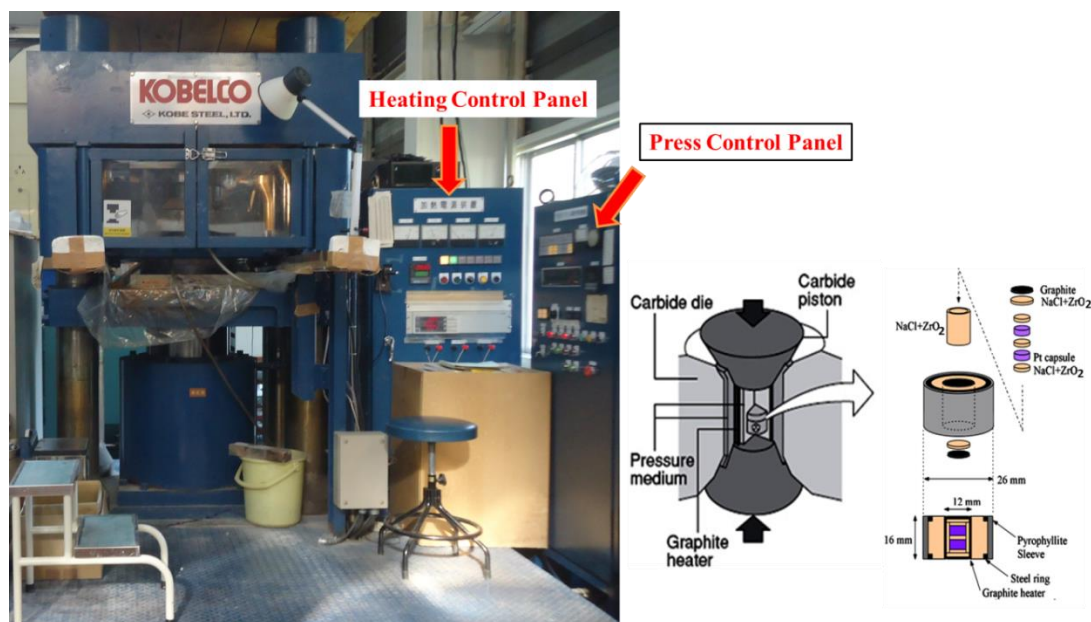


**Fig. 2.1** Belt-type high pressure apparatus set in National Institute for Materials Science (NIMS), and the schematic diagram of the capsule and sample container.

### 2.1.2 Multi-anvil-type high-pressure apparatus (CTF-MA1500P, C&T Factory Co., Ltd, Japan)

The multi-anvil-type apparatus utilized to synthesize part of samples in this thesis can give support for reaching a high pressure of 6 GPa and simultaneously temperatures up to 1700 °C. A multi-anvil press is a high-pressure apparatus in which samples can be compressed with more than three anvils. In the multi-anvil apparatus used in this thesis, six anvils with guide blocks create a cubic compression space. Therefore, a cubic pyrophyllite cell was used in the high-pressure experiment. The preparation of starting materials and the procedure of high-pressure and high-temperature experiment operated in multi-anvil-type apparatus are same as which in belt-type apparatus.



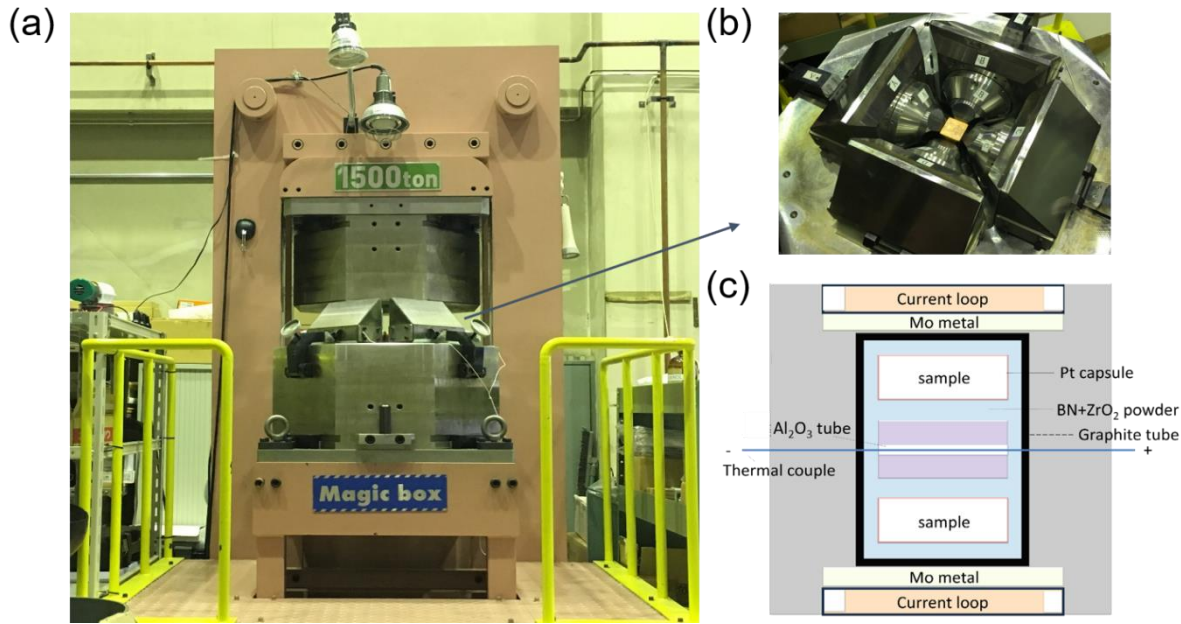


**Fig. 2.2** (a) Image of multi-anvil-type apparatus. (b) Image of the four anvils and the cubic compression space. (c) The schematic of cubic pyrophyllite cell.

## 2.2 X-ray diffraction measurement

X-rays are electromagnetic radiation of wavelength ranging from  $10^{-8}$  to  $10^{-11}$  m. The spectrum of X-rays occurs in that part of the electromagnetic spectrum, shown in **Fig. 2.3**.

Bragg's law is used to treat diffraction by crystals, which can be written as follow:

$$2d\sin\theta = n/\lambda,$$

where  $d$  is the perpendicular distance between pairs of adjacent planes,  $\theta$  is the angle of incidence. **Fig. 2.4** shows the derivation of Bragg's law.

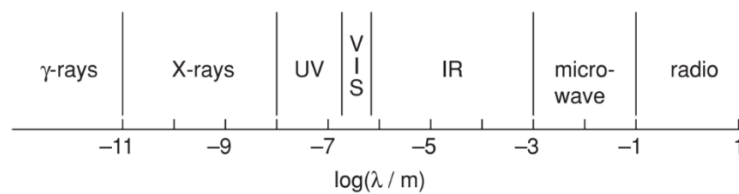


**Fig. 2.3** The electromagnetic spectrum [2]

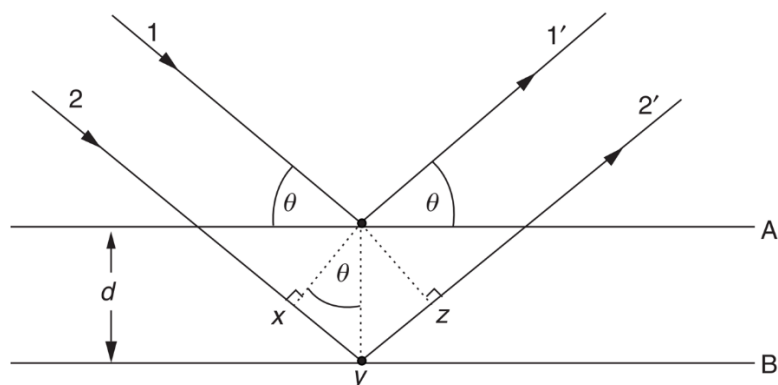


**Fig. 2.4** Derivation of Bragg's law. Two X-ray beams, 1 and 2, are reflected from adjacent planes, A and B. The reflected beams 1' and 2' are in-plane. [2]

### 2.2.1 Laboratory powder X-ray diffraction

Laboratory powder X-ray diffraction (XRD) is convenient to be used for phase identification and structure determination. In this thesis, the laboratory XRD measurements were carried out using a Desktop X-ray Diffractometer MiniFlex (Rigaku) equipped with a graphite monochromator and Cu-K $\alpha$  radiation ( $\lambda = 1.5418 \text{ \AA}$ ).



**Fig. 2.5** Image of Desktop X-ray Diffractometer MiniFlex (Rigaku)

### 2.2.2 Synchrotron powder X-ray diffraction

Synchrotron X-ray is emitted when electrons are accelerated and circulate in ultra-high vacuum tubes or storage rings. A simplified sketch of a storage ring is shown in **Fig. 2.6**.

Synchrotron radiation can give higher resolution in powder XRD data than laboratory X-ray source since the beams are accurately parallel and of extremely high intensity.

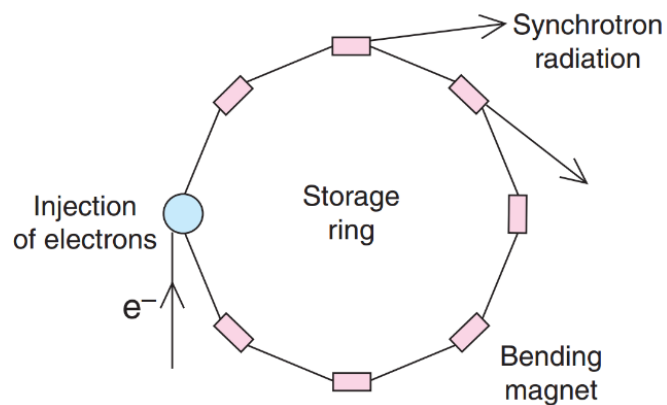


**Fig. 2.6** Schematic diagram of a synchrotron storage ring

The synchrotron XRD data were collected in BL15XU beamline, Spring-8, Japan. A high-precision powder X-ray diffractometer Debye-Scherrer camera is installed on the BL15XU beamline (see **Fig. 2.7**) and the incident X-ray wavelength of 0.65298 Å was used for measurements in this thesis.

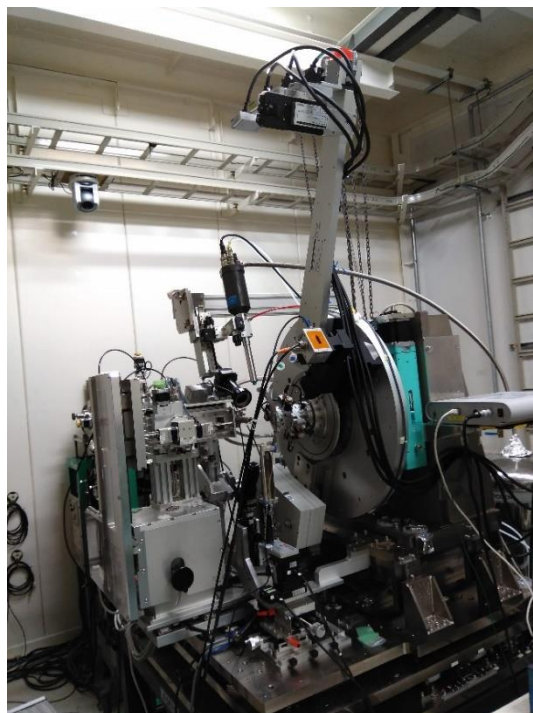


**Fig. 2.7** Picture of the BL15XU in Spring-8.

The powder sample were put in glass capillaries of 0.1 mm in diameter and the XRD patterns were collected in  $0.003^\circ$  increments over the range of  $5^\circ \leq 2\theta \leq 50^\circ$ . A Rietveld analysis was applied to the synchrotron XRD pattern by using the RIETAN-FP and VESTA software packages [3, 4].

### 2.2.3 Single crystal X-ray diffraction

Single crystal of  $\text{HgPbO}_3$  was also examined by single crystal XRD in a RIGAKU Saturn CCD diffractometer equipped with VariMax confocal optics for Mo- $K\alpha$  radiation ( $\lambda = 0.71073 \text{ \AA}$ ) at temperatures of 113 K and 300 K. Preliminary structure was solved by SHELXT [5] and refined by applying a full-matrix least-squares method to  $F^2$  by using the SHELXL-2016/6 program [6].

## 2.3 Magnetic properties measurement

Magnetic properties were measured in a magnetic property measurement system (MPMS, Quantum Design, Inc.), as shown in **Fig. 2.8**. Magnetic susceptibility ( $\chi$ ) can be measured at temperatures between 2 and 400 K under field-cooling (FC) and zero-field-cooling (ZFC) conditions. The field dependence isothermal magnetizations can be collected between +70 kOe and -70 kOe.



**Fig. 2.8** Picture of the MPMS-7T in NIMS Namiki-site

## 2.4 Electrical properties measurement

The electrical transport properties were measured using the Physical Property Measurement System (PPMS, Quantum Design Inc.), as shown in **Fig. 2.9**. The resistivity ( $\rho$ ) or Hall resistivity ( $\rho_H$ ) of polycrystalline samples were measured at temperatures of between 2 K and 400 K by using a four-probe method. Silver paste and gold or platinum wires (30  $\mu\text{m}$  in diameter) were utilized to connect the platelet to the device terminals.

The magnetoresistance (MR) was also measured in PPMS at 5 K via  $\text{MR} = [\rho(H) - \rho(H=0)]/\rho(H=0) \times 100\%$ , in which  $H$  is an applied magnetic field with a range of - 50–50 kOe.



**Fig. 2.9** Picture of the PPMS-9T in NIMS Namiki-site

## 2.5 Thermal properties measurement

The specific heat capacity ( $C_p$ ) was measured by applying a thermal-relaxation method from 2 K to 300 K with Apiezon N grease, which thermally connects the material to the holder stage. In some cases, the  $C_p$  - $T$  curves were measured using Apiezon-H grease in a temperature range from 350 to 200 K. The measurements of  $C_p$  were also carried out in PPMS.

## References in chapter 2

- [1] W.B. Holzapfel, N.S. Isaacs, High Pressure Techniques in Chemistry and Physics-A Practical Approach, High Pressure Techniques in Chemistry and Physics-A Practical Approach, by Edited by Wilfried B Holzapfel and Neil S Isaacs, pp. 398. Oxford University Press, Jul 1997. ISBN-10: 0198558112. ISBN-13: 9780198558118 (1997) 398.
- [2] A.R. West, Solid state chemistry and its applications, John Wiley & Sons 2014.
- [3] K. Momma, F. Izumi, VESTA 3 for three-dimensional visualization of crystal, volumetric and morphology data, Journal of Applied Crystallography 44(6) (2011) 1272-1276.
- [4] F. Izumi, A Rietveld-Analysis Programm RIETAN-98 and its Applications to Zeolite, Materials Science Forum 321 (2000) 198-205.
- [5] G.M. Sheldrick, SHELXT - Integrated space-group and crystal-structure determination, Acta Crystallographica Section A: Foundations and Advances 71(1) (2015) 3-8.
- [6] G.M. Sheldrick, Crystal structure refinement with SHELXL, Acta Crystallographica Section C: Structural Chemistry 71(1) (2015) 3-8.

# Chapter 3 High-pressure synthesis, crystal structure, and semi-metallic properties of $\text{HgPbO}_3$

## 3.1 Introduction

The provision of new material seeds for assisting the development of multifunctional devices that can simultaneously perform magnetic, electronic, and optical functions is a goal of materials research. The recent discovery of the coexistence of ferroelectric lattice instability and metallic conductivity in bulk  $\text{LiOsO}_3$  [1] and thin-film  $\text{LaNiO}_3$  on a  $\text{LaAlO}_3$  substrate [2] implies that electronic polarization and conduction could be combined in a device.[3, 4] The generalized concept of a “polar metal” is thus no longer hypothetical,[5] but rather multifunctional. Certainly, polar metals appear to be moving away from the materials development stage and into practical applications.[2-4, 6-8]

Li et al. recently demonstrated, using first-principles calculations, that ferroelectricity can also coexist with a Weyl semi-metal.[9] This coexistence is predicted to occur when the space group changes from  $R\bar{3}c$  to  $R3c$  as a result of a bulk oxide  $\text{HgPbO}_3$  losing its centrosymmetry. The proposed concept is entirely new, and we therefore believe that  $\text{HgPbO}_3$  should be studied further to determine whether the theoretical prediction is correct.

Ternary oxide  $\text{HgPbO}_3$  was synthesized for the first time by Sleight and Prewitt in 1973.[10] A polycrystalline bulk was synthesized by a solid-state reaction under pressures of 3–6.5 GPa and a temperature of 600–1000 °C. The electrical resistivity ( $\rho$ ) was reported as being in the order of  $10^{-3} \Omega\text{cm}$  at room temperature, suggesting the presence of metallic conduction (no further transport data have been reported to date). At the same time, mercury titanite ( $\text{HgTiO}_3$ ) was synthesized in the same manner under a pressure of 6.5 GPa and a temperature of 800–1100 °C. It was reported to be electrically insulating ( $\rho \approx 10^9 \Omega\text{cm}$  at room

temperature). It should be emphasized that a structural analysis was conducted only for the  $\text{HgTiO}_3$  and not for the  $\text{HgPbO}_3$ . This was “because problems with oxygen placement would be even more severe than for  $\text{HgTiO}_3$ ,” [10] so the structure of the  $\text{HgPbO}_3$  was assumed to be similar to that of  $\text{HgTiO}_3$ . In the present study, oxygen problems were not an issue given that the accuracy of the instrumentation technology had been improved in the interim.

In the same way as the common  $\text{LiNbO}_3$  ferroelectric oxide, it was clarified that the structure of electrically insulating  $\text{HgTiO}_3$  is also non-centrosymmetric ( $R3c$ ) at room temperature.[10, 11] To date, however, it has not been clear whether the structure of conductive  $\text{HgPbO}_3$  is centrosymmetric. In the present study, we synthesized a polycrystalline bulk of  $\text{HgPbO}_3$  using a similar technique under a high pressure of 6 GPa and a temperature of 800 °C. As such, we were able to grow single crystals (< 0.2 mm) under the high-pressure conditions at 1000 °C by adding a mixture of  $\text{PbO}$  and  $\text{PbF}_2$ . Based on single-crystal X-ray diffraction (XRD) as well as the powder synchrotron XRD of  $\text{HgPbO}_3$ , the structure at room temperature cannot be described by any of  $R-3c$ ,  $R3c$ , or  $R3m$ , but can be described by  $R-3m$ , indicating that  $\text{HgPbO}_3$  is other than non-centrosymmetric at room temperature.

Furthermore, phonon excitation of an anharmonic vibrational mode occurs around 50 K upon cooling, suggesting that the probability of a martensitic transition from  $R-3m$  to  $R3m$  is considerably lower, even at low temperatures. At 113 K, single-crystal XRD did not detect any trace of a non-centrosymmetric transition. In addition to the structural studies, electronic transport measurements revealed that  $\text{HgPbO}_3$  is an oxide semi-metal, which is very rare.

### 3.2 Experimental details

Polycrystalline  $\text{HgPbO}_3$  was synthesized by a solid-state reaction from powders of  $\text{HgO}$  (99.9%, Kojundo Chem. Lab. Co., Ltd.),  $\text{PbO}_2$  (99.9%, Kojundo Chem. Lab. Co., Ltd.), and  $\text{KClO}_4$  (> 99.5%, Kishida Chem. Lab. Co., Ltd.). The powders were thoroughly mixed at



10 at.% Pb-rich stoichiometry, followed by sealing in a Pt capsule. The mixing procedures were conducted in an Ar-filled glove box. Under a pressure of 6 GPa, generated in a multi-anvil-type apparatus, the capsule was heated to 800 °C for 30 min, after which the pressure was gradually released. Single crystals of HgPbO<sub>3</sub> were grown in the same apparatus by adding a mixture of 10 mole% PbO (99.999%, Kojundo Chem. Lab. Co., Ltd.) and 11.7 mole% PbF<sub>2</sub> (99.9%, Kojundo Chem. Lab. Co., Ltd.) to the starting mixture. The pressure of 6 GPa was maintained during heating to 1000 °C for 1 h. The crystals obtained were rinsed with water and dried in an oven at a temperature of less than 100 °C. The resulting crystals were shiny and black. Typically, the crystals measured no more than 200 μm in their largest dimension.

The high-pressure-synthesized product was investigated by powder XRD at room temperature using Cu-Kα radiation ( $\lambda = 1.5432 \text{ \AA}$ ) in a commercial apparatus (RIGAKU-MiniFlex 600). A selected product was subjected to a synchrotron XRD study at room temperature using the high-precision powder X-ray diffractometer installed at the BL15XU beamline, SPring-8, Japan.[12, 13] A Rietveld analysis was applied to the synchrotron XRD pattern by using the RIETAN-FP and VESTA software packages.[14, 15] Selected single crystals, having the largest dimension no more than 60 μm, of HgPbO<sub>3</sub> were examined by XRD in a RIGAKU Saturn CCD diffractometer equipped with VariMax confocal optics for Mo-Kα radiation ( $\lambda = 0.71073 \text{ \AA}$ ) at temperatures of 113 K and 300 K. Preliminary structure was solved by SHELXT [16] and refined by applying a full-matrix least-squares method to  $F^2$  by using the SHELXL-2016/6 program.[17]

The  $\rho$  of polycrystalline HgPbO<sub>3</sub> was measured at temperatures of between 2 K and 300 K by using a four-probe method. The gauge current was 3 mA. The Hall resistivity ( $\rho_H$ ) was measured on a rectangular polycrystalline platelet ( $2.58 \times 1.90 \times 0.60 \text{ mm}^3$ ) using a four-probe method combined with alternating current transport (10 mA). Silver paste and gold wires (30 μm in diameter) were utilized to connect the platelet to the device terminals. The specific

heat capacity ( $C_p$ ) was measured by applying a thermal-relaxation method from 2 K to 300 K with Apiezon N grease, which thermally connects the material to the holder stage. The values of  $C_p$  as well as  $\rho$  and  $\rho_H$  were measured using the Physical Property Measurement System (PPMS, Quantum Design Inc.). The magnetoresistance (MR) was also measured in PPMS at 5 K via  $MR = [\rho(H) - \rho(H=0)] / \rho(H=0) \times 100\%$ , in which  $H$  is an applied magnetic field with a range of - 50–50 kOe. The magnetic properties were measured using the Magnetic Properties Measurement System (MPMS, Quantum Design Inc.). The magnetic susceptibility ( $\chi$ ) was measured at temperatures of between 2 K and 400 K in a fixed applied magnetic field of 10 kOe under field-cooling (FC) and zero-field-cooling (ZFC) conditions. For reference, the temperature dependence of  $\chi$  of loosely compacted Bi powder (99%, 200 mesh, Rare Metallic Co., Ltd.) was measured under the same conditions. The isothermal magnetization ( $M-H$ ) was measured for a sweeping field ranging from - 70–70 kOe at various temperatures. Sample holder contributions to all magnetic data measured in MPMS were subtracted using null data.

### 3.3 Results and discussion

By adjusting the ratio of the HgO and PbO<sub>2</sub> starting materials, the 10 at.% Pb-rich stoichiometry was found to be optimum for minimizing the formation of impurities in the target polycrystalline HgPbO<sub>3</sub> product. The need for excess PbO<sub>2</sub> in the starting materials may be due to the reaction between the Pt capsule and the outer parts of the starting materials under the synthesis condition. Indeed, the inner surface of the Pt capsule after synthesis was impure, supporting the possibility. In the absence of excess PbO<sub>2</sub>, a small amount of HgO was present in the products (**Fig. 3.1**). While, PbO<sub>2</sub> was detected by XRD when excess PbO<sub>2</sub> higher than 10 at.% was added. Furthermore, to avoid possible oxygen deficiency, an excess KClO<sub>4</sub> oxygen source was added to the starting mixture according to the reaction formula  $HgO + 1.1PbO_2 + (y/4)KClO_4$  ( $0 \leq y \leq 0.3$ ). Overall, the XRD patterns were well characterized by assuming a hexagonal unit cell with a space group of  $R-3m$  (clarified by single-crystal XRD, as shown

later), regardless of the value of  $y$ . All the peaks were indexed by  $hkl$  numbers, except for the one very small peak which is indicated by an asterisk (bottom pattern in **Fig. 3.2a**). The uncharacterized peak was most likely caused by unidentified impurities. The hexagonal lattice parameters were calculated from the pattern analysis and plotted against  $y$  (**Fig. 3.2b**); we were able to see a small but systematic change. With an increase in the amount of  $\text{KClO}_4$  from  $y = 0$  to 0.3, the major peaks exhibited a tiny right-shift trend (inset of **Fig. 3.2a**), reflecting a probable change in the oxygen content of the compound. As a result, the quality of the compound synthesized at a  $\text{HgO}:\text{PbO}_2:\text{KClO}_4$  ratio of 1:1.1:0.075 was the highest under the high-pressure synthesis conditions. The highest-quality polycrystalline  $\text{HgPbO}_3$  was nearly oxygen-stoichiometric because the lattice parameters did not change by much when a further oxygen source was added. In addition, the single-crystal XRD also did not detect any feature suggesting oxygen deficiency beyond the resolution.

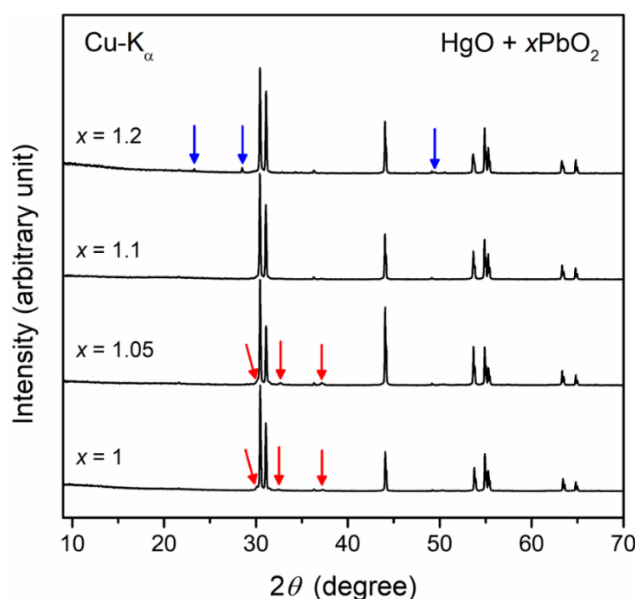


**Fig. 3.1** Powder XRD patterns of high-pressure synthesized products with various ratios of starting powders  $\text{HgO}$  and  $\text{PbO}_2$ . The red and blue arrows point  $\text{HgO}$  and  $\text{PbO}_2$  peaks, respectively. Residual  $\text{HgO}$  or  $\text{PbO}_2$  is present if the ratio of  $\text{HgO}$  to  $\text{PbO}_2$  is less than or greater than 1.1.

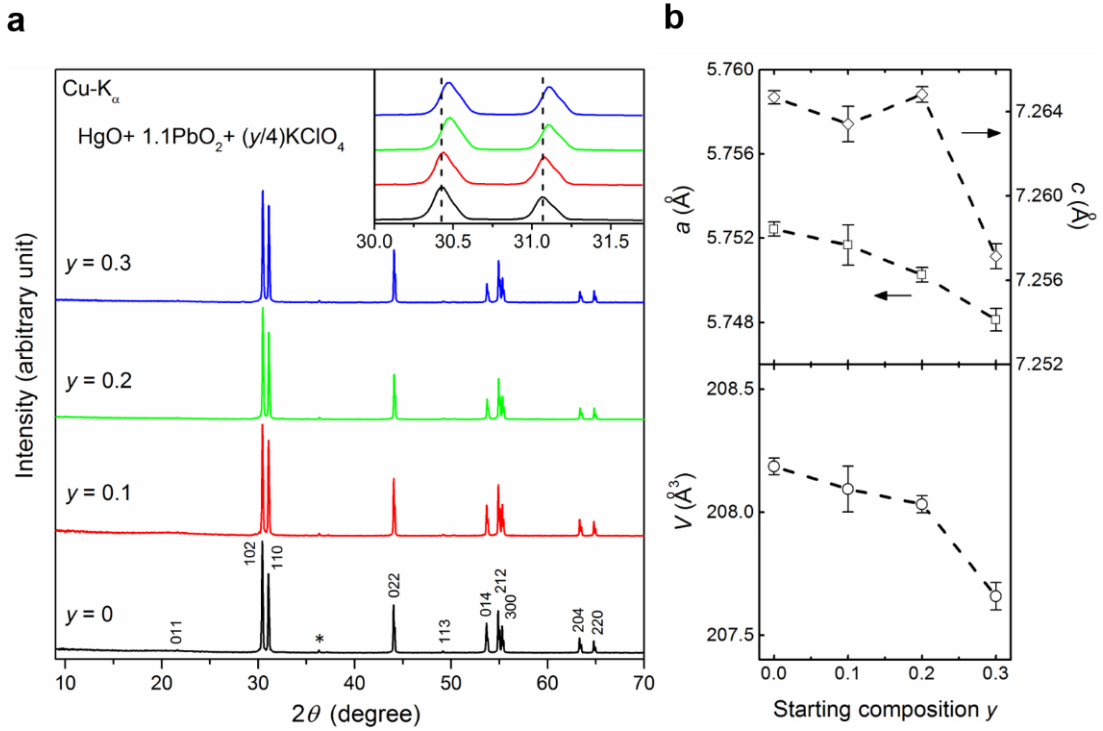


**Fig. 3.2** (a) Powder XRD patterns of high-pressure synthesized products with various starting compositions. The inset is a horizontal expansion. The vertical broken line is for reference. Every pattern can be fully characterized by a trigonal cell with a space group of  $R\bar{3}m$  (hexagonal setting). The asterisk indicates the largest impurity peak, which presumably comes from HgO. (b) Unit cell parameters and volume,  $V$ , estimated by the powder XRD, vs. the starting composition  $y$ .

Selected single crystals of  $\text{HgPbO}_3$  ( $< 60 \mu\text{m}$ ; **Fig. 3.3a**) were investigated using a single-crystal XRD method and the structural parameters were successfully refined. The measurement conditions and refined parameters are summarized in Tables 1 and 2, respectively. Often,  $\text{HgPbO}_3$  appears as a  $\text{LiNbO}_3$ -type oxide with a non-centrosymmetric lattice (space group  $R3c$ ) in the literature.[18, 19] The present study, however, could not confirm the non-centrosymmetric feature. **Fig. 3.3b–d** show synthetic precession photographs of the diffractions observed from a single  $\text{HgPbO}_3$  crystal. Along the projections, both odd and even numbers of  $hkl$  reflections can be confirmed. The combination of odd and even numbers is unlikely to be caused by twinning. Therefore, the reflection condition does not satisfy the requirement for the  $R3c$  and  $R\bar{3}c$  space groups but satisfies the condition for either the  $R\bar{3}m$

or  $R3m$  space group. Although the  $R3c$  and  $R-3c$  space groups are rather common in  $\text{LiNbO}_3$ -type oxides,[18]  $R-3m$  or  $R3m$  have been observed in limited numbers in related oxides such as  $\text{RbNbO}_3$  [20] and  $\text{KNbO}_3$ . [21]

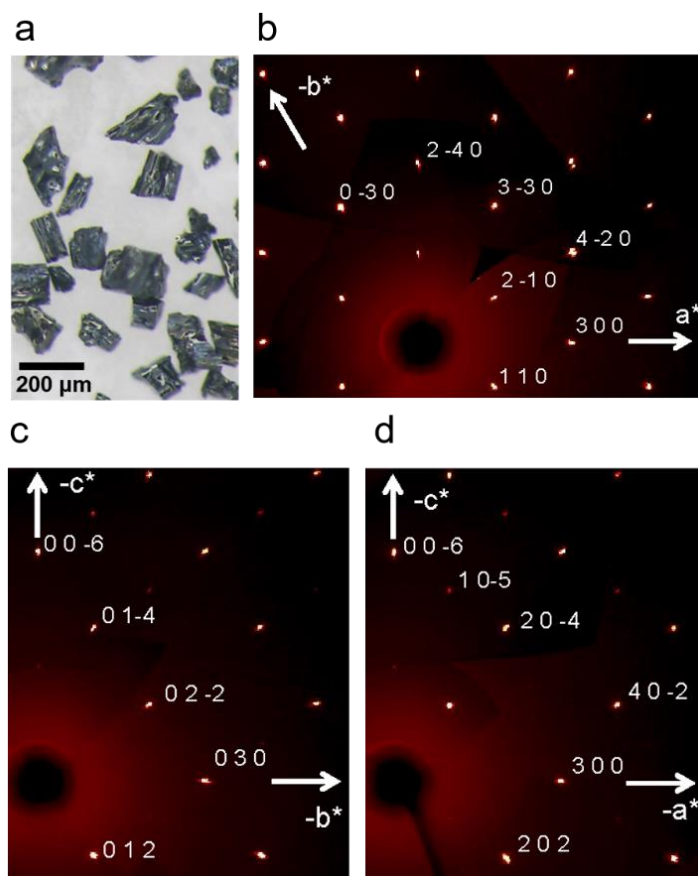


**Fig. 3.3** (a) Photograph of crystals of  $\text{HgPbO}_3$  grown under high pressure. (b) Synthetic precession photographs of all observed diffractions for a selected crystal of  $\text{HgPbO}_3$ ;  $hk0$  projection, (c)  $0kl$  projection, and (d)  $h0l$  projection.

**Table 3.1** Crystallographic and structure refinement data for HgPbO<sub>3</sub> at 300 K.<sup>a</sup>

Empirical formula	Hg <sub>1.02</sub> PbO <sub>3</sub>
Formula weight	459.63
Temperature	300(2) K
Wavelength	0.71073 Å (Mo K <sub>α</sub> )
Crystal system	Trigonal
Space group	<i>R</i> -3 <i>m</i> : <i>H</i>
Unit cell dimensions	<i>a</i> = 5.7631(2) Å, <i>c</i> = 7.2903(3) Å
Volume	209.695(17) Å <sup>3</sup>
<i>Z</i>	3
Density (calculated)	10.848 g cm <sup>-3</sup>
Absorption coefficient	114.966 mm <sup>-1</sup>
<i>F</i> <sub>000</sub>	559
Crystal size	0.058 × 0.054 × 0.040 mm <sup>3</sup>
2θ for data collection	4.950– 46.189°
Index ranges	-9 ≤ <i>h</i> ≤ 10, -11 ≤ <i>k</i> ≤ 9, -14 ≤ <i>l</i> ≤ 14
Reflections collected	1926
Independent reflections	246 [ <i>R</i> (int) = 0.0416]
Completeness to θ = 25.242°	98.2%
Absorption correction	Semi-empirical from equivalents
Max. and min. transmission	0.1083 and 0.2894
Refinement method	Full-matrix least-squares on <i>F</i> <sup>2</sup>
Data/restraints/parameters	246/1/17
Goodness-of-fit on <i>F</i> <sup>2</sup>	1.258
Final <i>R</i> indices [ <i>I</i> > 2σ( <i>I</i> )]	<i>R</i> <sub>1</sub> = 0.0131, w <i>R</i> <sub>2</sub> = 0.0362
<i>R</i> indices (all data)	<i>R</i> <sub>1</sub> = 0.0132, w <i>R</i> <sub>2</sub> = 0.0369
Extinction coefficient	0.0080(6)
Largest diff. peak and hole	2.181 and -2.550 eÅ <sup>-3</sup>

<sup>a</sup> Accession code to the Cambridge Crystallographic Data Centre (CCDC) is 1824924.

**Table 3.2** Atomic coordinates and equivalent isotropic displacement parameters ( $U_{eq}$ ,  $10^{-3} \text{ \AA}^2$ ) and anisotropic displacement parameters ( $U_{ij}$ ;  $10^{-3} \text{ \AA}^2$ ) as measured by X-ray diffraction on a single-crystal  $\text{HgPbO}_3$  at 300 K.<sup>a</sup>

Site	WP <sup>b</sup>	Occp.	$x$	$y$	$z$	$U_{eq}$ <sup>c</sup>
Pb	3b	1	1/3	2/3	1/6	6(1)
Hg1	3a	0.948(8)	2/3	1/3	1/3	17(1)
Hg2	6c	0.035(4)	2/3	1/3	0.2520(20)	5(2)
O	18f	0.5	1/3	0.0448(7)	2/3	18(1)
Site	$U_{11}$	$U_{22}$	$U_{33}$	$U_{23}$	$U_{13}$	$U_{12}$
Pb	6(1)	$= U_{11}$	7(1)	0	0	$= 0.5 \times U_{11}$
Hg1	10(1)	$= U_{11}$	30(1)	0	0	$= 0.5 \times U_{11}$
Hg2	3(1)	$= U_{11}$	9(5)	0	0	$= 0.5 \times U_{11}$
O	19(2)	13(1)	24(2)	$= 2 \times U_{13}$	-16(1)	$= 0.5 \times U_{22}$

<sup>a</sup> Accession code to the Cambridge Crystallographic Data Centre (CCDC) is 1824924.

<sup>b</sup> Wyckoff positions

<sup>c</sup>  $U_{eq}$  is defined as one third of the trace of the orthogonalized  $U_{ij}$  tensor. The anisotropic displacement factor exponent takes the form  $-2\pi^2 [h^2 a^{*2} U_{11} + \dots + 2hka^*b^* U_{12}]$ .

To further confirm the structural symmetry either centrosymmetric ( $R\bar{3}m$ ) or non-centrosymmetric ( $R3m$ ), we carefully refined the Hg1 and Hg2 sites. **Fig. 3.4a** and **Fig. 3.4b** show structure images of the final  $R\bar{3}m$  model drawn perpendicular and parallel to the c-axis, respectively. The ordinal orange color balls indicate the centrosymmetric Hg1 site (Wyckoff site: 3a, Site symmetry:  $\bar{3}m$ ) sharing a plane with neighbor oxygen atoms, and the light orange balls indicate a split Hg2 site (Wyckoff site: 6c, Site symmetry:  $3m$ ). The refined occupancy factor clearly shows that the major Hg atoms (~95%) occupies the centrosymmetric Hg1 site locating at  $\bar{3}m$  and only few% occupies the lower symmetric Hg2 site ( $3m$ ). Moreover, in a trial, we examined the  $R3m$  model. However, it did not give any reasonable analytical result with significantly higher R1 value (>3%). We can conclude, therefore, that the possibility of non-centrosymmetric ( $R3m$ )  $\text{HgPbO}_3$  is very small. At 113 K, the crystal structural analysis was conducted in the same manner, and the result again supported the conclusion. The 113 K

data are summarized in **Tables 3.3** and **3.4**.

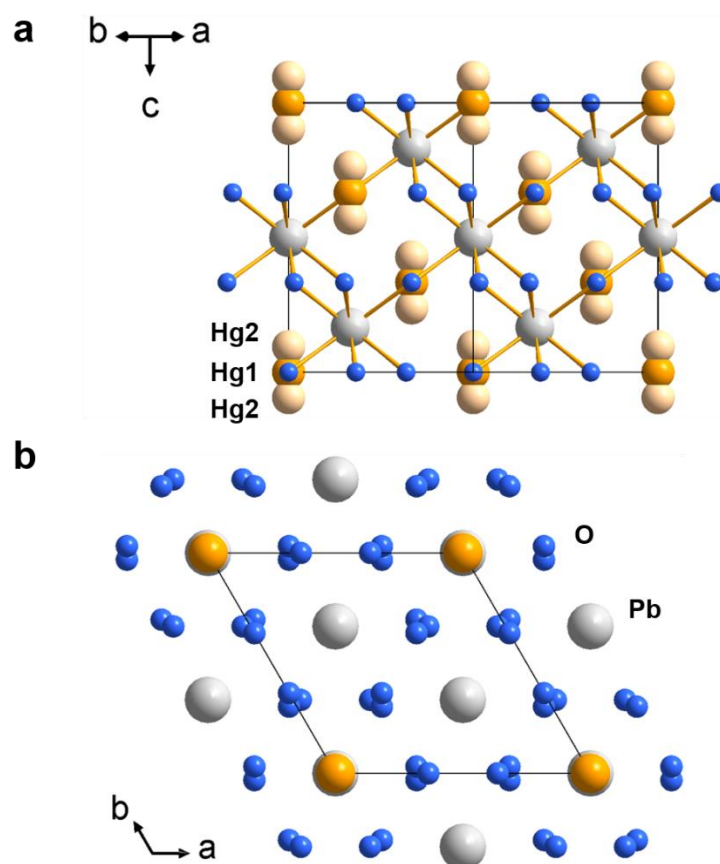


**Fig. 3.4** Structural images of  $\text{HgPbO}_3$  drawn using the refined parameters of a single crystal XRD study. (a) View along the  $[110]$  direction and (b) the  $[001]$  direction. The crystal structure symmetry is trigonal ( $R\bar{3}m$ : hexagonal setting). The blue balls represent oxygen sites, which are half-occupied. The plain and light-orange balls represent mercury sites, which are occupied by majority (around 93%) and minority (around 7%), respectively. The gray balls represent the lead sites which are fully occupied.



**Table 3.3** Crystallographic and structure refinement data for HgPbO<sub>3</sub> at 113 K.<sup>a</sup>

Empirical formula	Hg <sub>1.01</sub> PbO <sub>3</sub>
Formula weight	458.28
Temperature	113(2) K
Wavelength	0.71073 Å (Mo K <sub>α</sub> )
Crystal system	Trigonal
Space group	<i>R</i> -3 <i>m</i> : <i>H</i>
Unit cell dimensions	<i>a</i> = 5.7443(8)Å, <i>c</i> = 7.2570(11) Å
Volume	207.38(7) Å <sup>3</sup>
<i>Z</i>	3
Density (calculated)	11.009 g cm <sup>-3</sup>
Absorption coefficient	116.704 mm <sup>-1</sup>
<i>F</i> <sub>000</sub>	561
Crystal size	0.022 × 0.021 × 0.020 mm <sup>3</sup>
2θ for data collection	4.968– 46.393°
Index ranges	−8 ≤ <i>h</i> ≤ 11, −11 ≤ <i>k</i> ≤ 11, −9 ≤ <i>l</i> ≤ 14
Reflections collected	1672
Independent reflections	242 [ <i>R</i> (int) = 0.0539]
Completeness to θ = 25.242°	98.2 %
Absorption correction	Semi-empirical from equivalents
Max. and min. transmission	0.2891 and 0.1717
Refinement method	Full-matrix least-squares on <i>F</i> <sup>2</sup>
Data/restraints/parameters	242/0/18
Goodness-of-fit on <i>F</i> <sup>2</sup>	1.266
Final <i>R</i> indices [ <i>I</i> > 2σ( <i>I</i> )]	<i>R</i> <sub>1</sub> = 0.0305, w <i>R</i> <sub>2</sub> = 0.0607
<i>R</i> indices (all data)	<i>R</i> <sub>1</sub> = 0.0325, w <i>R</i> <sub>2</sub> = 0.0644
Extinction coefficient	0.0116(10)
Largest diff. peak and hole	5.251 and −7.972 eÅ <sup>-3</sup>

<sup>a</sup> Accession code to the Cambridge Crystallographic Data Centre (CCDC) is 1824925.

**Table 3.4** Atomic coordinates and equivalent isotropic displacement parameters ( $U_{eq}$ ,  $10^{-3} \text{ \AA}^2$ ) and anisotropic displacement parameters ( $U_{ij}$ ;  $10^{-3} \text{ \AA}^2$ ) as measured by X-ray diffraction on a single-crystal  $\text{HgPbO}_3$  at 113 K.<sup>a</sup>

Site	WP <sup>b</sup>	Occp.	$x$	$y$	$z$	$U_{eq}$ <sup>c</sup>
Pb	3 <i>b</i>	1	1/3	2/3	1/6	6.1(2)
Hg1	3 <i>a</i>	0.943(6)	2/3	1/3	1/3	12.7(1)
Hg2	6 <i>c</i>	0.035(3)	2/3	1/3	0.248(3)	10(2)
O	18 <i>f</i>	0.5	1/3	0.0417(10)	2/3	17(1)
Site	$U_{11}$	$U_{22}$	$U_{33}$	$U_{23}$	$U_{13}$	$U_{12}$
Pb	5.9(2)	= $U_{11}$	7(2)	0	0	= $0.5 \times U_{11}$
Hg1	7.8(2)	= $U_{11}$	23(1)	0	0	= $0.5 \times U_{11}$
Hg2	10(2)	= $U_{11}$	10(6)	0	0	= $0.5 \times U_{11}$
O	22(3)	15(2)	17(2)	= $2 \times U_{13}$	-9(2)	= $0.5 \times U_{22}$

<sup>a</sup> Wyckoff positions

<sup>b</sup>  $U_{eq}$  is defined as one third of the trace of the orthogonalized  $U_{ij}$  tensor. The anisotropic displacement factor exponent takes the form  $-2\pi^2 [h^2 a^{*2} U_{11} + \dots + 2hka^* b^* U_{12}]$ .

The final structural solution obtained from the single-crystal XRD study was employed to investigate the average structure of  $\text{HgPbO}_3$  powder. The powder synchrotron XRD pattern was analyzed using the Rietveld method. **Fig. 3.5** shows the final refined pattern for a refinement quality of  $R_{wp} = 1.677\%$  and  $R_p = 1.302\%$ . No noticeable impurities were detected. The refined structural parameters are summarized in **Table 3.5**, showing that there is no significant mismatch between the sets of parameters for the single crystal and those for the powder  $\text{HgPbO}_3$ . Both sets seem to accurately represent the crystal structure of  $\text{HgPbO}_3$ , synthesized under a high pressure of 6 GPa. Note that the structure refinement reveals large thermal displacement parameters of the major Hg atoms at Hg1 site, especially anisotropic displacement parameter  $U_{33}$  [=  $23(5) \times 10^{-3} \text{ \AA}^2$ ]. The large atomic displacement parameters were also discovered in the  $\beta$ -pyrochlore oxides  $\text{RbOs}_2\text{O}_6$  [ $U_{iso} = 34.1(9) \times 10^{-3} \text{ \AA}^2$ ] [22] and  $\text{CuCu}_3\text{V}_4\text{O}_{12}$  [ $U_{iso} = 44.6(9) \times 10^{-3} \text{ \AA}^2$ ] at 300 K.[23] The characteristic thermal displacement features may be connected to phonon excitation of an anharmonic vibrational mode (shown later) as discussed previously.[23]

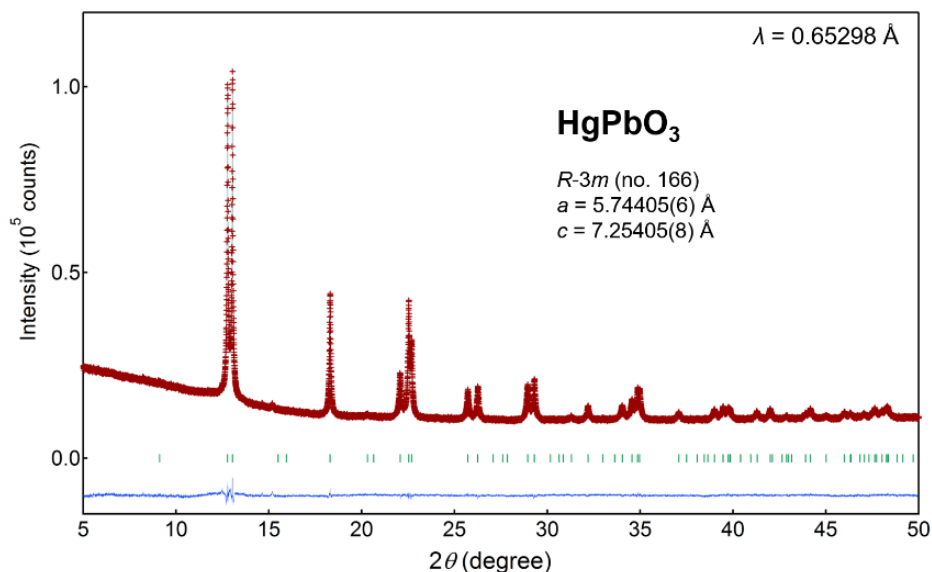


**Fig. 3.5** Rietveld refinement of the powder synchrotron XRD profile ( $\lambda = 0.65298 \text{ \AA}$ ) collected at room temperature. The crosses and solid lines show the observed and calculated patterns, respectively, with their differences shown at the bottom. The expected Bragg reflections for the  $R\text{-}3m$  cell are marked by ticks.

**Table 3.5** Atomic coordinates and equivalent isotropic displacement parameters ( $U_{\text{eq}}$ ,  $10^{-3} \text{ \AA}^2$ ) and anisotropic displacement parameters ( $U_{ij}$ ,  $10^{-3} \text{ \AA}^2$ ) as measured by synchrotron X-ray diffraction of powder  $\text{HgPbO}_3$  at 300 K.<sup>a</sup>

Site	WP	Occp.	$x$	$y$	$z$	$U_{\text{eq}}$
Pb	$3b$	1	$1/3$	$2/3$	$1/6$	4.7(3)
Hg1	$3a$	0.927(3)	$2/3$	$1/3$	$1/3$	18.8(5)
Hg2	$6c$	0.037	$2/3$	$1/3$	0.243(3)	= Hg1
O	$18f$	0.5	$1/3$	0.037(1)	$2/3$	38(3)
Site	$U_{11}$	$U_{22}$	$U_{33}$	$U_{23}$	$U_{13}$	$U_{12}$
Pb	3.4(5)	= $U_{11}$	7.2(8)	0	0	= $0.5 \times U_{11}$
Hg1	13.9(7)	= $U_{11}$	23(5)	0	0	= $0.5 \times U_{11}$

<sup>a</sup> Accession code to the Cambridge Crystallographic Data Centre (CCDC) is 1824962.

Space group:  $R\text{-}3m$  (Trigonal; A-166); lattice constants  $a = 5.74405(6) \text{ \AA}$  and  $c = 7.25405(8) \text{ \AA}$ ; cell volume =  $207.289(4) \text{ \AA}^3$ ;  $d_{\text{cal}} = 10.943 \text{ g cm}^{-3}$ ; Chemical formula sum:  $\text{HgPbO}_3$  ( $Z = 3$ ); and the final  $R$  values are 1.677% ( $R_{\text{wp}}$ ), 1.302% ( $R_{\text{p}}$ ), 0.479% ( $R_{\text{B}}$ ), and 0.307% ( $R_{\text{F}}$ ), respectively. Temperature factors of Hg2 site were fixed as same values at Hg1 site, and also at O site it was refined at the isotropic temperature factors level.

The average bond length of Pb–O calculated from the powder synchrotron XRD data

is 2.183 Å ( $\times 6$ ), giving a bond valence sum (BVS) [24] is 4.10. This is slightly higher than the expectation obtained from the tetravalent state of Pb, implying that Pb is somewhat over-bonded.[25] Note that the constants  $B = 0.37$  and  $R_0(\text{Pb}^{4+}) = 2.042$  were used in this calculation.[24] As shown in **Fig. 3.6a**, the Pb atom is coordinated by 6 oxygen atoms to form octahedral  $\text{PbO}_6$ . This appears to be typical for Pb oxides such as  $\text{APbO}_3$  ( $A = \text{Ca}, \text{Sr}, \text{Ba}$ ) [26] and  $\text{ZnPbO}_3$ . [27] However, the coordination of the Hg atoms is highly unusual (**Fig. 3.6b**). To the best of our knowledge, a planar-coordinated  $\text{HgO}_3$  has been reported only for  $\text{HgTiO}_3$ . [10, 11] Even in complexes, the coordination examples such as the planar  $\text{HgX}_3$  ( $X = \text{Cl}^-, \text{Br}^-, \text{I}^-$ ) are quite limited. [28, 29]

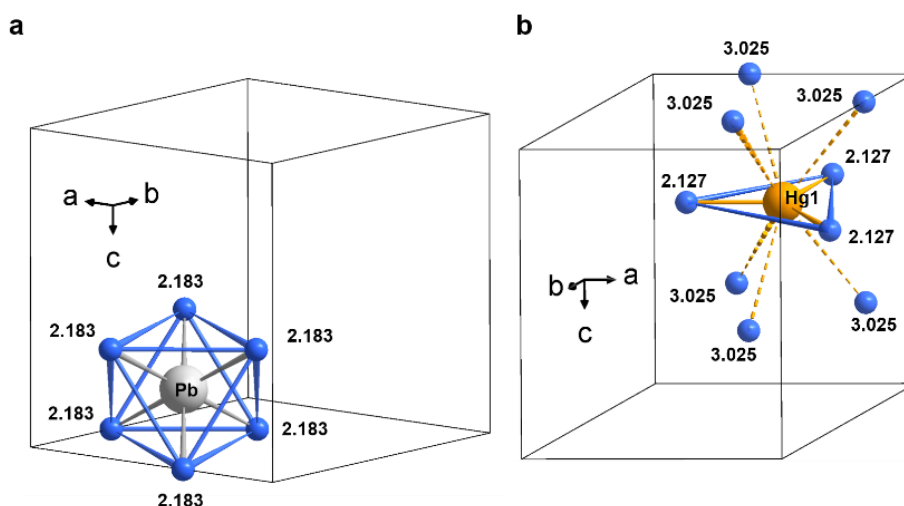


**Fig. 3.6** Sketches of the local coordination of (a) Pb and (b) Hg atoms with O atoms. The number indicates the bond length (unit: Å) between the Pb/Hg and O atoms. The solid lines indicate a hexagonal cell for which with  $a = 5.74413(6)$  Å and  $c = 7.25464(8)$  Å.

To further analyze the coordination environment of Hg, we calculated the BVS of Hg. To date, several parameters of  $R_0$  and  $B$  have been proposed for the  $\text{Hg}^{2+}$ –O bond. We employed the empirical set [ $B = 0.37$  and  $R_0(\text{Hg}^{2+}) = 1.972$ ] [30] for this calculation. The planar coordinated  $\text{HgO}_3$  (coordination number: 3) yielded 1.97; while  $\text{HgO}_9$  (coordination number:  $3 + 6$ ) consisting of the in-plane bonds (solid bonds in **Fig. 3.6b**, 2.127 Å  $\times 3$ ) and additional out-of-plane bonds (dotted bonds in **Fig. 3.6b**, 3.025 Å  $\times 6$ ) yielded 2.32. The BVS values give

little indication of whether the out-of-plane bond (3.025 Å) plays a significant role in the local environment. Note that other combinations of B and  $R_0$  were examined in the same manner; however, it was not possible to attain a clearer understanding.

It was confirmed that HgPbO<sub>3</sub> exhibits metallic temperature dependence of  $\rho$  at temperatures of less than 300 K (**Fig. 3.7**). At room temperature,  $\rho$  is approximately  $6 \times 10^{-4}$  Ωcm, which is comparable to the values obtained for polycrystalline metallic oxides,[31] but the temperature dependence is minimal. The roughly estimated residual-resistivity ratio (RRR) is 1.5 and rather, the temperature dependence is similar to that of PtO<sub>2</sub> (which may be a semi-metal) ( $6 \times 10^{-4}$  Ωcm at 300 K).[32] The coefficient A for the temperature dependence is  $2.629(3) \times 10^{-9}$  Ωcm/K<sup>2</sup> determined from quadratic fitting ( $\rho = \rho_0 + AT^2$ ;  $T > 2$  K), which of semi-metal Bi is  $12.5(5) \times 10^{-9}$  Ωcm/K<sup>2</sup> ( $T > 6$  K).[33] The parameters directly indicate that  $\rho$  of HgPbO<sub>3</sub> is much weakly dependent on temperature; however, the integrated scattering mechanism due to polycrystallinity needs to be qualitatively and quantitatively evaluated for further analysis of the carrier transport. Since a significant MR has been observed for semi-metals,[34, 35] we investigated the MR of HgPbO<sub>3</sub> at a low temperature of 5 K. It was, however, remarkably small within the field range (see the inset in **Fig. 3.7**).

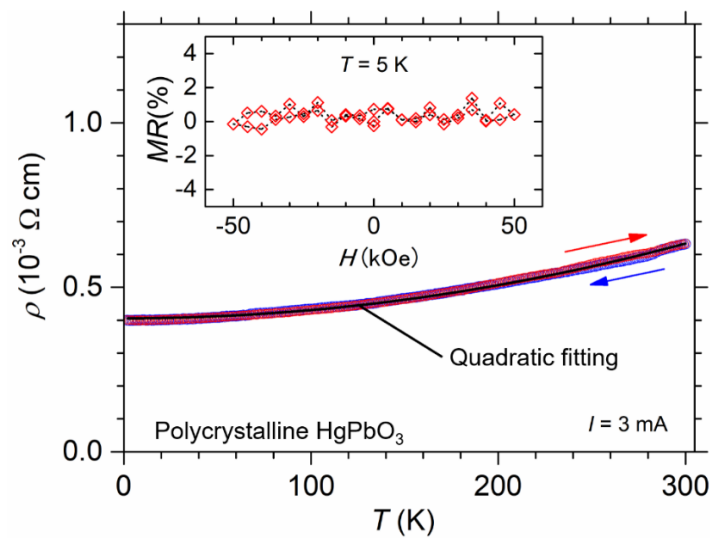


**Fig. 3.7** Temperature dependence of  $\rho$  of the polycrystalline HgPbO<sub>3</sub>, and (inset) MR at 5 K.

We measured  $\rho_H$  at several temperatures between 5–300 K. Because the curve of  $\rho_H$  vs  $H$  shows a linear trend at every temperature within the field range (see the inset in **Fig. 3.8**), we considered only the ordinary Hall term to analyze the data. The fitting was undertaken by applying  $\rho_H = R_H B$  to the curve, where the slope ( $R_H$ ) is the Hall coefficient. The  $R_H$  is plotted against the temperature (**Fig. 3.8a**) and exhibits a weak temperature dependence. The plot shows that the dominant carrier is positively charged, and the carrier concentration ( $n$ ) is  $7.3\text{--}8.5 \times 10^{20} \text{ cm}^{-3}$ , which was calculated from the formula  $n = (R_H \cdot q)^{-1}$ , where  $q$  is the elementary charge. The value of  $n$  is essentially independent of the temperature and corresponds to around 0.05/f.u. Note that  $n$  of Bi (a semi-metal) is in the order of  $3.5 \times 10^{17} \text{ cm}^{-3}$ , which is three orders of magnitude lower.[36]

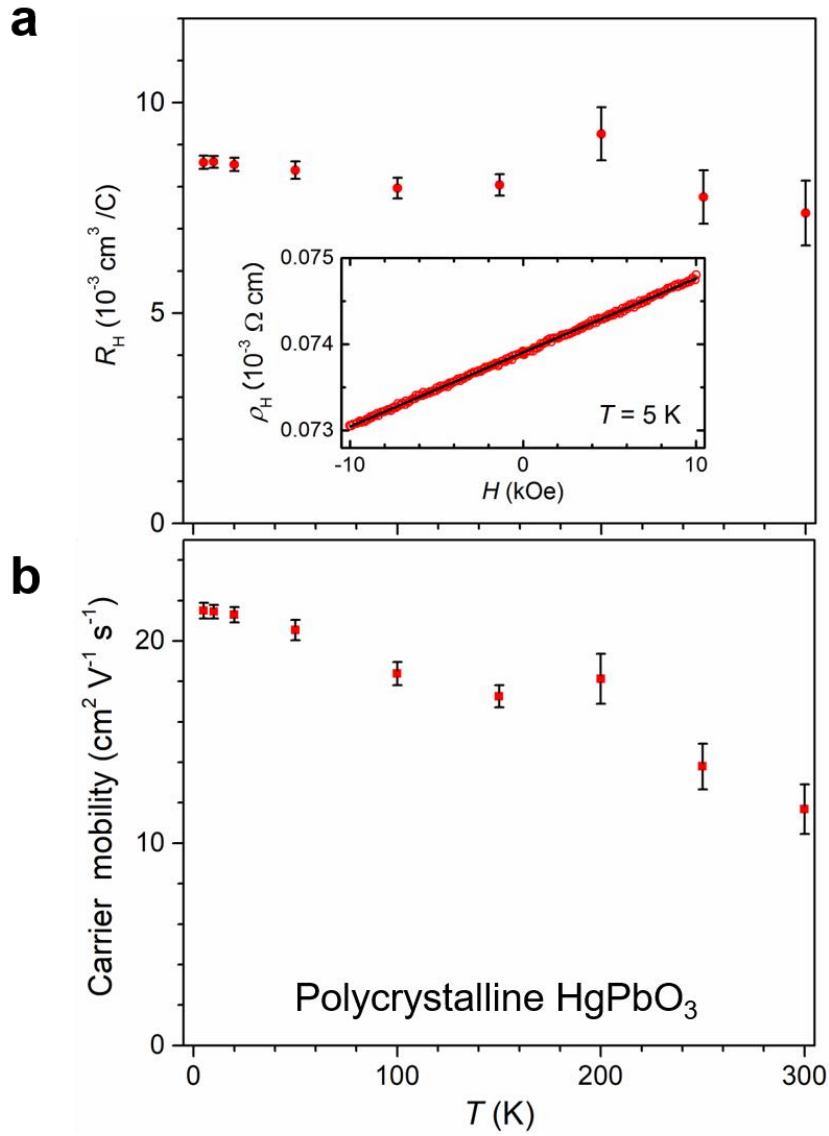


**Fig. 3.8** (a) Temperature dependence of  $R_H$  and (inset) magnetic field dependence of  $\rho_H$  at 5 K. The solid line is a fit to the data. (b) Temperature dependence of carrier mobility of the polycrystalline HgPbO<sub>3</sub>.

Conductivity ( $\sigma$ ) of the material is determined not only by the carrier concentration but also by the carrier mobility. This relationship is usually given by  $\sigma = q(\mu_n n + \mu_p p)$ , where  $\mu_n$  and  $\mu_p$  represent the mobilities of electrons and holes, and  $n$  and  $p$  represent the concentration of electrons and holes, respectively. In the present case, because the dominant carrier of HgPbO<sub>3</sub> is positively charged, we applied the simplified equation  $\sigma = q\mu_p p$  to estimate the carrier mobility. The carrier mobility was 11.7–21.5  $\text{cm}^2 \text{ V}^{-1} \text{ s}^{-1}$  over the temperature range

from 300 K to 5 K, which is remarkably lower than that of Bi ( $2.1 \times 10^5 \text{ cm}^2 \text{ V}^{-1} \text{ s}^{-1}$ ).[37] **Fig. 3.8b** shows the carrier mobility decreases with increasing temperature, indicating the influence of lattice scattering is dominant even at low temperature.

The  $\chi$  of  $\text{HgPbO}_3$  is only very slightly dependent on the temperature (except the low-temperature Curie–Weiss part) as well as the transport properties (**Fig. 3.9**). The room temperature  $\chi$  is negative at about  $-1.02 \times 10^{-4} \text{ emu mol}^{-1}$ , with a value that is as in the same order as that of the Bi powder. As far as we know, the largest diamagnetism of elements and inorganic compounds in the normal state (not the superconducting state) was observed for Bi.[38] The value of  $\chi$  rapidly rises around 80 K upon cooling, crossing zero at 67 K. The low temperature part of the  $\chi$  vs. T curve closely follows the Curie–Weiss law (solid curve in **Fig. 3.9**). The analytical formula,  $\chi = \chi_0 + C/(T-T_0)$ , was used to fit the curve below 20 K, in which  $\chi_0$ ,  $C$ , and  $T_0$  are the temperature-independent term, Curie constant, and Weiss temperature, respectively. The effective moment defined by  $\mu_{\text{eff}} = (8C)^{1/2} \mu_B$  was estimated to be  $1.02(9) \mu_B$  while  $T_0$  was  $-31(4) \text{ K}$ . Since magnetic impurities in the diamagnetic host usually involve a near-zero  $T_0$ ,[39] the formation of magnetic impurities is very unlikely for this compound. In addition, given that there is no qualitative information about the magnetic impurities, we therefore cannot refer to the value of  $\mu_{\text{eff}}$ .

The inset in **Fig. 3.9** shows the magnetic-field-induced isothermal magnetization at 5 K, 20 K, and 300 K. At 300 K, it exhibits a linearly negative slope that is consistent with the diamagnetism observed in the  $\chi$  vs. T measurement. However, at 5 K, a qualitatively different behavior appears; when the applied magnetic field increases, the magnetization increases, and when the strength of the magnetic field is further increased, the magnetization gradually saturates. Therefore, the 5 K curve appears to be composed of a saturation moment of approximately  $0.005 \mu_B \text{ mol}^{-1}$ . Although the origin of the small magnetization cannot be elucidated at this stage, since the starting powders were high-purity oxides containing only



nonmagnetic Pb and Hg metals (and  $\text{KClO}_4$ ), and since no magnetic impurities were detected by XRD, the small degree of magnetization is unlikely to have been caused by unexpected magnetic impurities in the compound.

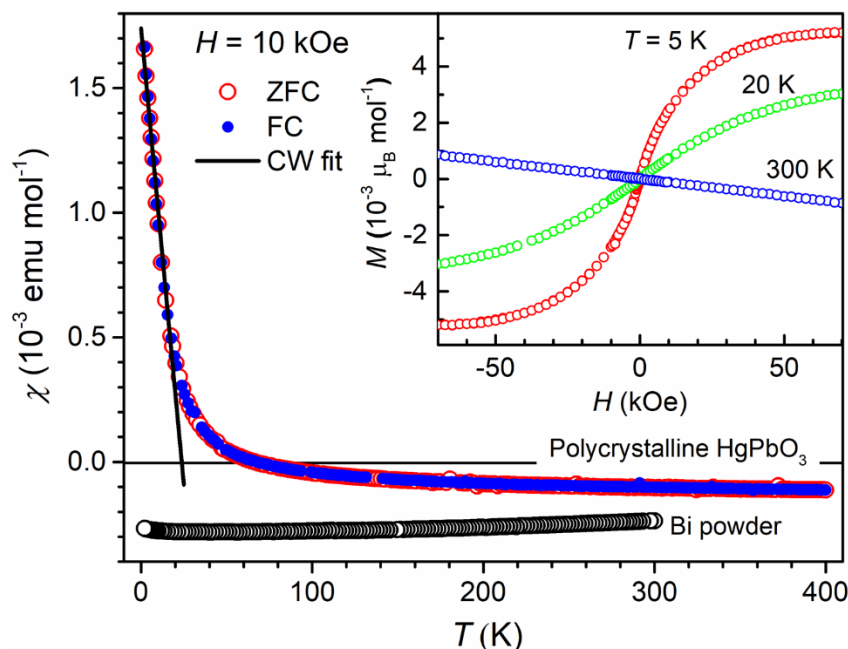


**Fig. 3.9** Temperature dependence of  $\chi$  of polycrystalline  $\text{HgPbO}_3$ , measured in a field of 10 kOe. The dotted curve is simulated by the Curie-Weiss law. The inset shows the isothermal magnetization at various temperatures. For comparison, the temperature dependence of  $\chi$  of Bi powder is shown, measured in the same magnetic field (FC).

**Fig. 3.10** shows the temperature dependence of the  $C_p$  value of  $\text{HgPbO}_3$ . There is no obvious anomaly over a temperature range of 2–300 K. The absence of any anomalies implies that the possibility of magnetic moment ordering around 80 K is very low. The low-temperature limit of the total value of  $C_p$  was analyzed by applying the approximate Debye model,  $C_p/T = \beta_0 T^2 + \gamma$ , where  $\beta_0$  is a constant and  $\gamma$  is the Sommerfeld coefficient. A linear feature appears in the  $C_p/T$  vs.  $T^2$  plot below approximately 3 K. As shown in the inset in **Fig. 3.10**, fitting to the linear part by the model yielded  $\beta_0 = 7.6(2) \times 10^{-4} \text{ J mol}^{-1} \text{ K}^{-4}$  and  $\gamma = 1.6(1) \times 10^{-3} \text{ J mol}^{-1} \text{ K}^{-2}$ . The Debye temperature ( $T_D$ ) was calculated from the observed  $\beta_0$  as  $T_D = 234(2) \text{ K}$ . This  $\gamma$  value is much smaller than those of metallic oxides such as  $\text{LiOsO}_3$  [ $7.7(2) \text{ mJ mol}^{-1} \text{ K}^{-2}$ ] [1],

CaOsO<sub>3</sub> [18.1(1)mJ mol<sup>-1</sup> K<sup>-2</sup>],[40] SrOsO<sub>3</sub> [27.3(2) mJ mol<sup>-1</sup> K<sup>-2</sup>],[40] BaOsO<sub>3</sub> [16.8(1) mJ mol<sup>-1</sup> K<sup>-2</sup>],[40] Cd<sub>2</sub>Re<sub>2</sub>O<sub>7</sub> [26.5 mJ mol<sup>-1</sup> K<sup>-2</sup>],[41] and Cd<sub>2</sub>Ru<sub>2</sub>O<sub>7</sub> [12.3 mJ mol<sup>-1</sup> K<sup>-2</sup>].[41] On the other hand, it is comparable with those of nearly free electron oxides such as Ag<sub>5</sub>Pb<sub>2</sub>O<sub>6</sub> [3.42 mJ mol<sup>-1</sup> K<sup>-2</sup>] [42, 43] and PdCoO<sub>2</sub> [1.28 mJ mol<sup>-1</sup> K<sup>-2</sup>].[44, 45] The present result of the small  $\gamma$  value implies a weak electron-electron interaction in HgPbO<sub>3</sub>, and may be consistent with the result of relatively small number of carrier concentration and the resulting feature of large demagnetization.

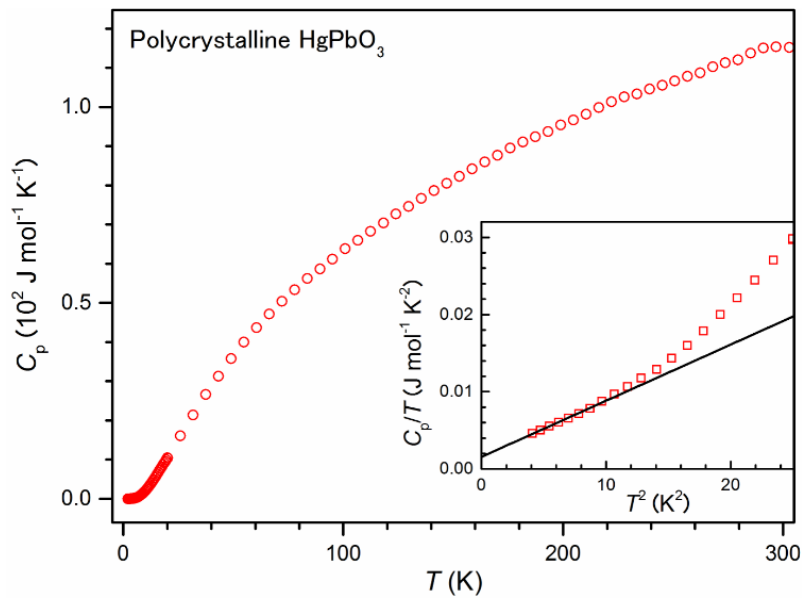


**Fig. 3.10**  $C_p$  vs.  $T$  curve of HgPbO<sub>3</sub>. The upper axis corresponds to the Dulong-Petit limit of the lattice specific heat. (Inset) Linear fit to the  $C_p/T$  vs.  $T^2$  curve for low-temperature limit.

The Debye–Einstein model [46] was applied to analyze the lattice-specific heat ( $C_p - \gamma T$ )/ $T^3$  vs.  $T$  curve as shown in **Fig. 3.11**. The following analytical formula:

$$C(T) - \gamma T = n_D \times 9N_A k_B \left( \frac{T}{T_D} \right)^3 \int_0^{T_D/T} \frac{x^4 e^x}{(e^x - 1)^2} dx + n_E \times 3N_A k_B \left( \frac{T_E}{T} \right)^2 \frac{e^{T_E/T}}{(e^{T_E/T} - 1)^2},$$

where  $T_E$  is the Einstein temperature,  $N_A$  is Avogadro's constant,  $k_B$  is Boltzmann's constant, fits the curve well over a temperature range between 2 K and 300 K with the variable

parameters of  $T_D = 171(4)$  K,  $T_E = 50.2(3)$  K,  $n_D = 2.1(1)$ , and  $n_E = 0.313(5)$ . Scale factors  $n_D$  and  $n_E$  correspond to the numbers of vibrating modes per formula unit in the Debye and Einstein models, respectively. The fitting curve is decomposed into two components, as shown in **Fig. 3.11**, indicating that the noticeable peak-like anomaly can be well characterized by the Einstein term, implying that phonon excitation of an anharmonic vibrational mode occurs at temperatures below 50 K. Although the low-temperature lattice specific heat is quantitatively and qualitatively similar to that which was observed for the  $\beta$ -pyrochlore oxide  $\text{RbOs}_2\text{O}_6$  [47] and the quadruple perovskite  $\text{CuCu}_3\text{V}_4\text{O}_{12,23}$   $\text{HgPbO}_3$  does not have any cage-like structures. For comparison, the lattice-specific heat of  $\text{RbOs}_2\text{O}_6$  is plotted in **Fig. 3.11** (the data were taken from Ref. [47]). Note that the scale factors  $n_D$  and  $n_E$  do not satisfy the expected relation  $n_D + n_E = 5$  (5 atoms per formula unit) from a simple Debye model with Einstein oscillators. This is in part because the applicable temperature range of the model is much narrower than the temperature range used in the analysis. At the very least, we can tell that the phonon density of states (DOS) at frequencies corresponding to temperatures below 50 K constitutes a much more complex DOS structure than the model.

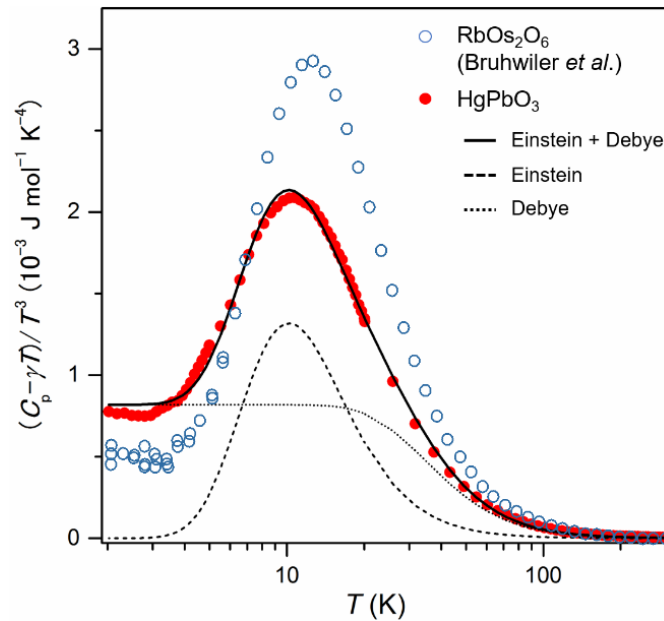


**Fig. 3.11** Lattice specific heat capacity of  $\text{HgPbO}_3$ , compared with that of  $\text{RbOs}_2\text{O}_6$ . [47] The

adaptation of the Debye and Einstein models to the lattice contribution is shown by the dotted and broken curves, respectively. Their total is indicated by the solid curve.

### 3.4 Summary of Chapter 3

Through single-crystal XRD and powder-synchrotron XRD studies, the crystal structure of  $\text{HgPbO}_3$  was well characterized by a centrosymmetric model with a space group of  $R\bar{3}m$ , rather than a non-centrosymmetric model, unlike that of  $\text{HgTiO}_3$ . [10] (i) The centrosymmetry is likely to be resilient to cooling because around 93 at.% of the Hg atoms occupy the crystallographic  $3a$  site ( $\bar{3}m$ ) sharing a plane with the neighboring oxygen atoms. (ii) The phonon excitation of an anharmonic vibrational mode was clearly observed at low temperature ( $< 50$  K), in contrast to the rather static lattice feature of  $\text{LiOsO}_3$ , [1, 48] (iii) Peak-like anomalies associated with phase transitions were not evident for a temperature range of 2–300 K in the  $C_p$  measurement. Based on the experimental results (i–iii), we can conclude that  $\text{HgPbO}_3$  is unlikely to exhibit any martensitic transitions with a loss of centrosymmetry at temperatures above 2 K. This conclusion, however, appears to contradict the results of theoretical studies.[9] Measurements of second harmonic generation, electron diffraction, and neutron diffraction can help to ensure the centrosymmetric feature of the  $\text{HgPbO}_3$  structure in future experiments.

The electronic transport measurements revealed that  $\text{HgPbO}_3$  is metallic in nature such that  $\rho$  at room temperature ( $\sim 6 \times 10^{-4} \Omega\text{cm}$ ) is as low as that of metallic oxides, and it falls further upon cooling. The carrier concentration ( $= 7.3\text{--}8.5 \times 10^{20} \text{ cm}^{-3}$ ) is as high as that of metallic oxides. However, the temperature dependence of  $\rho$  is very weak as to be the small quadratic fitting parameter  $A [= 2.629(3) \times 10^{-9} \Omega\text{cm/K}^2]$  and the RRR value of 1.5, the large diamagnetism is of the same level as Bi powder, and the value of  $\gamma [= 1.6(1) \times 10^{-3} \text{ J mol}^{-1} \text{ K}^{-2}]$  is remarkably small. These results imply that  $\text{HgPbO}_3$  is not a normal metal but rather a semi-metal. To the best of our knowledge, very few semi-metallic oxides have been identified.

Unlike  $AOs_2O_6$  ( $A = K, Rb$ ) and  $CuCu_3V_4O_{12}$ ,  $HgPbO_3$  does not have a cage-like structure, but  $HgPbO_3$  exhibits phonon excitation of an anharmonic vibrational mode that is as significant as those of  $RbOs_2O_6$  and  $CuCu_3V_4O_{12}$ . Furthermore, the Curie-Weiss-like magnetism, which appears at low temperatures, may be coupled to the unusual lattice dynamics occurring at those temperatures. The mechanism that causes the cage-free anharmonic lattice dynamics and the possible coupling to the Curie-Weiss-like magnetism requires further study in the future.

### References in Chapter 3

- [1] Y. Shi, Y. Guo, X. Wang, A.J. Princep, D. Khalyavin, P. Manuel, Y. Michiue, A. Sato, K. Tsuda, S. Yu, M. Arai, Y. Shirako, M. Akaogi, N. Wang, K. Yamaura, A.T. Boothroyd, A ferroelectric-like structural transition in a metal, *Nature Materials* 12 (2013) 1024.
- [2] T.H. Kim, D. Puggioni, Y. Yuan, L. Xie, H. Zhou, N. Campbell, P.J. Ryan, Y. Choi, J.W. Kim, J.R. Patzner, S. Ryu, J.P. Podkaminer, J. Irwin, Y. Ma, C.J. Fennie, M.S. Rzchowski, X.Q. Pan, V. Gopalan, J.M. Rondinelli, C.B. Eom, Polar metals by geometric design, *Nature* 533(7601) (2016) 68.
- [3] C. Ma, X. He, K.J. Jin, Polar instability under electrostatic doping in tetragonal  $SnTiO_3$ , *Physical Review B* 96(3) (2017) 7.
- [4] D. Puggioni, G. Giovannetti, M. Capone, J.M. Rondinelli, Design of a Mott Multiferroic from a Nonmagnetic Polar Metal, *Physical Review Letters* 115(8) (2015) 6.
- [5] P.W. Anderson, E.I. Blount, Symmetry Considerations on Martensitic Transformations: "Ferroelectric" Metals?, *Physical Review Letters* 14(7) (1965) 217-219.
- [6] H. Sakai, K. Ikeura, M.S. Bahramy, N. Ogawa, D. Hashizume, J. Fujioka, Y. Tokura, S. Ishiwata, Critical enhancement of thermopower in a chemically tuned polar semimetal  $MoTe_2$ , *Science Advances* 2(11) (2016) 7.

- [7] J. Fujioka, A. Doi, D. Okuyama, D. Morikawa, T. Arima, K.N. Okada, Y. Kaneko, T. Fukuda, H. Uchiyama, D. Ishikawa, A.Q.R. Baron, K. Kato, M. Takata, Y. Tokura, Ferroelectric-like metallic state in electron doped BaTiO<sub>3</sub>, *Scientific Reports* 5 (2015) 9.
- [8] D. Puggioni, J.M. Rondinelli, Designing a robustly metallic noncentrosymmetric ruthenate oxide with large thermopower anisotropy, *Nature Communications* 5 (2014) 3432.
- [9] R. Li, Y. Xu, J. He, S. Ullah, J. Li, J.-M. Liu, D. Li, C. Franchini, H. Weng, X.-Q. Chen, Weyl Ferroelectric Semimetal, eprint arXiv 1610.07142v1 (2016).
- [10] A.W. Sleight, C.T. Prewitt, High-pressure HgTiO<sub>3</sub> and HgPbO<sub>3</sub>: Preparation, characterization, and structure, *Journal of Solid State Chemistry* 6(4) (1973) 509-512.
- [11] A.I. Lebedev, Ferroelectricity and pressure-induced phase transitions in HgTiO<sub>3</sub>, *Physics of the Solid State* 54(8) (2012) 1663-1668.
- [12] M. Tanaka, Y. Katsuya, Y. Matsushita, O. Sakata, Development of a synchrotron powder diffractometer with a one-dimensional X-ray detector for analysis of advanced materials, *Journal of the Ceramic Society of Japan* 121(1411) (2013) 287-290.
- [13] M. Tanaka, Y. Katsuya, A. Yamamoto, A new large radius imaging plate camera for high-resolution and high-throughput synchrotron x-ray powder diffraction by multiexposure method, *Review of Scientific Instruments* 79(7) (2008) 075106.
- [14] K. Momma, F. Izumi, VESTA 3 for three-dimensional visualization of crystal, volumetric and morphology data, *Journal of Applied Crystallography* 44(6) (2011) 1272-1276.
- [15] F. Izumi, A Rietveld-Analysis Programm RIETAN-98 and its Applications to Zeolite, *Materials Science Forum* 321 (2000) 198-205.
- [16] G.M. Sheldrick, SHELXT - Integrated space-group and crystal-structure determination, *Acta Crystallographica Section A: Foundations and Advances* 71(1) (2015) 3-8.
- [17] G.M. Sheldrick, Crystal structure refinement with SHELXL, *Acta Crystallographica Section C: Structural Chemistry* 71(1) (2015) 3-8.

- [18] J. He, C. Franchini, J.M. Rondinelli, Lithium Niobate-Type Oxides as Visible Light Photovoltaic Materials, *Chemistry of Materials* 28(1) (2016) 25-29.
- [19] N. Hasan Sadat, P. Rossitza, R. Rajeev, Ab initio electronic structures of rhombohedral and cubic  $\text{HgXO}_3$  ( $X = \text{Ti, Pb}$ ), *Journal of Physics: Condensed Matter* 22(4) (2010) 045504.
- [20] A.I. Lebedev, Ferroelectric properties of  $\text{RbNbO}_3$  and  $\text{RbTaO}_3$ , *Physics of the Solid State* 57(2) (2015) 331-336.
- [21] H. Xu, Y.-J. Ko, T.-G. Lee, S.-J. Park, M.-S. Noh, B.-Y. Kim, J.S. Kim, S. Nahm, Structural and Piezoelectric Properties of  $(\text{Na}_{1-x}\text{K}_x)\text{NbO}_3$  Platelets and Their Application for Piezoelectric Nanogenerator, *Journal of the American Ceramic Society* 99(10) (2016) 3476-3484.
- [22] R. Galati, R.W. Hughes, C.S. Knee, P.F. Henry, M.T. Weller, The structure of superconducting  $\text{RbOs}_2\text{O}_6$  between 2 K and 300 K, *Journal of Materials Chemistry* 17(2) (2007) 160-163.
- [23] Y. Akizuki, I. Yamada, K. Fujita, K. Taga, T. Kawakami, M. Mizumaki, K. Tanaka, Rattling in the Quadruple Perovskite  $\text{CuCu}_3\text{V}_4\text{O}_{12}$ , *Angewandte Chemie International Edition* 54(37) (2015) 10870-10874.
- [24] D. Altermatt, I.D. Brown, The automatic searching for chemical bonds in inorganic crystal structures, *Acta Crystallographica Section B* 41(4) (1985) 240-244.
- [25] I. Grinberg, V.R. Cooper, A.M. Rappe, Oxide chemistry and local structure of  $\text{PbZr}_x\text{Ti}_{1-x}\text{O}_3$  studied by density-functional theory supercell calculations, *Physical Review B* 69(14) (2004) 144118.
- [26] A. Yamamoto, N.R. Khasanova, F. Izumi, X.J. Wu, T. Kamiyama, S. Torii, S. Tajima, Crystal Structure and Its Role in Electrical Properties of the Perovskite  $\text{CaPbO}_3$  Synthesized at High Pressure, *Chemistry of Materials* 11(3) (1999) 747-753.

- [27] R. Yu, H. Hojo, T. Mizoguchi, M. Azuma, A new  $\text{LiNbO}_3$ -type polar oxide with closed-shell cations:  $\text{ZnPbO}_3$ , *Journal of Applied Physics* 118(9) (2015) 094103.
- [28] H. Terao, M. Hashimoto, S. Hashimoto, Y. Furukawa, Studies of structure and phase transition in  $\text{C}(\text{NH}_2)_3\text{HgBr}_3$  and  $\text{C}(\text{NH}_2)_3\text{HgI}_3$  by means of halogen NQR,  $\text{H}^{-1}$  NMR, and single crystal X-ray diffraction, *Zeitschrift Fur Naturforschung Section a-a Journal of Physical Sciences* 55(1-2) (2000) 230-236.
- [29] T.R. Griffiths, R.A. Anderson, Electronic spectra, formation constants, and geometries of  $\text{HgX}^{3-}$  in methanol, *Inorganic Chemistry* 30(8) (1991) 1912-1918.
- [30] I. Brown, D. Altermatt, Bond-valence parameters obtained from a systematic analysis of the inorganic crystal structure database, *Acta Crystallographica Section B: Structural Science* 41(4) (1985) 244-247.
- [31] J.B. Goodenough, Metallic oxides, *Progress in Solid State Chemistry* 5 (1971) 145-399.
- [32] R.D. Shannon, Synthesis and properties of two new members of the rutile family  $\text{RhO}_2$  and  $\text{PtO}_2$ , *Solid State Communications* 6(3) (1968) 139-143.
- [33] G. Kuka, W. Kraak, H.J. Gollnest, R. Herrmann, Temperature dependence of the resistivity in semimetals of the Bismuth type, *physica status solidi (b)* 89(2) (1978) 547-551.
- [34] A. Narayanan, M.D. Watson, S.F. Blake, N. Bruyant, L. Drigo, Y.L. Chen, D. Prabhakaran, B. Yan, C. Felser, T. Kong, P.C. Canfield, A.I. Coldea, Linear Magnetoresistance Caused by Mobility Fluctuations in *n*-Doped  $\text{Cd}_3\text{As}_2$ , *Physical Review Letters* 114(11) (2015) 117201.
- [35] C. Shekhar, A.K. Nayak, Y. Sun, M. Schmidt, M. Nicklas, I. Leermakers, U. Zeitler, Y. Skourski, J. Wosnitza, Z. Liu, Y. Chen, W. Schnelle, H. Borrmann, Y. Grin, C. Felser, B. Yan, Extremely large magnetoresistance and ultrahigh mobility in the topological Weyl semimetal candidate NbP, *Nature Physics* 11 (2015) 645.



- [36] A.N. Friedman, S.H. Koenig, Size Effects for Conduction in Thin Bismuth Crystals, IBM Journal of Research and Development 4(2) (1960) 158-162.
- [37] J.-P. Issi, J.-P. Michenaud, J. Heremans, Electron scattering in compensated bismuth, Physical Review B 14(12) (1976) 5156.
- [38] Young, Hugh D. University physics / Hugh D. Young Edition 8th ed. / extended version with modern physics. Imprint Reading, Mass. ; Wokingham : Addison-Wesley, 1992.
- [39] M. Khalid, A. Setzer, M. Ziese, P. Esquinazi, D. Spemann, A. Pöpl, E. Goering, Ubiquity of ferromagnetic signals in common diamagnetic oxide crystals, Physical Review B 81(21) (2010) 214414.
- [40] Y. Shi, Y. Guo, Y. Shirako, W. Yi, X. Wang, A.A. Belik, Y. Matsushita, H.L. Feng, Y. Tsujimoto, M. Arai, High-pressure synthesis of 5d cubic perovskite BaOsO<sub>3</sub> at 17 GPa: ferromagnetic evolution over 3d to 5d series, Journal of the American Chemical Society 135(44) (2013) 16507-16516.
- [41] K. Blacklock, H. White, Specific heats of the pyrochlore compounds Cd<sub>2</sub>Re<sub>2</sub>O<sub>7</sub> and Cd<sub>2</sub>Ru<sub>2</sub>O<sub>7</sub>, The Journal of Chemical Physics 71(12) (1979) 5287-5289.
- [42] M. Sutherland, P.D. Mann, C. Bergemann, S. Yonezawa, Y. Maeno, Nearly free electrons in the layered oxide superconductor Ag<sub>5</sub>Pb<sub>2</sub>O<sub>6</sub>, Physical review letters 96(9) (2006) 097008.
- [43] S. Yonezawa, Y. Maeno, Nonlinear temperature dependence of resistivity in single crystal Ag<sub>5</sub>Pb<sub>2</sub>O<sub>6</sub>, Physical Review B 70(18) (2004) 184523.
- [44] P. Kushwaha, V. Sunko, P.J. Moll, L. Bawden, J.M. Riley, N. Nandi, H. Rosner, M.P. Schmidt, F. Arnold, E. Hassinger, Nearly free electrons in a 5d delafossite oxide metal, Science advances 1(9) (2015) e1500692.
- [45] H. Takatsu, S. Yonezawa, S. Mouri, S. Nakatsuji, K. Tanaka, Y. Maeno, Roles of High-Frequency Optical Phonons in the Physical Properties of the Conductive Delafossite PdCoO<sub>2</sub>, Journal of the Physical Society of Japan 76(10) (2007) 104701.

- [46] O. Prakash, A. Thamizhavel, S. Ramakrishnan, Ferromagnetic ordering of minority  $\text{Ce}^{3+}$  spins in a quasi-skutterudite  $\text{Ce}_3\text{Os}_4\text{Ge}_{13}$  single crystal, *Physical Review B* 93(6) (2016) 064427.
- [47] M. Brühwiler, S.M. Kazakov, J. Karpinski, B. Batlogg, Mass enhancement, correlations, and strong-coupling superconductivity in the beta-pyrochlore  $\text{KOs}_2\text{O}_6$ , *Physical Review B* 73(9) (2006) 094518.
- [48] R.A. Cowley, The lattice dynamics of an anharmonic crystal, *Advances in Physics* 12(48) (1963) 421-480.

## Chapter 4 High-pressure synthesis, crystal structure, and magnetic properties of $\text{Ba}_3\text{CuOs}_2\text{O}_9$ and $\text{Ba}_3\text{NiOs}_2\text{O}_9$

The synthesis of new materials with useful properties is among the main goals of fundamental materials science and technology research. Particularly interesting recent progress has been seen in the study of perovskite and related osmium oxides, leading to the syntheses of  $\text{Sr}_2\text{CrOsO}_6$  and  $\text{Sr}_2\text{CrReO}_6$ , which exhibit an extremely high-magnetic-transition temperatures [1, 2],  $\text{LiOsO}_3$  displaying a ferroelectric-type structural transition in the metallic state [3], and  $\text{Ba}_2\text{NiOsO}_6$  featuring a ferromagnetic Dirac-Mott insulating state [4]. Most of these interesting properties are due to the extended valence orbitals of the 5d electrons, remarkable crystal-field splitting, and strong spin-orbit coupling [5, 6].

Furthermore, double-perovskite oxides have garnered significant attention recently because their magnetic properties seem to be widely tunable by incorporating different cations into  $A_2BB'\text{O}_6$  ( $A$  = typically alkaline earth or rare-earth elements,  $B$  = typically transition metal elements) [7, 8]. However, so-called triple-perovskite oxides have been studied to a less extent [9-11]. Most of known triple-perovskite oxides were prepared by conventional solid-state method or aqueous sol-gel process, as reported for such as  $\text{Ba}_3\text{BiM}_2\text{O}_9$  ( $M = \text{Ir, Ru}$ ) [12, 13],  $\text{Ba}_3\text{LnIr}_2\text{O}_9$  ( $\text{Ln} = \text{Y, La-Nd, Sm-Lu}$ ) [14],  $\text{Ba}_3\text{Fe}_2\text{MO}_9$  ( $M = \text{Re, Te, W, or Mo}$ ) [15, 16],  $\text{Ba}_3\text{Cr}_2\text{MO}_9$  ( $M = \text{Mo or W}$ ) [17, 18],  $\text{Ba}_3\text{MRu}_2\text{O}_9$  ( $M = \text{Cu, In, Co, Ni, Fe, Y, La, Sm, Eu, or Lu}$ ) [19, 20],  $\text{Ba}_3\text{M}_1\text{Ir}_2\text{O}_9$  ( $M = \text{Mg, Ca, Sc, Ti, Zn, Sr, Zr, Cd, or In}$ ) [21], and  $\text{Ba}_3\text{M}_x\text{Ti}_{3-x}\text{O}_9$  ( $M = \text{Ir or Rh}$ ) [22].

High-pressure synthesis methods have been employed in studies on triple-perovskite osmium oxides. For example, single crystals of  $\text{Ba}_3\text{LiOs}_2\text{O}_9$  and  $\text{Ba}_3\text{NaOs}_2\text{O}_9$  grown under high-pressure exhibit remarkable magnetic characteristics below 10 K [10]; and an

antiferromagnetically ordered state below 47 K and intradimer exchange interaction have been found for  $\text{Ba}_3\text{CuOs}_2\text{O}_9$  and  $\text{Ba}_3\text{ZnOs}_2\text{O}_9$ , respectively [23]. However, to the best of our knowledge, a triple-perovskite osmium oxide with a magnetic transition above room temperature has not yet been synthesized, regardless of the method employed.

The reported triple-perovskite oxide  $\text{Ba}_3\text{CuOs}_2\text{O}_9$  crystalizes in an orthorhombic structure (*Cmcm*) comprising dimeric units of face-sharing octahedra ( $\text{Os}_2\text{O}_9$ ) and normal octahedra ( $\text{CuO}_6$ ) [23]. The two different components are connected by shared corners, making the structure somewhat like that of 6H perovskites (**Fig. 4.1a**) [20, 24].

In the present study, we found that the orthorhombic  $\text{Ba}_3\text{CuOs}_2\text{O}_9$  (*Cmcm*) transforms into a hexagonal polymorph (*P6<sub>3</sub>/mmc*) under high-pressure and high-temperature treatment at 6 GPa and 1100 °C. Although  $\text{Ba}_3\text{CuOs}_2\text{O}_9$  maintains its 6H perovskite-type structure, the distribution of Cu and Os atoms are dramatically altered; structural analysis revealed that the face-sharing octahedra ( $\text{Os}_2\text{O}_9$ ) and normal octahedra ( $\text{CuO}_6$ ) transit to the face-sharing octahedra ( $\text{OsCuO}_9$ ) and normal octahedra ( $\text{OsO}_6$ ), respectively. A similar structure transition caused by heating under high pressure was found for  $\text{Ba}_3\text{NiSb}_2\text{O}_9$  by Darie *et al.* [25, 26]. This structural transition results in a remarkable increase in the magnetic transition temperature from 47 to 290 K, accompanied by a large coercive field greater than 70 kOe (at 5 K).

The same high-pressure structure phase was also found in polymorph  $\text{Ba}_3\text{NiOs}_2\text{O}_9$ . The magnetic transition temperature was improved from 290 K to 370 K further by replace Cu of Ni. Herein, we report synthesis and bulk magnetic properties of the new hexagonal polymorph of  $\text{Ba}_3\text{CuOs}_2\text{O}_9$  and  $\text{Ba}_3\text{NiOs}_2\text{O}_9$ , for which the magnetic transition temperature are both above room temperature.

## **4.1 Crystal structure and magnetic properties of hexagonal Ba<sub>3</sub>CuOs<sub>2</sub>O<sub>9</sub>: a ferrimagnetic material with large coercive field**

### **4.1.1 Experimental Details**

Polycrystalline Ba<sub>3</sub>CuOs<sub>2</sub>O<sub>9</sub> was synthesized from BaO (99.9%, Soekawa Chemicals, Co., Ltd., Japan), CuO (99.99%, Kojundo Chemical Lab. Co., Ltd., Japan), and OsO<sub>2</sub> (Lab made from Os powder). Os powder (99.95%) was supplied by the Nanjing Dongrui Platinum Co., Ltd. BaO, CuO and OsO<sub>2</sub> at a molar ratio of 3:1:2.4 were thoroughly mixed and pressed into a pellet. The mixing and pressing procedures were conducted in an Ar-filled glovebox. Note that the Os source was over stoichiometric to compensate the loss during heating. The pellet was then loaded into a corundum crucible, which was placed into a quartz tube together with another corundum crucible containing MnO<sub>2</sub> as an oxygen source. The molar ratio of OsO<sub>2</sub> and MnO<sub>2</sub> was 1:1. The quartz tube was sealed under dynamic vacuum and heated at 950 °C for 48 h in a furnace. For safety, the ampoule was opened in a fume hood to avoid exposure to toxic OsO<sub>4</sub> gas produced during the heating. The product was investigated by powder X-ray diffraction (XRD) using CuK<sub>α</sub> radiation at room temperature in a commercial apparatus (RIGAKU-MiniFlex 600). The XRD pattern was manifestly comparable with that reported previously [23].

The polycrystalline Ba<sub>3</sub>CuOs<sub>2</sub>O<sub>9</sub> was thoroughly ground and sealed in a Pt capsule. The capsule was heated at 1100 °C for 30 min under a pressure of 6 GPa generated in a multi-anvil-type apparatus (CTF-MA1500P, C&T Factory Co., Ltd, Japan), after which the pressure was gradually released over several hours. The product was investigated by XRD (**Fig. 4.2**) followed by synchrotron XRD at 90 K, room temperature, and 410 K in the high-precision powder X-ray diffractometer installed at the BL15XU beamline, SPring-8, Japan [27, 28]. Rietveld analysis was applied to the synchrotron XRD patterns using the RIETAN-FP and VESTA software packages [29, 30].

The Cu-K edge X-ray absorption near-edge spectroscopy (XANES) was measured in transmission mode at room temperature on the 1W2B beamline at the Beijing Synchrotron Radiation Facility. The beam size was smaller than  $1 \times 0.6$  mm at the sample position. The software package Athena was used to normalize the XANES spectra [31].

Magnetic properties were measured in a magnetic property measurement system (MPMS, Quantum Design, Inc.). Magnetic susceptibility ( $\chi$ ) was measured at temperatures between 2 and 400 K in a fixed applied magnetic field of 10 kOe and 100 Oe under field-cooling (FC) and zero-field-cooling (ZFC) conditions. In addition,  $\chi$  vs.  $T$  curves were obtained at temperatures between 300 and 700 K under an applied magnetic field of 10 kOe using an oven installed in an independent physical property measurement system (PPMS, Quantum Design, Inc.). The field dependence of magnetization was measured between 70 and -70 kOe at temperatures of 5, 25, 50, 100, 200, and 300 K.

The electrical transport and thermal properties were measured in PPMS. The temperature dependence of the electrical resistivity ( $\rho$ ) for hexagonal  $\text{Ba}_3\text{CuOs}_2\text{O}_9$  was measured at temperatures between 2 and 400 K using a four-probe method. Silver paste and platinum wires (30  $\mu\text{m}$  in diameter) were used to connect the polycrystalline platelet to the device terminals. The gauge current was 1 mA. The specific heat capacity ( $C_p$ ) was measured by the thermal-relaxation method using Apiezon-H grease in a temperature range from 350 to 200 K on cooling and Apiezon-N grease from 200 K to 2 K for thermal contact between the sample and a holder stage.

#### 4.1.2 Results and Discussion

Comparing the XRD patterns for  $\text{Ba}_3\text{CuOs}_2\text{O}_9$  measured before and after the high-pressure treatment, a notable change is observed (see **Figs. 4.2a** and **2b**). The pattern after high-pressure treatment indicates that a hexagonal lattice has been formed. To confirm the structure,

the same powder was also investigated by synchrotron XRD at 410 K, which is sufficiently above the magnetic transition temperature (290 K, see below). As a result, reasonable agreement between the observed and calculated patterns was attained by a Rietveld method with a hexagonal model having a space group of  $P6_3/mmc$ . Note that this model has been previously used to investigate the structures of triple-perovskite oxides such as  $\text{Ba}_3\text{MOs}_2\text{O}_9$  ( $M = \text{Li}$  or  $\text{Na}$ ) [10],  $\text{Ba}_3\text{Fe}_2\text{TeO}_9$  [32], and  $\text{Ba}_3\text{ZnOs}_2\text{O}_9$  [23].

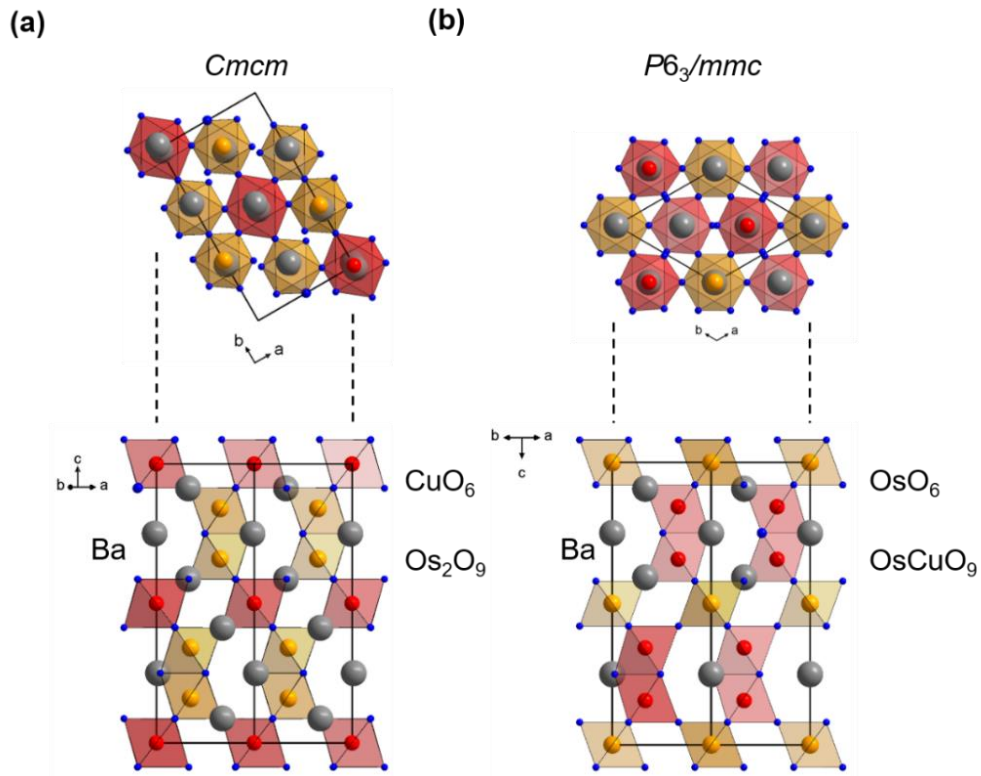


**Fig. 4.1** Crystal structures drawn (top) parallel and (bottom) perpendicular to the  $c$ -axis of (a) orthorhombic [Feng *et al.* Ref. 23] and (b) hexagonal  $\text{Ba}_3\text{CuOs}_2\text{O}_9$ . Octahedra represent  $\text{OsO}_6$  or  $\text{CuO}_6$  as indicated in the diagrams. The grey balls represent  $\text{Ba}$  atoms.

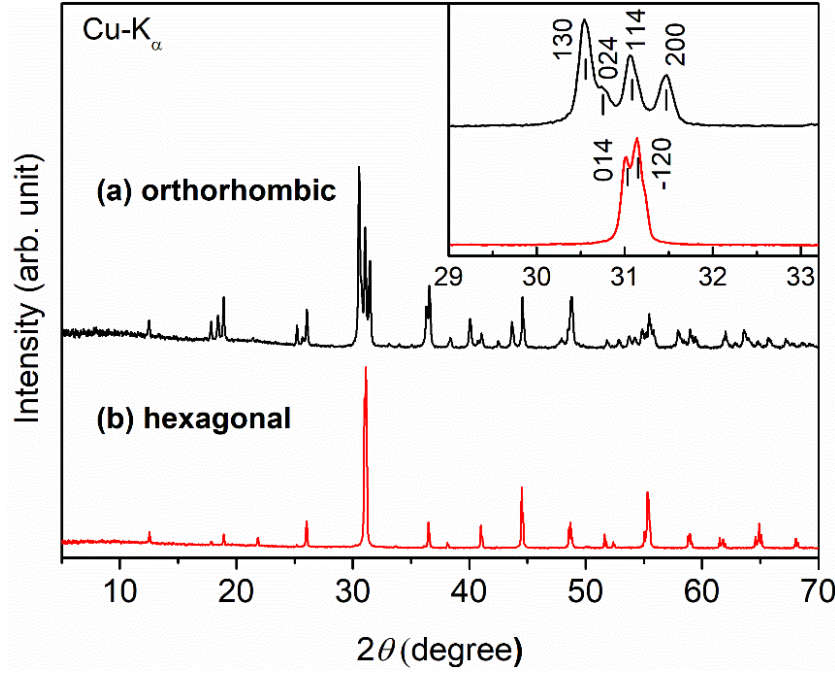


**Fig. 4.2** Powder XRD patterns for  $\text{Ba}_3\text{CuOs}_2\text{O}_9$  at room temperature (a) before and (b) after high-pressure treatment. The inset is a horizontal expansion of the main peaks.

The analyzed synchrotron XRD pattern and the refined crystallographic parameters obtained at 410 K are presented in **Fig. 4.3 (a)** and **Table 4.1**, respectively. For reference, the corresponding synchrotron XRD pattern and crystallographic parameters obtained at room temperature and 90 K are shown in **Figs. 4.3 (b)** and **4.3 (c)** and **Table 4.2**. No significant difference among the sets of data obtained at 410 K, room temperature, and 90 K is observed. In tentative refinement, we evaluated several possible space groups, including  $P-3m1$  (#164),  $P6_3mc$  (#186),  $P-62c$  (#190), and  $P6_3/mmc$  (#194), for the 410 K pattern because these space groups have been frequently assigned to similar structures, such as  $\text{Ba}_2\text{NiOsO}_6$  [4],  $\text{Ba}_2\text{Fe}_{0.92}\text{Os}_{1.08}\text{O}_6$  [33], and  $\text{Ba}_3\text{Cr}_2\text{WO}_9$  [18]. When assuming space groups  $P-62c$  and  $P-3m1$ , refinements always resulted in negative or unreasonably large isotropic atomic displacement parameters. However, reasonable solutions were obtained with the  $P6_3mc$  and  $P6_3/mmc$  models. Although the  $R$  indices were comparable between the models, we decided to select the  $P6_3/mmc$  model in the final refinement because the total number of variable parameters was much lower than that for the other. For example, the number of variable atom coordination parameters was



5 for  $P6_3/mmc$  but 12 for  $P6_3mc$ .

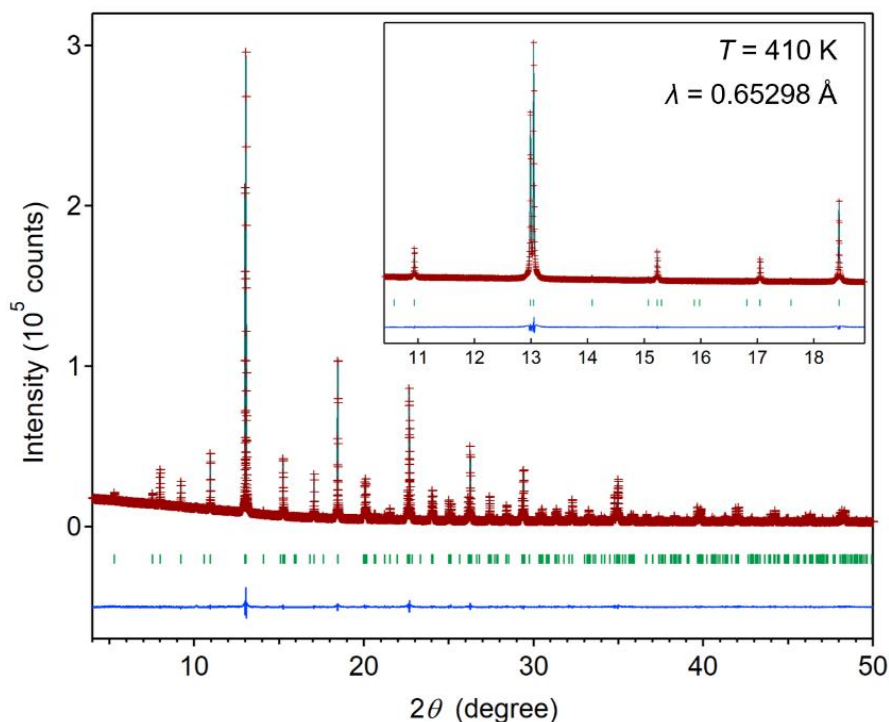


**Fig. 4.3 (a)** Rietveld refinement of the powder synchrotron XRD profile ( $\lambda = 0.65298 \text{ \AA}$ ) collected at 410 K. The crosses and solid lines show the observed and calculated patterns, respectively, with their differences shown at the bottom. The expected Bragg reflections for the  $P6_3/mmc$  cell are marked by ticks. The inset is a horizontal expansion of the main peaks.

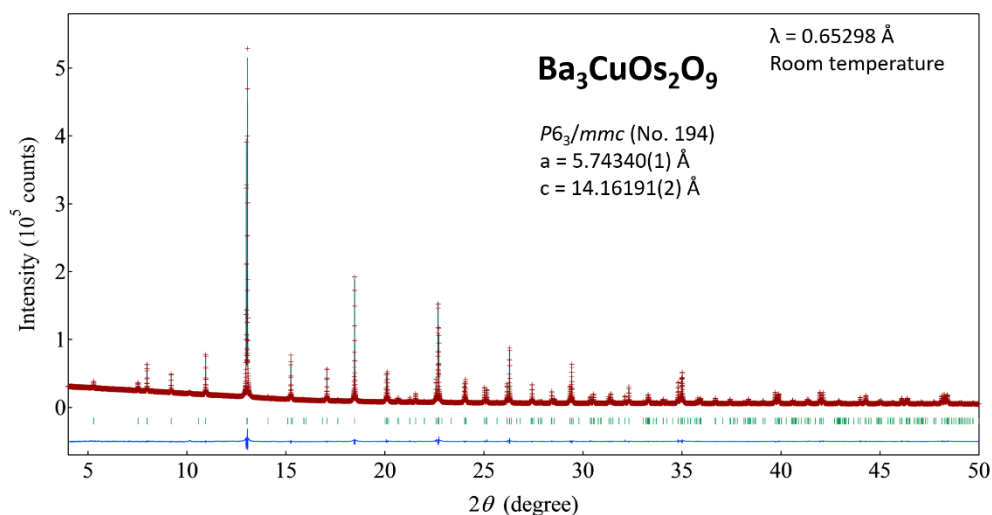


**Fig. 4.3 (b)** Rietveld refinement of the powder synchrotron XRD profile ( $\lambda = 0.65298 \text{ \AA}$ ) collected at room temperature. The crosses and solid lines show the observed and calculated patterns, respectively, with their differences shown at the bottom. The expected Bragg reflections for the  $P6_3/mmc$  cell are marked by ticks.

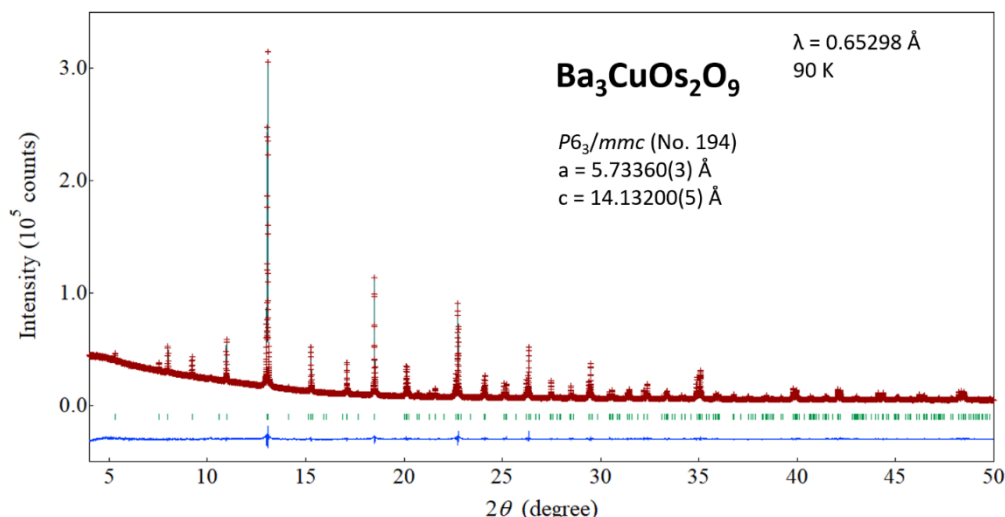


**Fig. 4.3 (c)** Rietveld refinement of the powder synchrotron XRD profile ( $\lambda = 0.65298 \text{ \AA}$ ) collected at 90 K. The crosses and solid lines show the observed and calculated patterns, respectively, with their differences shown at the bottom. The expected Bragg reflections for the  $P6_3/mmc$  cell are marked by ticks. The final  $R$  indices are 2.743% ( $R_{wp}$ ), 1.924% ( $R_p$ ), 6.151% ( $R_B$ ), and 2.576% ( $R_F$ ).

In the final structure model ( $P6_3/mmc$ ) (**Fig. 4.1b**), Ba atoms are located at the two crystallographic sites  $4f(2/3, 1/3, -z)$  and  $2b(0, 0, 1/4)$ , and oxygen atoms are distributed at the  $12k(x, 2x, z)$  and  $6h(x, 2x, 1/4)$  sites, while Os and Cu atoms are distributed over the  $2a(0, 0, 0)$  and  $4f(1/3, 2/3, z)$  sites. The order of Os and Cu distribution was carefully investigated, revealing that the site occupancy at  $2a$  by Os is 0.996(3), indicating that the  $2a$  site is fully occupied by Os (labeled as Os1, see **Table 4.1** and **4.2**) within the standard deviation. Therefore, it was fixed as 1 in the final refinement (see **Tables 4.1** and **4.2**). We also assessed the site occupancy at  $2a$  by Cu, revealing that the site is not occupied by Cu.

For the  $4f$  Wyckoff position, Os and Cu atoms were assumed to occupy the site independently, and a preliminary refinement without applying any constraint indicated that it is occupied approximately 1:1 by Os and Cu and the total occupation is almost 1. Thus, a constraint at the  $4f$  site was introduced in the final refinement, as indicated in the **Table 4.1**. The final solution with the  $P6_3/mmc$  model confirmed that occupation at the  $4f$  site is 0.498(3) for Os (labeled as Os2) and 0.502 for Cu. Considering the composition of the initial synthesis

mixture, the actual chemical composition is concluded to be stoichiometric in terms of the metal atoms. In addition, we could reasonably assume that the compound is also oxygen stoichiometric because perovskite-related Os oxides are normally oxygen stoichiometric according to many neutron diffraction studies [3, 4, 34]. The oxygen stoichiometry may be due to the chemical nature of Os. Note that we did not attempt thermogravimetric analysis of  $\text{Ba}_3\text{CuOs}_2\text{O}_9$  to avoid possible contact with highly toxic  $\text{OsO}_4$ .

**Table 4.1** Atomic coordinates and equivalent isotropic displacement parameters ( $U_{\text{eq}}$ ,  $10^{-3} \text{ \AA}^2$ ) and anisotropic displacement parameters ( $U_{ij}$ ,  $10^{-3} \text{ \AA}^2$ ) for hexagonal  $\text{Ba}_3\text{CuOs}_2\text{O}_9$  at 410 K as revealed by synchrotron XRD

Atom	Site	Occp.	$x$	$y$	$z$	$U_{\text{eq}}$
Ba1	$4f$	1	$2/3$	$1/3$	0.09309(4)	16.7
Ba2	$2b$	1	0	0	$1/4$	8.3
Os1	$2a$	1	0	0	0	6.8
Os2	$4f$	0.498(3)	$1/3$	$2/3$	0.15682(4)	6.6
Cu	$4f$	0.502	$1/3$	$2/3$	0.15682	6.6
O1	$12k$	1	0.1650(4)	0.3300 (=2 $x$ )	0.0796(3)	21(1)
O2	$6h$	1	0.4880(6)	0.9761 (=2 $x$ )	$1/4$	40.6
Atom	$U_{11}$	$U_{22}$	$U_{33}$	$U_{12}$	$U_{13}$	$U_{23}$
Ba1	15.3(3)	= $U_{11}$	19.4(6)	= $0.5 \times U_{11}$	0	0
Ba2	7.6(5)	= $U_{11}$	9.8(9)	= $0.5 \times U_{11}$	0	0
Os1	7.8(3)	= $U_{11}$	4.7(6)	= $0.5 \times U_{11}$	0	0
Os2	6.4(3)	= $U_{11}$	6.9(5)	= $0.5 \times U_{11}$	0	0
Cu	6.4	= $U_{11}$	6.9	= $0.5 \times U_{11}$	0	0
O1	20.7	= $U_{11}$	= $U_{11}$	= $0.5 \times U_{11}$	0	0
O2	30(4)	12(5)	74(7)	= $0.5 \times U_{22}$	0	0

Space group:  $P6_3/mmc$  (hexagonal; no. 194); lattice constants  $a = 5.75178(1) \text{ \AA}$  and  $c = 14.18320(2) \text{ \AA}$ ; cell volume =  $406.359(1) \text{ \AA}^3$ ;  $d_{\text{cal}} = 8.169 \text{ g cm}^{-3}$ ; chemical formula sum:  $\text{Ba}_3\text{CuOs}_2\text{O}_9$  ( $Z = 2$ ); and the final  $R$  indices are 2.905% ( $R_{\text{wp}}$ ), 2.034% ( $R_{\text{p}}$ ), 3.630% ( $R_{\text{B}}$ ), and 1.552% ( $R_{\text{F}}$ ). The anisotropic displacement parameters of Cu atom were fixed to the values of Os2, and the isotropic displacement parameter of O1 was refined.

**Table 4.2** Atomic coordinates and equivalent isotropic displacement parameters ( $U_{\text{eq}}$ ,  $10^{-3} \text{ \AA}^2$ ) and anisotropic displacement parameters ( $U_{\text{ij}}$ ,  $10^{-3} \text{ \AA}^2$ ) for hexagonal  $\text{Ba}_3\text{CuOs}_2\text{O}_9$  at room temperature as revealed by synchrotron XRD

Atom	Site	Occp.	$x$	$y$	$z$	$U_{\text{eq}}$
Ba1	$4f$	1	$2/3$	$1/3$	0.09314(4)	14.2
Ba2	$2b$	1	0	0	$1/4$	5.7
Os1	$2a$	1	0	0	0	5.6
Os2	$4f$	0.500(3)	$1/3$	$2/3$	0.15674(4)	5.2
Cu	$4f$	0.501	$1/3$	$2/3$	0.15674	5.2
O1	$12k$	1	0.1649(5)	$0.3299 (=2x)$	0.0793(3)	17(1)
O2	$6h$	1	0.4880(6)	$0.9759 (=2x)$	$1/4$	35.7
Atom	$U_{11}$	$U_{22}$	$U_{33}$	$U_{12}$	$U_{13}$	$U_{23}$
Ba1	13.4(3)	$= U_{11}$	19.4(6)	$= 0.5 \times U_{11}$	0	0
Ba2	5.5(5)	$= U_{11}$	9.8(9)	$= 0.5 \times U_{11}$	0	0
Os1	6.7(4)	$= U_{11}$	4.7(6)	$= 0.5 \times U_{11}$	0	0
Os2	5.4(3)	$= U_{11}$	6.9(5)	$= 0.5 \times U_{11}$	0	0
Cu	5.4	$= U_{11}$	6.9	$= 0.5 \times U_{11}$	0	0
O1	17.1	$= U_{11}$	$= U_{11}$	$= 0.5 \times U_{11}$	0	0
O2	31(4)	8(5)	60(6)	$= 0.5 \times U_{22}$	0	0

Space group:  $P6_3/mmc$  (hexagonal; no. 194); lattice constants  $a = 5.74340(1) \text{ \AA}$  and  $c = 14.16191(2) \text{ \AA}$ ; cell volume =  $404.566(1) \text{ \AA}^3$ ;  $d_{\text{cal}} = 8.208 \text{ g cm}^{-3}$ ; chemical formula sum:  $\text{Ba}_3\text{CuOs}_2\text{O}_9$  ( $Z = 2$ ); and the final  $R$  indices are 3.004% ( $R_{\text{wp}}$ ), 2.026% ( $R_{\text{p}}$ ), 4.026% ( $R_{\text{B}}$ ), and 1.719% ( $R_{\text{F}}$ ). The anisotropic displacement parameters of Cu atom were fixed to the values of Os2, and the isotropic displacement parameter of O1 was refined.

Based on the assumption that the chemical composition is stoichiometric and does not change via the high-pressure treatment, the final solution of refinement with the  $P6_3/mmc$  model gives the calculated density of hexagonal  $\text{Ba}_3\text{CuOs}_2\text{O}_9$  ( $8.21 \text{ g/cm}^3$ ) is by 1.36% higher than that of orthorhombic  $\text{Ba}_3\text{CuOs}_2\text{O}_9$  ( $8.10 \text{ g/cm}^3$  [23]). The density increment well reflects a common feature of high-pressure stabilized oxides such as the post-perovskite  $\text{MgSiO}_3$  (1.0–1.2% increase [35]) and  $\text{CaRhO}_3$  (1.8% increase [36]). Any exceptional trend regarding the structural transition of  $\text{Ba}_3\text{CuOs}_2\text{O}_9$  seems to be absent.

The major bond lengths were calculated from the refined parameters at 410 K, as shown in **Table 4.3**. The corresponding bond lengths measured at room temperature are shown in **Table 4.4** for reference. Os1 located at the  $2a$  site is coordinated by six oxygen atoms forming Os1–O1 bonds with a bond length of  $1.994(3) \text{ \AA}$ , which is comparable to the average  $\text{Os}^{5+}\text{--O}$  bond lengths in  $\text{Sr}_2\text{FeOsO}_6$  ( $1.996 \text{ \AA}$ ) [37],  $\text{Sr}_2\text{ScOsO}_6$  ( $1.96 \text{ \AA}$ ) [38], and  $\text{Pr}_2\text{NaOsO}_6$  ( $1.968 \text{ \AA}$ ) [39]. This indicates that Os1 in hexagonal  $\text{Ba}_3\text{CuOs}_2\text{O}_9$  is pentavalent.

**Table 4.3** Selected bond lengths and angles in hexagonal  $\text{Ba}_3\text{CuOs}_2\text{O}_9$  at 410 K

Bond	Bond length ( $\text{\AA}$ )	Bond / Angle	Bond length ( $\text{\AA}$ ) / Angle ( $^\circ$ )
Ba1–O1	$2.850(3) \times 3, 2.882(3) \times 6$	Os2/Cu–O1	$2.003(3) \times 3$
Ba1–O2	$2.849(4) \times 3$	Os2/Cu–O2	$2.030(4) \times 3$
Ba2–O1	$2.923(4) \times 6$	Os1–O1–Os2/Cu	$178.7(1)$
Ba2–O2	$2.878(8) \times 6$	Os2/Cu–O2–Os2/Cu	$81.2(1)$
Os1–O1	$1.994(3) \times 6$		

**Table 4.4** Selected bond Bond lengths and angles in hexagonal Ba<sub>3</sub>CuOs<sub>2</sub>O<sub>9</sub> at room temperature

Bond	Bond length (Å)	Bond	Bond length (Å) or angle (°)
Ba1–O1	2.961(3) ×3, 2.878(3) ×6	Os2/Cu–O1	2.002(4) ×3
Ba1–O2	2.845(4) ×3	Os2/Cu–O2	2.027(3) ×3
Ba2–O1	2.922(4) ×6	Os1–O1–Os2/Cu	178.8(2)
Ba2–O2	2.874(4) ×6	Os2/Cu–O2–Os2/Cu	81.3(1)
Os1–O1	1.988(4) ×6		

The distribution of Os and Cu atoms over the  $4f$  Wyckoff position leads to a difficulty to deduce the valence state of each Os and Cu from the average bond lengths obtained from the structure refinement. There are two distinct Cu(Os<sub>2</sub>)–O bond lengths in the dimer-like unit,  $l_{\text{Cu(Os}_2\text{)}-\text{O1}} = 2.003(3)$  Å and  $l_{\text{Cu(Os}_2\text{)}-\text{O2}} = 2.030(4)$  Å. The ratio  $l_{\text{Cu(Os}_2\text{)}-\text{O2}}/l_{\text{Cu(Os}_2\text{)}-\text{O1}}$  is 1.013. This ratio is significantly lower than that of orthorhombic Ba<sub>3</sub>CuOs<sub>2</sub>O<sub>9</sub> (1.096 [23]) and other CuO<sub>6</sub>-containing oxides, which show Jahn-Teller distortion with the ratio ranging from 1.16 to 1.21 [40–42]. This is probably due to the mixed occupation at the  $4f$  site enables to determine only the averaged local coordination of Cu and Os, not the individual one. The averaged Cu(Os<sub>2</sub>)–O bond length is 2.0165 Å, which is slightly longer than the Os1–O bond (shown above) and shorter than the Cu<sup>2+</sup>–O bonds in orthorhombic Ba<sub>3</sub>CuOs<sub>2</sub>O<sub>9</sub> (2.123 Å [23]), Ba<sub>2</sub>CuOsO<sub>6</sub> (2.095 Å [42]), and Ba<sub>2</sub>CuTeO<sub>6</sub> (2.153 Å [40]). This is confirming that the Os2/Cu–O bond length observed is most likely balanced between the shorter Os<sup>5+</sup>–O and longer Cu<sup>2+</sup>–O bonds. For the same reason, estimating the valence state of Os2 and Cu from bond length calculations is not possible. Although the total calculated bond valence sum [43] for the formula Ba<sub>3</sub>CuOs<sub>2</sub> (17.8) is close to that expected, the sum for each metal atom is not even close to the expected value (see **Table 4.5**). This deviation is likely caused in part by the mixing of Os and Cu atoms

at the same crystallographic site, and this may also be responsible for the difficulty in detecting the expected Jahn-Teller distortion of  $\text{Cu}^{2+}\text{O}_6$  octahedra by the XRD method, as mentioned above.

**Table 4.5** Bond valence sum (BVS) as revealed by SXRD at 410 K and room temperature for hexagonal  $\text{Ba}_3\text{CuOs}_2\text{O}_9$

Atom	Site	Occp.	BVS at 410 K	BVS at room temperature
Ba1	4f	1	2.35	2.37
Ba2	2b	1	2.31	2.33
Os1	2a	1	4.29	4.36
Os2	4f	0.5	4.04	4.06
Cu	4f	0.5	2.41	2.42
$\text{Ba}_3\text{CuOs}_2$			17.8	17.9

$\text{BVS} = \sum_{i=1}^N v_i$ , where  $v_i = e^{(R_0 - l_i)/B}$ ,  $N$  is the coordination number,  $l$  is the bond length,  $B = 0.37$ ,  $R_0(\text{Ba}^{2+}) = 2.29$ ,  $R_0(\text{Cu}^{2+}) = 1.679$  [43, 44], and  $R_0(\text{Os}^{5+}) = 1.87$  [45].

Because of the complexity of this situation, we investigate the valence states of Cu and Os further using Cu-K edge XANES at room temperature. The normalized Cu-K edge XANES spectra of hexagonal  $\text{Ba}_3\text{CuOs}_2\text{O}_9$  as well as those of Cu foil and CuO standards are shown in **Fig. 4.4**. Hexagonal  $\text{Ba}_3\text{CuOs}_2\text{O}_9$  exhibits a sharp absorption edge with the maximum peak at  $\sim 8995$  eV, which can be attributed to  $1s-4p^*(\pi)$  and  $1s-4p^*(\sigma)$  transitions [46]. The peak is close to the absorption edge of CuO. There is no shoulder in the leading edge for hexagonal  $\text{Ba}_3\text{CuOs}_2\text{O}_9$ , whereas CuO shows a small shoulder at  $\sim 8985$  eV. This absence may reflect the difference between the local coordination environment of Cu in the hexagonal  $\text{Ba}_3\text{CuOs}_2\text{O}_9$  and that in CuO. Indeed, Cu is in a planer four coordination by oxygen in CuO [47], while Cu is in octahedral coordination in hexagonal  $\text{Ba}_3\text{CuOs}_2\text{O}_9$  as shown in the present study. Note that the shoulder peak of Cu-K edge XANES spectra is usually not visible for octahedrally coordinated Cu by oxygen as observed for such as  $\text{La}_2\text{CuO}_4$  [48],  $\text{CuWO}_4$ , and  $\text{Cu}_3\text{AsO}_4$  [13].



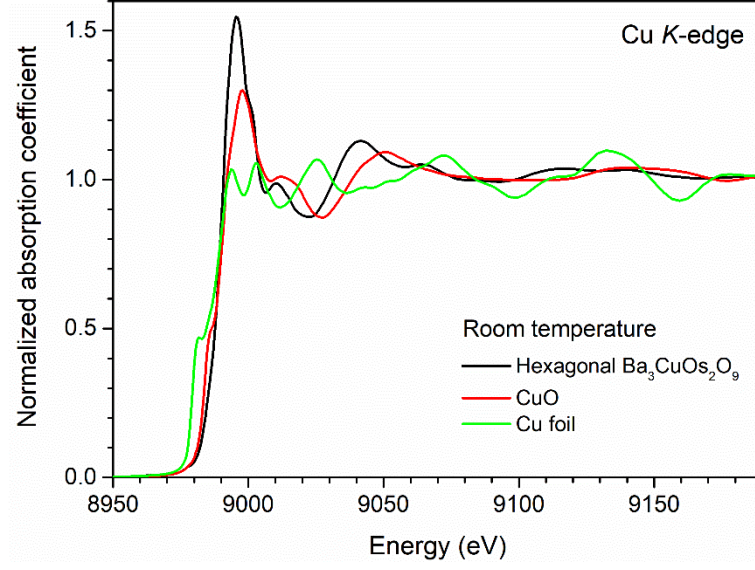


**Fig. 4.4** Normalized Cu *K*-edge XANES spectra of hexagonal Ba<sub>3</sub>CuOs<sub>2</sub>O<sub>9</sub>, CuO, and Cu foil recorded at room temperature.

Compared with the XANES spectra of Cu<sub>2</sub>O reported by Kim *et al.* and Kenney *et al.* [14, 49], the hexagonal Ba<sub>3</sub>CuOs<sub>2</sub>O<sub>9</sub> in the current study does not present a sharp peak at the lower energy of ~8982 eV, which is closed to where the Cu metal has a shoulder peak in the plot for the Cu foil. Because the hexagonal Ba<sub>3</sub>CuOs<sub>2</sub>O<sub>9</sub> does not show any comparable features in the region, it is reasonable to assign the valence state of Cu in the hexagonal Ba<sub>3</sub>CuOs<sub>2</sub>O<sub>9</sub> as divalent rather than monovalent. Considering the XANES data and the structure refinement results, both Os1 and Os2 atoms can be assigned as pentavalent in order to satisfy the total charge balance incorporated by the divalent Cu.

The temperature dependence of  $\rho$  for hexagonal Ba<sub>3</sub>CuOs<sub>2</sub>O<sub>9</sub> is shown in **Fig. 4.5a**. At room temperature,  $\rho$  is ~16  $\Omega$  cm, which is comparable to that of orthorhombic Ba<sub>3</sub>CuOs<sub>2</sub>O<sub>9</sub> (~13  $\Omega$  cm [23]), and  $\rho$  continuously increases upon cooling to 90 K. Upon further cooling,  $\rho$  exceeded the instrumental measurement limit. The electrical transport behavior over the entire temperature range follows a  $T^{-1/4}$  scaling rather than a  $T^{-1}$  scaling (see **Fig. 4.5b**), implying that the three-dimensional variable range hopping (VRH) is dominant in electron transport, as was also reported for Ca<sub>2</sub>CrOsO<sub>6</sub> and Sr<sub>2</sub>CrOsO<sub>6</sub> [50]. As the temperature dependence is

semiconductor-like, we applied the Arrhenius law to the  $T^{-1}$  scaled data in order to estimate the activation energy ( $E_a$ ) from  $\rho = \rho_0 \exp(E_a/k_B T)$ , where  $\rho_0$  and  $k_B$  are a temperature-independent constant and the Boltzmann constant, respectively. The fitting yielded a lower limit for  $E_a$  of 225.5(2) meV, as shown by the solid line in **Fig. 4.5b**.

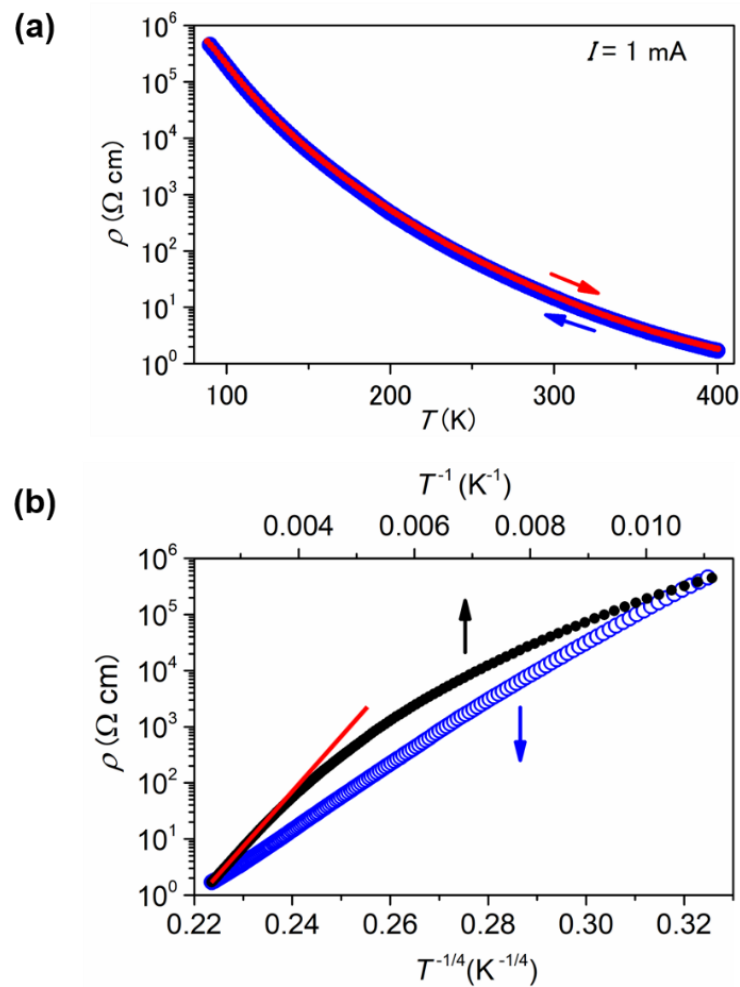


**Fig. 4.5** (a) Temperature dependence of electrical resistivity for polycrystalline hexagonal  $\text{Ba}_3\text{CuOs}_2\text{O}_9$  upon cooling and heating. (b) Alternative plots of the data. The red line indicates a fitting to the Arrhenius law in the high-temperature region.

The temperature dependence of  $\chi$  in an applied magnetic field of 10 kOe is shown in **Fig. 4.6a**. For comparison, that of orthorhombic  $\text{Ba}_3\text{CuOs}_2\text{O}_9$  is plotted in the same manner. The data for orthorhombic  $\text{Ba}_3\text{CuOs}_2\text{O}_9$  were reproduced from previous work by Feng and Jansen [23]. The  $\chi(T)$  curves for the hexagonal phase are plotted using a combination of two

independent sets of data measured in the ranges 2–400 K and 300–700 K. The ZFC and FC curves for hexagonal  $\text{Ba}_3\text{CuOs}_2\text{O}_9$  show a remarkable increase at room temperature, indicating the occurrence of long-range magnetic ordering. In a lower field measurement at 100 Oe, a comparable transition was confirmed, excluded possibilities of substantial impurity contribution and additional transitions (**Fig. 4.7**). Besides, a sharp peak appears in the ac- $\chi$  curves, as shown in **Figs. 4.8a** and **4.8b**, revealing that the magnetic transition occurs at 290 K.

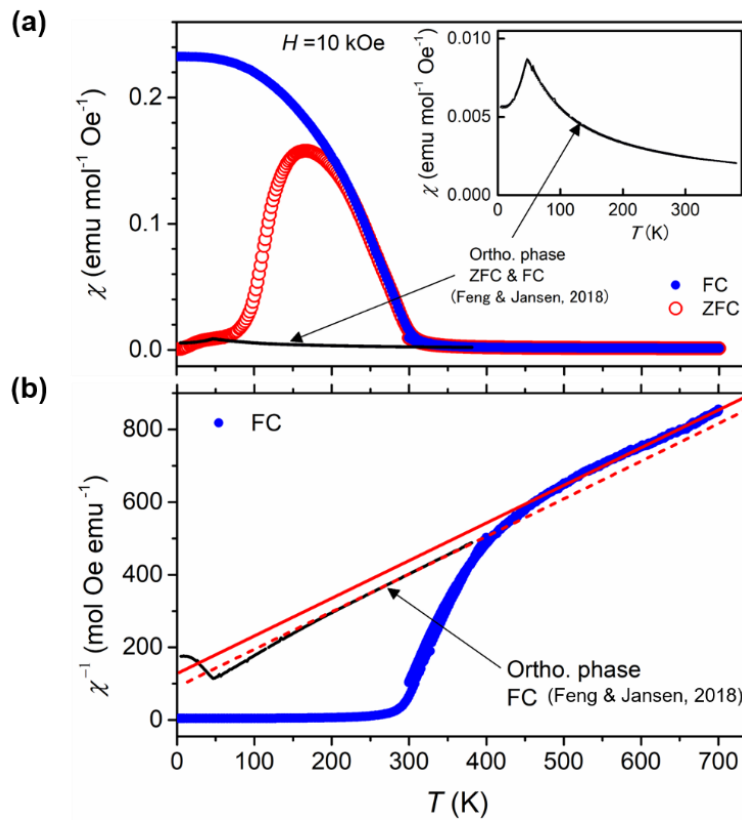


**Fig. 4.6** (a) Temperature dependence of ZFC and FC susceptibilities ( $H = 10 \text{ kOe}$ ) for hexagonal and orthorhombic  $\text{Ba}_3\text{CuOs}_2\text{O}_9$ . The data for the orthorhombic  $\text{Ba}_3\text{CuOs}_2\text{O}_9$  are reproduced from a previous report by Feng and Jansen [Ref. 23]. (b) Alternative plots of the FC data for fitting to the Curie-Weiss law. The fitting is shown by solid and broken lines.

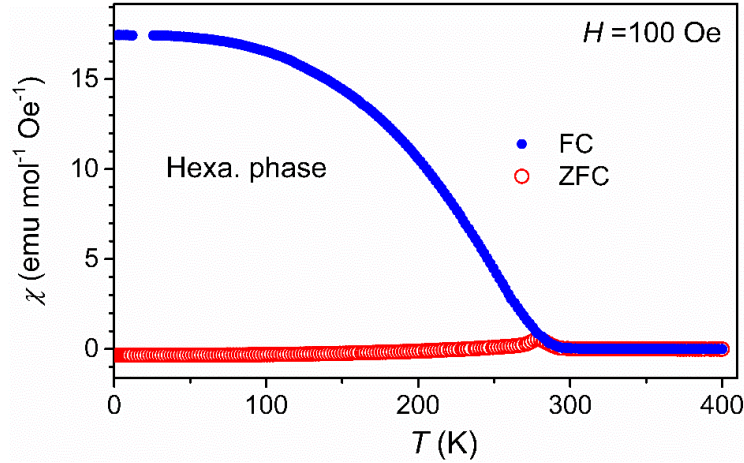


**Fig. 4.7** Temperature dependence of ZFC and FC susceptibilities ( $H = 100$  Oe) for hexagonal  $\text{Ba}_3\text{CuOs}_2\text{O}_9$ .

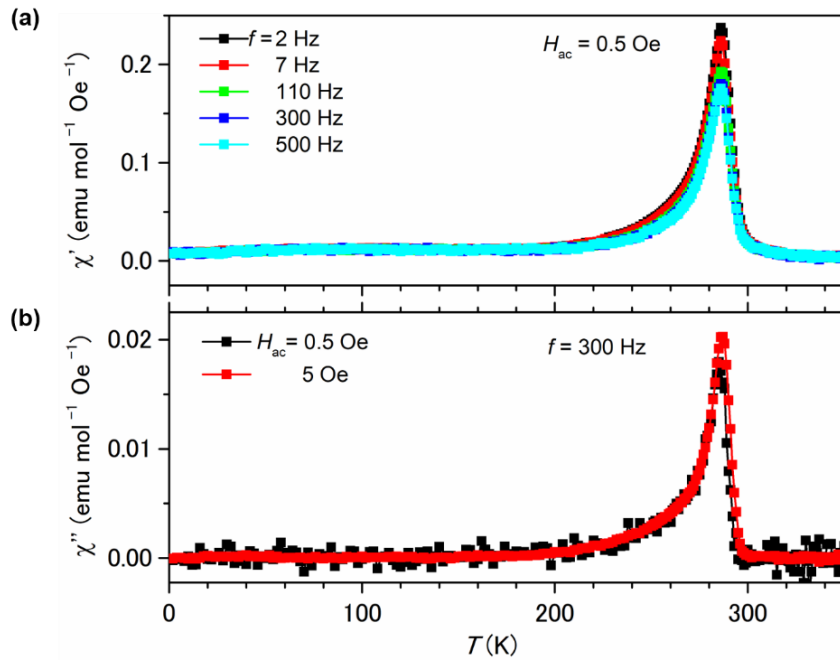


**Fig. 4.8** (a) Real and (b) imaginary components of ac magnetic susceptibility for hexagonal  $\text{Ba}_3\text{CuOs}_2\text{O}_9$  measured in different magnetic fields ( $H_{ac}$ ) at the frequencies ( $f$ ) indicated in each panel.

Isothermal magnetization of hexagonal  $\text{Ba}_3\text{CuOs}_2\text{O}_9$  was measured at 5, 25, 50, 100, 200, and 300 K, and compared with that of the orthorhombic phase (**Fig. 4.9a**). The curves are nonlinear, even at 300 K, and exhibit hysteresis, which is in stark contrast to the linear behavior of orthorhombic  $\text{Ba}_3\text{CuOs}_2\text{O}_9$ . The coercive field at 25 K, 50 K, 100 K, 200 K, 300 K are 63, 39, 21, 6, 0.1 kOe respectively (**Fig. 4.9b**). Neither ascending nor descending branches of  $M(H)$

at 5 K pass through the  $M = 0$  line, indicating the extreme field up to  $\pm 70$  kOe is insufficient to achieve demagnetization. In another word, the coercive field is higher than 70 kOe at 5 K. Remarkably high coercive fields were occasionally found for transition-metal oxides, such as  $\text{La}_2\text{Ni}_{1.19}\text{Os}_{0.81}\text{O}_6$  (41 kOe at 5 K),  $\text{LuFe}_2\text{O}_4$  (90 kOe at 4 K), and  $\text{Sr}_5\text{Ru}_{5-x}\text{O}_{15}$  (120 kOe at 2 K), although the coercive fields shrinks to nearly zero on heating to 200 K [51-53]. The atomic disorder of Os and Cu of hexagonal  $\text{Ba}_3\text{CuOs}_2\text{O}_9$  may contribute to cause such the high coercive field; detail is left for future study.

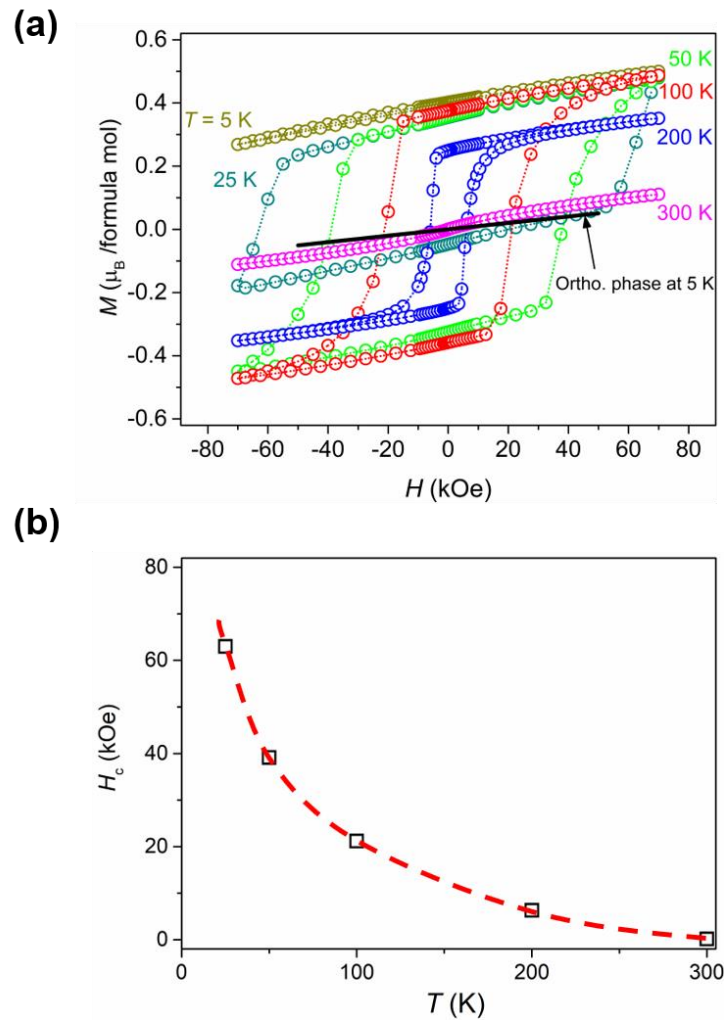


**Fig. 4.9** (a) Isothermal magnetization of hexagonal  $\text{Ba}_3\text{CuOs}_2\text{O}_9$  at 5, 25, 50, 100, 200, and 300 K. The curve for orthorhombic  $\text{Ba}_3\text{CuOs}_2\text{O}_9$  at 5 K is reproduced from a previous report by Feng and Jansen [Ref. 23]. (b) Temperature dependence of the coercive field ( $H_c$ ) deduced from the  $M$ - $H$  data. The broken curve is a guide for eyes.

The saturated magnetization for hexagonal Ba<sub>3</sub>CuOs<sub>2</sub>O<sub>9</sub> at 5 K and 25 K could not be measured because it requires higher magnetic fields beyond our instrumental limit. However, even considering this technical difficulty, the spontaneous magnetization was roughly estimated to be ~0.4  $\mu_B$ /mol. This value is much smaller than that expected for a ferromagnetic ordering of Cu<sup>2+</sup> and Os<sup>5+</sup> [23]. Therefore, the magnetic ground state can be assigned as a ferrimagnetic or closely similar state. Note that a comparable spontaneous magnetization was observed for La<sub>2</sub>Ni<sub>1.19</sub>Os<sub>0.81</sub>O<sub>6</sub> and a canted ferrimagnetic spin structure was revealed by analysis of neutron data [51].

To further investigate these magnetic properties, we applied the Curie-Weiss law  $1/\chi = (T-\theta)/C$  to the high-temperature portion of the  $1/\chi - T$  curve (440- 700 K), resulting in estimated values for  $C$  (the Curie constant) of 0.963(5) emu mol<sup>-1</sup> K and  $\theta$  (Weiss temperature) of - 122(3) K (**Fig. 4.6b**). Note that the  $1/\chi - T$  curve between 300 and 390 K is likely under the influence of developing short-range magnetic order, thus we did not apply the Curie-Weiss law since it is usually effective only for paramagnetism. The negative Weiss temperature indicates that the predominant magnetic interaction is antiferromagnetic in the localized electron regime. In this case, the effective magnetic moment ( $\mu_{\text{eff}}$ ) was calculated from the Curie constant to be 2.78(1)  $\mu_B$ , which is approximately comparable to that of the orthorhombic phase (2.37  $\mu_B$  [23]). This value of  $\mu_{\text{eff}}$  is however much lower than the spin-only moment 5.75  $\mu_B$  (assuming one Cu<sup>2+</sup> and two Os<sup>5+</sup> per the formula). For comparison, experimental  $\mu_{\text{eff}}$  values of Cu<sup>2+</sup>-containing compounds are 2.18  $\mu_B$  (BaCuO<sub>2</sub> [54]), 1.98  $\mu_B$  (Ba<sub>2</sub>CuTeO<sub>6</sub> [40]), and 1.93  $\mu_B$  (Ba<sub>2</sub>CuWO<sub>6</sub> [40]). The  $\mu_{\text{eff}}$  for hexagonal Ba<sub>3</sub>CuOs<sub>2</sub>O<sub>9</sub> is larger than these values, indicating that the magnetic moment of Os<sup>5+</sup> contributes to the bulk magnetic properties to some extent.

Regarding at the local structure around the Cu and Os atoms, the Os1–O–Os2/Cu (corner-sharing octahedra) and Os2/Cu–O–Os2/Cu (face-sharing octahedra) bond angles are 179° and 81°, respectively (**Table 4.3**). Therefore, the predominant antiferromagnetic

interaction ought to be via the Os1–O–Os2/Cu bond (consisting of Os<sup>5+</sup>–O–Os<sup>5+</sup> and Os<sup>5+</sup>–O–Cu<sup>2+</sup> bonds in equal proportions) because magnetic interactions conveyed via ~90° bonds are usually weaker. The nearly-180° Os<sup>5+</sup>–O–Cu<sup>2+</sup> bond presents in orthorhombic Ba<sub>3</sub>CuOs<sub>2</sub>O<sub>9</sub> instead of the nearly-180° Os1–O–Os2/Cu bond. However, the magnetic transition temperature (47 K) of orthorhombic Ba<sub>3</sub>CuOs<sub>2</sub>O<sub>9</sub> is approximately six-times lower than that of hexagonal Ba<sub>3</sub>CuOs<sub>2</sub>O<sub>9</sub>. The nearly-180° Os<sup>5+</sup>–O–Cu<sup>2+</sup> bond is therefore moderately antiferromagnetic. In other words, the nearly-180° Os<sup>5+</sup>–O–Os<sup>5+</sup> bond is strongly antiferromagnetic. The presence of both Os<sup>5+</sup>–O–Os<sup>5+</sup> and Os<sup>5+</sup>–O–Cu<sup>2+</sup> bonds in equal proportions likely drives the ferrimagnetic transition at 290 K, and the weaker magnetic properties of the orthorhombic polymorph are possibly due to the lack of the strongly antiferromagnetic 180° Os<sup>5+</sup>–O–Os<sup>5+</sup> bond. For reference, the nearly-180° Os<sup>5+</sup>–O–Os<sup>5+</sup> bond in NaOsO<sub>3</sub> results in an antiferromagnetic transition at 410 K [55, 56].

The temperature dependence of  $C_p$  is plotted in **Fig. 4.10**. An expected anomaly near 290 K is not clearly seen probably because the magnetic transition entropy is gradually lost in association with a developing short-range order over a wide temperature range. There is no additional anomaly, which is indicative of a bulk transition, over the entire temperature range except a small anomaly near 340 K. Considering the heat capacity was measured from 350 K, the anomaly was possibly caused by a technical issue near the initial temperature. The low-temperature region is plotted in the  $C_p/T$  vs.  $T^2$  form in the inset of **Fig. 4.10** and is well characterized by an approximated Debye model ( $C_p/T = \gamma + \beta_0 T^2$ ). The linear fitting gives a Sommerfeld coefficient ( $\gamma$ ) of  $4.2(3) \times 10^{-3} \text{ J mol}^{-1} \text{ K}^{-2}$  and the constant  $\beta_0$  of  $8.18(5) \times 10^{-4} \text{ J mol}^{-1} \text{ K}^{-4}$ . The Debye temperature was calculated from  $\beta_0$  to be 329(1) K. The rather small  $\gamma$  value may be associated with the VRH conduction observed. Otherwise, the magnetic contribution has some impact on the analysis.

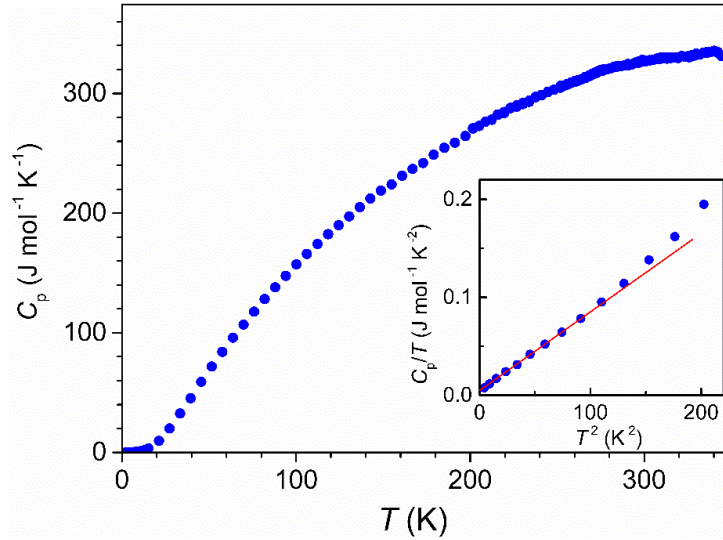


**Fig. 4.10** Temperature dependence of specific heat for hexagonal  $\text{Ba}_3\text{CuOs}_2\text{O}_9$ . The upper axis corresponds to the Dulong-Petit limit of the lattice specific heat. (Inset) Linear fit to the  $C_p/T$  vs.  $T^2$  curve for the low-temperature region.

## 4.2 Crystal structure and magnetic properties of hexagonal $\text{Ba}_3\text{NiOs}_2\text{O}_9$

### 4.2.1 Experiment Details

Polycrystalline  $\text{Ba}_3\text{NiOs}_2\text{O}_9$  was synthesized from  $\text{BaO}$  (99.9%, Soekawa Chemicals, Co., Ltd., Japan),  $\text{NiO}$  (99.97%, High Purity Chemicals Co., Ltd., Japan),  $\text{OsO}_2$  (Lab made from Os powder) and  $\text{KClO}_4$  (> 99.5%, Kishida Chem. Lab. Co., Ltd.). Os powder (99.95%) was supplied by the Nanjing Dongrui Platinum Co., Ltd.  $\text{BaO}$ ,  $\text{NiO}$ ,  $\text{OsO}_2$  and  $\text{KClO}_4$  at a molar ratio of 3:1:2:0.2625 were thoroughly mixed and sealed in a Pt capsule. The mixing procedures were conducted in an Ar-filled glove box. Under a pressure of 6 GPa, generated in a multi-anvil-type apparatus, the capsule was heated to 1100 °C for 30 min, after which the pressure was gradually released. The product was investigated by XRD followed by synchrotron XRD at room temperature and 410 K in the high-precision powder X-ray diffractometer installed at the BL15XU beamline, SPring-8, Japan [27, 28]. Rietveld analysis was applied to the synchrotron XRD patterns using the RIETAN-FP and VESTA software packages [29, 30].



The Ni-K edge X-ray absorption near-edge spectroscopy (XANES) was measured in transmission mode at room temperature on the 1W2B beamline at the Beijing Synchrotron Radiation Facility. The beam size was smaller than  $1 \times 0.6$  mm at the sample position. The software package Athena was used to normalize the XANES spectra [31].

Magnetic properties were measured in a magnetic property measurement system (MPMS, Quantum Design, Inc.). Magnetic susceptibility ( $\chi$ ) was measured at temperatures between 2 and 400 K in a fixed applied magnetic field of 10 kOe under field-cooling (FC) and zero-field-cooling (ZFC) conditions. In addition,  $\chi$  vs.  $T$  curves were obtained at temperatures between 300 and 700 K under an applied magnetic field of 10 kOe using an oven installed in an independent physical property measurement system (PPMS, Quantum Design, Inc.). The field dependence of magnetization was measured between 70 and - 70 kOe at temperatures of 5 K.

The electrical transport and thermal properties were measured in PPMS. The temperature dependence of the electrical resistivity ( $\rho$ ) for hexagonal  $\text{Ba}_3\text{CuOs}_2\text{O}_9$  was measured at temperatures between 2 and 400 K using a four-probe method. Silver paste and platinum wires (30  $\mu\text{m}$  in diameter) were used to connect the polycrystalline platelet to the device terminals. The gauge current was 1 mA. The specific heat capacity ( $C_p$ ) was measured by the thermal-relaxation method using Apiezon-N grease in a temperature range from 300 to 2 K on cooling for thermal contact between the sample and a holder stage.

#### 4.2.2 Results and Discussion

The analyzed synchrotron XRD pattern and the refined crystallographic parameters obtained at 410 K are presented in **Fig. 4.11 (a)** and **Table 4.6**, respectively. For reference, the corresponding synchrotron XRD pattern and crystallographic parameters obtained at room temperature is shown in **Figs. 4.11 (b)** and **Table 4.7**. No significant difference among the sets

of data obtained at 410 K and room temperature is observed.

The structure refinement for  $\text{Ba}_3\text{NiOs}_2\text{O}_9$  was carried out using the same model ( $P6_3/mmc$ ) as  $\text{Ba}_3\text{CuOs}_2\text{O}_9$ , yielding  $a = 5.74352(3) \text{ \AA}$  and  $c = 14.12970(5) \text{ \AA}$ . The distributions of Os and Ni were carefully investigated at  $2a$  (0, 0, 0) and  $4f$  ( $1/3, 2/3, z$ ) sites, revealing that the site occupancy at  $2a$  by Os and Ni are 0.916(4) and 0.084 respectively. The site occupancy at  $4f$  by Os and Ni was also assessed, revealing 0.55(2) for Os and 0.45 for Ni. Considering the composition of the initial synthesis mixture, the actual chemical composition  $\text{Ba}_3\text{Ni}_{0.98}\text{Os}_{2.02}\text{O}_9$  is still stoichiometric in terms of the metal atoms.

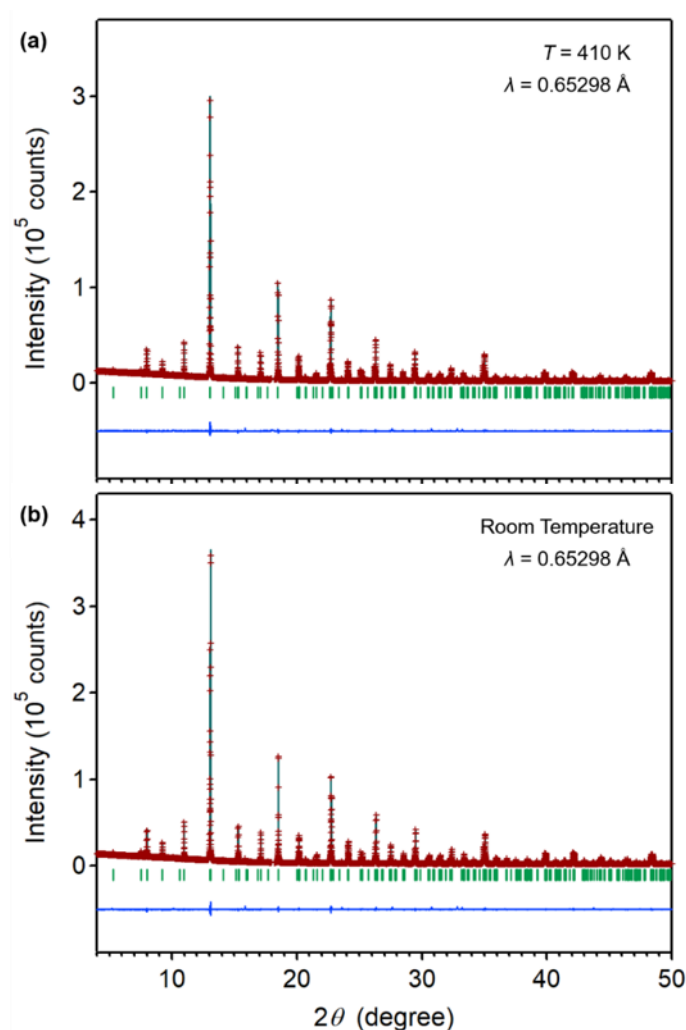


**Fig. 4.11** Rietveld refinement of the powder synchrotron XRD profile ( $\lambda = 0.65298 \text{ \AA}$ ) collected (a) at 410 K; (b) at room temperature. The crosses and solid lines show the observed

and calculated patterns, respectively, with their differences shown at the bottom. The expected Bragg reflections for the  $P6_3/mmc$  cell are marked by ticks.

The major bond lengths were calculated from the refined parameters at 410 K, as shown in **Table 4.8**. The corresponding bond lengths measured at room temperature are shown in **Table 4.9** for reference. The Os atoms at  $2a$  site are coordinated with 6 oxygens by six equal Os1-O bonds of 1.979(3) Å. The similar value was observed in  $\text{Ca}_2\text{FeOsO}_6$ ,  $\text{Sr}_2\text{ScOsO}_6$ ,  $\text{Sr}_2\text{CrOsO}_6$ , in which the oxidation state for Os were assigned to 5+ [38, 57, 58]. Due to the disorder exist over  $2a$  site, the bond valence sums for Os and Ni are less reliable. This deviation is more serious at  $4f$  site because of the higher degree of disorder between Os and Ni. The calculated bond valence sum for the formula  $\text{Ba}_3\text{NiOs}_2$  (18.0) is same as the expected (see **Table 4.10**).

The average Ni2/Os2-O bond length in face-shared octahedra is 2.013 Å obtained from the structure refinement. Compared to  $\text{Ni}^{2+}$ -O in other perovskite  $\text{Ba}_2\text{NiOsO}_6$  (2.078 Å) [4],  $\text{Sr}_2\text{NiOsO}_6$  (2.021 Å),  $\text{Ca}_2\text{NiOsO}_6$  (2.049 Å) [59] and  $\text{Ba}_2\text{NiWO}_6$  (2.097 Å) [60], the Ni2/Os2-O bond length observed in  $\text{Ba}_3\text{NiOs}_2\text{O}_9$  is slightly shorter. This indicates that Os2/Ni2-O bond length is most likely balanced between the shorter  $\text{Os}^{5+}$ -O and longer  $\text{Ni}^{2+}$ -O bonds. For comparison, if Ni shows trivalent at  $4f$  site, the valence state of Os at  $4f$  site will be deduced to be 4+. The bond length of  $\text{Ni}^{3+}$ -O is quite shorter than  $\text{Ni}^{2+}$ -O such as 1.960 Å for  $\text{LaNiO}_3$  [61] and 1.976 Å for  $\text{LiNiO}_2$  [62] while  $\text{Os}^{4+}$ -O bonds were observed in  $\text{CaOsO}_3$  (2.006 Å),  $\text{SrOsO}_3$  (1.983 Å) and  $\text{BaOsO}_3$  (2.013 Å) [63] that are smaller than the observed Ni2/Os2-O bond as well. Therefore, from the view of bond length, Os and Ni atoms at  $4f$  site should be assigned to 5+ and 2+ respectively.

Ni K-edge XANES can contribute to understanding the valence state of Ni atoms in the compound. **Fig. 4.12** shows the experimental Ni K-edge XANES of the sample  $\text{Ba}_3\text{NiOs}_2\text{O}_9$  and the standard sample Ni foil. In addition, the Ni K-edge XANES of NiO (JXAFS-

1202090019) and Ni foil (JXAFS-1202070029) from the XAFS database (Institute for Catalysis, Hokkaido University) was compared with our samples in **Fig. 4.12**. In the spectra of  $\text{Ba}_3\text{NiOs}_2\text{O}_9$  and NiO, two distinct edge features are marked as A and B. The pre-edge peak marked as A is located at 8333 eV due to the dipole-forbidden 1s–3d electronic transition with Ni 3d–4p orbital mixing in  $\text{NiO}_6$  octahedra [64, 65]. The peak position of this pre-edge in Ni K-edge XANES can reflect the difference of the oxidation state of Ni ion. With the increase of the oxidation state, the pre-edge peak position moves to higher energy [66]. The pre-edge peak of  $\text{Ba}_3\text{NiOs}_2\text{O}_9$  overlaps that of NiO, indicating Ni is present in the divalent state. The main absorption peak B located at ~8350 eV originates from the dipole-allowed transition of 1s electron to a vacant 4p orbital [64]. Compared to the data of NiO,  $\text{Ba}_3\text{NiOs}_2\text{O}_9$  does not show peak shift in the main-edge which further indicates the existence of  $\text{Ni}^{2+}$ . The divalent Ni was confirmed, the valent state for Os in  $\text{Ba}_3\text{NiOs}_2\text{O}_9$  can be deduced to be pentavalent.

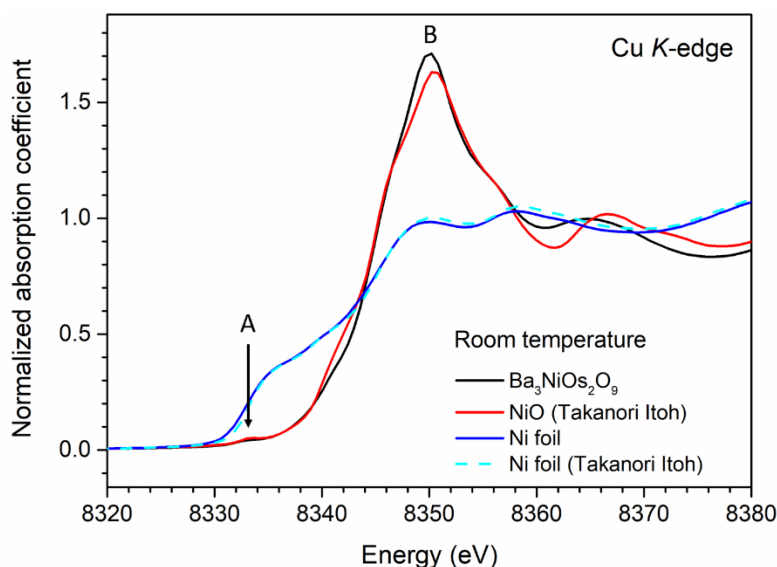


**Fig. 4.12** Normalized Ni K-edge XANES of  $\text{Ba}_3\text{NiOs}_2\text{O}_9$  and Ni foil recorded at room temperature. The Ni K-edge XANES of NiO (JXAFS-1202090019) and Ni foil (JXAFS-1202070029) are from the XAFS database (Institute for Catalysis, Hokkaido University).

The temperature dependence of  $\rho$  for  $\text{Ba}_3\text{NiOs}_2\text{O}_9$  is showed in **Fig. 4.13a**, indicating  $\rho$  continuously increases upon cooling to 110 K. The electrical transport behavior over the

entire temperature range follows a  $T^{-1/4}$  scaling well (see **Fig. 4.13b**), implying that the three-dimensional variable range hopping (VRH) is dominant in electron transport, as was also reported for  $\text{Ba}_3\text{CuOs}_2\text{O}_9$ . The Arrhenius law was applied to the  $T^{-1}$  scaled data in order to estimate the activation energy ( $E_a$ ) from  $\rho = \rho_0 \exp(E_a/k_B T)$ . The fitting yielded a lower limit for  $E_a$  of 351.4(9) meV, as shown by the solid line in **Fig. 4.13b**.

**Table 4.6** Atomic coordinates and equivalent isotropic displacement parameters ( $U_{\text{eq}}$ ,  $10^{-3} \text{ \AA}^2$ ) and anisotropic displacement parameters ( $U_{ij}$ ,  $10^{-3} \text{ \AA}^2$ ) for hexagonal  $\text{Ba}_3\text{NiOs}_2\text{O}_9$  at 410 K as revealed by synchrotron XRD

Atom	Site	Occp.	$x$	$y$	$z$	$U_{\text{eq}}$
Ba1	$4f$	1	$2/3$	$1/3$	0.09372(4)	11.5
Ba2	$2b$	1	0	0	$1/4$	7.4
Os1	$2a$	0.916(4)	0	0	0	2.8
Ni1	$2a$	0.084	0	0	0	2.8
Os2	$4f$	0.55(2)	$1/3$	$2/3$	0.15726(3)	3.3
Ni2	$4f$	0.45	$1/3$	$2/3$	0.15726	3.3
O1	$12k$	1	0.1633(2)	0.3265 ( $=2x$ )	0.0800(2)	13.1(9)
O2	$6h$	1	1.0267(9)	0.5133 ( $=0.5x$ )	$1/4$	15(2)
Atom	$U_{11}$	$U_{22}$	$U_{33}$	$U_{12}$	$U_{13}$	$U_{23}$
Ba1	9.9(3)	$= U_{11}$	14.7(5)	$= 0.5 \times U_{11}$	0	0
Ba2	7.8(4)	$= U_{11}$	6.6(8)	$= 0.5 \times U_{11}$	0	0
Os1	2.6(3)	$= U_{11}$	3.2(5)	$= 0.5 \times U_{11}$	0	0
Ni1	2.6	$= U_{11}$	3.2	$= 0.5 \times U_{11}$	0	0
Os2	3.0(2)	$= U_{11}$	3.8(4)	$= 0.5 \times U_{11}$	0	0
Ni2	3.0	$= U_{11}$	3.8	$= 0.5 \times U_{11}$	0	0
O1	13.1	$= U_{11}$	$= U_{11}$	$= 0.5 \times U_{11}$	0	0
O2	14.9	$= U_{11}$	$= U_{11}$	$= 0.5 \times U_{11}$	0	0

Space group:  $P6_3/mmc$  (hexagonal; no. 194); lattice constants  $a = 5.74352(3) \text{ \AA}$  and  $c = 14.12970(5) \text{ \AA}$ ; cell volume =  $403.664(3) \text{ \AA}^3$ ;  $d_{\text{cal}} = 8.206 \text{ g cm}^{-3}$ ; chemical formula sum:  $\text{Ba}_3\text{Ni}_{0.98}\text{Os}_{2.02}\text{O}_9$  ( $Z = 2$ ); and the final  $R$  indices are 3.292% ( $R_{\text{wp}}$ ), 1.956% ( $R_{\text{p}}$ ), 1.161% ( $R_{\text{B}}$ ), and 0.674% ( $R_{\text{F}}$ ). The anisotropic displacement parameters of Ni1/Ni2 atom were fixed to the values of Os1/Os2, and the isotropic displacement parameter of O1 and O2 were refined.

**Table 4.7** Atomic coordinates and equivalent isotropic displacement parameters ( $U_{\text{eq}}$ ,  $10^{-3} \text{ \AA}^2$ ) and anisotropic displacement parameters ( $U_{ij}$ ,  $10^{-3} \text{ \AA}^2$ ) for hexagonal  $\text{Ba}_3\text{NiOs}_2\text{O}_9$  at room temperature as revealed by synchrotron XRD

Atom	Site	Occp.	$x$	$y$	$z$	$U_{\text{eq}}$
Ba1	$4f$	1	$2/3$	$1/3$	0.09379(4)	9.1
Ba2	$2b$	1	0	0	$1/4$	5.4
Os1	$2a$	0.916(4)	0	0	0	2.0
Ni1	$2a$	0.084	0	0	0	2.0
Os2	$4f$	0.55(2)	$1/3$	$2/3$	0.15724(3)	2.3
Ni2	$4f$	0.45	$1/3$	$2/3$	0.15724	2.3
O1	$12k$	1	0.1635(4)	0.3265 ( $=2x$ )	0.0797(2)	11.6(9)
O2	$6h$	1	1.0237(9)	0.5133 ( $=0.5x$ )	$1/4$	9(14)
Atom	$U_{11}$	$U_{22}$	$U_{33}$	$U_{12}$	$U_{13}$	$U_{23}$
Ba1	7.6(3)	$= U_{11}$	12.0(5)	$= 0.5 \times U_{11}$	0	0
Ba2	6.3(4)	$= U_{11}$	3.6(7)	$= 0.5 \times U_{11}$	0	0
Os1	1.9(3)	$= U_{11}$	2.2(5)	$= 0.5 \times U_{11}$	0	0
Ni1	1.9	$= U_{11}$	2.2	$= 0.5 \times U_{11}$	0	0
Os2	2.3(2)	$= U_{11}$	2.4(4)	$= 0.5 \times U_{11}$	0	0
Ni2	2.3	$= U_{11}$	2.4	$= 0.5 \times U_{11}$	0	0
O1	11.6	$= U_{11}$	$= U_{11}$	$= 0.5 \times U_{11}$	0	0
O2	8.7	$= U_{11}$	$= U_{11}$	$= 0.5 \times U_{11}$	0	0

Space group:  $P6_3/mmc$  (hexagonal; no. 194); lattice constants  $a = 5.73508(2) \text{ \AA}$  and  $c = 14.10768(4) \text{ \AA}$ ; cell volume =  $401.852(2) \text{ \AA}^3$ ;  $d_{\text{cal}} = 8.243 \text{ g cm}^{-3}$ ; chemical formula sum:  $\text{Ba}_3\text{Ni}_{0.98}\text{Os}_{2.02}\text{O}_9$  ( $Z = 2$ ); and the final  $R$  indices are 3.409% ( $R_{\text{wp}}$ ), 1.978% ( $R_{\text{p}}$ ), 1.307% ( $R_{\text{B}}$ ), and 0.756% ( $R_{\text{F}}$ ). The anisotropic displacement parameters of Ni1/Ni2 atom were fixed to the values of Os1/Os2, and the isotropic displacement parameter of O1 and O2 were refined.

**Table 4.8** Selected bond lengths and angles in hexagonal Ba<sub>3</sub>NiOs<sub>2</sub>O<sub>9</sub> at 410 K

Bond	Bond length (Å)	Bond / Angle	Bond length (Å) / Angle (°)
Ba1–O1	2.982(3) ×3, 2.878(3) ×6	Os2/Ni2–O1	2.011(4) ×3
Ba1–O2	2.842(3) ×3	Os2/Ni2–O2	2.014(3) ×3
Ba2–O1	2.900(3) ×6	Os1/Ni1–O1–Os2/Ni2	177.99(15)
Ba2–O2	2.875(6) ×6	Os2/Ni2–O2–Os2/Ni2	81.34(17)
Os1/Ni1–O1	1.979(3) ×6		

**Table 4.9** Selected bond Bond lengths and angles in hexagonal Ba<sub>3</sub>NiOs<sub>2</sub>O<sub>9</sub> at room temperature

Bond	Bond length (Å)	Bond / Angle	Bond length (Å) / Angle (°)
Ba1–O1	2.972(3) ×3, 2.875(3) ×6	Os2/Ni2–O1	2.011(3) ×3
Ba1–O2	2.829(3) ×3	Os2/Ni2–O2	2.019(4) ×3
Ba2–O1	2.900(3) ×6	Os1/Ni1–O1–Os2/Ni2	178.27(15)
Ba2–O2	2.870(6) ×6	Os2/Ni2–O2–Os2/Ni2	80.79(17)
Os1/Ni1–O1	1.975(3) ×6		

**Table 4.10** Bond valence sum (BVS) as revealed by SXRD at 410 K and room temperature for hexagonal Ba<sub>3</sub>NiOs<sub>2</sub>O<sub>9</sub>

Atom	Site	Occp.	BVS at 410 K	BVS at room temperature
Ba1	4f	1	2.36	2.41
Ba2	2b	1	2.39	2.41
Os1	2a	0.916(4)	4.47	4.52
Ni1	2a	0.084	2.49	2.52
Os2	4f	0.55(2)	4.08	4.05
Ni2	4f	0.45	2.28	2.26
Ba <sub>3</sub> CuOs <sub>2</sub>			18.0	18.1

$BVS = \sum_{i=1}^N v_i$ , where  $v_i = e^{(R_0 - l_i)/B}$ , N is the coordination number, l is the bond length, B =



0.37,  $R_0(\text{Ba}^{2+}) = 2.29$ ,  $R_0(\text{Ni}^{2+}) = 1.654$  [43, 44], and  $R_0(\text{Os}^{5+}) = 1.87$  [45].

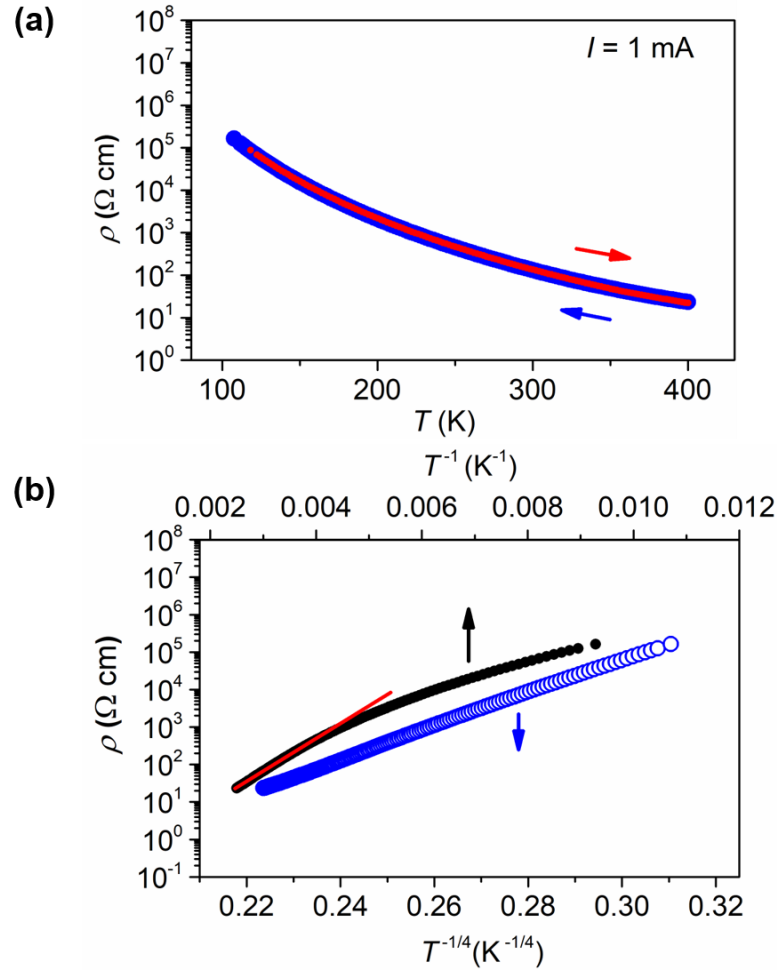


**Fig. 4.13** (a) Temperature dependence of electrical resistivity for polycrystalline  $\text{Ba}_3\text{NiOs}_2\text{O}_9$  upon cooling and heating. (b) Alternative plots of the data. The red line indicates a fitting to the Arrhenius law in the high-temperature region.

The temperature dependence of  $\chi$  in applied magnetic field of 10 kOe and 1 kOe are shown in **Fig. 4.14**. The  $\chi(T)$  curves under 10 kOe are plotted using a combination of two independent sets of data measured in the ranges 2–400 K and 300–700 K. The long-range magnetic ordering occurs at 370 K, where the magnetic susceptibility increases abruptly when cooling. Even though the  $\chi(T)$  was measured until 700 K, it still not enough to reach a linear  $\chi^{-1}$  vs  $T$  curve above the transition temperature for fitting by Curie-Weiss model (see the inset of **Fig. 4.14a**). The ZFC and FC curves under 10 kOe bifurcate below 155 K under 10 kOe and

an antiferromagnetism-like peak was observed in ZFC curve at  $\sim 70$  K. The bifurcation between the ZFC and FC curves and AFM-like peak in ZFC curve under 1 kOe was found to shift to higher temperature (see **Fig. 4.14b**). The bifurcation is possible to be caused by the movement of magnetic domain walls in the material.[67]. The domain structure changes when the sample is cooled without magnetic field while it keeps same domain structure when cooling down with an appropriate field.

Isothermal magnetization of  $\text{Ba}_3\text{NiOs}_2\text{O}_9$  was measured at 5 K, 100 K and 300 K (**Fig. 4.15**). The spontaneous magnetization for  $\text{Ba}_3\text{NiOs}_2\text{O}_9$  is  $0.7 \mu_B/\text{mol}$  at either 5 K or 100 K, and the value is still nonzero even though at 300 K ( $0.35 \mu_B/\text{mol}$  at 300 K). The observed saturated or spontaneous magnetization, however, much smaller than the value of  $8 \mu_B/\text{mol}$  expected in the assignment of ferromagnetic ordering, assuming the spin only values of  $2 \mu_B$  for  $\text{Ni}^{2+}$  and  $3 \mu_B$  for  $\text{Os}^{5+}$ . Therefore, the ferrimagnetic or closely similar state for the magnetic ground state can be assigned. The coercive field at 5 K is 20 kOe for  $\text{Ba}_3\text{NiOs}_2\text{O}_9$ , which is smaller than hexagonal  $\text{Ba}_3\text{CuOs}_2\text{O}_9$  or double perovskite  $\text{La}_2\text{Ni}_{1.19}\text{Os}_{0.81}\text{O}_6$  [51] but larger than double perovskite  $\text{Ba}_2\text{NiOsO}_6$  [4].

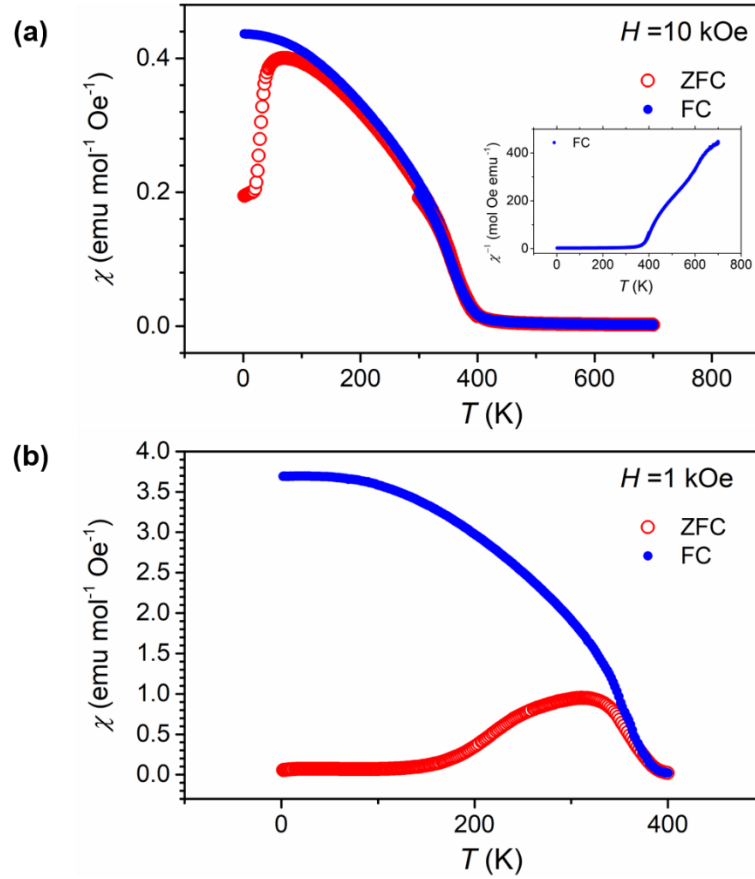


**Fig. 4.14** (a) Temperature dependence of ZFC and FC susceptibilities ( $H = 10$  kOe) for  $\text{Ba}_3\text{NiOs}_2\text{O}_9$ . The inset shows the inverse magnetic susceptibility. (b) Temperature dependence of ZFC and FC susceptibilities ( $H = 1$  kOe).

In the local structure around the Ni and Os atoms, the Os1/Ni1–O–Os2/Ni2 (corner-sharing octahedra) and Os2/Ni2–O–Os2/Ni2 (face-sharing octahedra) bond angles are  $178^\circ$  and  $81^\circ$  respectively (see **Table 4.9**), which are comparable with hexagonal  $\text{Ba}_3\text{CuOs}_2\text{O}_9$ . The same reason as hexagonal  $\text{Ba}_3\text{CuOs}_2\text{O}_9$ , the predominant antiferromagnetic interaction via a nearly- $180^\circ$  bond, drives the ferrimagnetic transition at 400 K, although small amount of Ni/Os disorder exists in  $\text{Ba}_3\text{NiOs}_2\text{O}_9$ .

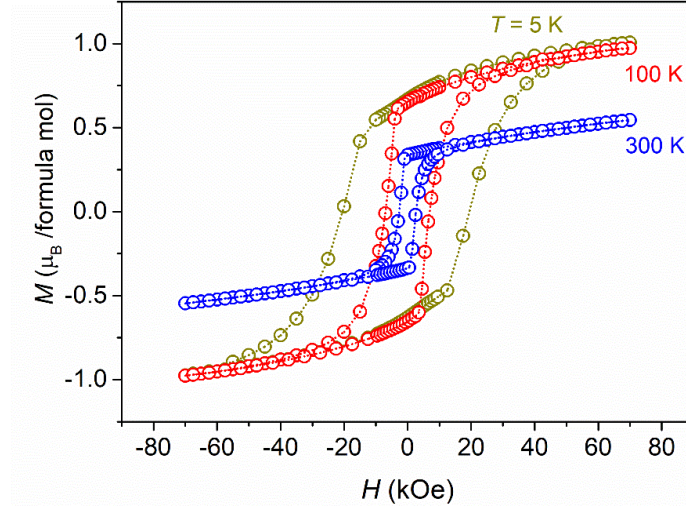


**Fig. 4.15** Isothermal magnetization of  $\text{Ba}_3\text{NiOs}_2\text{O}_9$  at 5 K, 100 K and 300 K.

The temperature dependence of  $C_p$  is plotted in **Fig. 4.16**. The low-temperature region is plotted in the  $C_p/T$  vs.  $T^2$  form in the inset of **Fig. 4.16** and is fitted by an approximated Debye model ( $C_p/T = \gamma + \beta_0 T^2$ ). The linear fitting gives a Sommerfeld coefficient ( $\gamma$ ) of  $3.3(13) \times 10^{-3} \text{ J mol}^{-1} \text{ K}^{-2}$  and the constant  $\beta_0$  of  $6.41(4) \times 10^{-4} \text{ J mol}^{-1} \text{ K}^{-4}$ . The Debye temperature was calculated from  $\beta_0$  to be  $357.0(7) \text{ K}$ . The small  $\gamma$  value is consistent with the 3D VRH conduction.

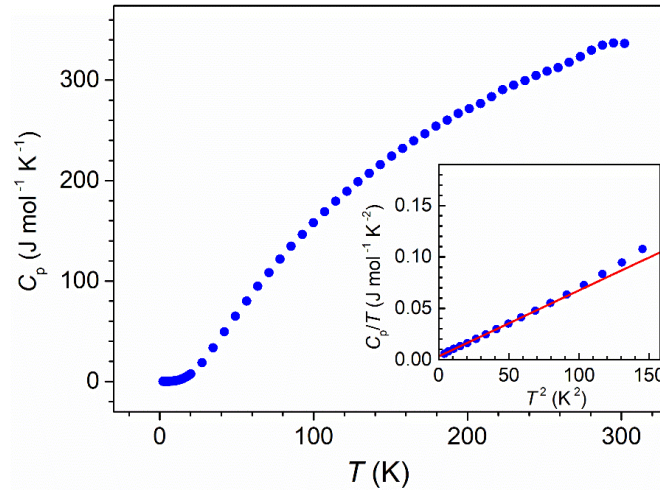


**Fig. 4.16** Temperature dependence of specific heat for  $\text{Ba}_3\text{NiOs}_2\text{O}_9$ . The upper axis corresponds to the Dulong-Petit limit of the lattice specific heat. (Inset) Linear fit to the  $C_p/T$  vs.  $T^2$  curve for the low-temperature region.

### 4.3 Summary of Chapter 4

A hexagonal polymorph of  $\text{Ba}_3\text{CuOs}_2\text{O}_9$  was newly synthesized under high-pressure (6 GPa) and it retained the general structure type of orthorhombic  $\text{Ba}_3\text{CuOs}_2\text{O}_9$  but underwent a 1.36% density increment. In the denser structure, the Os and Cu distribution is largely altered, leading to the formation of strongly antiferromagnetic  $\text{Os}^{5+}\text{--O--Os}^{5+}$  bonds with an angle of nearly  $180^\circ$  and moderately antiferromagnetic  $\text{Os}^{5+}\text{--O--Cu}^{2+}$  bonds with an angle of nearly  $180^\circ$ . The structure analysis combined with the Curie-Weiss analysis showed that the two distinctive antiferromagnetic bonds present at an equal ratio likely drive the ferrimagnetic transition at 290 K for the hexagonal  $\text{Ba}_3\text{CuOs}_2\text{O}_9$ . This room temperature transition is in stark contrast to the 47 K antiferromagnetic transition of the orthorhombic  $\text{Ba}_3\text{CuOs}_2\text{O}_9$ .

Another new triple perovskite  $\text{Ba}_3\text{NiOs}_2\text{O}_9$  was synthesized under high-pressure and high-temperature conditions by replace Cu of Ni and the replacement does not change the hexagonal structure.  $\text{Ba}_3\text{NiOs}_2\text{O}_9$  still crystallizes into the hexagonal polymorph ( $P6_3/mmc$ ) structure. The distribution of Os and Ni in  $\text{Ba}_3\text{NiOs}_2\text{O}_9$  is the same as that of Os and Cu in hexagonal  $\text{Ba}_3\text{CuOs}_2\text{O}_9$ . The observed magnetization value suggests  $\text{Ba}_3\text{NiOs}_2\text{O}_9$  should be ferrimagnetic or similar property even though the Curie-Weiss analysis cannot apply to the  $\chi^{-1}$  vs  $T$  curve. The observed data lead to our speculation that two distinctive antiferromagnetic bonds play the same role in driving a high ferrimagnetic transition at 370 K for the  $\text{Ba}_3\text{NiOs}_2\text{O}_9$  as it does for the hexagonal  $\text{Ba}_3\text{NiOs}_2\text{O}_9$ . Note that the detailed magnetic structure for both hexagonal  $\text{Ba}_3\text{CuOs}_2\text{O}_9$  and  $\text{Ba}_3\text{NiOs}_2\text{O}_9$  require to be confirmed by neutron diffraction further.

Either hexagonal  $\text{Ba}_3\text{CuOs}_2\text{O}_9$  or  $\text{Ba}_3\text{NiOs}_2\text{O}_9$  shows disorder at  $4f$  sites (face-sharing octahedra) in sense but not like orthorhombic  $\text{Ba}_3\text{CuOs}_2\text{O}_9$  with the ordered structure. However, this disorder leads to improve the magnetic property in this case. It inspires us to rethink what the role does disorder play in materials' magnetism. Besides, a remarkably large coercive field

( $H_C > 70$  kOe at 5 K) was observed in hexagonal  $\text{Ba}_3\text{CuOs}_2\text{O}_9$ , which opens up possibilities for designing of rare-earth-free hard magnets.

## References in chapter 4

- [1] H. Kato, T. Okuda, Y. Okimoto, Y. Tomioka, Y. Takenoya, A. Ohkubo, M. Kawasaki, Y. Tokura, Metallic ordered double-perovskite  $\text{Sr}_2\text{CrReO}_6$  with maximal Curie temperature of 635 K, *Applied physics letters* 81(2) (2002) 328-330.
- [2] Y. Krockenberger, K. Mogare, M. Reehuis, M. Tovar, M. Jansen, G. Vaitheeswaran, V. Kanchana, F. Bultmark, A. Delin, F. Wilhelm,  $\text{Sr}_2\text{CrOsO}_6$ : End point of a spin-polarized metal-insulator transition by 5d band filling, *Physical Review B* 75(2) (2007) 020404.
- [3] Y. Shi, Y. Guo, X. Wang, A.J. Princep, D. Khalyavin, P. Manuel, Y. Michiue, A. Sato, K. Tsuda, S. Yu, M. Arai, Y. Shirako, M. Akaogi, N. Wang, K. Yamaura, A.T. Boothroyd, A ferroelectric-like structural transition in a metal, *Nature materials* 12(11) (2013) 1024.
- [4] H.L. Feng, S. Calder, M.P. Ghimire, Y.-H. Yuan, Y. Shirako, Y. Tsujimoto, Y. Matsushita, Z. Hu, C.-Y. Kuo, L.H. Tjeng, T.-W. Pi, Y.-L. Soo, J. He, M. Tanaka, Y. Katsuya, M. Richter, K. Yamaura,  $\text{Ba}_2\text{NiOsO}_6$ : A Dirac-Mott insulator with ferromagnetism near 100 K, *Physical Review B* 94(23) (2016) 235158.
- [5] H.Y. Hwang, Y. Iwasa, M. Kawasaki, B. Keimer, N. Nagaosa, Y. Tokura, Emergent phenomena at oxide interfaces, *Nature Materials* 11(2) (2012) 103-113.
- [6] W. Witczak-Krempa, G. Chen, Y.B. Kim, L. Balents, Correlated Quantum Phenomena in the Strong Spin-Orbit Regime, in: J.S. Langer (Ed.), *Annual Review of Condensed Matter Physics*, Vol 5, Annual Reviews, Palo Alto, 2014, pp. 57-82.
- [7] D. Serrate, J.M. De Teresa, M.R. Ibarra, Double perovskites with ferromagnetism above room temperature, *Journal of Physics-Condensed Matter* 19(2) (2007).
- [8] S. Vasala, M. Karppinen,  $\text{A}_2\text{B}'\text{B}''\text{O}_6$  perovskites: A review, *Progress in Solid State Chemistry* 43(1-2) (2015) 1-36.

- [9] K.E. Stitzer, M.D. Smith, W.R. Gemmill, H.C. zur Loye, Novel mixed-valent (V/VI) triple perovskite ruthenates: Observation of a complex low-temperature structural and magnetic transition, *Journal of the American Chemical Society* 124(46) (2002) 13877-13885.
- [10] K.E. Stitzer, A.E. Abed, M.D. Smith, M.J. Davis, S.-J. Kim, J. Darriet, H.-C. Zur Loye, Crystal growth of novel osmium-containing triple perovskites, *Inorganic chemistry* 42(4) (2003) 947-949.
- [11] S.J. Kim, M.D. Smith, J. Darriet, H.C. zur Loye, Crystal growth of new perovskite and perovskite related iridates:  $\text{Ba}_3\text{LiIr}_2\text{O}_9$ ,  $\text{Ba}_3\text{NaIr}_2\text{O}_9$ , and  $\text{Ba}_{3.44}\text{K}_{1.56}\text{Ir}_2\text{O}_{10}$ , *Journal of Solid State Chemistry* 177(4-5) (2004) 1493-1500.
- [12] J. Darriet, C. Dussarrat, F. Weill, B. Darriet, R. Bontchev, The system  $\text{BaRuO}_3$ - $\text{BaBiO}_3$ . I. Crystal structures of  $\text{Ba}_3\text{Ru}_2\text{BiO}_9$  and  $\text{Ba}_2\text{Ru}_x\text{Bi}_{2-x}\text{O}_6$  ( $0 < x \leq 0.67$ ), *European Journal of Solid State and Inorganic Chemistry* 30(3) (1993) 273-286.
- [13] C.D. Ling, B.J. Kennedy, Q. Zhou, J.R. Spencer, M. Avdeev, Synthesis, structures, and phase transitions of barium bismuth iridium oxide perovskites  $\text{Ba}_2\text{BiIrO}_6$  and  $\text{Ba}_3\text{BiIr}_2\text{O}_9$ , *Journal of Solid State Chemistry* 183(3) (2010) 727-735.
- [14] Y. Doi, Y. Hinatsu, The structural and magnetic characterization of 6H-perovskite-type oxides  $\text{Ba}_3\text{LnIr}_2\text{O}_9$  (Ln= Y, lanthanides), *Journal of Physics: Condensed Matter* 16(16) (2004) 2849.
- [15] V. Gagulin, N. Fadeeva, A. Belous, A. Titov, K. Mitrofanov, M. Plotnikova, S. Soloviev, Y.N. Venevtsev, New seignette - magnets with hexagonal barium titanate structure, *Physica Status Solidi (a)* 48(1) (1978) 183-189.
- [16] I. Djerdj, J. Popović, S. Mal, T. Weller, M. Nuskol, Z. Jagličić, Z.e. Skoko, D. Pajić, C. Suchomski, P. Voepel, Aqueous Sol–Gel Route toward Selected Quaternary Metal Oxides with Single and Double Perovskite-Type Structure Containing Tellurium, *Crystal Growth & Design* 16(5) (2016) 2535-2541.

- [17] D. Ballutaud-Harari, P. Poix, Structural chemistry of  $\text{Sr}_3\text{Cr}_2\text{WO}_9$ ,  $\text{Ca}_3\text{Cr}_2\text{WO}_9$ , and  $\text{Ba}_3\text{Cr}_2\text{WO}_9$ , *Journal of Solid State Chemistry* 14(4) (1975) 354-358.
- [18] M. Shikano, O. Ishiyama, Y. Inaguma, T. Nakamura, M. Itoh, Structure and Magnetic Properties of 6-Layered Hexagonal Oxides  $\text{Ba}_3\text{Cr}_2\text{MO}_9$  ( $M = \text{Mo}$  and  $\text{W}$ ), *Journal of Solid State Chemistry* 120(2) (1995) 238-243.
- [19] J. Rijssenbeek, Q. Huang, R. Erwin, H. Zandbergen, R. Cava, The crystal structure of  $\text{Ba}_3\text{CuRu}_2\text{O}_9$  and comparison to  $\text{Ba}_3\text{MRu}_2\text{O}_9$  ( $M = \text{In}$ ,  $\text{Co}$ ,  $\text{Ni}$ , and  $\text{Fe}$ ), *Journal of Solid State Chemistry* 146(1) (1999) 65-72.
- [20] Y. Doi, K. Matsuhira, Y. Hinatsu, Crystal structures and magnetic properties of 6H-perovskites  $\text{Ba}_3\text{MRu}_2\text{O}_9$  ( $M = \text{Y}$ ,  $\text{In}$ ,  $\text{La}$ ,  $\text{Sm}$ ,  $\text{Eu}$ , and  $\text{Lu}$ ), *Journal of Solid State Chemistry* 165(2) (2002) 317-323.
- [21] T. Sakamoto, Y. Doi, Y. Hinatsu, Crystal structures and magnetic properties of 6H-perovskite-type oxides  $\text{Ba}_3\text{M}\text{Ir}_2\text{O}_9$  ( $M = \text{Mg}$ ,  $\text{Ca}$ ,  $\text{Sc}$ ,  $\text{Ti}$ ,  $\text{Zn}$ ,  $\text{Sr}$ ,  $\text{Zr}$ ,  $\text{Cd}$  and  $\text{In}$ ), *Journal of Solid State Chemistry* 179(8) (2006) 2595-2601.
- [22] R. Kumar, D. Sheptyakov, P. Khuntia, K. Rolfs, P. Freeman, H.M. Rønnow, T. Dey, M. Baenitz, A. Mahajan,  $\text{Ba}_3\text{M}_x\text{Ti}_{3-x}\text{O}_9$  ( $M = \text{Ir}$ ,  $\text{Rh}$ ): A family of 5d/4d-based diluted quantum spin liquids, *Physical Review B* 94(17) (2016) 174410.
- [23] H.L. Feng, M. Jansen,  $\text{Ba}_3\text{CuOs}_2\text{O}_9$  and  $\text{Ba}_3\text{ZnOs}_2\text{O}_9$ , a comparative study, *Journal of Solid State Chemistry* 258 (2018) 776-780.
- [24] Y. Doi, Y. Hinatsu, Y. Shimojo, Y. Ishii, Crystal structure and magnetic properties of 6H-perovskite  $\text{Ba}_3\text{NdRu}_2\text{O}_9$ , *Journal of Solid State Chemistry* 161(1) (2001) 113-120.
- [25] J. Cheng, G. Li, L. Balicas, J. Zhou, J. Goodenough, C. Xu, H. Zhou, High-Pressure Sequence of  $\text{Ba}_3\text{NiSb}_2\text{O}_9$  Structural Phases: New  $S = 1$  Quantum Spin Liquids Based on  $\text{Ni}^{2+}$ , *Physical Review Letters* 107(19) (2011) 197204.



- [26] C. Darie, C. Lepoittevin, H. Klein, S. Kodjikian, P. Bordet, C.V. Colin, O.I. Lebedev, C. Deudon, C. Payen, A new high pressure form of  $\text{Ba}_3\text{NiSb}_2\text{O}_9$ , *Journal of Solid State Chemistry* 237 (2016) 166-173.
- [27] M. Tanaka, Y. Katsuya, A. Yamamoto, A new large radius imaging plate camera for high-resolution and high-throughput synchrotron x-ray powder diffraction by multiexposure method, *Review of Scientific Instruments* 79(7) (2008) 075106.
- [28] M. Tanaka, Y. Katsuya, Y. Matsushita, O. Sakata, Development of a synchrotron powder diffractometer with a one-dimensional X-ray detector for analysis of advanced materials, *Journal of the Ceramic Society of Japan* 121(1411) (2013) 287-290.
- [29] F. Izumi, A Rietveld-analysis program RIETAN-98 and its applications to zeolites, *Mater. Sci. Forum*, 2000, pp. 198-203.
- [30] K. Momma, F. Izumi, VESTA3 for three-dimensional visualization of crystal, volumetric and morphology data, *Journal of applied crystallography* 44(6) (2011) 1272-1276.
- [31] B. Ravel, M. Newville, ATHENA, ARTEMIS, HEPHAESTUS: data analysis for X-ray absorption spectroscopy using IFEFFIT, *Journal of Synchrotron Radiation* 12(4) (2005) 537-541.
- [32] Y. Tang, R.P. Sena, M. Avdeev, P.D. Battle, J. Cadogan, J. Hadermann, E.C. Hunter, Magnetic properties of the 6H perovskite  $\text{Ba}_3\text{Fe}_2\text{TeO}_9$ , *Journal of Solid State Chemistry* 253 (2017) 347-354.
- [33] W.R. Gemmill, M.D. Smith, H.-C. zur Loye, Synthesis and structural characterization of two new hexagonal osmates:  $\text{Ba}_2\text{Fe}_{0.92}\text{Os}_{1.08}\text{O}_6$  and  $\text{Ba}_2\text{Co}_{0.77}\text{Os}_{1.23}\text{O}_6$ , *Solid state sciences* 9(5) (2007) 380-384.
- [34] S. Calder, M.D. Lumsden, V.O. Garlea, J.W. Kim, Y.G. Shi, H.L. Feng, K. Yamaura, A.D. Christianson, Magnetic structure determination of  $\text{Ca}_3\text{LiOsO}_6$  using neutron and x-ray scattering, *Physical Review B* 86(5) (2012) 054403.

- [35] M. Murakami, K. Hirose, K. Kawamura, N. Sata, Y. Ohishi, Post-perovskite phase transition in  $\text{MgSiO}_3$ , *Science* 304(5672) (2004) 855-858.
- [36] K. Yamaura, Y. Shirako, H. Kojitani, M. Arai, D.P. Young, M. Akaogi, M. Nakashima, T. Katsumata, Y. Inaguma, E. Takayama-Muromachi, Synthesis and Magnetic and Charge-Transport Properties of the Correlated 4d Post-Perovskite  $\text{CaRhO}_3$ , *Journal of the American Chemical Society* 131(7) (2009) 2722-2726.
- [37] A.K. Paul, M. Jansen, B. Yan, C. Felser, M. Reehuis, P.M. Abdala, Synthesis, crystal structure, and physical properties of  $\text{Sr}_2\text{FeOsO}_6$ , *Inorganic chemistry* 52(11) (2013) 6713-6719.
- [38] A. Taylor, R. Morrow, D. Singh, S. Calder, M. Lumsden, P. Woodward, A. Christianson, Magnetic order and electronic structure of the  $5d^3$  double perovskite  $\text{Sr}_2\text{ScOsO}_6$ , *Physical Review B* 91(10) (2015) 100406.
- [39] W.R. Gemmill, M.D. Smith, R. Prozorov, H.-C. zur Loye, Crystal growth and magnetic properties of lanthanide-containing osmium double perovskites,  $\text{Ln}_2\text{NaOsO}_6$  ( $\text{Ln} = \text{La, Pr, Nd}$ ), *Inorganic chemistry* 44(8) (2005) 2639-2646.
- [40] D. Iwanaga, Y. Inaguma, M. Itoh, Crystal Structure and Magnetic Properties of B-Site Ordered Perovskite-type Oxides  $\text{A}_2\text{CuB}'\text{O}_6$  ( $\text{A} = \text{Ba, Sr}$ ;  $\text{B}' = \text{W, Te}$ ), *Journal of Solid State Chemistry* 147(1) (1999) 291-295.
- [41] Q. Zhou, B.J. Kennedy, A variable temperature structural study of the Jahn–Teller distortion in  $\text{Ba}_2\text{CuUO}_6$ , *Journal of Physics and Chemistry of Solids* 68(9) (2007) 1643-1647.
- [42] H.L. Feng, M. Arai, Y. Matsushita, Y. Tsujimoto, Y. Yuan, C.I. Sathish, J. He, M. Tanaka, K. Yamaura, High-pressure synthesis, crystal structure and magnetic properties of double perovskite oxide  $\text{Ba}_2\text{CuOsO}_6$ , *Journal of Solid State Chemistry* 217 (2014) 9-15.
- [43] I. Brown, D. Altermatt, Bond-valence parameters obtained from a systematic analysis of the inorganic crystal structure database, *Acta Crystallographica Section B: Structural Science* 41(4) (1985) 244-247.

- [44] D. Altermatt, I.D. Brown, The automatic searching for chemical bonds in inorganic crystal structures, *Acta Crystallographica Section B* 41(4) (1985) 240-244.
- [45] J.-I. Yamaura, S. Yonezawa, Y. Muraoka, Z. Hiroi, Crystal structure of the pyrochlore oxide superconductor  $\text{KOs}_2\text{O}_6$ , *Journal of Solid State Chemistry* 179(1) (2006) 336-340.
- [46] C. Zhang, H. Oyanagi, B. Kim, Y. Park, Y. Zhang, Local lattice structure in Mn-doped  $\text{La}_{2-x}\text{Sr}_x\text{CuO}_4$  studied by Cu and Mn K-edge XAFS, *Physical Review B* 75(17) (2007) 174504.
- [47] S. Åsbrink, L.J. Norrby, A refinement of the crystal structure of copper (II) oxide with a discussion of some exceptional esd's, *Acta Crystallographica Section B* 26(1) (1970) 8-15.
- [48] J.M. Tranquada, S.M. Heald, A. Moodenbaugh, M. Suenaga, X-ray absorption studies of  $\text{La}_{2-x}(\text{Ba},\text{Sr})_x\text{CuO}_4$  superconductors, *Physical Review B* 35(13) (1987) 7187-7190.
- [49] J.Y. Kim, J.A. Rodriguez, J.C. Hanson, A.I. Frenkel, P.L. Lee, Reduction of  $\text{CuO}$  and  $\text{Cu}_2\text{O}$  with  $\text{H}_2$ : H embedding and kinetic effects in the formation of suboxides, *Journal of the American Chemical Society* 125(35) (2003) 10684-10692.
- [50] R. Morrow, J.R. Soliz, A.J. Hauser, J.C. Gallagher, M.A. Susner, M.D. Sumption, A.A. Aczel, J. Yan, F. Yang, P.M. Woodward, The effect of chemical pressure on the structure and properties of  $\text{A}_2\text{CrOsO}_6$  ( $\text{A} = \text{Sr}, \text{Ca}$ ) ferrimagnetic double perovskite, *Journal of Solid State Chemistry* 238 (2016) 46-52.
- [51] H.L. Feng, M. Reehuis, P. Adler, Z. Hu, M. Nicklas, A. Hoser, S.-C. Weng, C. Felser, M. Jansen, Canted ferrimagnetism and giant coercivity in the nonstoichiometric double perovskite  $\text{La}_2\text{Ni}_{1.19}\text{Os}_{0.81}\text{O}_6$ , *Physical Review B* 97(18) (2018) 184407.
- [52] W. Wu, V. Kiryukhin, H.-J. Noh, K.-T. Ko, J.-H. Park, I. W Ratcliff, P. Sharma, N. Harrison, Y. Choi, Y. Horibe, Formation of pancakelike Ising domains and giant magnetic coercivity in ferrimagnetic  $\text{LuFe}_2\text{O}_4$ , *Physical review letters* 101(13) (2008) 137203.
- [53] A. Yamamoto, D. Hashizume, H.A. Katori, T. Sasaki, E. Ohmichi, T. Nishizaki, N. Kobayashi, H. Takagi, Ten Layered Hexagonal Perovskite  $\text{Sr}_5\text{Ru}_{5-x}\text{O}_{15}$  ( $x = 0.90$ ), a Weak

Ferromagnet with a Giant Coercive Field  $H_c \sim 12$  T, Chemistry of Materials 22(20) (2010) 5712-5717.

[54] R. Troć, Z. Bukowski, R. Horyń, J. Klamut, Possible antiferromagnetic ordering in  $\text{Y}_2\text{Cu}_2\text{O}_5$ . Paramagnetic behaviour of  $\text{BaCuO}_2$ , Physics Letters A 125(4) (1987) 222-224.

[55] Y.G. Shi, Y.F. Guo, S. Yu, M. Arai, A.A. Belik, A. Sato, K. Yamaura, E. Takayama-Muromachi, H.F. Tian, H.X. Yang, J.Q. Li, T. Varga, J.F. Mitchell, S. Okamoto, Continuous metal-insulator transition of the antiferromagnetic perovskite  $\text{NaOsO}_3$ , Physical Review B 80(16) (2009).

[56] S. Calder, V.O. Garlea, D.F. McMorrow, M.D. Lumsden, M.B. Stone, J.C. Lang, J.W. Kim, J.A. Schlueter, Y.G. Shi, K. Yamaura, Y.S. Sun, Y. Tsujimoto, A.D. Christianson, Magnetically Driven Metal-Insulator Transition in  $\text{NaOsO}_3$ , Physical Review Letters 108(25) (2012).

[57] Y. Krockenberger, K. Mogare, M. Reehuis, M. Tovar, M. Jansen, G. Vaitheeswaran, V. Kanchana, F. Bultmark, A. Delin, F. Wilhelm,  $\text{Sr}_2\text{CrOsO}_6$ : End point of a spin-polarized metal-insulator transition by 5 d band filling, Physical Review B 75(2) (2007) 020404.

[58] R. Morrow, J.W. Freeland, P.M. Woodward, Probing the Links between Structure and Magnetism in  $\text{Sr}_{2-x}\text{Ca}_x\text{FeOsO}_6$  Double Perovskites, Inorganic Chemistry 53(15) (2014) 7983-7992.

[59] R. Macquart, S.-J. Kim, W.R. Gemmill, J.K. Stalick, Y. Lee, T. Vogt, H.-C. zur Loye, Synthesis, structure, and magnetic properties of  $\text{Sr}_2\text{NiOsO}_6$  and  $\text{Ca}_2\text{NiOsO}_6$ : Two new osmium-containing double perovskites, Inorganic chemistry 44(26) (2005) 9676-9683.

[60] D. Cox, G. Shirane, B. Frazer, Neutron-Diffraction Study of Antiferromagnetic  $\text{Ba}_2\text{CoWO}_6$  and  $\text{Ba}_2\text{NiWO}_6$ , Journal of Applied Physics 38(3) (1967) 1459-1460.

[61] H. Falcon, A. Goeta, G. Punte, R. Carbonio, Crystal structure refinement and stability of  $\text{LaFe}_x\text{Ni}_{1-x}\text{O}_3$  solid solutions, Journal of Solid State Chemistry 133(2) (1997) 379-385.

- [62] A. Hirano, R. Kanno, Y. Kawamoto, Y. Takeda, K. Yamaura, M. Takano, K. Ohyama, M. Ohashi, Y. Yamaguchi, Relationship between non-stoichiometry and physical properties in  $\text{LiNiO}_2$ , *Solid State Ionics* 78(1-2) (1995) 123-131.
- [63] Y. Shi, Y. Guo, Y. Shirako, W. Yi, X. Wang, A.A. Belik, Y. Matsushita, H.L. Feng, Y. Tsujimoto, M. Arai, High-pressure synthesis of 5d cubic perovskite  $\text{BaOsO}_3$  at 17 GPa: ferromagnetic evolution over 3d to 5d series, *Journal of the American Chemical Society* 135(44) (2013) 16507-16516.
- [64] S.-M. Bak, K.-W. Nam, W. Chang, X. Yu, E. Hu, S. Hwang, E.A. Stach, K.-B. Kim, K.Y. Chung, X.-Q. Yang, Correlating Structural Changes and Gas Evolution during the Thermal Decomposition of Charged  $\text{Li}_x\text{Ni}_{0.8}\text{Co}_{0.15}\text{Al}_{0.05}\text{O}_2$  Cathode Materials, *Chemistry of Materials* 25(3) (2013) 337-351.
- [65] A.V. Chadwick, S.L. Savin, S. Fiddy, R. Alcantara, D. Fernández Lisboa, P. Lavela, G.F. Ortiz, J.L. Tirado, Formation and oxidation of nanosized metal particles by electrochemical reaction of Li and Na with  $\text{NiCo}_2\text{O}_4$ : X-ray absorption spectroscopic study, *The Journal of Physical Chemistry C* 111(12) (2007) 4636-4642.
- [66] W.-S. Yoon, C.P. Grey, M. Balasubramanian, X.-Q. Yang, J. McBreen, In situ X-ray absorption spectroscopic study on  $\text{LiNi}_{0.5}\text{Mn}_{0.5}\text{O}_2$  cathode material during electrochemical cycling, *Chemistry of Materials* 15(16) (2003) 3161-3169.
- [67] H. Chang, Y.-q. Guo, J.-k. Liang, G.-h. Rao, Magnetic ordering and irreversible magnetization between ZFC and FC states in  $\text{RCO}_5\text{Ga}_7$  compounds, *Journal of magnetism and magnetic materials* 278(3) (2004) 306-310.

## Chapter 5 The evolution of structure and magnetic properties from $\text{Sr}_2\text{CrOsO}_6$ to $\text{Sr}_2\text{NiOsO}_6$ by substitution

### 5.1 Introduction

Half-metallic materials possessing high Curie temperature ( $T_c$ ) have attracted considerable interest for recent 20 years. Half metallic compounds are promised to be use as spintronic materials, in addition, high  $T_c$  can make it feasible to build practice devices at room temperature. Half-metallicity and high  $T_c$  ( $= 420$  K) were found in  $\text{Sr}_2\text{FeMoO}_6$  by K.-I. Kobayashi and et.al [1]. Since spins of  $\text{Fe}^{3+}$  ( $S = 5/2$ ) and  $\text{Mo}^{5+}$  ( $S = 1/2$ ) couple antiferromagnetically in a cubic ordered perovskite structure, it has only one electron in the  $5d$   $t_{2g}$  minority-spin orbital which is located at the Fermi level. This delocalized electron shared by Fe and Mo through the oxygen orbitals, behaving like a conduction electron and show spin-polarized. Following the discovery of  $\text{Sr}_2\text{FeMoO}_6$ , a number of similar compounds have been studied, such as  $\text{Sr}_2\text{CrWO}_6$ ,  $\text{Sr}_2\text{CrReO}_6$ ,  $\text{Sr}_2\text{CrMoO}_6$ ,  $\text{Sr}_2\text{FeReO}_6$  [2-5]. These compounds belong to the family of double perovskite oxides and the general formula can be denoted as  $A_2\text{BB}'\text{O}_6$ , where B and B' sites are occupied by transition metal ions. Among these unique ordered double perovskites,  $\text{Sr}_2\text{CrOsO}_6$  was thought to be a special case. Resulting from the electronic configuration of  $\text{Cr}^{3+}$  ( $3d^3$ ,  $t_{2g}^3$ ) and  $\text{Os}^{5+}$  ( $5d^3$ ,  $t_{2g}^3$ ),  $5d$   $t_{2g}$  minority-spin orbital is completely filled whereas the majority-spin orbital is empty. It leads to the end point of ideally spin-polarized metal-insulator transition occurs in  $\text{Sr}_2\text{CrOsO}_6$  [6]. K.-W. Lee and W. E. Pickett proposed that  $\text{Sr}_2\text{CrOsO}_6$  is a near-half metallic antiferromagnet and a large spin-orbit coupling reduces Os spin moment [7]. However, the significant SOC of Os is not supported by x-ray magnetic circular dichroism (XMCD) experimental results, a quite small magnetic moment of  $0.015 \mu_B/\text{f.u.}$  was observed on Os orbital [6]. A model for multiorbital material was applied to  $\text{Sr}_2\text{CrOsO}_6$ , suggesting that it is a Mott insulator and the net moment observed in  $\text{Sr}_2\text{CrOsO}_6$

arises from spin canting [8]. But the canted magnetic structure did not confirm with neutron powder diffraction measurement [9].

Ferrimagnetism or ferromagnetism can survive up to temperature above room temperature that is a remarkable feature for application. The half-metallic double perovskite oxides have considerably high  $T_c$ , which is understood within the kinetic energy driven exchange model [6, 10, 11]. The  $T_c$  of  $\text{Sr}_2\text{CrOsO}_6$  was reported to be 725 K by Y. Krockenberger et al. [6] and 660 K by Ryan Morrow et al. [9], respectively. The deviation in  $T_c$  may be caused by different amount of antisites. Nevertheless, such high  $T_c$  is higher than any other double perovskite so far reported in the literature. Cr and Os in  $\text{Sr}_2\text{CrOsO}_6$  show 3+ and 5+ respectively. The electronic configurations of  $\text{Cr}^{3+}$  ( $3d^3$ ,  $t_{2g}^3$ ) and  $\text{Os}^{5+}$  ( $5d^3$ ,  $t_{2g}^3$ ) are taken into account, the kinetic energy gain is only feasible for the minority-spin carriers. In addition, the magnetic transition temperature of these compounds is positively related to the bandwidth in this minority-spin channel [6, 12]. Doping  $\text{La}^{3+}$  into A sites is a way to change the band filling, for example, the  $T_c$  was increased by more than 100 K by  $\text{La}^{3+}$  doping in  $\text{LaSrFeMoO}_6$  and  $\text{LaCaCrWO}_6$  [13, 14]. Alternatively, replacement of 5d transition metal ion on B' sites can also lead to the change of  $T_c$ , for example,  $\text{Sr}_2\text{CrReO}_6$  ( $\text{Re}^{5+}$ :  $5d^2$ ) shows higher  $T_c$  than  $\text{Sr}_2\text{CrWO}_6$  ( $\text{W}^{5+}$ :  $5d^1$ ) [2, 3].

In this study, the substitutional series samples polycrystalline  $\text{Sr}_2\text{Cr}_{1-x}\text{Ni}_x\text{OsO}_6$  ( $x = 0, 0.25, 0.5, 0.75$  and 1) were prepared under high-pressure and high-temperature conditions. Introduction of  $\text{Ni}^{2+}$  into  $\text{Cr}^{3+}$  sites leads to variations of structure, electronic and magnetic properties. These Ni-substituted  $\text{Sr}_2\text{CrOsO}_6$  compounds give insight into understanding the origin of half-metallic materials with high ferrimagnetic  $T_c$ . Besides, synthesizing samples under high pressure rather than ambient pressure is for checking out the influence of pressure on electron transport. Ninning Zu et al. proposed double perovskite oxide  $\text{La}_2\text{VMnO}_6$  can become a half-metallic ferrimagnet under critical pressure [15].

## 5.2 Experimental Details

Polycrystalline  $\text{Sr}_2\text{Cr}_{1-x}\text{Ni}_x\text{OsO}_6$  ( $x = 0, 0.25, 0.5, 0.75$  and  $1$ ) were synthesized from powders of SrO (99.9%, Strem Chemicals, Inc., USA),  $\text{CrO}_2$  (Magtrieve, Sigma-Aldrich Co., USA), NiO (99.97%, High Purity Chemicals Co., Ltd., Japan),  $\text{OsO}_2$  [Lab made from Os powder and Os powder (99.95%) was supplied by the Nanjing Dongrui Platinum Co., Ltd.] and  $\text{KClO}_4$  ( $> 99.5\%$ , Kishida Chem. Lab. Co., Ltd.). The powders were thoroughly mixed, followed by sealing in a Pt capsule, the process of which were all conducted in an Ar-filled glove box. Under a pressure of 6 GPa, generated in a belt-type high pressure apparatus (Kobe Steel, Ltd., Japan), the capsules were heated to a temperature for 30 min. The heating temperature is sample-dependent. For  $\text{Sr}_2\text{Cr}_{1-x}\text{Ni}_x\text{OsO}_6$  ( $x = 0, 0.25$  and  $0.5$ ), the capsules were heated at 1600 °C. The temperatures were lower for  $\text{Sr}_2\text{Cr}_{0.25}\text{Ni}_{0.75}\text{OsO}_6$  and  $\text{Sr}_2\text{NiOsO}_6$ , 1500 °C and 1300 °C, respectively. After the heating, the temperature was then quenched to room temperature, following which the pressure was gradually released.

All the prepared samples were investigated by powder XRD at room temperature using  $\text{Cu-K}\alpha$  radiation ( $\lambda = 1.5432 \text{ \AA}$ ) in a commercial apparatus (RIGAKU-MiniFlex 600). The fine powder samples were subjected to a synchrotron XRD study by using the high-precision powder X-ray diffractometer installed at the BL15XU beamline, Spring-8, Japan.

Magnetic properties were measured in a magnetic property measurement system (MPMS, Quantum Design, Inc.). The electrical transport and thermal properties were measured in physical property measurement system (PPMS, Quantum Design, Inc.). Silver paste and platinum wires were used to connect the polycrystalline platelet to the device terminals. The specific heat capacity ( $C_p$ ) was measured by the thermal-relaxation method using Apiezon-N grease from 300 K to 2 K for thermal contact between the sample and a holder stage.



### 5.3 Results and Discussion

The XRD patterns of synthesized  $\text{Sr}_2\text{CrOsO}_6$  and  $\text{Sr}_2\text{NiOsO}_6$  are the same as the ones reported by other groups [9, 16]. Compared to the end points, the substitutional series  $\text{Sr}_2\text{Cr}_{1-x}\text{Ni}_x\text{OsO}_6$  ( $x = 0.25, 0.5$  and  $0.75$ ) show phase transition gradually (see **Fig. 5.1**). We can see the obvious peak position shift to lower degree from  $\text{Sr}_2\text{CrOsO}_6$  to  $\text{Sr}_2\text{NiOsO}_6$  and peaks of [110] and [104] transfer to [112] and [200] in the inset of **Fig. 5.1**. For better understand how the structure changes of these substitutional series, the same samples were investigated by synchrotron XRD. Considering the magnetic transition temperature of each sample (the exact  $T_m$  see below), the synchrotron XRD patterns for  $\text{Sr}_2\text{Cr}_{1-x}\text{Ni}_x\text{OsO}_6$  ( $x = 0, 0.25$  and  $0.5$ ) were collected at room temperature and another temperature higher than their  $T_m$ , respectively. Samples  $\text{Sr}_2\text{NiOsO}_6$  and  $\text{Sr}_2\text{Cr}_{0.25}\text{Ni}_{0.75}\text{OsO}_6$  were only measured at room temperature because their  $T_m$  are much lower.

The analyzed synchrotron XRD patterns and the refined crystallographic parameters for two end points samples are presented in **Fig. 5.2 and 5.3** and **Table 5.1, 5.2 and 5.3**, reasonable agreement between observed and calculated patterns for  $\text{Sr}_2\text{CrOsO}_6$  were attained by a Rietveld method with a trigonal model at room temperature and a cubic model at 750 K (above magnetic transition temperature, discussed later). The similar phase transition has also been observed in neutron powder diffraction data [6]. A tetragonal model is refined well for  $\text{Sr}_2\text{NiOsO}_6$ , which are reconciled with the previously reported results. We carefully refined the data of  $\text{Sr}_2\text{CrOsO}_6$  collected at 750 K (higher than  $T_m$ ) and room temperature and confirmed that no any phase transition below its  $T_m$  was observed. The occupancies of Os and Cr atoms at  $3b$  and  $3a$  Wyckoff positions were refined independently. A small amount of disorder was found at both  $3b$  and  $3a$  sites, but the actual chemical composition is concluded to be  $\text{Sr}_2\text{Cr}_{0.96}\text{Os}_{1.04}\text{O}_6$  that is still closed to the composition of the initial synthesis mixture. The occupancy of the Cr ion on Cr-rich octahedral ( $3a$ ) site is 91.1% that is higher than 80.2%

found in ambient-pressure prepared  $\text{Sr}_2\text{CrOsO}_6$  sample [9]. In contrast, the structure refinement of  $\text{Sr}_2\text{NiOsO}_6$  indicates full Ni/Os cation order.

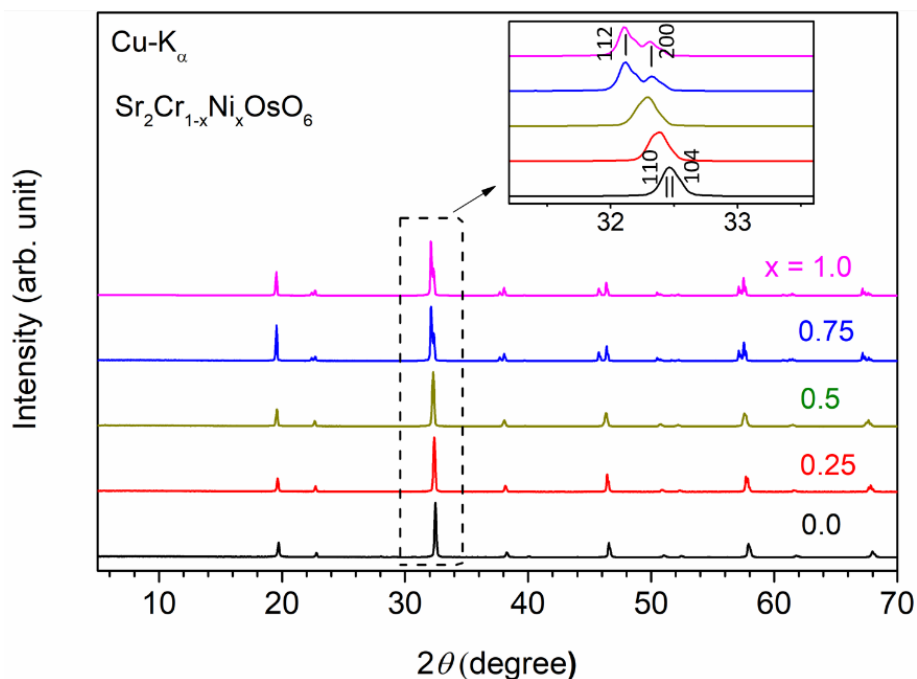


**Fig. 5.1** Powder XRD patterns for  $\text{Sr}_2\text{Cr}_{1-x}\text{Ni}_x\text{OsO}_6$  ( $x = 0, 0.25, 0.5, 0.75$  and  $1$ ) at room temperature. The inset is a horizontal expansion of the main peaks.

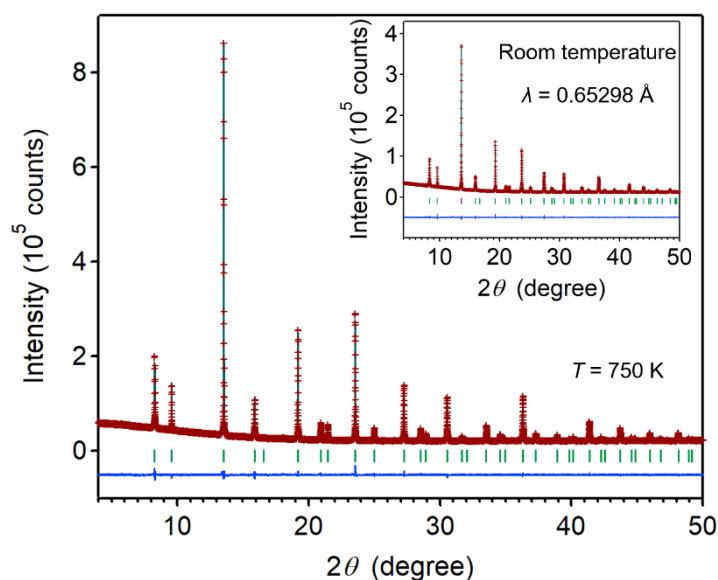


**Fig. 5.2** Rietveld refinement of the powder synchrotron XRD profile of  $\text{Sr}_2\text{CrOsO}_6$  ( $\lambda = 0.65298 \text{ \AA}$ ) collected at  $750 \text{ K}$ . The crosses and solid lines show the observed and calculated patterns, respectively, with their differences shown at the bottom. The expected Bragg

reflections for the  $Fm-3m$  cell are marked by ticks. The inset is the data at room temperature, the expected Bragg reflections for the  $R-3$  cell are marked by ticks.

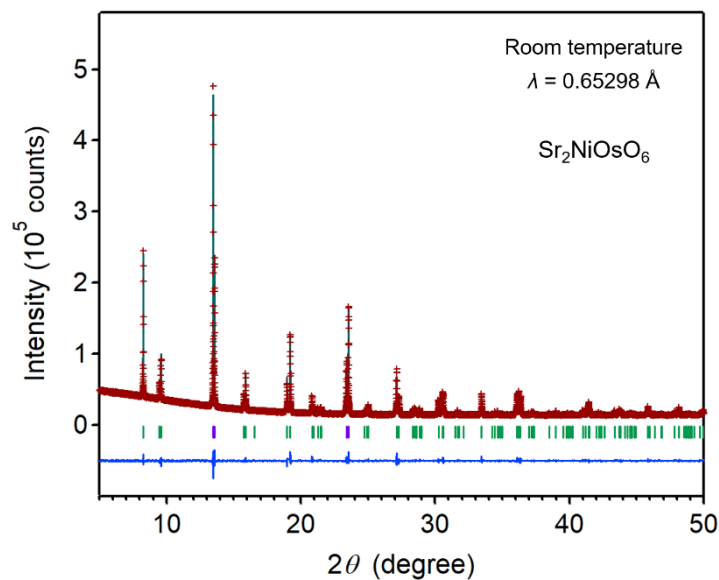


**Fig. 5.3** Rietveld refinement of the powder synchrotron XRD profile of  $\text{Sr}_2\text{NiOsO}_6$  ( $\lambda = 0.65298 \text{ \AA}$ ) collected at room temperature. The crosses and solid lines show the observed and calculated patterns, respectively, with their differences shown at the bottom. The expected Bragg reflections for the  $I4/m$  cell are marked by ticks.

**Table 5.1** Atomic coordinates and equivalent isotropic displacement parameters ( $U_{\text{eq}}$ ,  $10^{-3} \text{ \AA}^2$ ) and anisotropic displacement parameters ( $U_{\text{ij}}$ ,  $10^{-3} \text{ \AA}^2$ ) for  $\text{Sr}_2\text{CrOsO}_6$  at 750 K as revealed by synchrotron XRD

Atom	Site	Occp.	$x$	$y$	$z$	$U_{\text{eq}}$
Sr1	8c	1	0.25	0.25	0.25	13.0
Cr1	4b	0.911(16)	0.5	0.5	0.5	5.25
Os1	4b	0.089	0.5	0.5	0.5	5.25
Os2	4a	0.955(3)	0	0	0	3.43
Cr2	4a	0.045	0	0	0	3.43
O1	24e	1	0.2457(3)	0	0	14.9(5)
Atom	$U_{11}$	$U_{22}$	$U_{33}$	$U_{12}$	$U_{13}$	$U_{23}$
Sr1	13.0(15)	$= U_{11}$	$= U_{11}$	0	0	0
Cr1	5.3(3)	$= U_{11}$	$= U_{11}$	0	0	0
Os1	5.3	$= U_{11}$	$= U_{11}$	0	0	0
Os2	3.4(11)	$= U_{11}$	$= U_{11}$	0	0	0
Cr2	3.4	$= U_{11}$	$= U_{11}$	0	0	0
O1	14.9	14.9	14.9	0	0	0

Space group:  $Fm\bar{3}m$  (cubic; no. 225); lattice constants  $a = 7.84460(5) \text{ \AA}$ ; cell volume =  $482.739(5) \text{ \AA}^3$ ;  $d_{\text{cal}} = 7.149 \text{ g cm}^{-3}$ ; chemical formula sum:  $\text{Sr}_2\text{Cr}_{0.96}\text{Os}_{1.04}\text{O}_6$  ( $Z = 4$ ); and the final  $R$  indices are 1.942% ( $R_{\text{wp}}$ ), 1.335% ( $R_{\text{p}}$ ), 0.831% ( $R_{\text{B}}$ ), and 0.430% ( $R_{\text{F}}$ ).

**Table 5.2** Atomic coordinates and equivalent isotropic displacement parameters ( $U_{\text{eq}}$ ,  $10^{-3} \text{ \AA}^2$ ) and anisotropic displacement parameters ( $U_{ij}$ ,  $10^{-3} \text{ \AA}^2$ ) for  $\text{Sr}_2\text{CrOsO}_6$  at room temperature as revealed by synchrotron XRD

Atom	Site	Occp.	$x$	$y$	$z$	$U_{\text{eq}}$
Sr1	6c	1	0	0	0.2488(18)	12.7
Cr1	3b	0.911(16)	0	0	0.5	10.1
Os1	3b	0.089	0	0	0.5	10.1
Os2	3a	0.955(3)	0	0	0	9.7
Cr2	3a	0.045	0	0	0	9.7
O1	18f	1	0.477(13)	0.015(10)	0.2463(5)	1(1)
Atom	$U_{11}$	$U_{22}$	$U_{33}$	$U_{12}$	$U_{13}$	$U_{23}$
Sr1	12.9(5)	$= U_{11}$	12.3(9)	$= 0.5 \times U_{11}$	0	0
Cr1	11.2(9)	$= U_{11}$	8(15)	$= 0.5 \times U_{11}$	0	0
Os1	11.2	$= U_{11}$	8	$= 0.5 \times U_{11}$	0	0
Os2	6.6(4)	$= U_{11}$	15.9(8)	$= 0.5 \times U_{11}$	0	0
Cr2	6.6	$= U_{11}$	15.9	$= 0.5 \times U_{11}$	0	0
O1	1.4	1.4	1.4	0.7	0	0

Space group:  $R\bar{3}$  (trigonal; no. 148); lattice constants  $a = 5.5147(12) \text{ \AA}$  and  $c = 13.4879(2) \text{ \AA}$ ; cell volume =  $355.24(12) \text{ \AA}^3$ ;  $d_{\text{cal}} = 7.286 \text{ g cm}^{-3}$ ; chemical formula sum:  $\text{Sr}_2\text{Cr}_{0.96}\text{Os}_{1.04}\text{O}_6$  ( $Z = 3$ ); and the final  $R$  indices are 1.863% ( $R_{\text{wp}}$ ), 1.320% ( $R_{\text{p}}$ ), 0.714% ( $R_{\text{B}}$ ), and 0.314% ( $R_{\text{F}}$ ).

**Table 5.3** Atomic coordinates and equivalent isotropic displacement parameters ( $U_{\text{eq}}$ ,  $10^{-3} \text{ \AA}^2$ ) and anisotropic displacement parameters ( $U_{ij}$ ,  $10^{-3} \text{ \AA}^2$ ) for  $\text{Sr}_2\text{NiOsO}_6$  at room temperature as revealed by synchrotron XRD

Atom	Site	Occp.	$x$	$y$	$z$	$U_{\text{eq}}$
Sr1	$4d$	1	0	0.5	0.25	10.7
Ni1	$2a$	1	0	0	0	4.8
Os1	$2b$	1	0	0	0.5	3.5
O1	$4e$	1	0	0	0.2601(7)	20.0
O2	$8h$	1	0.2237(8)	0.2962(9)	0	16(2)
Atom	$U_{11}$	$U_{22}$	$U_{33}$	$U_{12}$	$U_{13}$	$U_{23}$
Sr1	8.8(3)	$= U_{11}$	14.3(6)	0	0	0
Ni1	1.3(5)	$= U_{11}$	12(1)	0	0	0
Os1	1.9(2)	$= U_{11}$	6.7(4)	0	0	0
O1	13(2)	$= U_{11}$	35(4)	0	0	0
O2	16.1	$= U_{11}$	$= U_{11}$	0	0	0

Space group:  $I4/m$  (tetragonal; no. 87); lattice constants  $a = 5.5320(2) \text{ \AA}$  and  $c = 7.9204(3) \text{ \AA}$ ; cell volume =  $242.39(2) \text{ \AA}^3$ ;  $d_{\text{cal}} = 7.127 \text{ g cm}^{-3}$ ; chemical formula sum:  $\text{Sr}_2\text{NiOsO}_6$  ( $Z = 2$ ); and the final  $R$  indices are 2.376% ( $R_{\text{wp}}$ ), 1.480% ( $R_{\text{p}}$ ), 0.908% ( $R_{\text{B}}$ ), and 0.426% ( $R_{\text{F}}$ ).

The synchrotron XRD patterns for  $\text{Sr}_2\text{Cr}_{0.75}\text{Ni}_{0.25}\text{OsO}_6$  and  $\text{Sr}_2\text{Cr}_{0.25}\text{Ni}_{0.75}\text{OsO}_6$  were successful refined, the results of which are shown in **Fig. 5.4** and **5.5**.  $\text{Sr}_2\text{Cr}_{0.75}\text{Ni}_{0.25}\text{OsO}_6$  was found to crystallize into the same cubic structure ( $Fm\text{-}3m$ ) as  $\text{Sr}_2\text{CrOsO}_6$  at 550 K and changes to trigonal structure ( $R\text{-}3$ ) at room temperature (below  $T_{\text{m}}$ ). The refinement result indicates the Ni atom occupies the  $3b$  site with Cr atom, although the occupation is slightly lower than 25% (see **Table 5.4** and **5.5**). The refined crystallographic parameters for  $\text{Sr}_2\text{Cr}_{0.25}\text{Ni}_{0.75}\text{OsO}_6$  is presented in **Table 5.6**, indicating that 74% Ni and 26% Cr distribute at  $2a$  site.

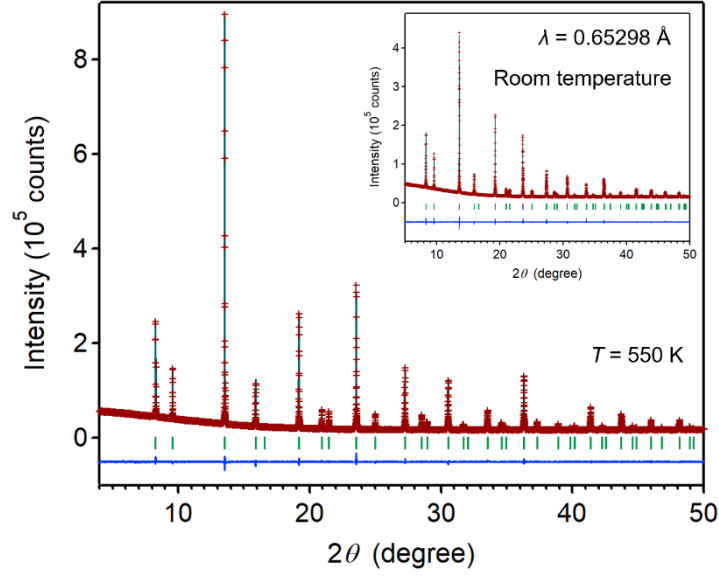


**Fig. 5.4** Rietveld refinement of the powder synchrotron XRD profile of  $\text{Sr}_2\text{Cr}_{0.75}\text{Ni}_{0.25}\text{OsO}_6$  ( $\lambda = 0.65298 \text{ \AA}$ ) collected at 550 K. The crosses and solid lines show the observed and calculated patterns, respectively, with their differences shown at the bottom. The expected Bragg reflections for the  $Fm\text{-}3m$  cell are marked by ticks. The inset is the data at room temperature, the expected Bragg reflections for the  $R\text{-}3$  cell are marked by ticks.

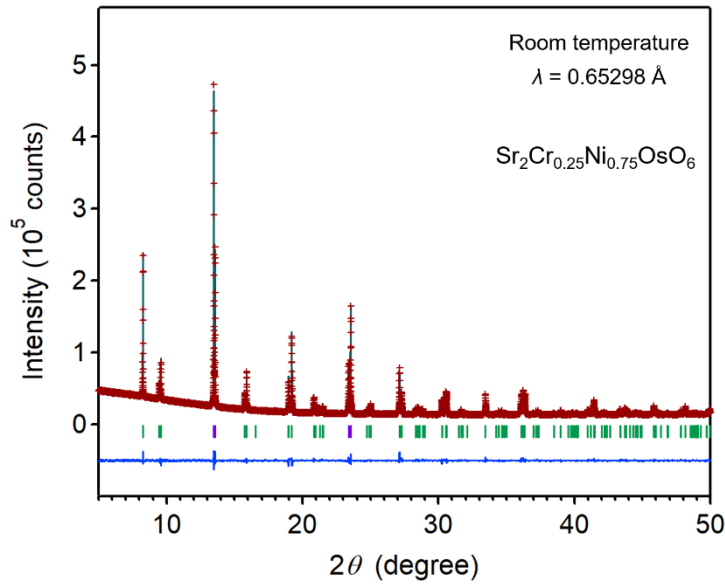


**Fig. 5.5** Rietveld refinement of the powder synchrotron XRD profile of  $\text{Sr}_2\text{Cr}_{0.25}\text{Ni}_{0.75}\text{OsO}_6$  ( $\lambda = 0.65298 \text{ \AA}$ ) collected at room temperature. The crosses and solid lines show the observed and calculated patterns, respectively, with their differences shown at the bottom. The expected Bragg reflections for the  $I4/m$  cell are marked by ticks.

**Table 5.4** Atomic coordinates and equivalent isotropic displacement parameters ( $U_{\text{eq}}$ ,  $10^{-3} \text{ \AA}^2$ ) and anisotropic displacement parameters ( $U_{ij}$ ,  $10^{-3} \text{ \AA}^2$ ) for  $\text{Sr}_2\text{Cr}_{0.75}\text{Ni}_{0.25}\text{OsO}_6$  at 550 K as revealed by synchrotron XRD

Atom	Site	Occp.	$x$	$y$	$z$	$U_{\text{eq}}$
Sr1	8c	1	0.25	0.25	0.25	14.4
Cr1	4b	0.72(17)	0.5	0.5	0.5	1.7
Ni1	4b	0.23	0.5	0.5	0.5	1.7
Os1	4b	0.053(16)	0.5	0.5	0.5	1.7
Os2	4a	0.994(3)	0	0	0	6.1
Cr2	4a	0.006	0	0	0	6.1
O1	24e	1	0.2433(2)	0	0	16.4(5)
Atom	$U_{11}$	$U_{22}$	$U_{33}$	$U_{12}$	$U_{13}$	$U_{23}$
Sr1	14.4(12)	$= U_{11}$	$= U_{11}$	0	0	0
Cr1	1.7(2)	$= U_{11}$	$= U_{11}$	0	0	0
Ni1	1.7	$= U_{11}$	$= U_{11}$	0	0	0
Os1	1.7	$= U_{11}$	$= U_{11}$	0	0	0
Os2	6.1(8)	$= U_{11}$	$= U_{11}$	0	0	0
Cr2	6.1	$= U_{11}$	$= U_{11}$	0	0	0
O1	16.4	16.4	16.4	0	0	0

Space group:  $Fm\bar{3}m$  (cubic; no. 225); lattice constants  $a = 7.84115(3) \text{ \AA}$ ; cell volume =  $482.10(3) \text{ \AA}^3$ ;  $d_{\text{cal}} = 7.185 \text{ g cm}^{-3}$ ; chemical formula sum:  $\text{Sr}_2\text{Cr}_{0.72}\text{Ni}_{0.23}\text{Os}_{1.05}\text{O}_6$  ( $Z = 4$ ); and the final  $R$  indices are 1.785% ( $R_{\text{wp}}$ ), 1.218% ( $R_{\text{p}}$ ), 0.730% ( $R_{\text{B}}$ ), and 0.348% ( $R_{\text{F}}$ ).



**Table 5.5** Atomic coordinates and equivalent isotropic displacement parameters ( $U_{\text{eq}}$ ,  $10^{-3} \text{ \AA}^2$ ) and anisotropic displacement parameters ( $U_{ij}$ ,  $10^{-3} \text{ \AA}^2$ ) for  $\text{Sr}_2\text{Cr}_{0.75}\text{Ni}_{0.25}\text{OsO}_6$  at room temperature as revealed by synchrotron XRD

Atom	Site	Occp.	$x$	$y$	$z$	$U_{\text{eq}}$
Sr1	6c	1	0	0	0.25005(7)	12.0
Cr1	3b	0.72(17)	0	0	0.5	2.7
Ni1	3b	0.23	0	0	0.5	2.7
Os1	3b	0.053(16)	0	0	0.5	2.7
Os2	3a	0.994(3)	0	0	0	7.2
Cr2	3a	0.006	0	0	0	7.2
O1	18f	1	0.478(11)	0.0117(6)	0.2508(2)	6.0(8)
Atom	$U_{11}$	$U_{22}$	$U_{33}$	$U_{12}$	$U_{13}$	$U_{23}$
Sr1	13.4(3)	$= U_{11}$	9.3(5)	$= 0.5 \times U_{11}$	0	0
Cr1	2.7(6)	$= U_{11}$	2.7(8)	$= 0.5 \times U_{11}$	0	0
Ni1	2.7	$= U_{11}$	2.7	$= 0.5 \times U_{11}$	0	0
Os1	2.7	$= U_{11}$	2.7	$= 0.5 \times U_{11}$	0	0
Os2	7.9(2)	$= U_{11}$	5.7(3)	$= 0.5 \times U_{11}$	0	0
Cr2	7.9	$= U_{11}$	5.7	$= 0.5 \times U_{11}$	0	0
O1	6.0	6.0	6.0	3.0	0	0

Space group:  $R\bar{3}$  (trigonal; no. 148); lattice constants  $a = 5.5566(3) \text{ \AA}$  and  $c = 13.5674(5) \text{ \AA}$ ; cell volume  $= 362.78(3) \text{ \AA}^3$ ;  $d_{\text{cal}} = 7.160 \text{ g cm}^{-3}$ ; chemical formula sum:  $\text{Sr}_2\text{Cr}_{0.72}\text{Ni}_{0.23}\text{Os}_{1.05}\text{O}_6$  ( $Z = 4$ ); and the final  $R$  indices are 1.854% ( $R_{\text{wp}}$ ), 1.250% ( $R_{\text{p}}$ ), 0.753% ( $R_{\text{B}}$ ), and 0.370% ( $R_{\text{F}}$ ).

**Table 5.6** Atomic coordinates and equivalent isotropic displacement parameters ( $U_{\text{eq}}$ ,  $10^{-3} \text{ \AA}^2$ ) and anisotropic displacement parameters ( $U_{ij}$ ,  $10^{-3} \text{ \AA}^2$ ) for  $\text{Sr}_2\text{Cr}_{0.25}\text{Ni}_{0.75}\text{OsO}_6$  at room temperature as revealed by synchrotron XRD

Atom	Site	Occp.	$x$	$y$	$z$	$U_{\text{eq}}$
Sr1	$4d$	1	0	0.5	0.25	12.8
Ni1	$2a$	0.74(2)	0	0	0	2.7
Cr1	$2a$	0.26	0	0	0	2.7
Os2	$2b$	1	0	0	0.5	5.0
O1	$4e$	1	0	0	0.2594(6)	18.5
O2	$8h$	1	0.2312(9)	0.2885(9)	0	22(14)
Atom	$U_{11}$	$U_{22}$	$U_{33}$	$U_{12}$	$U_{13}$	$U_{23}$
Sr1	12.5(3)	$= U_{11}$	13.4(6)	0	0	0
Ni1	1.7(6)	$= U_{11}$	5(1)	0	0	0
Cr1	1.7	$= U_{11}$	5	0	0	0
Os2	4.6(2)	$= U_{11}$	5.8(3)	0	0	0
O1	20(2)	$= U_{11}$	16(3)	0	0	0
O2	22.4	$= U_{11}$	$= U_{11}$	0	0	0

Space group:  $I4/m$  (tetragonal; no. 87); lattice constants  $a = 5.5341(2) \text{ \AA}$  and  $c = 7.9247(3) \text{ \AA}$ ; cell volume =  $242.70(15) \text{ \AA}^3$ ;  $d_{\text{cal}} = 7.094 \text{ g cm}^{-3}$ ; chemical formula sum:  $\text{Sr}_2\text{Cr}_{0.26}\text{Ni}_{0.74}\text{OsO}_6$  ( $Z = 2$ ); and the final  $R$  indices are 2.184% ( $R_{\text{wp}}$ ), 1.403% ( $R_{\text{p}}$ ), 0.838% ( $R_{\text{B}}$ ), and 0.344% ( $R_{\text{F}}$ ).

The synchrotron XRD patterns for  $\text{Sr}_2\text{Cr}_{0.5}\text{Ni}_{0.5}\text{OsO}_6$  at 454 K and room temperature are presented in **Fig. 5.6** and **5.7**. The structure refinements for  $\text{Sr}_2\text{Cr}_{0.5}\text{Ni}_{0.5}\text{OsO}_6$  indicate it crystallizes into a different structure at room temperature (below  $T_{\text{m}}$ ) from the structure at 454 K. The high-temperature structure of  $\text{Sr}_2\text{Cr}_{0.5}\text{Ni}_{0.5}\text{OsO}_6$  was well refined in the tetragonal structure ( $I4/m$ ), which is same structure that the other two Ni-rich samples,  $\text{Sr}_2\text{NiOsO}_6$  and  $\text{Sr}_2\text{Cr}_{0.25}\text{Ni}_{0.75}\text{OsO}_6$ , crystallize into. Ni and Cr atoms distribute over  $2a$  site by approximately 1:1 and the occupation of Os atom at  $2a$  site is given to be 0.02 by the refinement (see **Table**

5.7). The  $2b$  Wyckoff position is 100% occupied by Os atom (labeled as Os2). It was failed to reach a reasonable solution for the synchrotron XRD pattern of the same powder sample at room temperature when assuming the space group  $I4/m$ . Compared to the XRD pattern collected at 454 K, the split of peaks was realized by zooming in the room-temperature XRD pattern, for example, the peaks with the maximum at  $23.5^\circ$  split into multiple peaks in the room-temperature pattern (see the inset of **Fig. 5.7**). Based on the feature of split, a monoclinic model ( $I12/m1$ , No.12) and a triclinic ( $I-1$ , No.2) were assumed for the XRD pattern at room temperature. A more reasonable agreement between the observed and calculated patterns and the refined crystallographic parameters was obtained by assuming the monoclinic model, presented in **Table 5.8**. Note that this monoclinic model has been applied to many double perovskite oxides such as  $\text{Sr}_2\text{CoOsO}_6$  [17],  $\text{Sr}_2\text{FeIrO}_6$  [18],  $\text{Sr}_2\text{FeSbO}_6$  [19],  $\text{Sr}_2\text{NiTeO}_6$  [20], and  $\text{Sr}_2\text{Ni}_{0.5}\text{Mg}_{0.5}\text{TeO}_6$  [21].

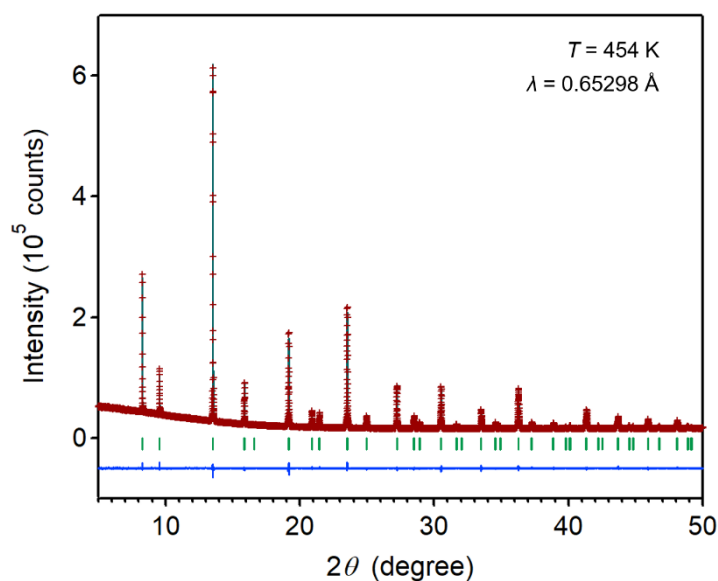


**Fig. 5.6** Rietveld refinement of the powder synchrotron XRD profile of  $\text{Sr}_2\text{Cr}_{0.5}\text{Ni}_{0.5}\text{OsO}_6$  ( $\lambda = 0.65298 \text{ \AA}$ ) collected at 454 K. The crosses and solid lines show the observed and calculated patterns, respectively, with their differences shown at the bottom. The expected Bragg reflections for the  $I4/m$  cell are marked by ticks.

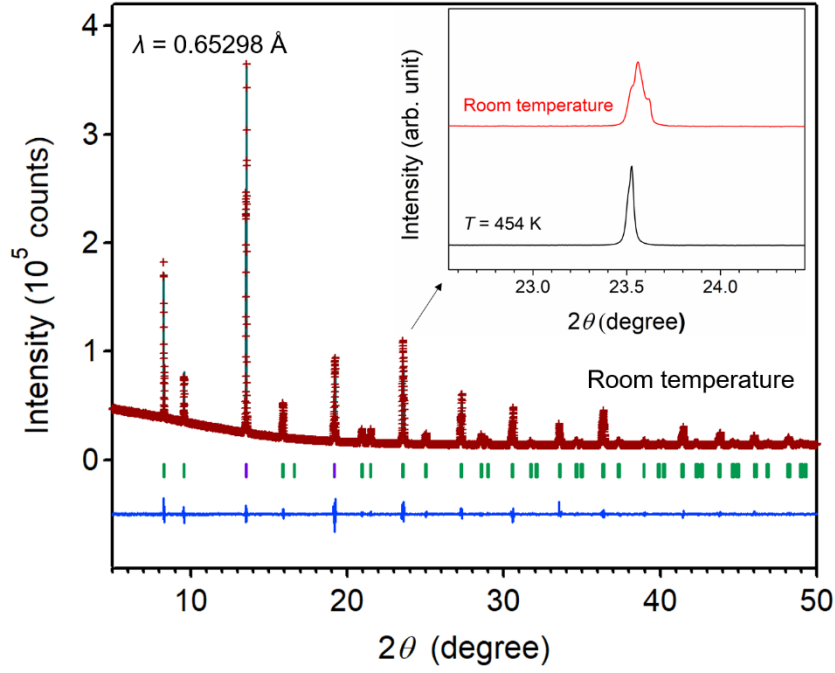


**Fig. 5.7** Rietveld refinement of the powder synchrotron XRD profile of  $\text{Sr}_2\text{Cr}_{0.5}\text{Ni}_{0.5}\text{OsO}_6$  ( $\lambda = 0.65298 \text{ \AA}$ ) collected at room temperature. The crosses and solid lines show the observed and calculated patterns, respectively, with their differences shown at the bottom. The expected Bragg reflections for the  $I12/m1$  cell are marked by ticks. The inset is the horizontal expansion and compared with the data at 454 K.

**Table 5.7** Atomic coordinates and equivalent isotropic displacement parameters ( $U_{\text{eq}}$ ,  $10^{-3} \text{ \AA}^2$ ) and anisotropic displacement parameters ( $U_{ij}$ ,  $10^{-3} \text{ \AA}^2$ ) for  $\text{Sr}_2\text{Cr}_{0.5}\text{Ni}_{0.5}\text{OsO}_6$  at 454 K as revealed by synchrotron XRD

Atom	Site	Occp.	$x$	$y$	$z$	$U_{\text{eq}}$
Sr1	$4d$	1	0	0.5	0.25	16.8
Ni1	$2a$	0.52(13)	0	0	0	2.2(3)
Cr1	$2a$	0.46	0	0	0	2.2
Os1	$2a$	0.020(12)	0	0	0	2.2
Os2	$2b$	1	0	0	0.5	7.7
O1	$4e$	1	0	0	0.2641(7)	23(2)
O2	$8h$	1	0.239(11)	0.281(13)	0	16(12)
Atom	$U_{11}$	$U_{22}$	$U_{33}$	$U_{12}$	$U_{13}$	$U_{23}$
Sr1	14.9(3)	$= U_{11}$	20.7(5)	0	0	0
Ni1	2.2	$= U_{11}$	$= U_{11}$	0	0	0
Cr1	2.2	$= U_{11}$	$= U_{11}$	0	0	0
Os1	2.2	$= U_{11}$	$= U_{11}$	0	0	0
Os2	5.4(2)	$= U_{11}$	12.4(4)	0	0	0
O1	23.0	$= U_{11}$	$= U_{11}$	0	0	0
O2	16.1	$= U_{11}$	$= U_{11}$	0	0	0

Space group:  $I4/m$  (tetragonal; no. 87); lattice constants  $a = 5.5475(2) \text{ \AA}$  and  $c = 7.8580(2) \text{ \AA}$ ; cell volume =  $241.83(12) \text{ \AA}^3$ ;  $d_{\text{cal}} = 7.138 \text{ g cm}^{-3}$ ; chemical formula sum:  $\text{Sr}_2\text{Cr}_{0.46}\text{Ni}_{0.52}\text{Os}_{1.02}\text{O}_6$  ( $Z = 2$ ); and the final  $R$  indices are 1.808% ( $R_{\text{wp}}$ ), 1.222% ( $R_{\text{p}}$ ), 0.906% ( $R_{\text{B}}$ ), and 0.424% ( $R_{\text{F}}$ ).

**Table 5.8** Atomic coordinates and equivalent isotropic displacement parameters ( $U_{eq}$ ,  $10^{-3} \text{ \AA}^2$ ) and anisotropic displacement parameters ( $U_{ij}$ ,  $10^{-3} \text{ \AA}^2$ ) for  $\text{Sr}_2\text{Cr}_{0.5}\text{Ni}_{0.5}\text{OsO}_6$  at room temperature as revealed by synchrotron XRD

Atom	Site	Occp.	$x$	$y$	$z$	$U_{eq}$
Sr1	4 <i>d</i>	1	0.0050(4)	0.5	0.2478(6)	13.8(3)
Ni1	2 <i>a</i>	0.52(2)	0	0	0	1.4(6)
Cr1	2 <i>a</i>	0.45	0	0	0	1.4
Os1	2 <i>a</i>	0.024(2)	0	0	0	1.4
Os2	2 <i>b</i>	1	0	0	0.5	9.6(2)
O1	4 <i>i</i>	1	0.029(2)	0	0.260(16)	9(14)
O2	8 <i>h</i>	1	-0.285(16)	0.231(15)	-0.030(10)	9

Space group:  $I12/m1$  (monoclinic; no. 12); lattice constants  $a = 5.5365(8) \text{ \AA}$ ,  $b = 5.5422(7) \text{ \AA}$ ,  $c = 7.851(10) \text{ \AA}$  and  $\beta = 89.8080(8)$ ; cell volume =  $240.91(6) \text{ \AA}^3$ ;  $d_{cal} = 7.172 \text{ g cm}^{-3}$ ; chemical formula sum:  $\text{Sr}_2\text{Cr}_{0.46}\text{Ni}_{0.52}\text{Os}_{1.02}\text{O}_6$  ( $Z = 2$ ); and the final  $R$  indices are 2.858% ( $R_{wp}$ ), 1.565% ( $R_p$ ), 1.343% ( $R_B$ ), and 0.743% ( $R_F$ ).

The major bond lengths were calculated for each sample from the refined parameters, as shown in **Table 5.9**. The BVSs for Sr at A-site and transition metal ions at B/B'-sites (B is the transition metal ion at 4*b* in cubic or 3*b* in trigonal or 2*a* in tetragonal or 2*a* in monoclinic structure; B' is the transition metal ion at 4*a* in cubic or 3*a* in trigonal or 2*b* in tetragonal or 2*d* in monoclinic structure) are also listed in **Table 5.9**. The BVS for Sr in each sample is always closed to divalent. But for the transition metal ions at B/B' sites, the situation becomes more complicated. For the end points, the BVSs for Cr, Ni and Os are nearly comparable with expected values. The Cr and Os are 3+ and 5+ in  $\text{Sr}_2\text{CrOsO}_6$  while Ni and Os are 2+ and 6+ in  $\text{Sr}_2\text{NiOsO}_6$ . Because of Cr and Ni showing different valence states in the end points sample, it may cause potential complexities of identifying valence states for substitutional series samples. Unsurprisingly, the complexities were confirmed from the calculation of BVSs for Cr/Os at B/B' especially for the 50% substitutional sample  $\text{Sr}_2\text{Cr}_{0.5}\text{Ni}_{0.5}\text{OsO}_6$ . The BVSs for Cr in

$\text{Sr}_2\text{Cr}_{0.5}\text{Ni}_{0.5}\text{OsO}_6$  were calculated from the bond-valence parameters of  $\text{Cr}^{3+}$  and  $\text{Cr}^{2+}$  respectively, both of these BVSs are shown in the **Table 5.9**, however, neither of them is closed to the expectation. The bond-valence parameters of  $\text{Os}^{5+}$  and  $\text{Os}^{6+}$  are used to deduce the BVSs for Os on B' site of  $\text{Sr}_2\text{Cr}_{0.5}\text{Ni}_{0.5}\text{OsO}_6$ . The difficulty to distinguish the valence state at B sites through BVS calculation is likely caused by three different transition metal ions mixing at the same position. The average length for B-O and B'-O bonds above the  $T_m$  are shown in **Fig. 5.8**. The B'-O bonds in  $\text{Sr}_2\text{Cr}_{1-x}\text{Ni}_x\text{OsO}_6$  ( $x = 0$  and  $0.25$ ) are longer than that in  $\text{Sr}_2\text{Cr}_{1-x}\text{Ni}_x\text{OsO}_6$  ( $x = 0.5, 0.75$  and  $1$ ), which may indicate the valence state of Os metal ion increases with the transition from cubic to tetragonal structure. For comparison, the average length of B'-O bonds in  $\text{Sr}_2\text{CrOsO}_6$  reported previously is  $1.955 \text{ \AA}$  at room temperature [9]. The Os-O bond length of our  $\text{Sr}_2\text{CrOsO}_6$  sample is slightly shorter than the reported value either at  $750 \text{ K}$  ( $1.927 \text{ \AA}$ , cubic structure) or room temperature ( $1.928 \text{ \AA}$ , trigonal structure). The BVS for Os in  $\text{Sr}_2\text{CrOsO}_6$  is still close to pentavalent, although the bond length is slightly shorter than the  $\text{Os}^{5+}$ -O bonds in reported previously  $\text{Sr}_2\text{FeOsO}_6$  ( $1.996 \text{ \AA}$ ) [22],  $\text{Sr}_2\text{ScOsO}_6$  ( $1.96 \text{ \AA}$ ) [23],  $\text{Ba}_2\text{YOsO}_6$  ( $1.961 \text{ \AA}$ ) [24] and  $\text{Pr}_2\text{NaOsO}_6$  ( $1.968 \text{ \AA}$ ) [25]. Furthermore, the Os-O bond length of  $\text{Sr}_2\text{Cr}_{0.75}\text{Ni}_{0.25}\text{OsO}_6$  is more closed to the average  $\text{Os}^{6+}$ -O bond length. The average  $\text{Os}^{6+}$ -O bond lengths were reported in some other double perovskite oxides such as  $\text{Ca}_2\text{CoOsO}_6$  ( $1.933 \text{ \AA}$ ) [26],  $\text{Sr}_2\text{CoOsO}_6$  ( $1.917 \text{ \AA}$ ) [17],  $\text{Ca}_2\text{NiOsO}_6$  ( $1.925 \text{ \AA}$ ) [16] and  $\text{Ba}_2\text{NiOsO}_6$  ( $1.943 \text{ \AA}$ ) [27]. Cr atoms locate at the center of octahedra in cubic structure of  $\text{Sr}_2\text{CrOsO}_6$  and they are coordinated with six Cr-O bonds with equal length. The undistorted octahedra suggests  $\text{Cr}^{2+}$  should be ruled out. The trivalent Cr can be deduced from the  $1.995(3) \text{ \AA}$  of Cr-O bond length that is close to average  $\text{Cr}^{3+}$ -O bond in simple or double perovskite oxides such as  $\text{BiCrO}_3$  ( $1.990 \text{ \AA}$ ),  $\text{ErCrO}_3$  ( $1.976 \text{ \AA}$ ) [28] and  $\text{Ca}_2\text{CrSbO}_6$  ( $1.986 \text{ \AA}$ ) [29]. Although the structure transfers from cubic or trigonal to tetragonal structure, the distortions of  $(\text{BO}_6)$  octahedra are subtle and the average B-O bond lengths increases to  $2.056 \text{ \AA}$  with the 50% substitution of Cr

by Ni. Resulted from the mixture of Cr and Ni at B sites, the bond length of B-O should be the balanced result between Cr-O with Ni-O. The length of Ni-O in another end point  $\text{Sr}_2\text{NiOsO}_6$  and is comparable to  $\text{Sr}_2\text{NiOsO}_6$  or  $\text{Ca}_2\text{NiOsO}_6$  reported previously [16], which are consistent with the BVSs of Ni. Similarly, the BVSs for Ni in substitutional series  $\text{Sr}_2\text{Cr}_{1-x}\text{Ni}_x\text{OsO}_6$  ( $x = 0.5, 0.75$ ) are 2.03 and 2.05 respectively. In contrast, the BVSs for Cr are still tricky. To identify the exact valence states for Cr, Ni and Os in  $\text{Sr}_2\text{Cr}_{1-x}\text{Ni}_x\text{OsO}_6$  ( $x = 0.25, 0.5$  and  $0.75$ ) still requires additional measurement.

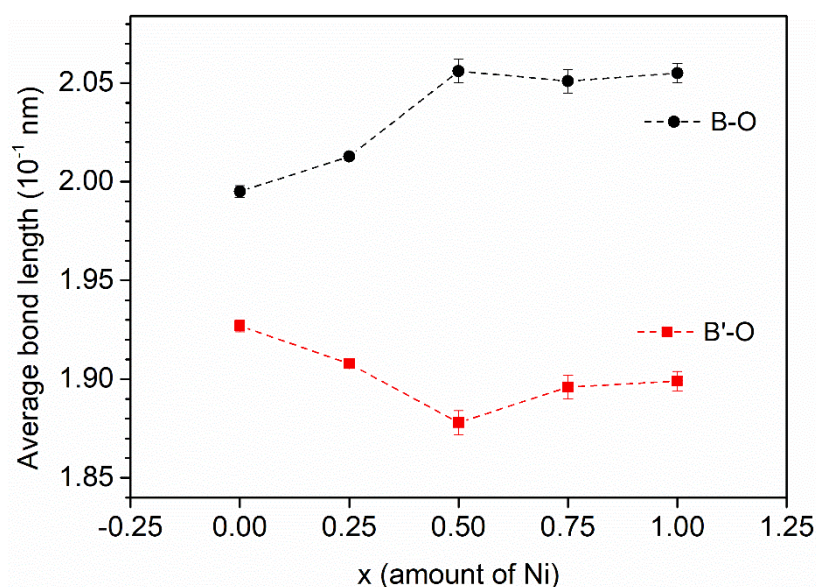


**Fig. 5.8** Average bond length of B-O and B'-O in  $\text{Sr}_2\text{Cr}_{1-x}\text{Ni}_x\text{OsO}_6$  ( $x = 0, 0.25, 0.5, 0.75$  and  $1$ ), estimated from structure refinement above their own  $T_m$ .



**Table 5.9** Comparison of the Lattice and Structural Parameters of the series  $\text{Sr}_2\text{Cr}_{1-x}\text{Ni}_x\text{OsO}_6$  ( $x = 0, 0.25, 0.5, 0.75$  and  $1$ )

	$x = 0$ (750 K)	$x = 0.25$ (550 K)	$x = 0.5$ (454 K)	$x = 0.75$	$x = 1$
Space group	$Fm -3m$	$Fm -3m$	$I4/m$	$I4/m$	$I4/m$
$a$ (Å)	7.84460(5)	7.84115(3)	5.5475(2)	5.5341(2)	5.5320(2)
$c$ (Å)			7.8580(2)	7.9247(3)	7.9204(3)
$d_{\text{calcd}}$ (g/cm <sup>3</sup> )	7.149	7.185	7.138	7.094	7.127
$R_{\text{wp}}$ (%)	1.942	1.785	1.808	2.184	2.376
$R_{\text{p}}$ (%)	1.335	1.218	1.222	1.403	1.480
$R_{\text{B}}$ (%)	0.831	0.730	0.906	0.838	0.908
$R_{\text{F}}$ (%)	0.430	0.348	0.424	0.344	0.426
B-O1 (Å)	$1.995(3) \times 6$	$2.0128(16) \times 6$	$2.075(6) \times 2$	$2.056(5) \times 2$	$2.060(6) \times 2$
B-O2 (Å)			$2.046(6) \times 4$	$2.048(6) \times 4$	$2.053(5) \times 4$
B'-O1 (Å)	$1.927(3) \times 6$	$1.9078(16) \times 6$	$1.854(6) \times 2$	$1.907(5) \times 2$	$1.900(6) \times 2$
B'-O2 (Å)			$1.890(6) \times 4$	$1.891(6) \times 4$	$1.899(5) \times 4$
B-O1-B' (deg)	180.0	180.0	180.0	180.0	180.0
B-O2-B' (deg)			170.4(4)	166.8(4)	163.5(3)
Average (deg)	180.0	180.0	175.2(4)	173.4(4)	171.8(3)
Atom	BVS				
Sr	2.04	2.04	2.08	2.11	2.18
Cr at B-site	2.88	2.75	2.45/2.49	2.48/2.52	
Ni at B-site		2.28	2.03	2.05	2.03
Os at B'-site	5.14	5.42/5.94	5.88/6.44	5.59/6.13	6.08

	x = 0 (RT)	x = 0.25 (RT)	x = 0.5 (RT)
Space group	<i>R</i> -3	<i>R</i> -3	<i>I</i> 12/ <i>m</i> 1
<i>a</i> (Å)	5.5147(12)	5.5566(3)	5.5365(8)
<i>b</i> (Å)			5.5422(7)
<i>c</i> (Å)	13.4879(2)	13.5674(5)	7.851(10)
<i>d</i> <sub>calcd</sub> (g/cm <sup>3</sup> )	7.286	7.161	7.172
<i>R</i> <sub>wp</sub> (%)	1.863	1.854	2.858
<i>R</i> <sub>p</sub> (%)	1.320	1.250	1.565
<i>R</i> <sub>B</sub> (%)	0.714	0.753	1.343
<i>R</i> <sub>F</sub> (%)	0.314	0.370	0.743
B-O1 (Å)	1.987(6)	2.021(3)	2.048(16) ×2
B-O2 (Å)			2.046(10) ×4
B'-O1 (Å)	1.928(6)	1.916(3)	1.891(16) ×2
B'-O2 (Å)			1.922(9) ×4
B-O1-B' (deg)	169.0(4)	170.9(4)	170.6(7)
B-O2-B' (deg)			161.6(5)
Average (deg)	169.0(4)	170.9(4)	166.1(6)
Atom	BVS		
Sr	2.27	2.11	2.28
Cr at B-site	2.95	2.69	2.51/2.55
Ni at B-site		2.23	2.08
Os at B'-site	5.13	5.30/5.81	5.37/5.88

BVS =  $\sum_{i=1}^N v_i$ , where  $v_i = e^{(R_0 - l_i)/B}$ , *N* is the coordination number, *l* is the bond length, *B* = 0.37 [30],  $R_0(\text{Sr}^{2+}) = 2.118$  [30],  $R_0(\text{Cr}^{3+}) = 1.724$  [30],  $R_0(\text{Cr}^{2+}) = 1.73$  [30],  $R_0(\text{Ni}^{2+}) = 1.654$  [30],  $R_0(\text{Os}^{5+}) = 1.87$  [31, 32], and  $R_0(\text{Os}^{6+}) = 1.904$  [33]. The BVS for Cr before the slash is calculated from  $R_0(\text{Cr}^{3+})$ , the latter one is calculated from  $R_0(\text{Cr}^{2+})$ . The BVS for Os before the slash is calculated from  $R_0(\text{Os}^{5+})$ , the latter one is calculated from  $R_0(\text{Os}^{6+})$ .

The temperature dependence of  $\rho$  for  $\text{Sr}_2\text{Cr}_{1-x}\text{Ni}_x\text{OsO}_6$  (*x* = 0, 0.25, 0.5, 0.75 and 1) is

shown in **Fig. 5.9**. The resistivity ( $\rho$ ) for each sample continuously increases upon cooling, which is an indicative of the insulating behavior. At room temperature, the resistivities of  $\text{Sr}_2\text{Cr}_{1-x}\text{Ni}_x\text{OsO}_6$  ( $x = 0, 0.25, 0.5, 0.75$  and  $1$ ) are  $0.98, 0.37, 1.36, 128.01$  and  $43.51 \text{ } \Omega \text{ cm}$  respectively. The order of magnitude of the observed values of  $0.98 \text{ } \Omega \text{ cm}$  for  $\text{Sr}_2\text{CrOsO}_6$  is smaller than the value of  $8.6 \times 10^2 \text{ } \Omega \text{ cm}$  or  $10 \text{ } \Omega \text{ cm}$  reported previously by different groups for  $\text{Sr}_2\text{CrOsO}_6$  [6, 9]. The grain boundaries play a key role in measuring the resistivity of polycrystalline samples, which may cause the distinction between different  $\text{Sr}_2\text{CrOsO}_6$  samples. Among the substitutional series samples, the resistivities of  $\text{Sr}_2\text{Cr}_{1-x}\text{Ni}_x\text{OsO}_6$  ( $x = 0, 0.25$  and  $0.5$ ) are smaller than  $\text{Sr}_2\text{Cr}_{1-x}\text{Ni}_x\text{OsO}_6$  ( $x = 0.75$  and  $1$ ) at any temperatures and increases slower with cooling down. It indicates the intrinsic of these three samples  $\text{Sr}_2\text{Cr}_{1-x}\text{Ni}_x\text{OsO}_6$  ( $x = 0, 0.25$  and  $0.5$ ) should be more metallic than the other two Ni-rich samples. The two Cr-rich samples are cubic structure at temperatures above their  $T_c$  while Ni-rich samples  $\text{Sr}_2\text{Cr}_{1-x}\text{Ni}_x\text{OsO}_6$  ( $x = 0.75$  and  $1$ ) have distorted perovskite structure with the B-O2-B' bond deviating from  $180^\circ$  (see Table 5.9). This structural distortion may reduce the overlap between orbitals, resulting in Ni-rich samples show much poorer conductivity [2]. The Arrhenius law was applied to the  $T^{-1}$  scaled data of each sample over the high temperature range in order to estimate the activation energy ( $E_a$ ) from  $\rho = \rho_0 \exp(E_a/k_B T)$ , where  $\rho_0$  and  $k_B$  are a temperature-independent constant and the Boltzmann constant, respectively. The fitting to  $\text{Sr}_2\text{Cr}_{0.5}\text{Ni}_{0.5}\text{OsO}_6$  is shown by the solid line in **Fig. 5.10**. The comparison of  $E_a$  for the substitutional series samples is shown in the inset of **Fig. 5.9**. The activation energy increases with the substitution of Cr by Ni, confirming the conductivity is weakened by introducing Ni into B site. Variable range hopping (VRH) mechanism is expected at low temperatures, in which conduction occurs by hopping from localized centers. The electrical transport of  $\text{Sr}_2\text{Cr}_{0.5}\text{Ni}_{0.5}\text{OsO}_6$  on  $T^{-1/2}$  and  $T^{-1/4}$  scale is given in **Fig. 5.10**. The linear behavior on the  $T^{-1/2}$  scale is better than on the  $T^{-1/4}$  scale, in another word, the Efros-Shklovskii model gives a better

fit to the data of  $\text{Sr}_2\text{Cr}_{0.5}\text{Ni}_{0.5}\text{OsO}_6$  than Mott 3D model [34, 35]. It indicates a soft gap in the density of states near the Fermi level is created by Coulomb interaction [34]. Except  $\text{Sr}_2\text{CrOsO}_6$ , other four samples all show a better linear behavior on the  $T^{-1/2}$  scale rather than on the  $T^{-1/4}$  scale.

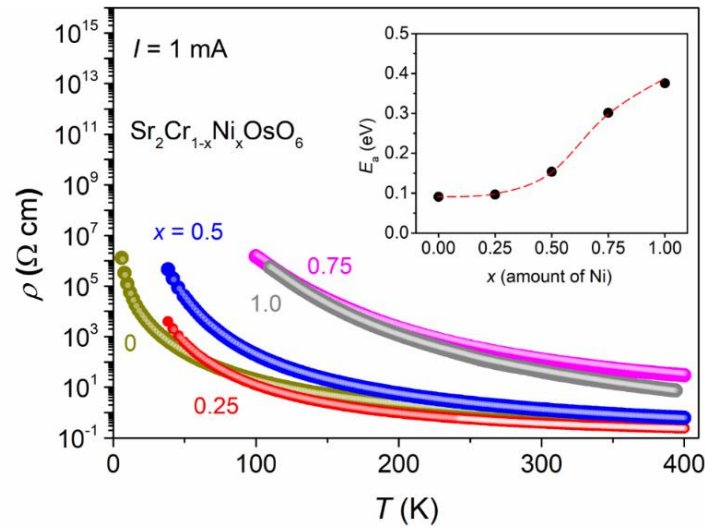


**Fig. 5.9** Temperature dependence of electrical resistivity for polycrystalline  $\text{Sr}_2\text{Cr}_{1-x}\text{Ni}_x\text{OsO}_6$  ( $x = 0, 0.25, 0.5, 0.75$  and  $1$ ) upon cooling (solid dot) and heating (open dot). The activation energy estimated from Arrhenius law for  $\text{Sr}_2\text{Cr}_{1-x}\text{Ni}_x\text{OsO}_6$  ( $x = 0, 0.25, 0.5, 0.75$  and  $1$ ). The dashed curve is a guide for eyes.

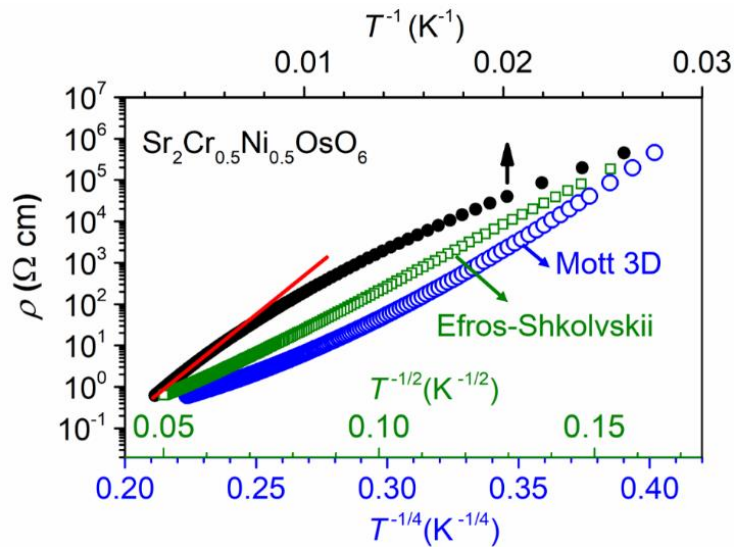


**Fig. 5.10** The alternative plots of the data. The red line indicates a fitting to the Arrhenius law in the high-temperature region for  $\text{Sr}_2\text{Cr}_{0.5}\text{Ni}_{0.5}\text{OsO}_6$ .

The temperature dependence of  $\chi$  in an applied magnetic field of 10 kOe is shown in **Fig. 5.11**. Because the transition temperatures of  $\text{Sr}_2\text{Cr}_{1-x}\text{Ni}_x\text{OsO}_6$  ( $x = 0, 0.25$  and  $0.5$ ) are higher than 400 K, the  $\chi(T)$  curves for these three samples were collected at higher temperature and the combined data shown in **Fig. 5.11 (a)**. Unlike  $\text{Sr}_2\text{Cr}_{1-x}\text{Ni}_x\text{OsO}_6$  ( $x = 0, 0.25$  and  $0.5$ ), the bifurcation of ZFC and FC magnetization were not observed in Ni-rich samples  $\text{Sr}_2\text{Cr}_{1-x}\text{Ni}_x\text{OsO}_6$  ( $x = 0.75$  and  $1$ ) and both of them show sharp peaks at 40 K, indicating a typical signature of antiferromagnetic order. We applied the Curie-Weiss law  $1/\chi = (T - \theta)/C$  to the high-temperature portion of the  $1/\chi - T$  curve (200- 400 K) for samples  $\text{Sr}_2\text{Cr}_{0.25}\text{Ni}_{0.25}\text{OsO}_6$  and  $\text{Sr}_2\text{NiOsO}_6$ . The best fitting gives the  $C$  (the Curie constant) of  $1.232(2) \text{ emu mol}^{-1} \text{ K}$  for  $\text{Sr}_2\text{Cr}_{0.25}\text{Ni}_{0.25}\text{OsO}_6$  and of  $1.362(17) \text{ K}$  for  $\text{Sr}_2\text{NiOsO}_6$ , resulting in the  $\theta$  (Weiss temperature) of  $46.4(6) \text{ K}$  for  $\text{Sr}_2\text{Cr}_{0.25}\text{Ni}_{0.25}\text{OsO}_6$  and of  $36.0(4) \text{ K}$  for  $\text{Sr}_2\text{NiOsO}_6$ . The effective magnetic moment ( $\mu_{\text{eff}}$ ) can be deduced from  $C$ , which are  $3.14 \mu_B$  for  $\text{Sr}_2\text{Cr}_{0.25}\text{Ni}_{0.25}\text{OsO}_6$  and  $3.30 \mu_B$  for  $\text{Sr}_2\text{NiOsO}_6$ . The theoretical spin-only moment of  $\text{Os}^{6+}$  and  $\text{Ni}^{2+}$  is  $4 \mu_B$  that is slightly larger than the observed value. The spin-orbit interaction may cause such underestimated  $\mu_{\text{eff}}$  value [36]. The high magnetic transition temperatures ( $T_m$ ) make it difficult to reach a linear  $\chi^{-1}$  vs  $T$  curve of  $\text{Sr}_2\text{Cr}_{1-x}\text{Ni}_x\text{OsO}_6$  ( $x = 0, 0.25$  and  $0.5$ ) above their  $T_m$  [see **Fig. 5.11 (b)**].

The magnetic transition temperatures for each sample were presented in the inset of **Fig. 5.11 (b)**, showing the  $T_m$  tends to decrease with the substitution of Cr by Ni. Sample  $\text{Sr}_2\text{CrOsO}_6$  shows the magnetic transition at 663 K, which is comparable to 660 K reported previously [9].  $\chi(T)$  curves of  $\text{Sr}_2\text{Cr}_{1-x}\text{Ni}_x\text{OsO}_6$  ( $x = 0, 0.25$  and  $0.5$ ) increase remarkably at their  $T_m$ , suggesting the occurrence of long-range magnetic ordering. The ferrimagnetism in double perovskites was thought to be driven by kinetic energy, which induces considerably high  $T_m$  in several cases [6, 37]. Electron doping was used to increase  $T_m$  in the double perovskite structures, for example, the  $T_m$  was increased by more than 100 K by  $\text{La}^{3+}$  doping in  $\text{LaSrFeMoO}_6$  and  $\text{LaCaCrWO}_6$  [13, 14]. Alternately, the higher  $T_m$  in  $\text{Sr}_2\text{BB}'\text{O}_6$  ( $B = \text{Cr}, B'$

= 5d transition metal) series can be achieved by replacement of 5d transition metal ion with more electrons, for instance, the  $T_m$  of  $\text{Sr}_2\text{CrWO}_6$  with  $\text{W}^{5+}$  ( $5d^1$ ),  $\text{Sr}_2\text{CrReO}_6$  with  $\text{Re}^{5+}$  ( $5d^2$ ) and  $\text{Sr}_2\text{CrOsO}_6$  with  $\text{Os}^{5+}$  ( $5d^3$ ) are 458 K [2], 635 K [3] and 660 K (from this study), respectively. In this study, the substitution of  $\text{Cr}^{3+}$  by  $\text{Ni}^{2+}$  partially leads to a part of  $\text{Os}^{5+}$  ( $5d^3$ ) replaced by  $\text{Os}^{6+}$  ( $5d^2$ ) corresponding to BVSS for Os in  $\text{Sr}_2\text{Cr}_{1-x}\text{Ni}_x\text{OsO}_6$  ( $x = 0, 0.25$  and  $0.5$ ), resulting in the decrease of  $T_m$  until  $x = 0.5$ .

The non-monotonic magnetic susceptibility of either ZFC or FC with the decrease of temperature can be clearly discerned in our high-pressure prepared  $\text{Sr}_2\text{CrOsO}_6$  sample, which is caused by the different temperature evolution of the magnetic moment for Os and Cr sublattice [9]. The similar phenomena are not obvious in the  $M$ - $T$  curves of the substitutional Cr-rich samples. It is notable that  $\text{Sr}_2\text{Cr}_{0.5}\text{Ni}_{0.5}\text{OsO}_6$  shows much higher FC magnetization at low temperature than any others, which is in good agreement with isothermal magnetization measurement.

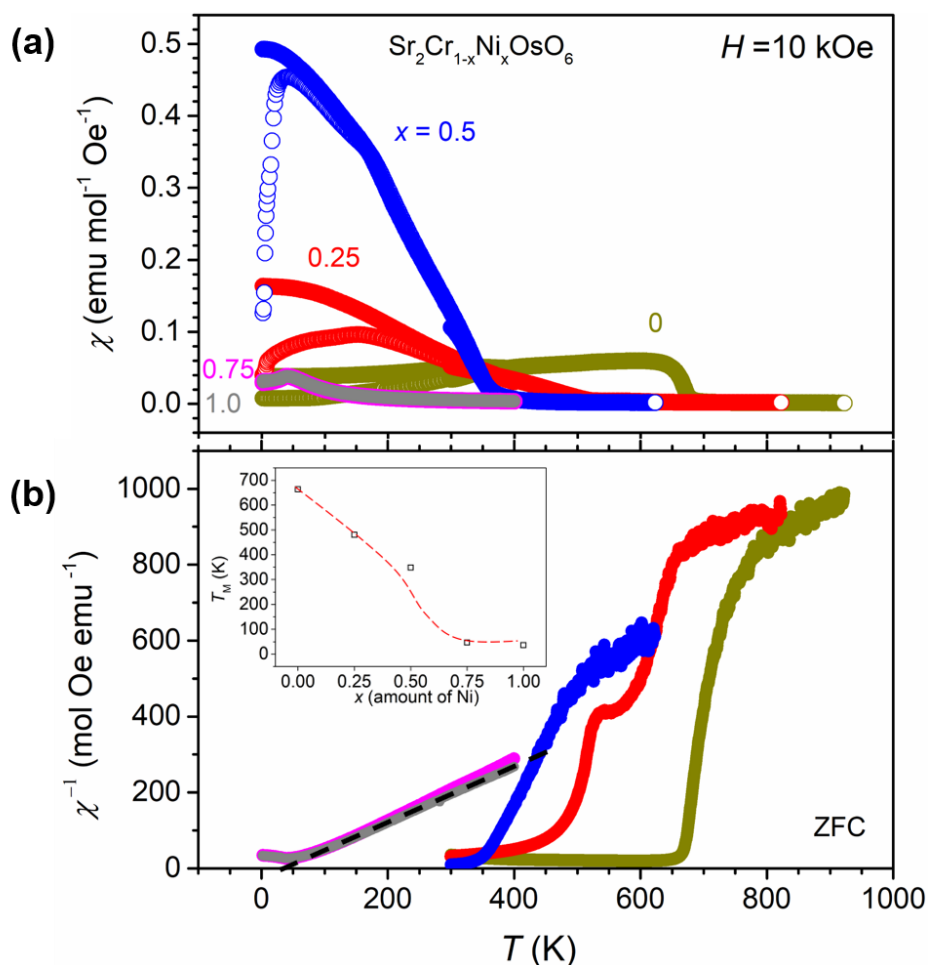


**Fig. 5.11** (a) Temperature dependence of ZFC (open dot) and FC (solid dot) susceptibilities ( $H = 10$  kOe) for  $\text{Sr}_2\text{Cr}_{1-x}\text{Ni}_x\text{OsO}_6$  ( $x = 0, 0.25, 0.5, 0.75$  and  $1$ ). (b) Alternative plots of the ZFC data for fitting to the Curie-Weiss law. The fitting is shown by black broken line. The inset is the magnetic transition temperature of  $\text{Sr}_2\text{Cr}_{1-x}\text{Ni}_x\text{OsO}_6$  ( $x = 0, 0.25, 0.5, 0.75$  and  $1$ ) and the red dashed curve is a guide for eyes.

Isothermal magnetization of each of these substitutional series at 5 K shown in **Fig. 5.12(a)**. A linear behavior was observed in the curves of two Ni-rich samples ( $x = 0.75$  and  $1$ ), while the samples with  $x = 0, 0.25$  and  $0.75$  all exhibit hysteresis, which are consistent with the ZFC and FC magnetization for each of sample. With the substitution of Ni for Cr, the electronic configuration ( $3d^3-5d^3$ ) of  $\text{Sr}_2\text{CrOsO}_6$  changes to electronic configuration ( $3d^8-5d^2$ ) of  $\text{Sr}_2\text{NiOsO}_6$  progressively, correspondingly, magnetism transfers from ferrimagnet to antiferromagnet. The spontaneous magnetizations are recorded in **Fig. 5.12(b)**. The value is improved by substituting of Ni for Cr and reaches the maximum when  $x = 0.5$ . The saturation

magnetization decreases with replacement of Ni by Cr was also observed in Cr-substituted nickel ferrite [38]. This might be ascribed to the diamagnetic nature of the  $\text{Cr}^{3+}$ .

The intermediated Ni-substituted sample  $\text{Sr}_2\text{Cr}_{0.5}\text{Ni}_{0.5}\text{OsO}_6$  possesses the highest saturated magnetization amongst this substitutional series. The saturated magnetization for  $\text{Sr}_2\text{Cr}_{0.5}\text{Ni}_{0.5}\text{OsO}_6$  is estimated to be  $\sim 1.2 \mu_B/\text{mol}$  from **Fig. 5.12(a)**. The ferromagnetic ordering below  $T_m$  is precluded for  $\text{Sr}_2\text{Cr}_{0.5}\text{Ni}_{0.5}\text{OsO}_6$  since the value of  $1.2 \mu_B/\text{mol}$  is still much smaller than the saturated magnetization of  $2.3 \mu_B/\text{mol}$  observed experimentally in the ferromagnetic material  $\text{Ba}_2\text{NiOsO}_6$  [39]. The end points samples,  $\text{Sr}_2\text{CrOsO}_6$  and  $\text{Sr}_2\text{NiOsO}_6$ , were assigned as ferrimagnetic and antiferromagnetic respectively by neutron powder diffraction studies [9, 16]. The magnetic ground state for  $\text{Sr}_2\text{Cr}_{0.5}\text{Ni}_{0.5}\text{OsO}_6$  or  $\text{Sr}_2\text{Cr}_{0.75}\text{Ni}_{0.25}\text{OsO}_6$  can be deduced to be ferrimagnetic or closely similar state. Spin-orbit coupling (SOC) plays a pivotal role in  $5d^3$  cases, allowing a small but non-negligible orbital contribution to both  $\text{Sr}_2\text{CrOsO}_6$  and  $\text{Ca}_2\text{CrOsO}_6$  [9]. Since the orbital contribution is involved in, magnetic moment on Os is reduced which the magnetic moment of spin-up and spin-down is not same. Samples  $\text{Sr}_2\text{Cr}_{1-x}\text{Ni}_x\text{OsO}_6$  ( $x = 0, 0.25$  and  $0.5$ ) are ferrimagnetic rather than antiferromagnetic, which are due to the SOC effect. In contrast, fully compensated magnetism occurs in  $\text{Sr}_2\text{Cr}_{1-x}\text{Ni}_x\text{OsO}_6$  ( $x = 0.75$  and  $1$ ). Since  $\text{Os}^{5+} (5d^3)$  is replaced by  $\text{Os}^{6+} (5d^2)$  with the substitution of Cr, SOC effect is weakened, which may cause the magnetic ground state jumps from ferrimagnetic to antiferromagnetic with the increase content of Ni from  $0.5$  to  $0.75$ .

A related double perovskite  $\text{Ca}_2\text{NiOsO}_6$  adopts a canted antiferromagnetic ordering below  $175 \text{ K}$  confirming with neutron diffraction measurement [16], the saturation magnetization for  $\text{Ca}_2\text{NiOsO}_6$  is only  $0.5 \mu_B/\text{mol}$ . A similar saturated magnetization of  $0.52 \mu_B/\text{mol}$  is observed experimentally in a double perovskite  $\text{Lu}_2\text{NiIrO}_6$  [40]. The saturation magnetization of another perovskite-structure oxide  $\text{La}_3\text{Ni}_2\text{SbO}_9$  is  $1.6 \mu_B/\text{mol}$ , which is contributed by two  $\text{Ni}^{2+}$ , in another word,  $0.8 \mu_B$  is contributed by per  $\text{Ni}^{2+}$  equally.



Ferrimagnetic ordering was proposed for both  $\text{La}_3\text{Ni}_2\text{SbO}_9$  and  $\text{Lu}_2\text{NiIrO}_6$  below  $T_m$ . Compared to these related compounds and  $\text{Sr}_2\text{Cr}_{1-x}\text{Ni}_x\text{OsO}_6$  ( $x = 0$  and  $0.25$ ), the enhancement of saturation magnetization for  $\text{Sr}_2\text{Cr}_{0.5}\text{Ni}_{0.5}\text{OsO}_6$  is significant. When 50% of B sites are occupied by Ni, the cubic structure is broken and  $\text{Sr}_2\text{Cr}_{0.5}\text{Ni}_{0.5}\text{OsO}_6$  crystallizes into a tetragonal structure. Accordingly, average B-O-B' bond angles deviate from  $180^\circ$  slightly (see **Table 5.9**). An analogous magnetism change induced by structural transition has been observed for  $A_2\text{NiOsO}_6$  ( $A = \text{Ca}, \text{Sr}, \text{Ba}$ ), wherein the lattice symmetry is decided by the size of  $A$  [39]. However, the Ni-substituted  $\text{Sr}_2\text{Cr}_{0.25}\text{Ni}_{0.75}\text{OsO}_6$  maintains the same symmetric lattice as  $\text{Sr}_2\text{Cr}_{0.5}\text{Ni}_{0.5}\text{OsO}_6$ , the net magnetic moment is not even present. The structural transition plays a minor role in the change of magnetic property for this case. According to current studies, the physical nature of  $\text{Sr}_2\text{Cr}_{0.5}\text{Ni}_{0.5}\text{OsO}_6$  remain elusive so far. To settle this open question, more measurements are required to carry on. For example, neutron diffraction and X-ray magnetic circular dichroism (XMCD) measurements may offer possibilities for distinguishing the effect of SOC on the magnetic properties of  $\text{Sr}_2\text{Cr}_{1-x}\text{Ni}_x\text{OsO}_6$  ( $x = 0, 0.25$  and  $0.5$ ). The first-principle calculation for the ordered phase of  $\text{Sr}_2\text{Cr}_{0.5}\text{Ni}_{0.5}\text{OsO}_6$  is shown in **Fig. 5.13**. In the band structure of ordered  $\text{Sr}_2\text{Cr}_{0.5}\text{Ni}_{0.5}\text{OsO}_6$  with tetragonal structure, the Fermi level lies in the spin-down bands, suggesting the compensated half metal property [1]. A possible reason why the insulating rather than half metal behavior was observed from **Fig. 5.9** is the disordered occupation at  $2a$  sites. It should be noted that the strength of the SOC has not been measured from the calculation. The effect of SOC on opening a gap will be considered in the further study.

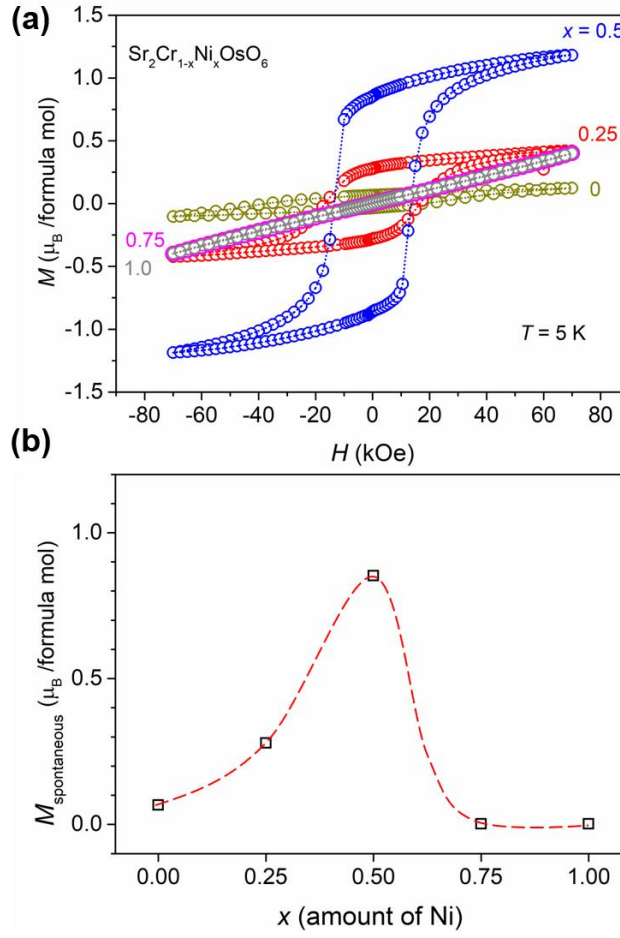


**Fig. 5.12** (a) Isothermal magnetization of  $\text{Sr}_2\text{Cr}_{1-x}\text{Ni}_x\text{OsO}_6$  ( $x = 0, 0.25, 0.5, 0.75$  and  $1$ ) at  $5$  K. (b) The spontaneous magnetization of  $\text{Sr}_2\text{Cr}_{1-x}\text{Ni}_x\text{OsO}_6$  ( $x = 0, 0.25, 0.5, 0.75$  and  $1$ ) at  $5$  K deduced from the  $M$ - $H$  data. The broken curve is a guide for eyes.

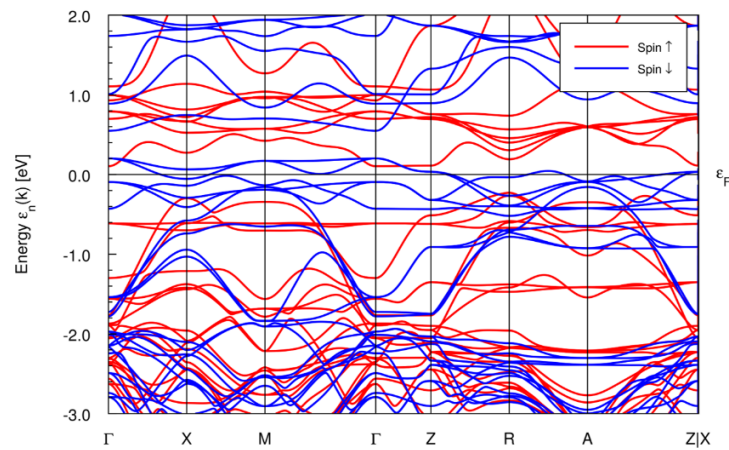


**Fig. 5.13** Band structure of the tetragonal ordered phase of  $\text{Sr}_2\text{Cr}_{0.5}\text{Ni}_{0.5}\text{OsO}_6$  within GGA (red: spin up; blue: spin down)

The temperature dependence of  $C_p$  for each sample is plotted in **Fig. 5.14**. There is no anomaly observed in any samples, which is indicative of a bulk transition, over the range of 2-300 K. The low-temperature region is plotted in the  $C_p/T$  vs.  $T^2$  form in the inset of **Fig. 5.14**. An approximated Debye model ( $C_p/T = \gamma + \beta_0 T^2$ ) was applied for samples  $\text{Sr}_2\text{Cr}_{1-x}\text{Ni}_x\text{OsO}_6$  ( $x = 0, 0.25$  and  $0.5$ ) while the plots of  $C_p/T$  vs.  $T^2$  for  $\text{Sr}_2\text{Cr}_{0.25}\text{Ni}_{0.75}\text{OsO}_6$  and  $\text{Sr}_2\text{NiOsO}_6$  deviate from linear behavior. The linear fitting on the data of  $\text{Sr}_2\text{Cr}_{0.5}\text{Ni}_{0.5}\text{OsO}_6$  gives a Sommerfeld coefficient ( $\gamma$ ) of  $3.9(17) \times 10^{-3} \text{ J mol}^{-1} \text{ K}^{-2}$  and the constant  $\beta_0$  of  $5.50(18) \times 10^{-4} \text{ J mol}^{-1} \text{ K}^{-4}$ . The Debye temperature was calculated from  $\beta_0$  to be 327.9(4) K. These values are listed in **Table 5.10**.

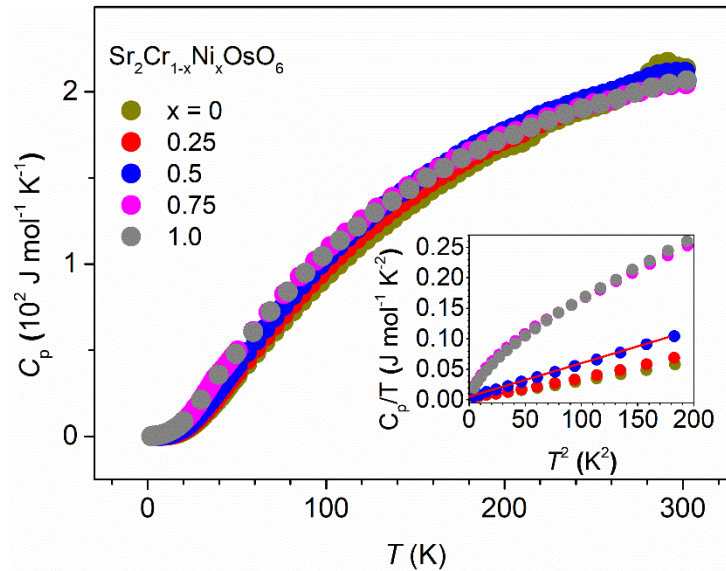


**Fig. 5.14** Temperature dependence of specific heat for  $\text{Sr}_2\text{Cr}_{1-x}\text{Ni}_x\text{OsO}_6$  ( $x = 0, 0.25, 0.5, 0.75$  and  $1$ ). The upper axis corresponds to the Dulong-Petit limit of the lattice specific heat. (Inset) Linear fit to the  $C_p/T$  vs.  $T^2$  curve for the low-temperature region for  $\text{Sr}_2\text{Cr}_{0.5}\text{Ni}_{0.5}\text{OsO}_6$ .

**Table 5.10** Comparison of the Sommerfeld coefficient ( $\gamma$ ), the constant  $\beta_0$  and Debye temperature of  $\text{Sr}_2\text{Cr}_{1-x}\text{Ni}_x\text{OsO}_6$  ( $x = 0, 0.25$  and  $0.5$ ) estimated from Debye model.

	$\text{Sr}_2\text{CrOsO}_6$	$\text{Sr}_2\text{Cr}_{0.75}\text{Ni}_{0.25}\text{OsO}_6$	$\text{Sr}_2\text{Cr}_{0.5}\text{Ni}_{0.5}\text{OsO}_6$
$\gamma (\times 10^{-3} \text{ J mol}^{-1} \text{ K}^{-2})$	2.6(4)	1.5(6)	3.9(17)
$\beta_0 (\times 10^{-4} \text{ J mol}^{-1} \text{ K}^{-4})$	2.94(4)	3.55(6)	5.50(18)
Debye $T$ . (K)	404(18)	379(2)	327.9(4)

## 5.4 Summary of chapter 5

The substitutional series samples of  $\text{Sr}_2\text{Cr}_{1-x}\text{Ni}_x\text{OsO}_6$  ( $x = 0, 0.25, 0.5, 0.75$  and  $1$ ) were synthesized successfully. The cubic structure is retained when 25% Cr atoms are replaced by Ni, since then, more substitution of Cr triggers cubic perovskite structure distort to tetragonal structure until substituted fully by Ni. Due to  $\text{Sr}_2\text{Cr}_{1-x}\text{Ni}_x\text{OsO}_6$  ( $x = 0, 0.25, 0.5$ ) show net magnetic moments below  $T_c$ , structures of these three samples changes to a lower symmetric lattice. The following discussion about the structure of each sample will be based on the synchrotron XRD measurements above their magnetic transition temperature. Structural comparison of Ni-substituted samples  $\text{Sr}_2\text{Cr}_{1-x}\text{Ni}_x\text{OsO}_6$  ( $x = 0, 0.25, 0.5$ ) are shown in **Fig. 5.15**. Compared to cubic crystal structure of  $\text{Sr}_2\text{CrOsO}_6$  and  $\text{Sr}_2\text{Cr}_{0.75}\text{Ni}_{0.25}\text{OsO}_6$ , other than octahedral tilting appears in tetragonal lattices of  $\text{Sr}_2\text{Cr}_{1-x}\text{Ni}_x\text{OsO}_6$  ( $x = 0.5$  and  $1$ ), the reduction in the B-O-B' bond angle from  $180^\circ$  in  $\text{Sr}_2\text{CrOsO}_6$  and  $\text{Sr}_2\text{Cr}_{0.75}\text{Ni}_{0.25}\text{OsO}_6$  to an average of  $171.8(8)^\circ$  in  $\text{Sr}_2\text{NiOsO}_6$  is observed. In general, the structural variation seems to have a large impact on the electronic and magnetic properties. But for this series substitutional samples, the structural transition is not the dominant reason driving either electronic or magnetic properties. Here exists more complicated physical mechanism may account for it, but it so far beyond our current research.

The electronic and magnetic properties of  $\text{Sr}_2\text{Cr}_{1-x}\text{Ni}_x\text{OsO}_6$  ( $x = 0, 0.25, 0.5, 0.75$  and

1) are summarized in **Table 5.11**, compared with several related half-metallic compounds. Although all of these samples show the semiconducting behavior from the temperature dependence of resistivity measurements, the values for  $\text{Sr}_2\text{Cr}_{1-x}\text{Ni}_x\text{OsO}_6$  ( $x = 0, 0.25$  and  $0.5$ ) are 1-2 orders of magnitude smaller than two Ni-rich samples. For the variation of magnetic properties, the 50% Ni-substituted sample  $\text{Sr}_2\text{Cr}_{0.5}\text{Ni}_{0.5}\text{OsO}_6$  shows the largest magnetization value of  $1.2 \mu_B/\text{mol}$  among the series samples along with a lower  $T_c$  (348 K), but it is still above room temperature. Same as typical antiferromagnetic material  $\text{Sr}_2\text{NiOsO}_6$ ,  $\text{Sr}_2\text{Cr}_{0.25}\text{Ni}_{0.75}\text{OsO}_6$  does not show hysteresis loop even at 5 K. A remarkable phenomenon is that  $\text{Sr}_2\text{Cr}_{0.5}\text{Ni}_{0.5}\text{OsO}_6$  crystallizes into the same tetragonal structure as  $\text{Sr}_2\text{NiOsO}_6$  or  $\text{Sr}_2\text{Cr}_{0.25}\text{Ni}_{0.75}\text{OsO}_6$ , but the magnetic property of  $\text{Sr}_2\text{Cr}_{0.5}\text{Ni}_{0.5}\text{OsO}_6$  is more closed to the ferrimagnetic  $\text{Sr}_2\text{CrOsO}_6$  and  $\text{Sr}_2\text{Cr}_{0.75}\text{Ni}_{0.25}\text{OsO}_6$  with cubic structure. In addition, the saturated magnetization is enhanced in  $\text{Sr}_2\text{Cr}_{0.5}\text{Ni}_{0.5}\text{OsO}_6$ .  $\text{Sr}_2\text{Cr}_{0.5}\text{Ni}_{0.5}\text{OsO}_6$  offers ample possibilities for the design of high-  $T_c$  ferrimagnetic materials.

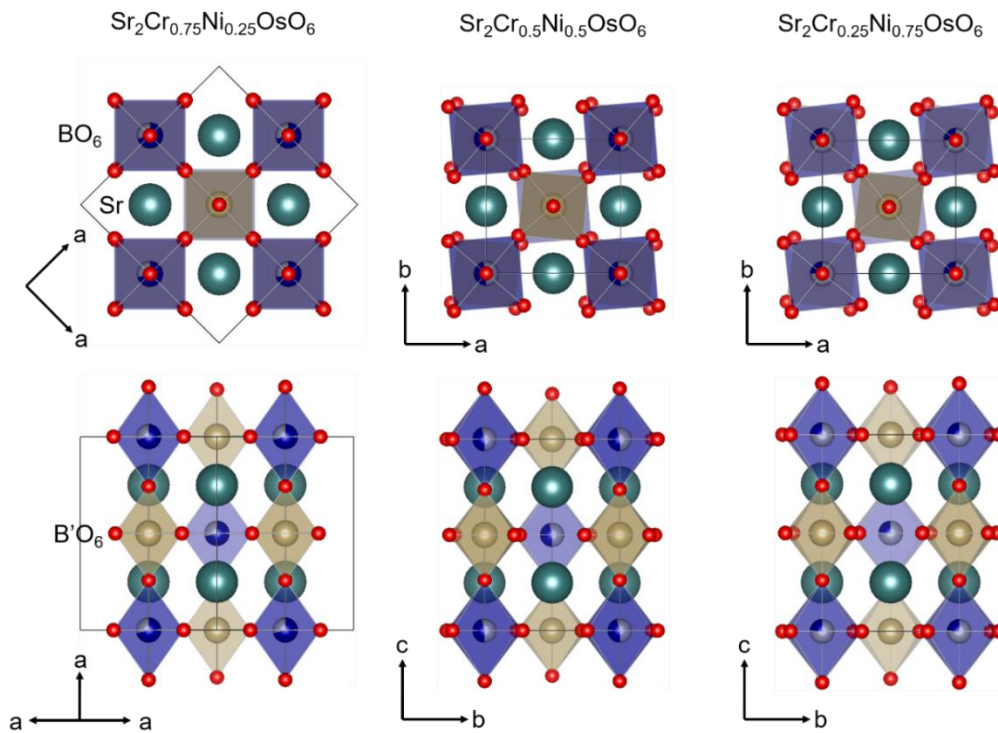


**Fig. 5.15** Structural comparison of  $\text{Sr}_2\text{Cr}_{1-x}\text{Ni}_x\text{OsO}_6$  ( $x = 0.25, 0.5$  and  $0.75$ ). The

crystal structure changes from cubic ( $Fm-3m$ ) structure of  $x = 0.25$  to tetragonal ( $I4/m$ ) structure of  $x = 0.5$  and  $0.75$ . bluish and brown octahedra represent  $BO_6$  and  $B'O_6$ . Cr, Ni and Os atoms are denoted as blue, silver and brown balls. The grey squares are the boundaries of single unit cell. Structures of  $Sr_2Cr_{1-x}Ni_xOsO_6$  ( $x = 0.25, 0.5$ ) shown here are the structure above  $T_c$ .

**Table 5.11** Comparison of the magnetic and transport properties for  $Sr_2Cr_{1-x}Ni_xOsO_6$  ( $x = 0, 0.25, 0.5, 0.75$  and  $1$ ) and several half-metallic compounds.  $\rho_{298\text{ K}}$ ,  $T_m$  and  $M_s$  are resistivity at 298 K, magnetic transition temperature and saturation magnetization, respectively.

Compound	$\rho_{298\text{ K}}$ ( $\Omega\text{ cm}$ )	$T_m$ (K)	$M_s$ ( $\mu_B/\text{f.u.}$ )	Reference
$Sr_2CrOsO_6$	$9.8 \times 10^{-1}$	663	$\sim 0.13$	[6] [9] and this work
$Sr_2Cr_{0.75}Ni_{0.25}OsO_6$	$3.7 \times 10^{-1}$	480	0.4	This work
$Sr_2Cr_{0.5}Ni_{0.5}OsO_6$	$1.4 \times 10^0$	348	1.2	This work
$Sr_2Cr_{0.25}Ni_{0.75}OsO_6$	$1.3 \times 10^2$	46		This work
$Sr_2NiOsO_6$	$4.4 \times 10^1$	36		[16] and this work
$Sr_2FeMoO_6$	$8 \times 10^{-3}$	420	3.1	[1]
$Sr_2CrMoO_6$	$8 \times 10^{-2}$	$\sim 300$	0.5	[5]
$Sr_2CrWO_6$	$\sim 1.1 \times 10^2$	458	1.1	[2]
$Sr_2CrReO_6$	$10^{-3}-10^{-2}$	635	0.86	[41]

## References in chapter 5

- [1] K.-I. Kobayashi, T. Kimura, H. Sawada, K. Terakura, Y. Tokura, Room-temperature magnetoresistance in an oxide material with an ordered double-perovskite structure, *Nature* 395(6703) (1998) 677.
- [2] J. Philipp, P. Majewski, L. Alff, A. Erb, R. Gross, T. Graf, M. Brandt, J. Simon, T. Walther, W. Mader, Structural and doping effects in the half-metallic double perovskite  $A_2CrWO_6$  ( $A = \text{Sr, Ba, and Ca}$ ), *Physical Review B* 68(14) (2003) 144431.

- [3] H. Kato, T. Okuda, Y. Okimoto, Y. Tomioka, Y. Takenoya, A. Ohkubo, M. Kawasaki, Y. Tokura, Metallic ordered double-perovskite  $\text{Sr}_2\text{CrReO}_6$  with maximal Curie temperature of 635 K, *Applied physics letters* 81(2) (2002) 328-330.
- [4] J. De Teresa, D. Serrate, C. Ritter, J. Blasco, M. Ibarra, L. Morellon, W. Tokarz, Investigation of the high Curie temperature in  $\text{Sr}_2\text{CrReO}_6$ , *Physical Review B* 71(9) (2005) 092408.
- [5] Y. Moritomo, S. Xu, A. Machida, T. Akimoto, E. Nishibori, M. Takata, M. Sakata, Electronic structure of double-perovskite transition-metal oxides, *Physical Review B* 61(12) (2000) R7827.
- [6] Y. Krockenberger, K. Mogare, M. Reehuis, M. Tovar, M. Jansen, G. Vaitheeswaran, V. Kanchana, F. Bultmark, A. Delin, F. Wilhelm,  $\text{Sr}_2\text{CrOsO}_6$ : End point of a spin-polarized metal-insulator transition by 5d band filling, *Physical Review B* 75(2) (2007) 020404.
- [7] K.-W. Lee, W. Pickett, Half semimetallic antiferromagnetism in the  $\text{Sr}_2\text{CrTO}_6$  system ( $T = \text{Os, Ru}$ ), *Physical Review B* 77(11) (2008) 115101.
- [8] O.N. Meetei, O. Erten, M. Randeria, N. Trivedi, P. Woodward, Theory of High  $T_C$  Ferrimagnetism in a Multiorbital Mott Insulator, *Physical review letters* 110(8) (2013) 087203.
- [9] R. Morrow, J.R. Soliz, A.J. Hauser, J.C. Gallagher, M.A. Susner, M.D. Sumption, A.A. Aczel, J. Yan, F. Yang, P.M. Woodward, The effect of chemical pressure on the structure and properties of  $\text{A}_2\text{CrOsO}_6$  ( $A = \text{Sr, Ca}$ ) ferrimagnetic double perovskite, *Journal of Solid State Chemistry* 238 (2016) 46-52.
- [10] P. Majewski, S. Geprägs, A. Boger, M. Opel, A. Erb, R. Gross, G. Vaitheeswaran, V. Kanchana, A. Delin, F. Wilhelm, Magnetic moments of W 5d in  $\text{Ca}_2\text{CrWO}_6$  and  $\text{Sr}_2\text{CrWO}_6$  double perovskites, *Physical Review B* 72(13) (2005) 132402.
- [11] P. Majewski, S. Geprägs, O. Sanganas, M. Opel, R. Gross, F. Wilhelm, A. Rogalev, L. Alff, X-ray magnetic circular dichroism study of Re 5d magnetism in  $\text{Sr}_2\text{CrReO}_6$ , *Applied physics*

letters 87(20) (2005) 202503.

[12] M. Wojcik, E. Jedryka, S. Nadolski, D. Rubi, C. Frontera, J. Fontcuberta, B. Jurca, N. Dragoe, P. Berthet, Electronic self-doping of Mo states in  $A_2\text{FeMoO}_6$  ( $A = \text{Ca, Sr, and Ba}$ ) half-metallic ferromagnets: A nuclear magnetic resonance study, *Physical Review B* 71(10) (2005) 104410.

[13] S. Geprägs, P. Majewski, R. Gross, C. Ritter, L. Alff, Electron doping in the double perovskite  $\text{La}_x\text{A}_{2-x}\text{CrWO}_6$  with  $A = \text{Sr and Ca}$ , *Journal of applied physics* 99(8) (2006) 08J102.

[14] J. Navarro, C. Frontera, L. Balcells, B. Martinez, J. Fontcuberta, Raising the Curie temperature in  $\text{Sr}_2\text{FeMoO}_6$  double perovskites by electron doping, *Physical Review B* 64(9) (2001) 092411.

[15] N. Zu, J. Wang, Z. Wu, Pressure-Induced Half-Metallic Ferrimagnetism in  $\text{La}_2\text{VMnO}_6$ , *The Journal of Physical Chemistry C* 117(14) (2013) 7231-7235.

[16] R. Macquart, S.-J. Kim, W.R. Gemmill, J.K. Stalick, Y. Lee, T. Vogt, H.-C. zur Loye, Synthesis, structure, and magnetic properties of  $\text{Sr}_2\text{NiOsO}_6$  and  $\text{Ca}_2\text{NiOsO}_6$ : Two new osmium-containing double perovskites, *Inorganic chemistry* 44(26) (2005) 9676-9683.

[17] A. Kumar Paul, M. Reehuis, C. Felser, P.M. Abdala, M. Jansen, Synthesis, Crystal Structure, and Properties of the Ordered Double Perovskite  $\text{Sr}_2\text{CoOsO}_6$ , *Zeitschrift für anorganische und allgemeine Chemie* 639(14) (2013) 2421-2425.

[18] I. Qasim, P.E. Blanchard, S. Liu, C. Tang, B.J. Kennedy, M. Avdeev, J.A. Kimpton, Ordered vs. disordered perovskites; structural studies of Fe-doped  $\text{SrIrO}_3$  and  $\text{SrRuO}_3$ , *Journal of Solid State Chemistry* 206 (2013) 242-250.

[19] A. Faik, J. Igartua, E. Iturbe-Zabalo, G. Cuello, A study of the crystal structures and the phase transitions of  $\text{Sr}_2\text{FeSbO}_6$ ,  $\text{SrCaFeSbO}_6$  and  $\text{Ca}_2\text{FeSbO}_6$  double perovskite oxides, *Journal of Molecular Structure* 963(2-3) (2010) 145-152.

[20] L.O.S. Martín, J. Chapman, G. Cuello, J. Gonzalez - Calbet, M. Arriortua, T. Rojo, *Crystal*



structure of the ordered double perovskite,  $\text{Sr}_2\text{NiTeO}_6$ , *Zeitschrift für anorganische und allgemeine Chemie* 631(11) (2005) 2127-2130.

[21] B. Orayech, L. Ortega-San-Martin, I. Urcelay-Olabarria, L. Lezama, T. Rojo, M.I. Arriortua, J. Igartua, The effect of partial substitution of Ni by Mg on the structural, magnetic and spectroscopic properties of the double perovskite  $\text{Sr}_2\text{NiTeO}_6$ , *Dalton Transactions* 45(36) (2016) 14378-14393.

[22] A.K. Paul, M. Jansen, B. Yan, C. Felser, M. Reehuis, P.M. Abdala, Synthesis, crystal structure, and physical properties of  $\text{Sr}_2\text{FeOsO}_6$ , *Inorganic chemistry* 52(11) (2013) 6713-6719.

[23] A. Taylor, R. Morrow, D. Singh, S. Calder, M. Lumsden, P. Woodward, A. Christianson, Magnetic order and electronic structure of the  $5d^3$  double perovskite  $\text{Sr}_2\text{ScOsO}_6$ , *Physical Review B* 91(10) (2015) 100406.

[24] E. Kermarrec, C.A. Marjerrison, C. Thompson, D.D. Maharaj, K. Levin, S. Kroeker, G.E. Granroth, R. Flacau, Z. Yamani, J.E. Greedan, Frustrated fcc antiferromagnet  $\text{Ba}_2\text{YOsO}_6$ : structural characterization, magnetic properties, and neutron scattering studies, *Physical Review B* 91(7) (2015) 075133.

[25] W.R. Gemmill, M.D. Smith, R. Prozorov, H.-C. zur Loye, Crystal growth and magnetic properties of lanthanide-containing osmium double perovskites,  $\text{Ln}_2\text{NaOsO}_6$  (Ln= La, Pr, Nd), *Inorganic chemistry* 44(8) (2005) 2639-2646.

[26] R. Morrow, K. Samanta, T. Saha Dasgupta, J. Xiong, J.W. Freeland, D. Haskel, P.M. Woodward, Magnetism in  $\text{Ca}_2\text{CoOsO}_6$  and  $\text{Ca}_2\text{NiOsO}_6$ : Unraveling the mystery of superexchange interactions between 3d and 5d ions, *Chemistry of Materials* 28(11) (2016) 3666-3675.

[27] H.L. Feng, S. Calder, M.P. Ghimire, Y.-H. Yuan, Y. Shirako, Y. Tsujimoto, Y. Matsushita, Z. Hu, C.-Y. Kuo, L.H. Tjeng, T.-W. Pi, Y.-L. Soo, J. He, M. Tanaka, Y. Katsuya, M. Richter, K. Yamaura,  $\text{Ba}_2\text{NiOsO}_6$ : A Dirac-Mott insulator with ferromagnetism near 100 K, *Physical*

Review B 94(23) (2016) 235158.

[28] L. Ortega-San-Martin, A.J. Williams, A. Storer, J.P. Attfield, Frustrated Orders in the Perovskite  $(\text{Bi}_{0.5}\text{Sr}_{0.5})\text{CrO}_3$ , *Chemistry of Materials* 21(12) (2009) 2436-2441.

[29] M. Retuerto, M. Garcia-Hernandez, M. Martinez-Lope, M. Fernandez-Diaz, J. Attfield, J. Alonso, Switching from ferro-to antiferromagnetism in  $\text{A}_2\text{CrSbO}_6$  (A= Ca, Sr) double perovskites: a neutron diffraction study, *Journal of Materials Chemistry* 17(33) (2007) 3555-3561.

[30] N. Brese, M. O'keeffe, Bond-valence parameters for solids, *Acta Crystallographica Section B: Structural Science* 47(2) (1991) 192-197.

[31] D. Altermatt, I. Brown, The automatic searching for chemical bonds in inorganic crystal structures, *Acta Crystallographica Section B: Structural Science* 41(4) (1985) 240-244.

[32] I. Brown, D. Altermatt, Bond-valence parameters obtained from a systematic analysis of the inorganic crystal structure database, *Acta Crystallographica Section B: Structural Science* 41(4) (1985) 244-247.

[33] J.-I. Yamaura, S. Yonezawa, Y. Muraoka, Z. Hiroi, Crystal structure of the pyrochlore oxide superconductor  $\text{KOs}_2\text{O}_6$ , *Journal of Solid State Chemistry* 179(1) (2006) 336-340.

[34] A. Efros, B. Shklovskii, Coulomb gap and low temperature conductivity of disordered systems, *Journal of Physics C: Solid State Physics* 8(4) (1975) L49.

[35] A.J. Rettie, H.C. Lee, L.G. Marshall, J.-F. Lin, C. Capan, J. Lindemuth, J.S. McCloy, J. Zhou, A.J. Bard, C.B. Mullins, Combined charge carrier transport and photoelectrochemical characterization of  $\text{BiVO}_4$  single crystals: intrinsic behavior of a complex metal oxide, *Journal of the American Chemical Society* 135(30) (2013) 11389-11396.

[36] A.J. Steele, P.J. Baker, T. Lancaster, F.L. Pratt, I. Franke, S. Ghannadzadeh, P.A. Goddard, W. Hayes, D. Prabhakaran, S.J. Blundell, Low-moment magnetism in the double perovskites  $\text{Ba}_2\text{MOsO}_6$  (M= Li, Na), *Physical Review B* 84(14) (2011) 144416.

- [37] D. Sarma, P. Mahadevan, T. Saha-Dasgupta, S. Ray, A. Kumar, Electronic Structure of  $\text{Sr}_2\text{FeMoO}_6$ , Physical review letters 85(12) (2000) 2549.
- [38] S. Singhal, K. Chandra, Cation distribution and magnetic properties in chromium-substituted nickel ferrites prepared using aerosol route, Journal of Solid State Chemistry 180(1) (2007) 296-300.
- [39] H.L. Feng, S. Calder, M.P. Ghimire, Y.-H. Yuan, Y. Shirako, Y. Tsujimoto, Y. Matsushita, Z. Hu, C.-Y. Kuo, L.H. Tjeng,  $\text{Ba}_2\text{NiOsO}_6$ : A Dirac-Mott insulator with ferromagnetism near 100 K, Physical Review B 94(23) (2016) 235158.
- [40] H.L. Feng, Z. Deng, M. Wu, M. Croft, S.H. Lapidus, S. Liu, T.A. Tyson, B.D. Ravel, N.F. Quackenbush, C.E. Frank, High-Pressure Synthesis of  $\text{Lu}_2\text{NiIrO}_6$  with Ferrimagnetism and Large Coercivity, Inorganic chemistry 58(1) (2018) 397-404.
- [41] H. Kato, T. Okuda, Y. Okimoto, Y. Tomioka, K. Oikawa, T. Kamiyama, Y. Tokura, Structural and electronic properties of the ordered double perovskites  $A_2M\text{ReO}_6$  ( $A = \text{Sr, Ca}$ ;  $M = \text{Mg, Sc, Cr, Mn, Fe, Co, Ni, Zn}$ ), Physical Review B 69(18) (2004) 184412.

## Chapter 6 General Conclusions and Future Prospects

### 6.1 General Conclusions

5d metal oxides have garnered significant interest in the past few years, leading to such spectacular phenomena as high  $T_c$  ferrimagnetism, half metallicity, ferroelectric metal, metal-insulator transition and etc. The explorations of new materials involve 5d metals where the interplay of spin-orbit coupling and strong correlations are expected to lead to more novel phases of matter. The work of this thesis targets 5d metal oxides materials and expects to complement experimental results for understanding their novel physical phenomena. Here are eight perovskite-related mercury or osmium oxides included in this thesis, which were synthesized under high-pressure and high-temperature (HPHT) conditions and characterized through crystal structure, physical properties measurements. The main achievements are summarized below:

#### (i) Crystal structure and semimetallic property of $\text{HgPbO}_3$

The polycrystalline and single crystal  $\text{HgPbO}_3$  were successfully synthesized under HPHT conditions. The crystal structure of it was well characterized as a centrosymmetric model with a space group of  $R\bar{3}m$  rather than as a noncentrosymmetric model as was expected.  $\text{Pb}^{4+}$  was found to be octahedrally coordinated by six oxygen atoms as usual, while  $\text{Hg}^{2+}$  is coordinated by three oxygen atoms in a planar manner, which is a very rare coordination for Hg in a solid-state material. The magnetic and electronic transport properties were investigated in terms of the magnetic susceptibility, magnetization, Hall coefficient, and specific heat capacity of polycrystalline  $\text{HgPbO}_3$ . Although  $\text{HgPbO}_3$  has a carrier concentration ( $= 7.3\text{--}8.5 \times 10^{20} \text{ cm}^{-3}$ ) that is equal to that of metallic oxides, the very weak temperature dependence of the electrical resistivity (residual-resistivity ratio  $\sim 1.5$ ), the significant diamagnetism ( $= -1.02 \times 10^{-4} \text{ emu}$

mol<sup>-1</sup> at 300 K) that is in the same order of that of Bi powder, and the remarkably small Sommerfeld coefficient [ $= 1.6(1) \times 10^{-3} \text{ J mol}^{-1} \text{ K}^{-2}$ ] implied that it is semi-metallic in nature. HgPbO<sub>3</sub> does not have a cage structure; nevertheless, at temperatures below approximately 50 K, it clearly exhibits phonon excitation of an anharmonic vibrational mode that are as significant as those of RbOs<sub>2</sub>O<sub>6</sub>.

## **(ii) New phase of Ba<sub>3</sub>CuOs<sub>2</sub>O<sub>9</sub> and Ba<sub>3</sub>NiOs<sub>2</sub>O<sub>9</sub> under high-pressure and high-temperature conditions**

The osmium perovskite oxide compounds with the composition of Ba<sub>3</sub>CuOs<sub>2</sub>O<sub>9</sub> and Ba<sub>3</sub>NiOs<sub>2</sub>O<sub>9</sub> can be synthesized using conventional solid-state reaction and both of them show antiferromagnetic properties below  $T_c$ . New polymorphs of these two compounds were synthesized under high-pressure and high-temperature conditions at 6 GPa and 1100 °C. Under the synthetic condition, Ba<sub>3</sub>CuOs<sub>2</sub>O<sub>9</sub> crystallizes into a hexagonal structure ( $P6_3/mmc$ ) with  $a = 5.75178(1) \text{ \AA}$  and  $c = 14.1832(1) \text{ \AA}$ , and undergoes a 1.36% increment in density, compared to that of the orthorhombic phase. Although Ba<sub>3</sub>CuOs<sub>2</sub>O<sub>9</sub> maintains its 6H perovskite-type structure, the distribution of Cu and Os atoms are dramatically altered; (Cu)<sub>4a</sub>(Os,Os)<sub>8f</sub> transits to (Os)<sub>2a</sub>(Cu,Os)<sub>4f</sub> ordering over the corner- and face-sharing sites, respectively. The hexagonal Ba<sub>3</sub>CuOs<sub>2</sub>O<sub>9</sub> exhibits a ferrimagnetic transition at 290 K, which is in stark contrast to the antiferromagnetic transition at 47 K exhibited by the orthorhombic Ba<sub>3</sub>CuOs<sub>2</sub>O<sub>9</sub>. The enhanced transition temperature is most likely due to the strongly antiferromagnetic Os<sup>5+</sup>–O–Os<sup>5+</sup> bonds and the moderately antiferromagnetic Os<sup>5+</sup>–O–Cu<sup>2+</sup> bonds, the angles of which are both approximately 180°. The 290 K ferrimagnetic transition temperature is the highest reported for triple-perovskite osmium oxides. Besides, the coercive field is greater than 70 kOe at 5 K, which is remarkable among the coercive fields of magnetic oxides. To better understand the magnetic properties of Ba<sub>3</sub>CuOs<sub>2</sub>O<sub>9</sub>, a comparative study was carried out. The replacement of Cu by Ni was to produce another hexagonal osmium perovskite oxides under HPHT conditions.

Compared to  $\text{Ba}_3\text{CuOs}_2\text{O}_9$ ,  $\text{Ba}_3\text{NiOs}_2\text{O}_9$  shows higher ferrimagnetic transition temperature at 370 K while the coercive field of  $\text{Ba}_3\text{NiOs}_2\text{O}_9$  becomes smaller.

**(iii) The structural transition and variation of magnetic properties for 3d-5d hybrid double perovskite oxides  $\text{Sr}_2\text{CrOsO}_6$  driven by Ni-substitution**

The substitutional series samples of  $\text{Sr}_2\text{Cr}_{1-x}\text{Ni}_x\text{OsO}_6$  ( $x = 0, 0.25, 0.5, 0.75$  and  $1$ ) were synthesized successfully. The structural transition from cubic to tetragonal occurs at  $x = 0.5$  while it is found that the magnetic property changes from ferrimagnetic to antiferromagnetic when the substitutional Ni increases from 0.5 to 0.75. All of these results make the intermediate Ni-substitution compound  $\text{Sr}_2\text{Cr}_{0.5}\text{Ni}_{0.5}\text{OsO}_6$  unique. The transition of magnetic property is not accompanied by obvious structural transition, indicating the mechanism of magnetic variation in this substitutional series samples is not driven by structure simply, in another word, there exists more complicated physical mechanism behind it.  $\text{Sr}_2\text{Cr}_{0.5}\text{Ni}_{0.5}\text{OsO}_6$  maintains the ferrimagnetic property below  $T_c$  of 348 K, meanwhile, it shows largest saturation magnetization value of  $1.2 \mu_B/\text{mol}$  among the series samples.

## **6.2 Future Prospects**

There are still several unraveled puzzles left by current experimental efforts of this thesis: (a) The exact magnetic structures of  $\text{Ba}_3\text{CuOs}_2\text{O}_9$  and  $\text{Ba}_3\text{NiOs}_2\text{O}_9$  in **chapter 4** require neutron diffraction measurements. (b) To better understand the mechanism of magnetic properties and crystal structure for  $\text{Sr}_2\text{Cr}_{0.5}\text{Ni}_{0.5}\text{OsO}_6$  and other Ni-substitution samples in **chapter 5**, more measurements and theoretical calculations should be involved and the valence states of Cr, Ni and Os need to be investigated by X-ray absorption measurements. These proposed scenarios will go on in the future for supplementing this thesis.

Except the 5d related compounds included in this thesis, I am still working on other

5d oxides. Recently, a double perovskite  $\text{Sr}_3\text{OsO}_6$  was reported to show ferromagnetism above 1000 K by Yuki K. Wakabayashi and et al [1]. That reported  $T_c$  of 1060 K is the highest value among all insulating oxides. The  $\text{Sr}_3\text{OsO}_6$  films in this paper were grew epitaxially on  $\text{SrTiO}_3$  substrates and crystallize into a cubic double-perovskite structure. However, the structure and magnetic properties of bulk  $\text{Sr}_3\text{OsO}_6$  has not reported yet so far, although the isoelectronic compound  $\text{Ca}_3\text{OsO}_6$  has been synthesized under HPHT conditions by Hai Luke Feng and et al. in 2013 [2]. Therefore, I have prepared the bulk sample of  $\text{Sr}_3\text{OsO}_6$  using high-pressure technique and the XRD pattern is shown in **Fig. 6.1**. The studies of bulk  $\text{Sr}_3\text{OsO}_6$  is still in progress.

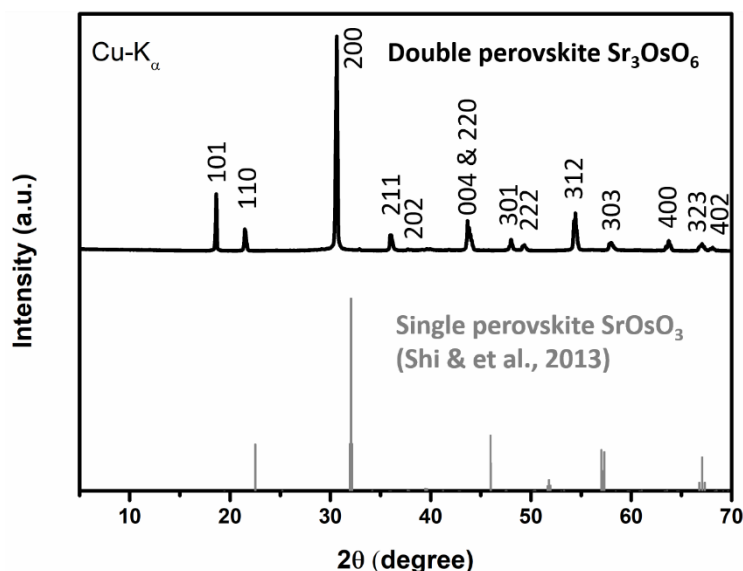


**Fig. 6.1** Powder XRD patterns for bulk  $\text{Sr}_3\text{OsO}_6$

## References in chapter 6

- [1] Y.K. Wakabayashi, Y. Krockenberger, N. Tsujimoto, T. Boykin, S. Tsuneyuki, Y. Taniyasu, H. Yamamoto, Ferromagnetism above 1000 K in a highly cation-ordered double-perovskite insulator  $\text{Sr}_3\text{OsO}_6$ , Nature Communications 10(1) (2019) 535.
- [2] H.L. Feng, Y. Shi, Y. Guo, J. Li, A. Sato, Y. Sun, X. Wang, S. Yu, C.I. Sathish, K. Yamaura, High-pressure crystal growth and electromagnetic properties of 5d double-perovskite  $\text{Ca}_3\text{OsO}_6$ ,

Journal of Solid State Chemistry 201 (2013) 186-190.



## List of appended publications

**This thesis is based on the following publications.**

### *1. Scientific papers*

- [1] Jie Chen, Hai L. Feng, Yoshitaka Matsushita, Alexei A. Belik, Yoshihiro Tsujimoto, Yoshio Katsuya, Masahiko Tanaka, Meixia Wu, Man-Rong Li, Rongfu Zhou, Weijie Zhou, Hongbin Liang, Lirong Zheng, Martin Jansen, Kazunari Yamaura. High-pressure synthesis, crystal structure, and magnetic properties of hexagonal Ba<sub>3</sub>CuOs<sub>2</sub>O<sub>9</sub>. Journal of Solid State Chemistry 2019. 272, 182-188.

DOI: 10.1016/j.jssc.2019.02.003

- [2] Jie Chen, Yoshitaka Matsushita, Taras Kolodiaznyy, Alexei A. Belik, Yoshihiro Tsujimoto, Yoshio Katsuya, Masahiko Tanaka, Yu Su, Youguo Shi, and Kazunari Yamaura. High-Pressure Synthesis, Crystal Structure, and Semimetallic Properties of HgPbO<sub>3</sub>. Inorganic chemistry 2018. 57, 7601-7609.

DOI: 10.1021/acs.inorgchem.8b00482

### *2. Presentation*

- [1] Jie Chen, *et al.*, “High-pressure synthesis, crystal structure, and magnetic properties of hexagonal Ba<sub>3</sub>CuOs<sub>2</sub>O<sub>9</sub>” The March Meeting 2019 of the American Physical Society (APS), Mar. 4-8, 2019, Boston, USA.
- [2] Jie Chen, *et al.*, “A new triple perovskite compound Ba<sub>3</sub>CuOs<sub>2</sub>O<sub>9</sub> synthesized under high pressure and its magnetic and electronic properties”. The 28th annual meeting of MRS-J, Dec. 18-20, 2018, Kitakyushu, Japan.

- [3] Jie Chen, *et al.*, “High-pressure synthesis and magnetic and electrical properties of  $\text{HgPbO}_3$ ”. The 27th annual meeting of MRS-J, Dec. 5-7, 2017, Yokohama, Japan.
- [4] Jie Chen, *et al.*, “High-pressure synthesis and magnetic and electrical properties of  $\text{HgPbO}_3$ ”. The 15th International Conference on Advanced Materials (IUMRS-ICAM 2017), Aug. 27-Sep. 1, 2017, Kyoto, Japan.
- [5] Jie Chen, *et al.*, “High-pressure synthesis and magnetic and electrical properties of  $\text{HgPbO}_3$ ”. The 26th International Conference on High Pressure Science and Technology (AIRAPT 26), Aug. 18-23, 2017, Beijing, China.
- [6] Jie Chen, *et al.*, “High-pressure synthesis and magnetic and electrical properties of  $\text{HgPbO}_3$ ”. The 10th International Conference on the Science and Technology for Advanced Ceramics (STAC-10), Aug. 1-3, 2017, Yokohama, Japan.

## Acknowledgement

There are many people that have earned my gratitude for their contribution to my dissertation work over the past three years. Firstly, I would like to express my sincere gratitude to my supervisor Prof. Kazunari Yamaura for the continuous support of my Ph.D study. His guidance helped me in all the time of research and writing of this thesis. On the academic level, Yamaura-san taught me fundamentals of conducting experiments and writing papers. Under his supervision, I learned that to be a scientist requires diligence, conscientiousness and curiosity about science. On a personal level, Yamaura-san is always kindness and offered a lot of help about my living in Tsukuba. I also want to thank Prof. Sadamu Takeda, Prof. Hidenori Noguchi, Prof. Taro Nagahama and Prof. Yoshihiro Tsujimoto for serving as my Ph. D advisory committee members.

Besides, I would like to thank Dr. Alexei A. Belik for helps in experiment and paper publication. I sincerely thank Dr. Yoshitaka Matsushita for help in single crystal XRD measurement and structural refinement, Dr. Yoshio Katsuya and Dr. Masahiro Tanaka for help in Synchrotron XRD measurement, Dr. Taras Kolodiaznyi for teaching me electric transport measurement, Prof. Man-Rong Li for high-temperature magnetic susceptibility measurement, and Prof. Hongbin Liang for XANES measurement. I would like to give my gratitude to Dr. Yu Su and Dr. Lei Zhang that they taught me how to use lab facilities and helped in daily life. I would like to thank Dr. Hai Feng for his helpful discussions and suggestions.

Last but not the least, I thank my families and friends for supporting me spiritually throughout completing my Ph.D study and my life in general.